Microscale dynamics of dilution-induced asphaltene precipitation

by

Jia Meng

A thesis submitted in partial fulfillment of the requirements for the degree of

Doctor of Philosophy

in

Chemical Engineering

Department of Chemical and Materials Engineering

University of Alberta

Abstract

Phase separation by dilution with poor solvents is important for many separation processes, notably asphaltene precipitation in paraffinic froth treatment (PFT) in oil sands extraction. PFT is a step of bitumen froth treatment in which paraffinic solvent is added to the bitumen froth to reduce the viscosity and remove impurities along with asphaltene precipitation. It remains challenging to quantitatively understand the early stage dynamics of asphaltene precipitation induced by paraffinic solvent addition. The mixing conditions in the conventional bulk system were not well controlled, which might have a great effect on asphaltene precipitation, and further affects oil sands extraction efficiency.

This thesis studied asphaltene precipitation under controlled mixing conditions. A microfluidic device is designed and fabricated to control the mixing under diffusive dominant between model oil and the paraffinic solvent to study asphaltene precipitation without convective flows. The total internal reflection fluorescence (TIRF) microscope, which has a high spatial resolution ($\sim$ 200 nm) and temporal resolution (4 frames per second) is used to follow the growth dynamics of individual asphaltene domains. We observed the basic units of asphaltene precipitation in the diffusive mixing and controlled external mixing processes, which are named PSMPs. The radius of which is 200 - 400 nm and independent of the change of solvents. The asphaltene first precipitates as primary submicron particles (PSMPs) in the early stage of precipitation and then PSMPs further aggregate, resulting in the increase of asphaltene particle

size. This study direct visualizes asphaltene precipitation and aggregation under controlled mixing at the submicron scale, which was absent in the previous studies.

Afterwards, we found that the relative frequency of PSMPs to the total quantity of the particles is affected by the type and concentration of the precipitants. The population balance model (PBM) based on Smoluchowski aggregation model can describe the aggregation process based on the collision frequency and efficiency of particles. The experimental and simulation results of size distribution agree well with each other in our examined 23 types of precipitants. Unlike the conventional bulk system, in the diffusive mixing system, the yield of asphaltene is not only dependent on the Hildebrand solubility parameter but also affected by the diffusion coefficient of solvents to the model oil. Compared with pure n-heptane and n-decane, the mixture of them produces a higher proportion of PSMPs due to the difference in diffusion coefficients. The above findings prove the influence of the hydrodynamics factor (i.e., diffusion coefficient) on asphaltene precipitation and lead to the important role of mixing conditions, which was neglected in the previous research.

To investigate the influence of mixing conditions, a related system was studied as a basis for studying the influence of mixing conditions on asphaltene precipitation: dilution-induced nanodroplets formation at high viscosity. Asphaltene precipitation and nanodroplets formation are comparable because they both are phase separation processes due to the addition of poor solvents. However, the viscosity of the asphaltene precipitation system is higher than the aqueous system. The total volume of the nanodroplets formed by the dilution-induced phase separation increases with the flow rate and reaches a plateau after a critical value. This is because the flow boundary layer becomes thicker than the concentration boundary layer due to the increase of viscosity, leading to the vanish of flow velocity on mass transfer at a high flow rate.

This work provides a fundamental understanding of the influence of mixing conditions on the dilution-induced phase separation process.

The following exploration used a model oil system to study the growth dynamics of asphaltene particles under 20 different mixing conditions. The morphology of the asphaltene particles, including surface coverage and particle size distribution in submicron scale and micron-scale are affected by the geometry of the microfluidic chamber, orientation, flow rate of mixing and temperature. COMSOL is used to simulate the flow profile to explore the mechanism behind the phenomenon. Shear force and local concentration are the two most important reasons for the influence of mixing dynamics on dilution-induced phase separation. The findings may potentially lead to technology innovation based on controlled solvent addition to achieve reduced use of solvents in the PFT process.

Preface

This thesis is my original work. The introduction in Chapter 1, literature review in Chapter 2, and conclusion in Chapter 8 are organized and written by myself only.

Chapter 3 is a modified version of a published journal article "Microfluidic device coupled with total internal reflection microscopy for in situ observation of precipitation" in *European Physical Journal E*. I am the first author of this paper. I was responsible for the fabrication of the microfluidic chamber, data collection of asphaltene precipitation, analysis of the results and drafting of the initial manuscript. Jae Bem You assisted in the revision of the draft. Gilmar F. Arends validated the device by crystallization. Hao Hao programmed the MATLAB codes for image analysis. Xiaoli Tan provided the sample for the experiments and assisted in the revision of the manuscript. Xuehua Zhang supervised the whole project and revised the manuscript. All the authors contributed to the discussion on the manuscript.

Chapter 4 of this thesis is a modified version of a published journal article "Primary submicron particles from early stage asphaltene precipitation revealed in situ by total internal reflection fluorescence microscopy in a model oil system" in *Fuel*. I am the first author and the main contributor. My responsibility was to collect data, organize analysis and wrote the manuscript. Jae Bem You assisted in the revision of the manuscript. Hao Hao made the MATLAB codes for image analysis. Xiaoli Tan provided samples and assisted in the revision of the manuscript. Xuehua Zhang supervised the whole project and revised the manuscript. All the authors contributed to the discussion on the manuscript.

Chapter 5 of this thesis is a modified version of a published journal arti-

cle "Size distribution of primary submicron particles and larger aggregates in solvent-induced asphaltene precipitation in a model oil system" in *Fuel*. I am the first author and main contributor. I was responsible for the data collection and analysis, as well as drafting the manuscript. Somasekhara Goud Sontti helped with the editing of the manuscript. Mohsen Sadeghi helped with the PBM model to verify the experimental results. Gilmar F. Arends helped with the modelling of the diffusion coefficient. Petr Nikrityuk provided tutorial materials on solving ODE equations of PBM. Xiaoli Tan provided the chemical samples and assisted in the revision of the manuscript. Xuehua Zhang supervised the whole project and revised the manuscript. All the authors contributed to the discussion on the manuscript

Chapter 6 of this thesis is a modified version of a published journal article "Viscosity-mediated growth and coalescence of surface nanodroplets" in *Journal of Physical Chemistry C*. I am the first author and the main contributor. I was responsible for the data collection and analysis, as well as drafting the initial manuscript. Jae Bem You assisted in the mechanism exploration of the phenomenon and revision of the draft. Xuehua Zhang supervised the whole project and revised the manuscript. All the authors contributed to the discussion on the manuscript

Chapter 7 of this thesis is a manuscript in preparation. I am the first author and the main contributor. I was responsible for the data collection and analysis, as well as drafting the initial manuscript. Chiranjeevi Kanike helped with the COMSOL simulation. Somasekhara Goud Sontti helped with the editing of the manuscript. Arnab Atta assisted in the revision of the manuscript. Xiaoli Tan provided the sample for the experiment and assisted in the revision of the manuscript. Xuehua Zhang supervised the whole project and revised the manuscript. All the authors contributed to the discussion on the manuscript

Acknowledgements

I would like to express my sincere appreciation to all people who have been supporting and helping me in my daily life.

I am sincerely grateful to my supervisor Prof. Xuehua Zhang, for her constant guidance, patience and encouragement throughout my Ph.D. study. She is always full of enthusiasm and passion for scientific research, which deeply affects me and gives me the motivation to explore the unknown. Her guidance and knowledge help me overcome difficulties in my research and inspire me to a better stage. I will never forget her for teaching me to seek novel ideas, to think critically and to teach me how to write. All of these will be with me for the rest of my life.

My hearty thank to my co-supervisor Prof. Xiaoli Tan, for his technical and intellectual help. He is my guide in the oil sands field. He always provides me with very good ideas and can solve my problems perfectly.

Special thanks to my group members: Dr. Petr Nikrityuk, Dr. Jae Bem You, Dr. Somasekhara Goud Sontti, Dr. Hao Hao, Dr. Shantanu Maheshwari, Chiranjeevi Kanike, Zixiang Wei, Qiuyun Lu, Mohsen Sadeghi, and Gilmar F. Arends for their direct contribution to the work in this thesis. I would like to also thank Dr. John M. Shaw, Dr. Murray Gray, Dr. Detlef Lohse, Dr. Brendan Dyett, Dr. Jiasheng Qian, Dr. Binglin Zeng, Zhengxin Li, Yawen Gao, Yanan Li, Haichang Yang, and Howon Choi for their discussion, suggestion and encouragement.

I would like to acknowledge Institute for Oil Sands Innovation (IOSI) (Imperial Oil Ltd., Alberta Innovates and University of Alberta) for the funding supports and our stewards Leyli Mirmontazeri and Sepideh Mortazavi Manesh for their help and discussion.

I would like to thank the staff of Cell Imaging Center at the University of Alberta, Dr. Stephen Ogg and Dr. Greg Plummber, the staff of IOSI, Lisa Brandt and Brittany Mackinnon, the staff of NanoFab, Dr. Aaron Hryciw, Stephanie Bozic, and Scott Munro for their help in the instrument training and technician support.

Great gratitude to my parents for their selfless support and continuous encouragement.

Finally, I would like to thank my girlfriend Tianzi Bai for her constant support, company, and love.

Contents

List of Tables

List of Figures

List of Symbols

α = Correction factor for mixing front shift

$\alpha_{i,j}$ = Collision frequency $(m^3/mol \cdot s)$

Ar = Archimedes number

AFM = Atomic force microscope

$\beta_{i,j}$ = Collision efficiency

b = Breakup rate coefficient $(m^{-1} \cdot s^{-1})$

B_j = Fragmentation rate of particle j (s^{-1})

B_k = Fragmentation rate of particle k (s^{-1})

χ = Flory-Huggins interaction parameter

c = Concentration

c_{asp} = Concentration of asphaltene

c_{onset} = Onset concentration of pentane

c_{pen} = Concentration of pentane

c_{pre} = Concentration of precipitant

c_{eth} = Saturation concentration of oil in ethanol

c_{∞} = Oil concentration in the flow

c_{tol} = Concentration of toluene

c_{wat} = Saturation concentration of oil in water

$C_1(0)$ = Initial concentration of unstable asphaltene

δ = Hildebrand solubility parameter $(MPa^{1/2})$

δ_{asp} = Hildebrand solubility parameter of asphaltene $(MPa^{1/2})$

δ_{dec} = Hildebrand solubility parameter of n-decane $(MPa^{1/2})$

δ_{hep} = Hildebrand solubility parameter of n-heptane $(MPa^{1/2})$

δ_i = Hildebrand solubility parameter of component i $(MPa^{1/2})$

δ_{mal} = Hildebrand solubility parameter of maltene ($MPa^{1/2}$)

$\delta_{mixture}$ = Hildebrand solubility parameter of mixture ($MPa^{1/2}$)

δ_{pen} = Hildebrand solubility parameter of n-pentane ($MPa^{1/2}$)

δ_{tol} = Hildebrand solubility parameter of toluene ($MPa^{1/2}$)

$\Delta\rho$ = Density difference between solutions (kg/m^3)

ΔG_{mixing} = Change in free energy of mixing (J/mol)

ΔH_ν = Heat vaporization (J/mol)

$\Delta\rho_i$ = Density difference between particle i and solution (kg/m^3)

$\Delta\rho_j$ = Density difference between particle j and solution (kg/m^3)

d_f = Fractal dimension

d_i = Diameter of particle with size i

d_j = Diameter of particle with size j

D = Diffusion coefficient (m^2/s)

D_{21} = Diffusion coefficient of n-alkane to toluene (m^2/s)

DBSA = 4-Dodecylbenzenesulfonic acid

DLA = Diffusion limited aggregation

D_{dt} = Diffusion coefficient of n-decane to toluene (m^2/s)

D_{ht} = Diffusion coefficient of n-heptane to toluene (m^2/s)

D_i^* = Self-diffusion coefficient of solute i ($cm^2 \cdot s^{-1}$)

D_j^* = Self-diffusion coefficient of solvent j ($cm^2 \cdot s^{-1}$)

D_{pt} = Diffusion coefficient of n-pentane to toluene (m^2/s)

η_a = numbers of moles of asphaltene

η_m = numbers of moles of maltene

F_{RI} = Refractive index function

γ_i = Activity coefficient of solute at T and x_i

$\gamma_{k,j}$ = Volume fraction of the fragments of size i originating from size j particles.

Γ = Thermodynamic factor

g = Gravity acceleration constant (m/s^2)

G = Shear rate (s^{-1})

h = Height of the quasi-2D channel (m)

HDODA = 1,6 - Hexanediol diacrylate

I = Normalized intensity

I_{max} = Maximum intensity

k_B = Boltzmann constant (J/K)

$K_{i,j}$ = Collision kernels of particles with size i, j $(m^3/mol \cdot s)$

$K_{i,k}$ = Collision kernels of particles with size i, k $(m^3/mol \cdot s)$

K_m = Correction for discontinuity of fluid

l = Distance to the side channel (μm)

L_0 = Length of the compressible polymer brush

λ = Thickness of the boundary layer (μm)

$\dot{m}$ = Mass growth rate (kg/s)

μ = Viscosity $(mPa \cdot s)$

μ_1 = Viscosity of component 1 $(mPa \cdot s)$

μ_2 = Viscosity of component 2 $(mPa \cdot s)$

m_p = Quantity of primary sub-micron particle in one aggregate

M_j = Molecular weight of solvent j (g/mol)

MMA = methylmethacrylate

ν = Kinematic viscosity (m^2/s)

ν_m = Molar volume of maltene

n = Refractive index

n_i = Units of aggregates with size i

n_j = Units of aggregates with size j

n_k = Units of aggregates with size k

n_o = Total units of primary sub-micron particle

N = Maximum primary sub-micron particles that one aggregate contains

N_a = Avogadro constant

N_1 = Molar fraction of component 1

N_2 = Molar fraction of component 2

NF = 4-Nonylphenol

NFT = Naphthenic froth treatment

$\dot{\omega_d}$ = Reduction rate of asphaltene by dilution (mol/s)

$\dot{\omega_p}$ = Reduction rate of asphaltene by precipitation (mol/s)

OTS = Octadecyltrichlorosilane

$\partial_r c|_{Rr}$ = Concentration gradient at the interface

ϕ_a = Volume fraction of asphaltene (%)

ϕ_i = Volume fraction of component i (%)

ϕ_m = Volume fraction of maltene (%)

ψ_e = Maximum energy barrier constant ($J \cdot MPa^{1/2}$)

$\phi(t, l)$ = Concentration of n-alkane at the given time and position

ϕ^{alk} = Concentration of n-alkane (%)

ϕ^{tol} = Concentration of toluene (%)

ϕ_0 = Initial concentration of n-alkane in the paraffinic solvent (%)

ϕ_0^{dec} = Initial concentration of n-decane in solution B_{DT} (%)

ϕ_0^{hep} = Initial concentration of n-heptane in solution B_{HT} (%)

ϕ_0^{pen} = Initial concentration of n-pentane in solution B_{PT} (%)

ψ_j = Association factor of solvent j

Pe = Péclet number

PAH = Polycyclic aromatic hydrocarbon

PBM = Population balance model

PFT = Paraffinic froth treatment

PSV = Primary separation vessel

Q = Particle quantity in the unit surface area

Q_p = Quantity of primary sub-micron particles at initial condition

ρ_B = Density of solution B (kg/m^3)

ρ_{oil} = Density of oil (kg/m^3)

r_{psmp} = Radius of the primary sub-micron particle (μm)

R = Ideal gas constant ($J \cdot K^{-1}\ mol^{-1}$)

RLA = Reaction limited aggregation

R_o = Initial particle radius (m)

R_p = Radius of particle (m)

R_r = Radius of nanodroplets

Ra = Rayleigh number

R_p = Ratio between primary sub-micron particle to the total quantity of asphaltene particles

SAGD = Steam-assisted gravity drainage

SARA = Saturates, aromatics, resins, asphaltenes

S/B ratio = Solvent to bitumen ratio

SC = Surface coverage (%)

SEM = Scanning electron microscope

τ = Duration of oversaturation pulse (s)

τ_D = Diffusion time (s)

τ_R = Reaction time (s)

t = Time (s)

$t_{detection}$ = Detection time of asphaltene particles (s)

t_{onset} = Moment that precipitant concentration reaches onset

t_{final} = Moment that asphaltene precipitation stops

t_{Rdec} = Mixing retention time of n-decane and asphaltene solution (s)

t_{Rhep} = Mixing retention time of n-heptane and asphaltene solution (s)

t_{Rpen} = Mixing retention time of n-pentane and asphaltene solution (s)

T = Temperature (K)

TIRF = Total internal reflection fluorescence microscope

V_1 = Volume of primary particles (m^3)

V_{drop} = Volume of nanodroplets (m^3)

V_i = Particle volume (m^3)

$V_{i,BP}$ = Molar volume of solute i at normal boiling temperature ($cm^3 \cdot mol^{-1}$)

V_m = Molar volume in the condensed phase (m^3)

Vol = Total volume of nanodroplets

w = Width of the chamber (cm)

$\overline{X}^2_{Brownian}$ = Moving distance due to Brownian motion (m)

$\overline{X}^2_{Settling}$ = Moving distance due to Settling (m)

ζ = Oversaturation

Chapter 1

Introduction

1.1 Background and motivations

The exploitation of heavy oils, such as bitumen, has become increasingly important as the rate at which high-quality fossil fuels are discovered is lower than the rate at which fossil fuels are consumed. About 10% of the proven oil reserves in the world are located in the Alberta oil sands, which are impregnated with high molar mass petroleum referred to as bitumen. Unlike most oil sands in other parts of the world, oil sands in Alberta are water-wet, making bitumen extraction feasible by using water-based extraction technologies.

In the water-based oil sands extraction process, the oil sands ores are crushed into lumps and mixed with warm water. The resulting slurry is transported to the primary separation vessel (PSV) through a pipeline. The top layer of PSV is called bitumen froth and is transported to the froth treatment facility to obtain bitumen for further upgrading or purification. There are two types of froth treatment technologies: naphthenic froth treatment (NFT) and paraffinic froth treatment (PFT). NFT was the only technology for froth treatment from the 1970s to the early 2000s. However, the PFT has been used leveraged in many oil sands operations newly because of the cleaner bitumen product.

In PFT, solvents containing primarily paraffin hydrocarbons, which is called the paraffinic solvent, are added to dilute the bitumen froth. The addition of the paraffinic solvent enables the removal of most of water and solids by gravity due to the reduction of viscosity. In addition, a mixture of hydrocar-

bons, which is called asphaltene, precipitates out from bitumen. Asphaltene particles can further agglomerate with remaining water and solids to result in a cleaner bitumen product.

Although asphaltene precipitation contributes to a better product, it does not mean that more asphaltene precipitation is better. This is because excessive asphaltene precipitation is not conducive to product quality enhancement. More asphaltene precipitation is associated with the loss of bitumen in tailings, resulting in a low overall bitumen recovery. To achieve optimal impurity removal and avoid problems caused by asphaltene precipitation, understanding the influence factors of asphaltene precipitation is very important.

Previous research usually only considered the thermodynamics effect, including S/B ratio, type of the paraffinic solvent, temperature, and pressure. There are remaining questions about the influence of hydrodynamics (i.e., mixing dynamics) on asphaltene precipitation. Recently, a similar process, dilution-induced liquid-liquid phase separation, has been studied by solvent exchange method for several years. Solvent exchange method utilizes a poor solvent to displace a solution of oil in a good solvent in a ternary system. The displacement causes oversaturation of oil, leading to the nanodroplets formation. In this process, the volume and size distribution of the final nanodroplets are highly affected by the mixing conditions, including the flow rate, geometry of the device, and the oversaturation level. Likewise, in the system of asphaltene precipitation, bitumen can be regarded as the solution of asphaltene in a good solvent, paraffinic solvent can be regarded as the poor solvent. The injection of paraffinic solvent into bitumen causes oversaturation of asphaltene in the mixture, resulting in asphaltene precipitation. Therefore, this project studies the asphaltene precipitation on the basis of dilution-induced liquid-liquid phase separation.

In this study, we investigated the asphaltene precipitation under controlled external mixing. We studied the asphaltene precipitation under different mixing conditions and the effect of different solvents on asphaltene precipitation under the same mixing conditions. In addition, we directly visualized the asphaltene particles at the submicron scale, which was smaller than that at the

micron scale in the previous study.

1.2 Research objectives and scope of the thesis

The main objective of this thesis is to correlate the physical parameters of the solvents with the amount and size of asphaltene precipitates under controlled external mixing and understand the effect of the mixing dynamics on the dilution-induced asphaltene precipitation. Custom-built microfluidic chambers were utilized to control the mixing of a model oil and paraffinic solvent to induce asphaltene precipitation. Total internal reflection fluorescence (TIRF) microscopy was used to in-situ visualized the early stage of asphaltene precipitation with high spatial resolution.

Chapter 3 introduced the design and fabrication of a quasi-2D microfluidic chamber, which could control the mixing between two solutions dominated by diffusion. Solution doped with Nile red was used to confirm the diffusive-dominated mixing. Asphaltene precipitation demonstrated the feasibility of this microfluidic device for liquid-solid phase separation studies.

In Chapter 4, the microfluidic chamber introduced in Chapter 3 was used to study early stage of asphaltene precipitation under diffusive-dominated mixing. Total internal reflection fluorescence microscope (TIRF) was used to directly visualize the details of asphaltene particles at the submicron scale. The asphaltene precipitation at the early stage was visualized and the primary submicron particles (PSMPs) were found as the basic units in the diffusive dominated dilution-induced asphaltene precipitation. The evolution of the aggregation of PSMPs in response to different concentrations of n-pentane was studied.

Chapter 5 was the expansion of the work of Chapter 4. More types of n-alkanes, as well as the mixture of n-alkanes, were used as paraffinic solvents to trigger asphaltene precipitation. The ubiquitous formation of PSMP was proved in this chapter. The size distribution of asphaltene particles precipitated at different types, concentrations, and presence of inhibitors were

studied. PBM was used to fit the experimental results. In addition to Hildebrand solubility parameter, this study provided new insights into the influence of physical parameters of hydrodynamics on asphaltene precipitation.

In Chapter 6, a poor solvent was added to displace the a solution of oil in a good solvent to induce phase separation of a water-ethanol-oil ternary mixture. This method was called the solvent exchange and the flow conditions were highly controlled. Solvent exchange includes external mixing in comparison to diffusive-dominated mixing discussed in Chapter 3,4, and 5. Glycerol was added into the mixture to adjust the viscosity to 7.4 cP, 12.8 cP, and 18.0 cP. The total volume of the nanodroplets formed at different flow rates was studied. The understanding of nanodroplets formation at high viscosity was the basis for further understanding of asphaltene precipitation.

Chapter 7 used the solvent exchange method proposed in Chapter 6 to study asphaltene precipitation induced by the addition of n-heptane. 20 different mixing conditions were investigated, including changes of the flow rate, channel height, orientation, and temperature. COMSOL was used to simulate the mixing dynamics in the system and predictions were made of the surface coverage and size distribution of asphaltene particles. The reasons behind the influence of mixing dynamics on asphaltene precipitation were explored. This study provided new insights into the influence of mixing conditions on asphaltene precipitation with using the same solvent.

1.3 Thesis outline

This thesis includes eight chapters. Chapters 3-6 are the modified version of the published papers, and Chapter 7 is a paper under preparation. The content of each chapter is as follows:

Chapter 1 gives a brief introduction of the background and motivation, as well as the structure of this thesis.

Chapter 2 provides a literature review of solvent exchange, asphaltene precipitation and the remaining challenges.

Chapter 3 is a method section, which proposed a design of a diffusive

dominated microfluidic chamber and introduces the fabrication process. The chamber is also calibrated by experiment to show the diffusive dominated mixing. The proposed microfluidic chamber can be used for dilution-induced phase separation. This chapter has been published:

Meng, J., You, J. B., Arends, G. F., Hao, H., Tan, X., & Zhang, X. (2021). Microfluidic device coupled with total internal reflection microscopy for in situ observation of precipitation. The European Physical Journal E, 44(4), 1-8.

Chapter 4 uses the quasi-2D microfluidic chamber proposed in Chapter 3 to study asphaltene precipitation under diffusive mixing. Primary submicron particles are formed at the early stage of asphaltene precipitation, which are the basic units of large particles. The influence of the concentration of paraffinic solvent on the size distribution of the asphaltene particles is also studied. Smoluchowski aggregation model is suggested to explain the results. This chapter has been published:

Meng, J., You, J. B., Hao, H., Tan, X., & Zhang, X. (2021). Primary submicron particles from early stage asphaltene precipitation revealed in situ by total internal reflection fluorescence microscopy in a model oil system. Fuel, 296, 120584.

Chapter 5 expands the type of the n-alkanes and mixture of two n-alkanes as the paraffinic solvent to study asphaltene precipitation under diffusive dominated mixing. Except for the Hildebrand solubility parameter, the diffusion coefficient is a significant parameter to determine the yield and size distribution of asphaltene particles. PBM model is used to rationalize the size distribution of asphaltene particles at the final stage. This chapter has been published:

Meng, J., Sontti, S. G., Sadeghi, M., Arends, G. F., Nikrityuk, P., Tan, X., & Zhang, X. (2022). Size distribution of primary submicron particles and larger aggregates in solvent-induced asphaltene precipitation in a model oil system. Fuel, 322, 124057

Chapter 6 is the study of solvent exchange induced nanodroplet formation in a model oil system. The mixing dynamics vary the morphology of the formation of the new phase. The mechanism of the phenomenon is explained

from the perspective of boundary layer thickness based on Prandtl-Blasius theory and no-slip boundary theory. This chapter has been published:

Meng, J., You, J. B., & Zhang, X. (2020). Viscosity-mediated growth and coalescence of surface nanodroplets. The Journal of Physical Chemistry C, 124(23), 12476-12484.

Chapter 7 utilizes the solvent exchange method to study asphaltene precipitation under controlled external flow conditions. COMSOL simulates the mixing dynamics at different flow rate, channel heights, orientation, and temperatures. The corresponding experiments are done to compare with the prediction from the simulations. The influence of the mixing dynamics on asphaltene precipitation is caused by the shear rate and local concentration. This chapter is under preparation for a manuscript.

Meng, J., Kanike, C. Sontti, S., Atta, A., Tan, X., & Zhang, X. (2022). In preparation.

Chapter 8 summarizes the findings of my research and prospects the future research direction.

Chapter 2

Literature Review

2.1 Oil sands extraction

Oil sands are a type of non-conventional reservoir of petroleum. Bitumen is a heavy complex hydrocarbon contained in oil sands. Oil sands extraction is the process to extract bitumen from oil sands ore. The extracted bitumen can be further upgraded and refined to produce gasoline, diesel, and lubricants [128]. Currently, there are two ways for bitumen extraction. One is surface mining, which means directly mining the entire deposit of the oil sands. The water-based oil sands extraction process is followed to recover bitumen as bitumen froth as shown in Figure 2.1. The other one is in-situ bitumen extraction such as steam-assisted gravity drainage (SAGD), where steam is introduced to the extraction well to heat the oil sands ores to liquefy the bitumen and pumped to the surface [189].

Bitumen froth contains significant amount of water and solids, which should be removed before downstream processes. The mineral solids may block and poison catalysts and water may carry salts that cause severe corrosive problems to downstream processes. Therefore, a froth treatment process is necessary to remove water and mineral solids [168].

In bitumen froth treatment, solvents are added to decrease the viscosity and density of bitumen to achieve gravity separation of solids. Two froth treatments are used in the oil sands industry: naphthenic froth treatment (NFT) and paraffinic froth treatment (PFT). The difference is the types of the solvents. Solvents containing primarily naphtha hydrocarbons are called naph-

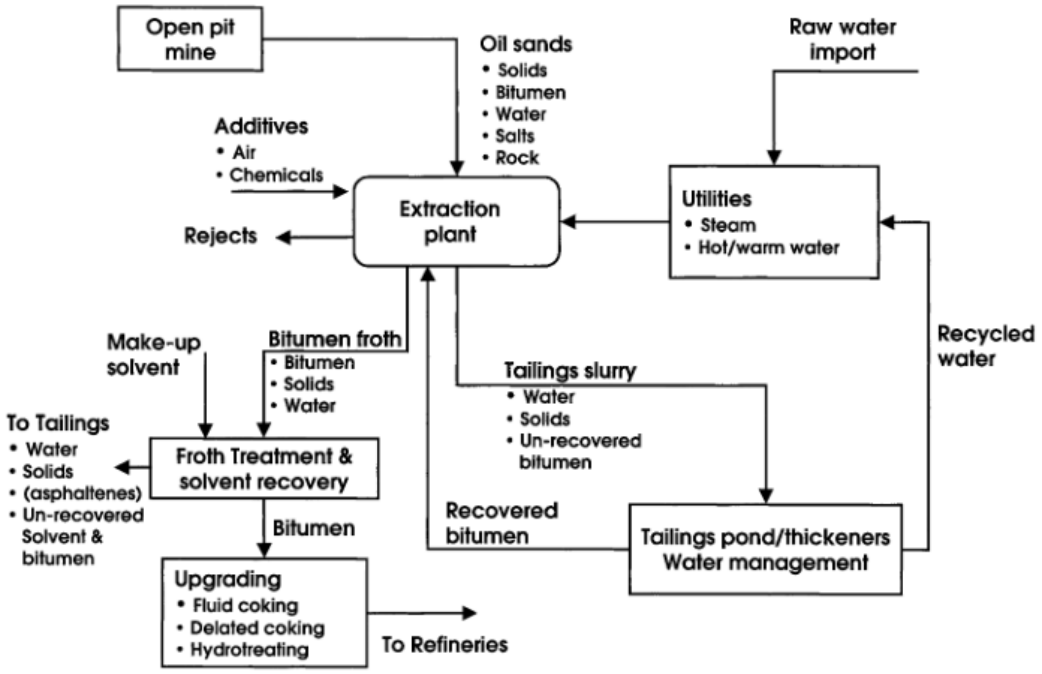

Figure 2.1: General scheme of water based oil sands extraction. (With permissions from Ref. [128]. Copyright (2004) Wiley)

thenic, while solvents containing primarily paraffin hydrocarbons are called paraffinic. Recently, PFT has been increasingly used because the products after PFT can be transported to downstream for further process without the need of on-site upgraders. Other than decreasing the viscosity and density of the bitumen froth, PFT induces asphaltene precipitation. The precipitated asphaltene agglomerates with water and mineral solids, resulting in the improvement of the quality of the bitumen product [188].

2.2 Asphaltene precipitation

Bitumen is a mixture of hydrocarbons with different physical and chemical properties. Bitumen is normally divided into four fractions: saturates, aromatics, resins, and asphaltene (SARA). The four classifications are defined in terms of solubility. Saturates, aromatics, and resins are soluble in n-alkanes. Asphaltene is the most complex fraction in petroleum and is defined as insoluble in normal n-alkanes (i.e., n-pentane and n-heptane) but soluble in

aromatic solvents (i.e., benzene and toluene). PFT takes advantage of the insoluble properties of asphaltene in n-alkanes for froth treatment. The precipitated asphaltene can agglomerate with impurities. However, beyond a certain threshold, more asphaltene precipitation has no more enhancement on the improvement of the quality of bitumen product with excessive hydrocarbon loss [17].

Outside the PFT, asphaltene precipitation is usually harmful. For example, in the transportation of bitumen and other type of heavy crude oils, asphaltene precipitation contributes to the fouling and eventually blockage of pipelines or tanks due to the accumulation of asphaltene deposition [198]. Therefore, it is necessary to explore the mechanism of asphaltene precipitation in order to control the asphaltene precipitation.

In addition to PFT and the transportation process in the oil sands industry, asphaltene precipitation is becoming increasingly important in the new era of carbon neutrality. Asphaltene contains the highest carbon to hydrogen ratio [172, 173]. The carbon dioxide emission can be decreased if the asphaltene was removed from the petroleum before combustion. Rather than being used as fuel, the precipitated asphaltene can be used as materials to make value-added product, including graphene [229], carbon fiber [177], activated carbon [105], and carbon nanotube [35].

2.2.1 Theories of asphaltene precipitation

Asphaltene and asphaltene precipitation have been studied for several decades. Now, some main findings have been achieved about the molecular structure and precipitation mechanism of asphaltene. This section summarizes the current status of asphaltene-related research.

Asphaltene molecules

Asphaltene molecules are complex polyaromatic hydrocarbons surrounded by aliphatic side chains, and compose heteroatoms such as sulphur, nitrogen, oxygen, and heavy metals. There are two models to describe the structure of asphaltene molecules: island and archipelago motifs, as shown in Figure 2.2.

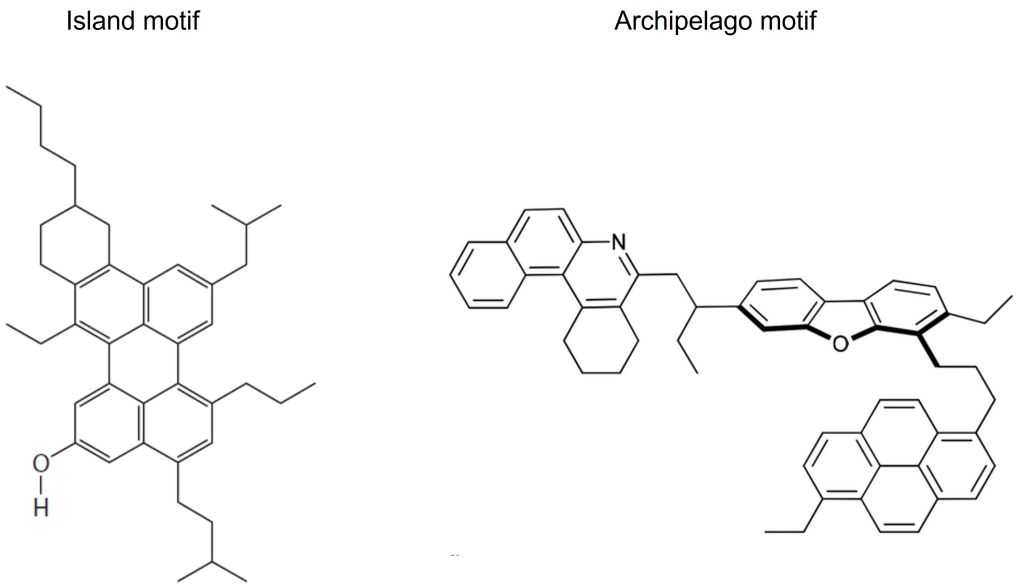

Figure 2.2: Two possible molecular structures for asphaltene: Island and archipelago motifs. (With permissions from Ref. [140]. Copyright (2007) Annual Reviews, Inc. and [184]. Copyright (2015) Royal Society of Chemistry)

The characteristic of the island motif is that a polycyclic aromatic hydrocarbon (PAH) is surrounded by side chains, while the character of the archipelago motif is that several PAHs are connected by alkane bridges [142]. Recent studies by Zhang et al. and Chacón-Patiño used atomic force microscopy (AFM) and Fourier transform ion cyclotron resonance mass spectrometry (FT-ICR MS) methods respectively to found that the island motif and archipelago motif coexist in asphaltene depending on the source of asphaltene and preparation methods [46, 261].

Driving force of asphaltene precipitation

The studies of the mechanism of asphaltene precipitation were based on either solubility theory or colloidal theory [40, 141]. The difference is that solubility theory regarded asphaltene as molecules, while colloidal theory regarded asphaltene as colloids. This work is based on colloidal theory because the asphaltene already aggregated into colloidal particles in the crude oil because asphaltene can be filtrated from the crude oil [68, 262]. In addition, the phase behaviour of asphaltene is similar to nanoparticles that there is close-loop two-

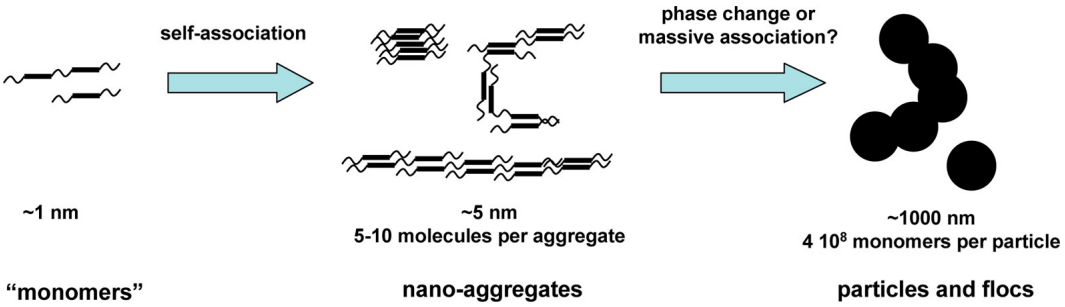

Figure 2.3: Aggregation and precipitation from molecules to nano-aggregate and particles. (With permissions from Ref. [235]. Copyright (2013) American Chemical Society)

phase region with two critical points on the boundary in the phase diagram [106].

In colloidal theory, as shown in Figure 2.3, a few molecules first form nano-aggregates through self-association [235]. Then, nano-aggregates form particles or flocs revealed as phase separation. Yen-Mullins model proposed that there was a cluster state ($\sim 5\ nm$) between nano-aggregates and phase separation states [142]. The asphaltene aggregation process consists of π - π bonding between PAHs as well as other molecular interactions such as hydrogen bonding and acid-base interactions [76, 184]. After the formation of the nano-aggregates, steric repulsion restricts adding more molecules [235].

In aromatic-based solutions, asphaltene colloids are in a favourable liquid environment, leading to the swelling and extended structures of asphaltene colloids. The asphaltene colloids repel each other due to the steric repulsion originating from the extended chains. In paraffinic-based solvents, the liquid surrounding becomes less favourable for stretching of the asphaltene colloids, resulting in the reduction of the steric repulsion. The van der Waals attraction leads the aggregation of the asphaltene colloids to grow to large particles [76, 217, 218, 243].

Smoluchowski aggregation model

Smoluchowski aggregation model can be used to describe the aggregation process of asphaltene colloids [194, 207] as shown in Equation (2.1). The physical meaning of this model is that the number density change (n_k) over time (t) of

particle with a specific size (k) depends on the rate at which smaller particles collide to form it minus the rate at which it collides with other particles to form larger particles. The larger the final particle size, the more intense the degree of aggregation in the system.

$$\frac{dn_k}{dt} = \frac{1}{2}\sum_{i+j=k} K_{i,j} n_i n_j - n_k \sum_{i\geq 1} K_{i,k} n_i \tag{2.1}$$

where n_i, n_j, and n_k are the number concentration of particles of size i, j, and k, respectively. t is time, and $K_{i,j}$ is aggregation kernel calculated by:

$$K_{i,j} = \alpha_{i,j}\beta_{i,j} \tag{2.2}$$

where $\alpha_{i,j}$ is the collision frequency. Under Brownian motion, $\alpha_{i,j}$ is calculated by:

$$\alpha_{i,j} = \frac{2}{3}\frac{RT}{\mu}\frac{(d_i + d_j)^2}{d_i d_j} \tag{2.3}$$

where R is the ideal gas constant, μ is viscosity, d_i, and d_j are the diameters of particles with size i and j, respectively. $\beta_{i,j}$ is collision efficiency. The collision efficiency is controlled by the interaction forces between two asphaltene particles. A well-accepted way to calculate $\beta_{i,j}$ is based on the maximum energy barrier (U_{max}) [125]. U_{max} was experimentally found inversely proportional to the squared difference between Hildebrand solubility parameters of asphaltene and the solvent [217]. Therefore, $\beta_{i,j}$ is calculated by:

$$\beta \propto exp[-\frac{\psi_e}{k_B T(\delta_{asp} - \delta_{sol})^2}] \tag{2.4}$$

where ψ_e is the maximum energy barrier constant, δ_{sol} is the Hildebrand solubility parameters of the paraffinic solvent.

Population balance model (PBM) has been established based on the colloidal theory to estimate the size distribution of asphaltene particles [126, 143], detection time to observe the phase separation [83, 125], and yield of asphaltene [84].

Hildebrand solubility parameter

The Hildebrand solubility parameter (δ) is very important to model the phase behaviour of asphaltene. Hildebrand solubility is defined as the square root of the cohesive energy density [26]:

$$\delta = \sqrt{\frac{\Delta H_\nu - RT}{V_m}} \tag{2.5}$$

where ΔH_ν is heat vaporization and V_m is the molar volume in the condensed phase. δ can be experimentally measured based on refractive index, as shown below [38]:

$$\delta = 52.042 F_{RI} + 2.904 \tag{2.6}$$

$$F_{RI} = \frac{n^2 - 1}{n^2 + 2} \tag{2.7}$$

where n is the refractive index. δ of mixture (δ_m) is calculated based on the volume fraction of the components [113]:

$$\delta_m = \sum \delta_i \phi_i \tag{2.8}$$

where δ_i and ϕ_i are the Hildebrand solubility parameter and volume fraction of component i.

Hildebrand solubility parameter is commonly used in the prediction of solubility of non hydrogen bond and non-polar system. In principle, the Hildebrand solubility parameter should not be used for the system of asphaltene and solvent because asphaltene contained polar chemical species contributed to hydrogen bonds and polarization [53, 224]. Simple use of Hildebrand solubility parameter as regular solution theory can not predict asphaltene phase behaviour well because it is not based on colloidal theory [145]. Using the Hildebrand solubility parameter in Equation (2.4) is more like an empirical approach. The effects of the solvents are not considered by δ may attribute to ψ_e. Therefore, the collision efficiency (β) is usually fitted from experimental data rather than directly estimated from the thermodynamic theoretical

model [125, 126].

Onset of asphaltene precipitation

The onset of asphaltene precipitation is usually attributed to the pressure or precipitant concentration to induce phase separation of asphaltene from crude oil [196]. The onset mentioned in this thesis is the latter case (i.e., onset precipitant concentration). So far, there are numerous techniques to determine the onset of asphaltene precipitation, including gravimetric method [41], viscosity measurement [87], refractive method [225], electronic method [74], thin-film method, and optical microscope method [58].

The onsets obtained by the different methods were not the same. Different techniques detected asphaltene at different scales. The thin-film method, which detected phase separation by film drainage could detect asphaltene at submicron scale [88], the optical microscope method normally detected asphaltene at micron-scale [58], and spectroscopic method such as near-infrared detected asphaltene at tens of microns scale [88].

In addition, asphaltene precipitation happens gradually rather than abruptly [88], different from the conventional critical dilution-induced phase separation. The duration after the contact between precipitant and asphaltene solution affects the size of the asphaltene particles. Therefore, the exact value of onset remains in the debate so far due to the difference in resolution and poorly defined contact time.

2.2.2 Factors that influence asphaltene precipitation and aggregation

Asphaltene precipitation and aggregation are affected by many factors of the surroundings. Part of them are thermodynamics factors, including solvent to bitumen (S/B) ratio, precipitant, inhibitors, and temperature. The changes in these factors lead to the shift of the thermodynamics equilibrium in the system, resulting in asphaltene precipitation. There have been many studies on the influence of thermodynamic factors on asphaltene precipitation. The effects of these factors, including S/B ratio, precipitant type, inhibitor, and

temperature, are summarized in this section.

Effect of solvent/bitumen ratio

S/B ratio is the mass ratio of the paraffinic solvent to bitumen. The rate of asphaltene precipitation increases with the increase of S/B ratio [5, 113]. Moreover, the mechanism of asphaltene aggregation changes from diffusion-limited aggregation (DLA) to reaction-limited aggregation (RLA) with the decrease in the S/B ratio (Figure 2.4). DLA is the process in which every contact between the particles results in aggregation. The particle size growth of DLA is [91]:

$$R_p = R_o(1 + \frac{t}{\tau_D})^{\frac{1}{d_f}} \tag{2.9}$$

where R_p and R_o are the particle radius and initial particle radius, respectively, τ_D is the diffusion time, and d_f is the fractal dimension of asphaltene particles. Not every contact results in aggregation in the RLA process. The particle size growth of RLA is:

$$R_p = R_o exp(\frac{t}{\tau_R d_f}) \tag{2.10}$$

where τ_R is the reaction time.

At a high S/B ratio, $(\delta_{asp} - \delta_{sol})^2$ is large, leading to a high collision efficiency described in Smoluchowski aggregation model in the previous section. Therefore, each contact between asphaltene particles is likely to cause a successful aggregation, which leads to a DLA process. However, the steric repulsion between asphaltene colloids is high when the S/B ratio is low, causing an RLA growth.

Effect of precipitant type

Hildebrand solubility parameters of different types of n-alkanes are different [26]. Therefore, the yield of asphaltene precipitates is different in different types of n-alkanes. For carbon numbers from five to nine, the requirement of n-alkane concentration to induce asphaltene precipitation increases with the

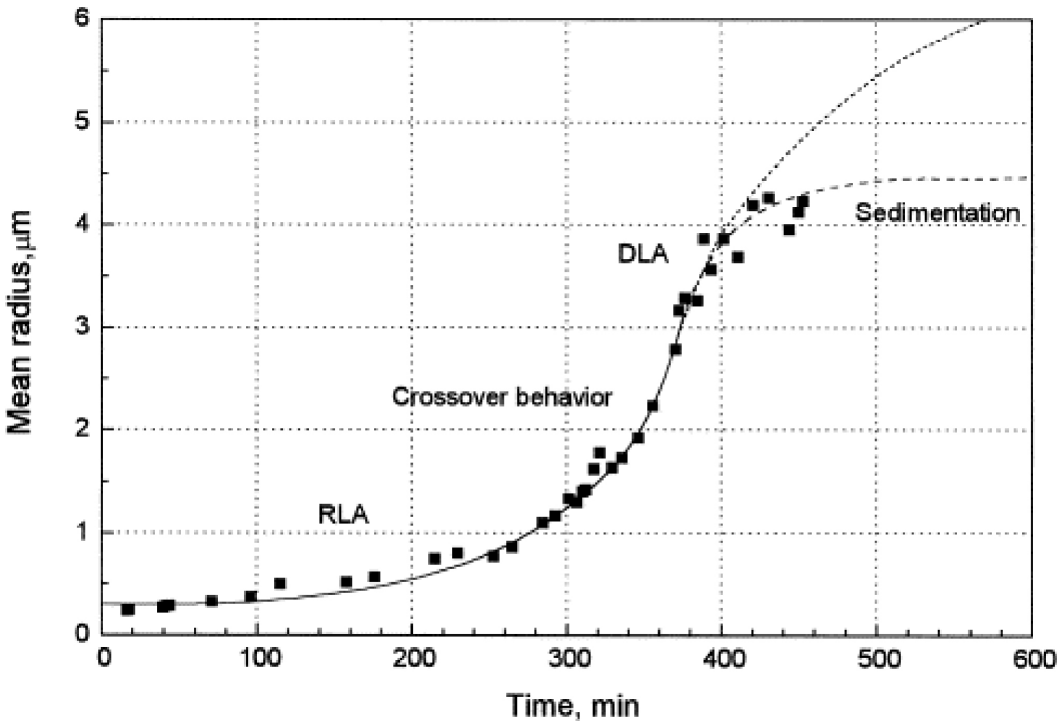

Figure 2.4: DLA and RLA behaviour of asphaltene aggregation (With permissions from Ref. [242]. Copyright (1998) Elsevier)

carbon number. However, for carbon numbers larger than nine, the request of the n-alkane fraction to induce asphaltene precipitation decreases with the increase of carbon number [227].

The aggregation rate of asphaltene does not change monotonically with the carbon number of solvents. The reason is the polydispersity of asphaltene. The longer-chain solvent tends to precipitate the most unstable asphaltene. The influence of solvent on detection time of asphaltene particles can be predicted by Equation 2.11 derived from Equation (2.1) [83, 84]. The longer detection time indicates a faster aggregation rate.

$$ln(\frac{t_{detection}\sqrt{C_1(0)}}{\mu}) \propto (\delta_{asp} - \delta_{sol})^{-2} \tag{2.11}$$

where $t_{detection}$ is detection time of asphaltene particles and $C_1(0)$ is the initial concentration of unstable asphaltene.

Effect of inhibitor

The addition of inhibitors is an efficient way to inhibit asphaltene precipitation. Nanoparticles [134] and some chemicals such as 4-dodecylbenzenesulfonic acid (DBSA) and 4-nonylphenol (NF) can act as inhibitors [7, 22, 174].

There are several explanations for the mechanism of inhibitors. For nanoparticles such as TiO_2, the inhibition effect mainly comes from the formation of hydrogen bonds between nanoparticles and asphaltene molecules [134]. The hydrogen bonds stabilize the asphaltene molecules in the solution. For chemicals such as DBSA, the inhibitor molecules attach to the active sites of the polyaromatic cores of asphaltene molecules and eventually become parts of the crown surrounding the cores. The incorporation of the attached inhibitor chains provides extra steric repulsion between asphaltene molecules. Thus, the asphaltene particles are less likely to aggregate in the presence of inhibitors [174]. The kinetic of aggregation changes from DLA to RLA after adding inhibitors, indicating the decrease of attraction between asphaltene molecules.

Effect of temperature

Temperature is an important influence factor for asphaltene precipitation. Temperature affects not only the collision frequency and collision efficiency between particles as shown in Equations (2.3)(2.4), but also many other physical parameters, including viscosity and Hildebrand solubility parameters. Due to the complex impact of temperature, it is still hard to conclude the influence of temperature on the yield and size of asphaltene particles. Some study found that the yield of asphaltene decreased with the increase of temperature from 20 °C to 65 °C [89]. But some other studies found that the amount of asphaltene precipitation only decreased with the increase of temperature from 75 °C to 100 °C and the yield of asphaltene increased with temperature when the temperature was higher than 100 °C [232].

The influence of temperature on particle size is also unknown. Some studies found that the size of asphaltene particles increased with temperature from 30 °C to 80 °C [118]. But other research found that the size of asphaltene particles

decreased with the increase of temperature from 10 °C to 50 °C [123].

The above studies on the influence of thermodynamic factors were based on the conventional bulk system, as summarized in Table 2.1. The mixing conditions in the conventional bulk system were not well controlled, which might have a great effect on asphaltene precipitation, and further affected PFT process efficiency. In the next sections, studies that consider the influence of mixing are discussed.

Table 2.1: Summary of mixing conditions reported in the previous literature

Author	**Mixing mechanism**	**Oil**	**Solvents**
Alboudwarej et al. [5]	Sonicated, centrifuged	Cold lake bitumen	n-Heptane, n-Pentane, n-Hexane, n-Octane
Li et al. [113]	Agitator	Venezuela bitumen	n-Heptane
Yudin et al. [242]	Pour into	Karazhanbas crude oil	n-Heptane
Wiehe et al. [227]	Pour into	Maya crude oil, Cold lake bitumen	C5 - C16
Haji-Akbari et al. [83]	Hand shaked	Crude oil	n-Heptane
Mohammadi et al. [134]	Agitator	Crude oil	n-Heptane
Hu et al. [89]	Hand shaked	Caoqiao crude oil	C5 - C12
Xu [232]	Agitator	McMurray bitumen froth	n-Pentane, isopentane, neopentane
Long et al. [118]	Agitator	Athabasca bitumen froth	n-Pentane, n-Hexane, n-Heptane

Effect of flow conditions in a bulk system

Some attempts have been done to investigate the effect of flow conditions in a bulk system. The shear rate in the system is controlled by the rotating rate of a mixer or a cylinder. Under the action of shear force, asphaltene precipitation is considered to be an equilibrium between the aggregation and fragmentation processes. The collision frequency is intensified by the shear rate. The collision frequency due to shear rate is [164]:

$$\alpha_{i,j} = \frac{G}{6}(d_i + d_j)^3 \tag{2.12}$$

where G is the shear rate of the system, d_i and d_j are the diameters of particles i and j, respectively. The difference in the settling rate of asphaltene particles may also strengthen the collision frequency [166]:

$$\alpha_{i,j} = \frac{\pi g}{72\mu}(d_i + d_j)^2 |\Delta\rho_i d_i^2 - \Delta\rho_j d_j^2| \tag{2.13}$$

where $\Delta\rho_i$ and $\Delta\rho_j$ are the density difference of particles i, j and liquid medium, respectively.

The fragmentation causes the breakage of particles. After considering the fragmentation, the Smoluchowski aggregation model became [143]:

$$\frac{dn_k}{dt} = \frac{1}{2}\sum_{i+j=k} K_{i,j} n_i n_j - n_k \sum_{i\geq 1} K_{i,k} n_i - B_k n_k + \sum_{j=k+1}^{n_{max}} \gamma_{k,j} B_j n_j \tag{2.14}$$

where B_k and B_j are the fragmentation rate of particles k and j, n_{max} is the largest particle size form fragments of size k by breakage, $\gamma_{k,j}$ is the volume fraction of the fragments of size i originating from size j particles. The fragmentation rate (B_k) is a function of particle volume (V_k) [150] [195]:

$$B_k = bV_k^{0.33} \tag{2.15}$$

where b is the breakup rate coefficient.

The presence of shear forces enhances aggregation and fragmentation simultaneously. At the beginning of mixing of asphaltene solution and the paraffinic solvent, the aggregation dominates the process, leading to the size increase of asphaltene particles until a maximum value. The fragmentation then dominates the process, resulting in the size decreases. Finally, aggregation and fragmentation reach a equilibrium and the size of the asphaltene particles remains stable [164, 166]. Under the large shear force, the particle aggregation rate is relatively fast, resulting in the rapid growth of particle size. However, the larger shear force results in greater fragmentation and the final size of asphaltene particles is relatively small (Figure 2.5).

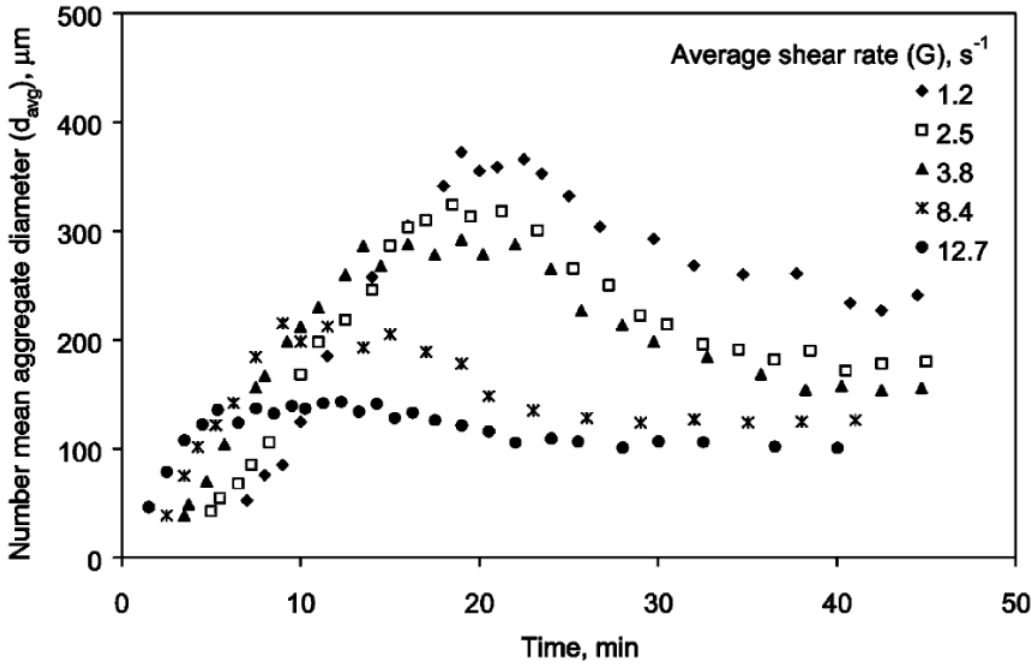

Figure 2.5: Growth kinetics of asphaltene aggregates under shear at Toluene:Heptane of 1:15 and particle concentration of 12.8 mg/L (With permission from [164]. Copyright (2004) Elsevier)

Effect of flow conditions in a microcapillary

Microcapillaries have been used to study the influence of flow rate on asphaltene precipitation [33, 34]. Two solutions (i.e, asphaltene solution and paraffinic solvent) are injected into the microcapillary with adjustment of the flow rates. When the injection rate of two solutions is the same, a higher injection rate causes earlier asphaltene precipitation. The asphaltene is also less likely to deposit on the surface to block the channel. Compared with a planar channel, the accumulation rate of asphaltene on the surface of a microcapillary is faster to stuck the channel [113]. This difference may be caused by the confinement of the microcapillary.

2.3 Solvent-induced phase separation

The effect of mixing on asphaltene precipitation has been observed by some studies as previously discussed. But studies of dilution-induced asphaltene

precipitation under well-controlled mixing conditions are lacking, especially at the early stage of asphaltene precipitation.

However, microphase separation induced by dilution is ubiquitous in many natural and industrial processes. Liquid-liquid phase separation in an aqueous-based system have been well studied in our group, named as solvent exchange. In the solvent exchange process, with mixing with a poor solvent, oil nucleates into microdroplets and spontaneously forms a new phase, causing the liquid to become cloudy and remain for a long time [193]. Bubbles, polymers and nanoparticles exhibit a similar phenomenon upon dilution by a poor solvent. The process is also called solvent shifting or nanoprecipitation [108, 182]. Mixing dynamics is essential for the total amount and size distribution of the nanodroplets formed in the solvent exchange process [182, 239, 240, 258].

2.3.1 Ouzo effect in mixtures consisting of water, co-solvent and oil

Ouzo effect, also called spontaneous emulsification, is a milky oil-in-water emulsion obtained by adding water to an anise-flavoured spirit. Such emulsion is formed by minimal mixing and is stable for a long time [43, 70, 181]. Recently, the Ouzo effect has been seen as a technique for the large-scale generation of surfactant-free emulsion without mechanical agitation [162].

A standard Ouzo effect system consists of three parts: oil, non-solvent (i.e., water), and co-solvent (i.e., ethanol). A typical phase diagram of the ternary system is shown in Figure 2.6 [112, 119, 221]. Oil is miscible with ethanol but immiscible with water. The ternary solution is a homogeneous solution with the composition above the binodal curve. With the addition of water, the oil solubility decreases, leading to oil oversaturation to form a new phase when the composition is below the binodal curve. The Ouzo region is a metastable region in which the Gibbs free energy is not a minimum but there is a large kinetic barrier for phase separation, resulting in a stable emulsion remaining for a long time [213].

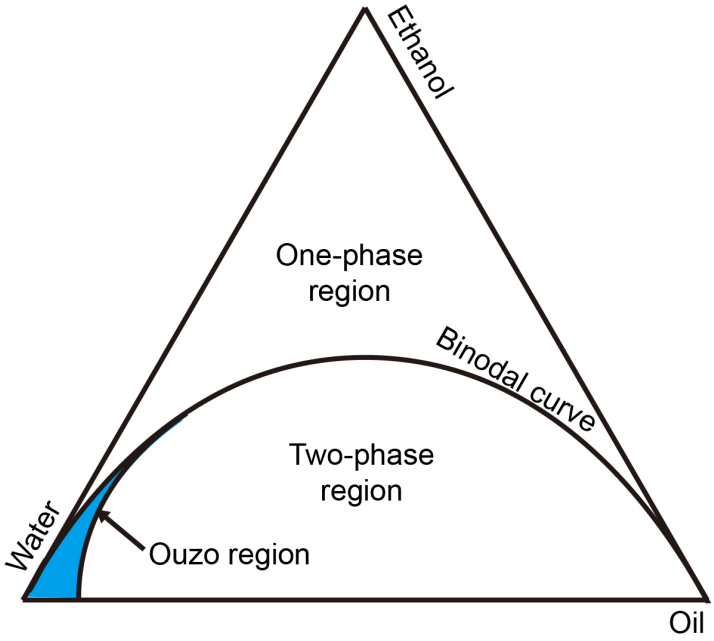

Figure 2.6: Ternary phase diagram of oil (oil), ethanol (good solvent), and water (poor solvent). Stable emulsion can be formed in the Ouzo region.

2.3.2 Formation of surface nanodroplets by solvent exchange

Based on the principle of the Ouzo effect, a protocol named solvent exchange is developed for the production of a large number of surface nanodroplets at the interface between a solid surface and an immiscible liquid [61, 109, 116, 215, 254, 258]. Solvent exchange is a reliable approach to control the volume, composition, and size distribution of the final surface droplets [238, 247, 258]. More importantly, the solvent exchange process is an efficient way to quantitatively understand the dilution-induced phase separation [162].

The microfluidic chamber for solvent exchange consists of a substrate, a spacer, and a transparent cover glass (Figure 2.7). In the solvent exchange process, ternary solution (i.e., solution A) with a high oil solubility is pre-filled in the channel and then displaced by a low oil solubility solution (i.e., solution B). There is a broadening mixing front between solutions A and B due to diffusion. The oil is oversaturated in the mixing front as oil diffuses from solution A towards solution B. For a specific position on the substrate, oil is not

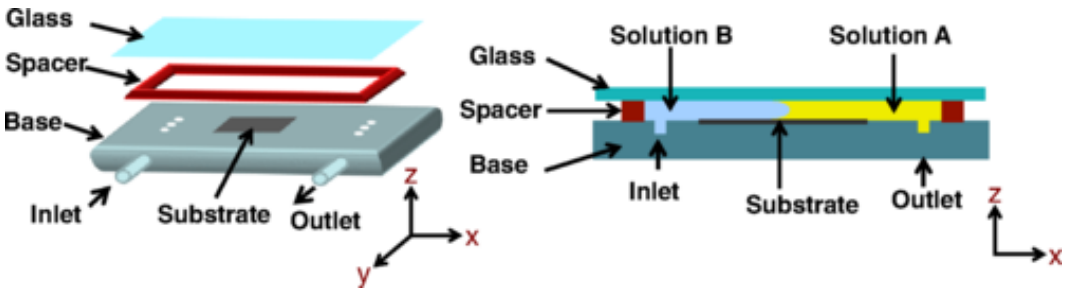

Figure 2.7: Sketch of a microfluidic chamber for the solvent exchange. The microfluidic chamber contains a substrate, a spacer, and a transparent cover glass. The channel height between the substrate and the cover glass can be adjusted by the thickness of the spacer. (With permissions from Ref. [116]. Copyright (2015) American Physical Society)

saturated initially as oil is in a good solvent (solution A) and not saturated at the end as oil is fully displaced (solution B). Oil is only oversaturated when the mixing front passes through the specific position and this is an oversaturation pulse. Droplets nucleate and grow at the specific position when the oversaturation pulse arrives and the nucleation and growth stop at the moment that solution B has entirely displaced solution A. Considering no-slip boundary, the formation of nanodroplets is mechanically caused by advection-diffusion of the oversaturated oil in the mixing front to the substrate [258].

The formation process of the surface nanodroplets can be in-situ visualized by microscopes [62, 63]. Moreover, some kinds of oil such as methyl methacrylate (MMA) and 1,6-hexanediol diacrylate (HDODA) [156, 257] can be cured by photo-initiated polymerization. The cured nanodroplets can be characterized in the air by many techniques such as atomic force microscope (AFM) and scanning electron microscope (SEM) to get more information on the nanodroplets in terms of dimension and resolution [156, 157].

Effect of flow conditions

The total volume of the nanodroplets formed by the solvent exchange is found influenced by the flow rate (Q) [62]. For a specific droplet, the mass growth rate ($\dot{m}$) of the nanodroplets follows:

$$\dot{m} = 4\pi\rho_{oil}R_r^2\dot{R}_r = 4\pi DR_r^2\partial_r c|_{Rr} \tag{2.16}$$

where R_r is the radius of the droplets, ρ_{oil} is the density of oil, D is the diffusion coefficient, and $\partial_r c|_{Rr}$ is the concentration gradient at the interface, which can be calculated by:

$$\partial_r c|_{Rr} \sim \frac{c_\infty(t) - c_{s,wat}}{\lambda} \sim c_{s,wat}\frac{\zeta(t)}{\lambda} \sim c_{s,wat}\sqrt{Pe}R_r^{-1}\zeta(t) \tag{2.17}$$

where c_∞ is the oil concentration in flow, $c_{s,wat}$ is the saturation concentration of oil in water, λ is the thickness of the boundary layer, which is assumed a Prandtl-Blasius-Pohlhausen behaviour and calculated by $\lambda \sim R_r/\sqrt{Pe}$ [79], and ζ is oversaturation. Pe of the system can be calculated by:

$$Pe = \frac{Q}{wD} \tag{2.18}$$

where w is the width of the channel. Substituting Equation (2.17) into Equation (2.16), the ordinary differential equation for $R_r(t)$ is:

$$R_r\dot{R}_r \sim \frac{Dc_{s,wat}}{\rho_{oil}}\sqrt{Pe}\zeta(t) \tag{2.19}$$

with the definition that $\int_{-\infty}^{\infty}\zeta(t)dt = \zeta_{max}\tau$, Equation (2.19) can be integrated to:

$$R_f \sim (\frac{Dc_{s,wat}}{\rho_{oil}}\zeta_{max}\tau Pe^{1/2})^{1/2} \tag{2.20}$$

where τ represents the duration of the oversaturation pulse and is defined as $\tau \sim h^2/D$, and ζ_{max} is the maximum oversaturation calculated by $\zeta_{max} = \frac{c_{s,eth}}{c_{s,wat}} - 1$. With these, the final volume of the nanodroplets (Vol_f) is [258]:

$$Vol_f \sim R_f^3 \sim h^3(\frac{c_{s,wat}}{\rho_{oil}})^{3/2}(\frac{c_{s,eth}}{c_{s,wat}} - 1)^{3/2}Pe^{3/4} \tag{2.21}$$

where h is the channel height and $c_{s,eth}$ is the saturation concentration of oil in ethanol. Therefore, the logarithm of the volume of the nanodroplets over the unit surface area increases linearly with the logarithm of Péclet number (Pe) as shown in Equation (2.21) [258].

Effect of chamber orientation

The profile of the mixing front is a perfect parabolic shape when the density difference of solutions A and B is not significant or when the device is placed vertically, as shown in Figure 2.8(b). However, when the density difference between solutions A and B is significant enough, the profile of the mixing front may not be symmetric anymore. Instead, the mixing front may shift downwards when the density of solution B is larger than solution A. Archimedes number (Ar) of the system can be used to infer if the shift occurs, as shown in Equation (2.22). The shift does not occur when Ar is much less than 1 [239].

$$Ar = \frac{gh^3}{\nu^2}\frac{\Delta\rho}{\rho} \tag{2.22}$$

where ν is the kinematic viscosity. An increase in the channel height and the difference in the densities of solutions A and B both lead to an increase in Ar, which further leads to the downwards shift of the mixing front. However, the shift of the mixing front never happens in the vertically placed device at any channel height and solutions because the direction of gravity is in parallel to the flow direction.

The shift of the mixing front causes the duration of the oversaturation pulse to change to $\tau \sim (\alpha h)^2/D$, where α is a correction factor. α is 0.5 for $Ar \to 0$, while α is 0 for $Ar \to \infty$. Therefore, the downwards shift of the mixing front leads to a decrease in the duration of the oversaturation pulse, which further leads to a decrease in the eventually total volume of nanodroplets [239].

Effect of channel geometry

In addition to the flow rate, the geometry of the microfluidic chamber affects the growth dynamics of nanodroplets. An increase in channel height automatically means an increase in the duration of the oversaturated pulses (τ) because of $\tau \sim h^2/D$, leading to a change in the growth dynamics of nanoparticles [239, 240]. In addition, previous studies noticed that there was buoyancy and gravity-driven convection when the channel height of the microfluidic chamber was higher than a critical value [258]. A defined Rayleigh number (Ra) was

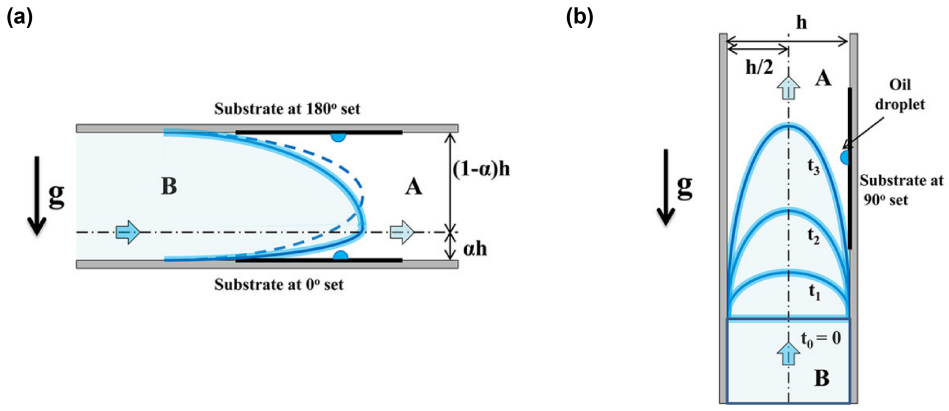

Figure 2.8: Schematics of the profile of solvent exchange process of the horizontally placed device, (b) vertically placed device. (With permission from [239]. Copyright (2015) American Chemical Society))

used to characterize the influence of the convection.

$$Ra = \frac{\Delta\rho g(h/2)^3}{\mu D} \tag{2.23}$$

where $\Delta\rho$ is the density difference between solution A and solution B and μ is viscosity.

The convective rolls were only observed with Ra larger than 1,708. The fingering and whirling patterns were observed when the convective rolls are significant [258]. The convective rolls led to better mixing of solution A and solution B, resulting in better transportation of oil towards the substrate to form larger surface nanodroplets. However, the scaling law of volume of the nanodroplets and Pe still held because the enhanced mixing only affects the prefactor in Equation (2.21).

Locally channel height change also affects the formation of the nanodroplets. The solvent exchange was processed in a microfluidic chamber with microgaps in the previous study [240]. The profile of the oversaturation pulse could be visualized by simulation such as COMSOL [240]. It was found that the profile of the mixing front was changed when the mixing front entered the microgap area, affecting the formation of the surface nanodroplets. When Pe was as low as 55, the mixing front passed the microgap smoothly with a nearly symmetric profile. At Pe larger than 55, the mixing front was disturbed to a large

extent by the microgap. More oil became available at the gap, leading to the formation of larger nanodroplets.

The properties change of the substrate also results in the change of growth dynamics change of the nanodroplets, such as the more uniform distribution and size of nanodroplets on physical or chemical patterned substrate [24]. This is because of the interaction between the nanodroplets and the substrate, which is different from the interaction between asphaltene particles and the substrate.

2.3.3 Diffusive mixing dominated quasi-2D microfluidic chamber

A microfluidic chamber consisting of a main channel flanked by two side channels has been proven to be used in a diffusive-dominated mixing process as shown in Figure 2.9(a) [120]. The main channel is pre-filled with solution A. Solution B is injected along with the side channel. The ratio of the side channel to the main channel is higher than 10 to provide a high hydraulic resistance, which prevents solution B from flowing into the main channel. Therefore, there is no convection in the mixing process in the main channel and the mixing is dominated by diffusion.

In the quasi-2D chamber, water in the side channel gradually diffuses into the main channel to displace the co-solvent. Oil in the main channel is gradually oversaturated and forms nanodroplets on the substrate [15]. Interestingly, the nanodroplets form a branch structure as shown in Figure 2.9 (b). The branch formation is independent of the flow rate of solution B in the side channel, oil concentration in solution A, and wettability of the substrate [120].

2.4 Microfluidic devices

Inspired by liquid-liquid separation, asphaltene precipitation should also be influenced by the mixing dynamics, including the amount and size distribution of asphaltene. Solvent exchange and diffusive-dominated mixing chamber are two applicable ways to control the mixing. The local concentration in the

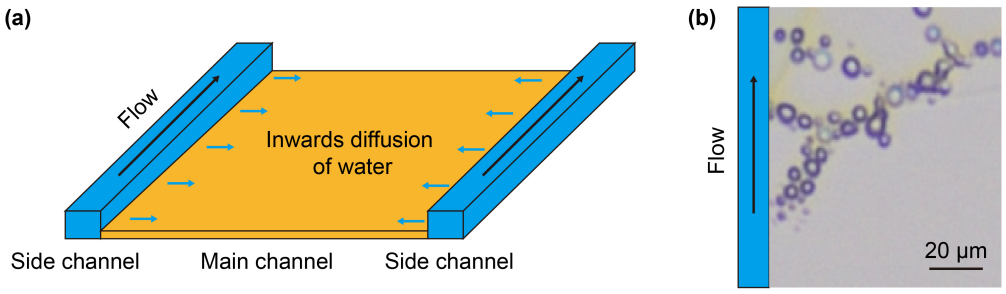

Figure 2.9: (a) Sketch of the quasi-2D chamber to induce diffusive-dominated mixing. (b) Optical image of the branch structure [120].

system can be visualized by simulation such as COMSOL. In addition, phase separation begins at the moment that the poor solvent arrives and stops at the moment that the oil is completely replaced in the solvent exchange process. Phase separation is not a continuous process, which potentially freezes the early stage of asphaltene precipitation at any time. The use of microfluidic devices to achieve solvent exchange and diffusive-dominated mixing is conducive to a better understanding of asphaltene precipitation under well-controlled mixing.

The traditional methods of studying of asphaltene precipitation were based on precipitation and subsequent collection, which required a large amount of solvent, a large reaction vessel, a long time, considerable manpower, and poor reproducibility [103, 141]. Because of the limitations of the traditional methods, microfluidic devices have attracted more attention and had shown promising results for heavy oil study [138].

Recently, microfluidic devices are used in several research topics in asphaltene precipitation. A Y-junction mixer was used to mix asphaltene solution and paraffinic solvent to study the onset of asphaltene precipitation [190, 191]. The results were consistent with the results of conventional methods but require less time and manpower for the experiments. The study of asphaltene deposition also benefits from the microfluidic device. The surface-to-volume ratio of a microfluidic device was very high and the surface property of the surface could be adjusted by surface modification. The deposition process could also be visualized due to the transparent nature of the microfluidic devices

[161].

The most important advantage of the microfluidic device is that the flow conditions can be well characterized and controlled. The intrinsic flow condition in the microfluidic device can be identified with adding dye [30] or software simulation [94, 228]. The mixing dynamics can be adjusted from only diffusion [120] to chaotic [137, 200] by fabricating different patterns in the device by photolithography.

Benefit from the advantages of microfluidic devices, it has been found that the flow usually resulted in a non-equilibrium concentration distribution in the mixing process, also called local concentration. Due to the existence of local concentration, different positions reached onset at different times, leading to uneven asphaltene precipitation and deposition. Compared with the slow diffusive mixing-induced asphaltene precipitation, the flow mixing-induced asphaltene precipitation produced firmly fixed asphaltene particles on the substrate [187].

2.5 Total internal reflection fluorescence microscopy (TIRF)

On top of the microfluidic chamber, high-spatial-resolution microscopy must be used to in-situ detect and track the growth of asphaltene particles at the early stage. Conventional optical microscopes do not provide sufficient spatial. In addition, the opaque nature of asphaltene limits the observation of conventional optical microscopes at higher asphaltene concentrations.

Total internal reflection fluorescence microscope (TIRF) is an efficient method to in-situ track the growth dynamics of phase separation [63]. Total internal reflection (TIR) is the basis of TIRF. Light might refract into the aqueous phase or be reflected back when light encounters the interface of the two media. However, when the incident angle is higher than a critical value, the refracted light disappears and all the light reflects, which is called total internal reflection. TIR produces a thin region called the evanescent field adjacent to the interface. The thickness of the evanescent field was $\sim 200\ nm$,

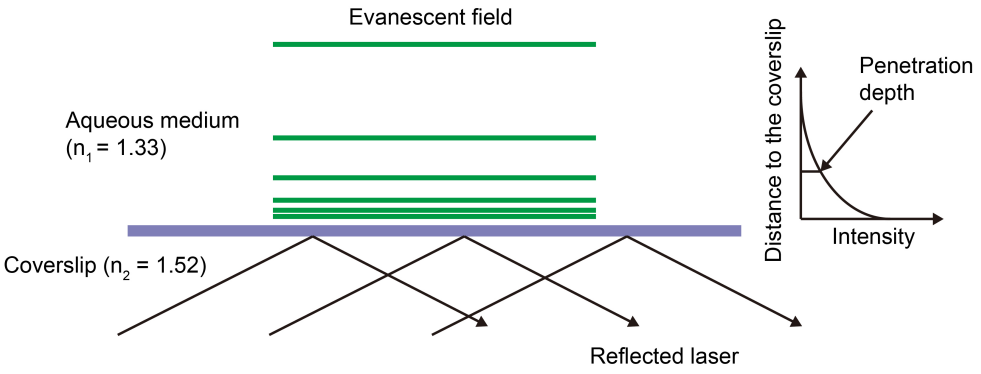

Figure 2.10: Principle of total internal reflection fluorescence (TIRF) microscope.

which is called penetration depth [21] (Figure 2.10).

TIRF utilizes evanescent waves to selectively illuminate and excite the fluorophores confined in a few hundred nanometers. The region above the evanescent field does not affect the observation, whether it is opaque or high absorbing. This is because the intensity of the wave decays exponentially with the distance to the interface [21]. Compared with the conventional optical microscope, the spatial resolution of TIRF is higher to resolve more details of the sample. In addition, TIRF can observe the early phase separation process without being affected by the high scattering background caused by the phase separation.

2.6 Research gaps

Microfluidic devices have shown advantages over conventional bulk system in the study of asphaltene precipitation. However, a device for mixing of the model oil and the paraffinic solvents under well-controlled conditions (e.g. diffusive-dominated mixing, or convective-dominated mixing) is still missing.

For several decades, extensive research has been done on understanding asphaltene precipitation. But most of the previous research studied asphaltene precipitation at a relatively large size (i.e, larger than 1 μm). A lack of study has been done to visualize asphaltene precipitation at an early stage (i.e., $<$ 1 μm). Although the theoretical resolution limit of the optical microscope is

$\sim$ 200 nm, the contrast is not enough to resolve submicron particles due to the interference of diffraction from different wavelengths of light. The opaque nature of asphaltene makes imaging even more difficult, especially at the early stage of asphaltene precipitation. To date, no studies have tracked asphaltene precipitation and aggregation at the early stage.

Dilution-induced asphaltene precipitation is still one of the most challenging topics. Except for the complexity of the physical and chemical properties of the asphaltene, the lack of good control of the mixing is also the cause of many remaining problems, because dilution-induced phase separation is not only controlled by the composition (i.e., thermodynamic aspect) but also by the mixing (hydrodynamic aspect). Previous studies mainly focused on the influence of thermodynamic factors of solution on asphaltene precipitation, while physical parameters related to hydrodynamics such as diffusion coefficient were not considered, which might be a key factor to affect asphaltene precipitation.

Quantitative analysis of the relationship between the mixing conditions and asphaltene precipitation is lacking. Our group have done numerous works on the effect of mixing conditions on surface nanodroplets formation. Many factors, including flow rate, orientation, and the geometry of the microfluidic chamber could affect the eventually total volume and size distribution of nanodroplets. However, these studies were conducted at low viscosity. Asphaltene precipitation occurs in a high viscosity system compared to the formation of nano-droplets in the aqueous system. Therefore, it is necessary to study the effect of mixing conditions on the growth dynamics of nanodroplets at high viscosity and it will be the basis for further research on asphaltene system.

The mixing dynamics of asphaltene solution and solvents can affect the dynamics of asphaltene precipitation. However, the mixing dynamics is not well controlled in the conventional study. The dilution-induced nanodroplets formation is similar to asphaltene precipitation. But asphaltene is solid-like rather than liquid at room temperature. In addition, the asphaltene precipitation is different from a conventional phase separation process induced by oversaturation. Therefore, the dynamics of asphaltene precipitation may be

different from that of nanodroplet formation. Therefore, it is necessary to study the real asphaltene system.

Chapter 3

Microfluidic Device Coupled with Total Internal Reflection Microscopy for In-situ Observation of Precipitation

Abstract

In situ observation of precipitation or phase separation induced by solvent addition is important in studying its dynamics. Combined with optical and fluorescence microscopy, microfluidic devices have been leveraged in studying the phase separation in various materials including biominerals, nanoparticles, and inorganic crystals. However, strong scattering from the subphases in the mixture is problematic for in situ study of phase separation with high temporal and spatial resolution. In this work, we present a quasi-2D microfluidic device combined with total internal reflection microscopy as an approach for in situ observation of phase separation. The quasi-2D microfluidic device comprises of a shallow main channel and a deep side channel. Mixing between a solution in the main channel (solution A) and another solution (solution B) in the side channel is predominantly driven by diffusion due to high fluid resistance from the shallow height of the main channel, which is confirmed using fluorescence microscopy. Moreover, relying on diffusive mixing, we can control the composition of the mixture in the main channel by tuning the composition of solution B. We demonstrate the application of our method for in situ observation of asphaltene precipitation and β-alanine crystallization.

3.1 Introduction

In situ observation and control of phase separation or precipitation process is important in many areas including growth of nanoparticles [85, 219], crystallization [211, 233], and biomineralization [220]. A dilution induced phase separation occurs when the concentration of a solute dissolved in a solvent reaches a critical concentration by the addition of an antisolvent. At the critical concentration, the solute is oversaturated, and the mixture is spontaneously separated into two subphases. Depending on the type of the solute, solid phase formation may be formed as precipitates or crystals. In all cases, both the chemical composition of the final mixture (i.e. solute + solvent + antisolvent) and controlled mixing between the solution (i.e. solute + solvent) and antisolvent determine the phase separation outcome. Precipitation is of particular interest during paraffinic froth treatment in oil sand extraction process, where asphaltene precipitates are formed from the addition of antisolvent [232].

Recently, microfluidic devices have been widely used for phase separation of various materials ranging from crystals [73, 104], drug nanoparticles [99], and lipid nanoparticles [263]. Phase separation is not only dominated by the composition (i.e. thermodynamic aspect) but also by the mixing dynamics (i.e. hydrodynamic aspect) [258]. Using a quasi-2D microfluidic device can control the mixing between the solution and the antisolvent predominantly driven by diffusion. By leveraging control of diffusion, we can disentangle the mixing dynamics and composition to better understand the formation and growth of the new phase. Moreover, the outcome of phase separation can be visualized in situ via optical or fluorescence microscopy. For instance, Sekine *et al.* was able to observe halite crystal growth in situ using a microfluidic channel [186]. Desportes *et al.* used fluorescence microscopy coupled with a microfluidic set-up to observe the nanocrystallization of rubrene [56]. However, the spatiotemporal resolutions of optical and fluorescence microscopy are not high enough for detailed study of the phase separation dynamics in early stage, due to the scattering of background from nanobubbles, nanodroplets or nanoparti-

cles. Furthermore, in some cases, an in situ precipitation study is complicated by the strong absorption of light by the dark medium, for example, asphaltene precipitation from toluene solution.

Coupling the advantages of microfluidics with total internal reflection fluorescence (TIRF) microscopy provides an attractive solution to study the phase separation precipitation dynamics. TIRF is an imaging method that uses the evanescent wave produced at an interface between two media with different refractive index. As the penetration depth of evanescent field is shallow ($\sim$ 160 nm), combining TIRF and microchamber is a powerful method to study any change that occurs near the chamber surface. Unlike the standard optical microscope that the scattering of the background may hinder visualization of phase separation, TIRF is capable of following the processes in a scattering medium. For instance, TIRF has been applied to investigate the liquid-liquid phase separation during mixing process [258], early stage diffusive growth of droplets [62], and real-time chemical reactions in surface nanodroplets [63].

In this work, we demonstrate a microfluidic method combined with TIRF for in situ observation of precipitation and phase separation. A bilayer quasi-2D microfluidic device – composed of a shallow main channel and a deeper side channel – is constructed to enable controlled diffusive mixing between two solutions to drive the phase separation. Using fluorescence microscopy, we validate the diffusive mixing process between solutions in the observation area in the main channel. By characterizing fluorescence intensity, we also quantify the change of chemical composition in space and in time in the observation area. We further demonstrate two examples of phase separation using the proposed setup (i.e. coupling the quasi-2D microfluidic chamber and TIRF), namely oiling out crystallization of β-alanine and early stage of asphaltene precipitation. We can decouple the composition and mixing dynamics on oiling out crystallization and better understand the crystal phase formation and growth. Moreover, the early stage of asphaltene precipitation in an opaque medium can be visualized so that asphaltene precipitation in a concentrated solution can be investigated.

3.2 Experimental

3.2.1 Device fabrication

The quasi-2D microfluidic device was fabricated via standard photolithography process followed by wet etching as shown in Figure 3.1. Borofloat glass wafer (81% SiO_2, 13% B_2O_2, 4% Na_2O/K_2O, 2% Al_2O_3. Borofloat wafer was first cleaned with piranha solution ($3:1 = H_2SO_4 : H_2O_2$) (Caution: piranha solution is highly caustic!) and rinsed by de-ionized water. Chrome (20 nm) and gold (150 nm) were sputtered on the surface of the Borofloat sequentially as masking layer. Photoresist (AZ1529) was spin coated on the metal-masked substrate, which was baked for 1 min. The substrate was exposed under UV light through a photo mask with pre-designed side channel pattern on it. The exposed patterned photoresist was removed by developer. Gold and chrome layers were then etched by gold and chrome etchant. The Borofloat substrate was then etched by HF (hydrofluoric acid) solution (4:1:5 mixture of water: HNO_3 (nitric acid): HF by volume, poured from stock bottles of concentrated nitric acid (69.0 – 70.0%) and HF (49%) by NanoFab staffs at the University of Alberta) (Caution: HF solution is highly caustic!) to create 240 μm side channel. After etching of side channel, blue tape was used to protect both ends of main channel. Photoresist on main channel was then manually removed by acetone wetted cotton swab. Gold, chrome and Borofloat etching steps were repeated to get 20 μm etch of the main channel. Borofloat was cleaned by de-ionized water and the remaining gold and chrome layer were stripped by etchants. The patterned Borofloat was then bonded with a glass cover slip (24 $mm \times 50\ mm \times 170 \pm 5\ \mu m$, Azer Scientific) by epoxy (WEST SYSTEM 105 epoxy resins). The spacing between the top and bottom glasses was not changed with epoxy, which was proved by changing the focal plane of the microscope from the top glass to the bottom glass. Similar to the structure of microchamber used in our previous work [120], the detailed dimensions of the quasi-2D microfluidic device are shown in Figure 3.2a. The narrow main channel is $\sim 20\ \mu m$ in depth and 6 mm in width, flanked with two deep side channels with $\sim 260\ \mu m$ in depth and 3 mm in width. The lengths of both

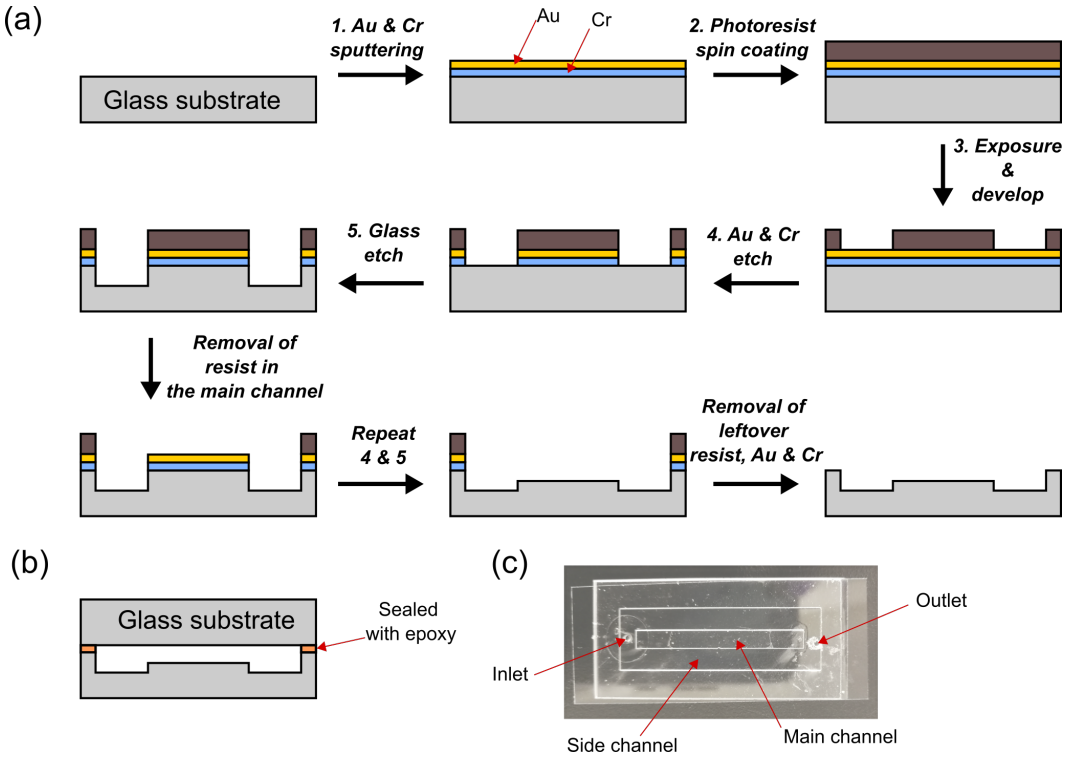

Figure 3.1: (a) Schematic showing photolithographic procedure for fabricating the channel on glass substrate. (b) The patterned glass substrate is sealed with a blank glass substrate using epoxy. (c) Photograph of the fabricated microfluidic chip.

the main channel and side channel are about 3 cm.

3.2.2 Visualization of diffusive mixing using the quasi-2D microfluidic device

All of the experiments were conducted at room temperature ($\sim$19 - 21 ^oC). To confirm the diffusive mixing inside the microchamber, the mixing process between toluene and n-pentane was followed by using a fluorescence microscope (Nikon ECLIPSE Ni) equipped with a camera (Nikon DS-Fi3). Toluene (ACS grade, Fisher Scientific, 99.9+%), doped with a trace amount of Nile Red (Fisher Scientific), was injected to fill the entire chamber. Then n-pentane (Fisher Scientific, 98%) was injected from one end of the side channel at a flow rate 5 mL/h by a syringe pump (NE-1000, Pumpsystems Inc.) as sketched in Figure 3.2. As flowing in the side channel along y-axis, n-pentane diffused transversely into the narrow quasi-2D main chamber to mix with toluene along

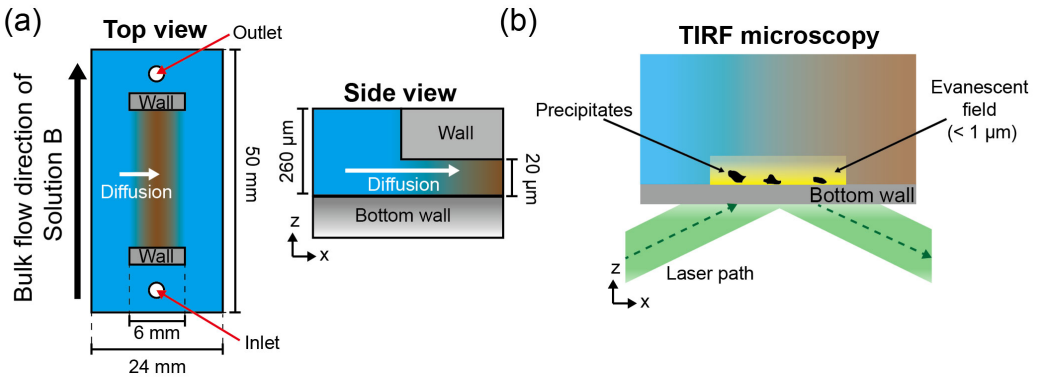

Figure 3.2: (a) Top view and side view of the fluid chamber. The chamber consists deep side channel with 260 μm depth (blue) and shallow main channel with 20 μm depth (brown). (b) Mechanism of total internal reflection fluorescence (TIRF) microscope. Only the asphaltene in evanescent flied (yellow) can be detected.

x-axis. The location of the field of view was set at a distance of 80 μm from the side channel through the transparent top glass of the main chamber.

Green laser (559 nm) was used to excite Nile Red and the emission was monitored at 635 nm. The change in the fluorescence intensity of the dye in the liquid was recorded at 2 frames per second by the fluorescence microscope (Nikon ECLIPSE Ni) equipped with a camera (Nikon DS-Fi3). The fluorescence intensity was converted to gray scale value and read using MATLAB software (The MathWorks Inc.). The fluorescence intensity as a function of time is governed by the mixing process, which is vital dataset to confirm whether diffusion mixing is dominant and to estimate the chemical composition of solution at given location.

3.2.3 In situ observation of precipitation and phase separation using the quasi-2D microfluidic chamber

The microfluidic device was initially filled with asphaltene solution in toluene (solution A). Then, solution B – n-pentane : toluene mixture at various ratios – was injected through the deep side channel with flow rate 5 mL/h by a syringe pump where n-pentane is an antisolvent of asphaltene. Part of solution B diffuses transversely into the main channel and mixes with solution A. Asphaltene gradually precipitated with n-pentane diffusion in the main channel

and can be detected by DeltaVision OMX Super-resolution microscope (TIRF 60×/1.49 NA objective lens) (GE Healthcare UK limited, UK). TIRF was used to detect asphaltene precipitates in the microchamber. The principle of TIRF detection is sketched in Figure 3.2b. Light refraction follows Snell's Law, as shown in Equation (3.1):

$$n_1 sin\theta_1 = n_2 sin\theta_2 \tag{3.1}$$

n_1 and n_2 are incident and refracted index of a given pair of media, separately, θ_1 and θ_2 are incident and refracted angle of light in the two media, separately. When the light propagates in a denser medium (e.g the glass substrate) and meets the interface with a less dense medium (e.g the sample on the substrate) above a critical angle, rays of light are no longer refracted but totally reflected in the denser medium. Total internal reflection (TIR) occurs, generating an evanescent field adjacent to the interface of the media. The electromagnetic wave in the evanescent field can excite the fluorophores in the sample with penetration depth around 100-200 nm, depending on the optical properties of the media and the incident angle [69].

In our measurements of asphaltene precipitation, the refractive index of asphaltene (RI = 1.72) was used base on the literature [39, 225], which is different to toluene (RI = 1.50) [100] and n-pentane (RI = 1.36) [101]. An excitation laser with wavelength $\lambda = 488\ nm$ was used to excite fluorophores and the emission wavelength detected by the detector was up to 576 nm. The TIRF images were taken on an 82.5 μm × 82.5 μm from the field of view in the area of the narrow main channel by a pco.edge sCMOS camera. Within this excitation and emission wavelength range, the asphaltene in n-pentane and toluene solution has much stronger signal than precipitated asphaltene particles, resulting in good contrast of image with the asphaltene particles shown as black particles.

For the visualization of β-alanine crystallization, the device was prefilled with a ternary mixture comprising of 6% β-alanine (Acros organics, 99%), 31.5% isopropyl alcohol (Fisher Scientific, 99.9%), and 62.5% water by weight.

Pure isopropyl alcohol was injected through the side channel at 12 mL/h to drive the crystallization. The process was monitored with the microscope in bright field imaging mode through a 10× magnification objective.

3.3 Results and discussion

3.3.1 Diffusive mixing characteristics in the form of spatial and temporal solvent concentration

Figure 3.3a shows the snapshots of fluorescence images of the diffusion of n-pentane in toluene solution with Nile Red in the microchamber. At time of 0 s, the fluorescence signal shown as red is strongest as n-pentane just starts to reach the shallow main channel from the deep side channel. With time, n-pentane moves along the x-direction into the main channel as revealed by expansion of the dark region along x-direction in the field of view because Nile Red does not fluoresce in n-pentane within the selected excitation. After 40 s, the entire field of view (691.2 μm × 491.5 μm) turns dark, suggesting that toluene is entirely displaced by n-pentane from the examined area. As n-pentane diffuses into the main channel, toluene also diffuses into the side channel. Toluene that diffuses into the side channel is pushed away by the flow in the side channel.

The fluorescence intensity at four locations is plotted as a function of time shown in Figure 3.3b. The locations are at 80-140 μm away from the junction of the side channel and the main channel. The decay of the intensity (i.e. fluorescence signal vs. time) at any given location was fitted well by a sigmoid function with Equation (3.2), derived by the same method for fluorescence in polymerase chain reaction (PCR) [42, 176]. As shown in Equation (3.2), time (t) is used to replace the number of cycles in PCR.

$$I = 1 - \left(0.993 + \left(\frac{-1.05}{1 + exp\left(\frac{t}{4.3} - A\right)}\right)\right) \tag{3.2}$$

I is normalized intensity, t is time and A is a constant depending on the location. The delay in the intensity drop of location correlated well with the

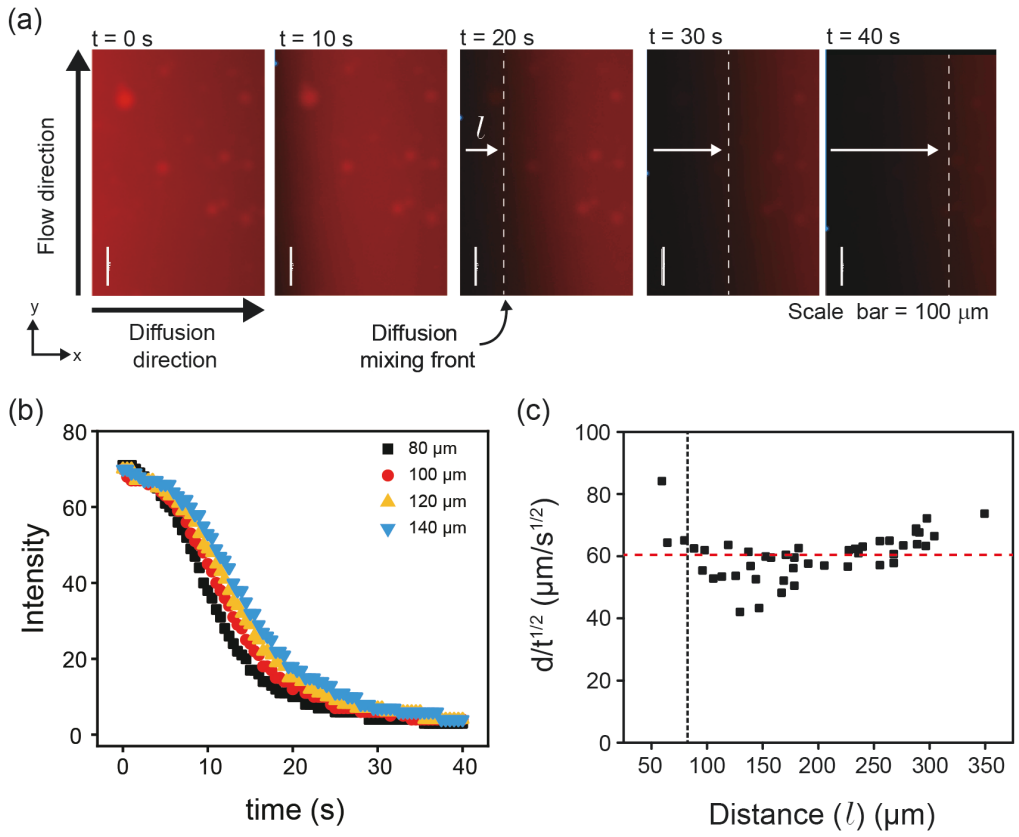

Figure 3.3: Fluid chamber characterization (a) Snapshots of n-pentane diffuses in Nile red, toluene solution. y-axis is the flow direction, while x-axis is the diffusive mixing direction. (b) Intensity versus time at different distances to the side channel. (c) Front layer diffusion distance over time square root at different times. Here the front layer diffusion distance is the distance between the side channel (x = 0) and the diffusion front obtained from fluorescent images. Black dot line indicates the minimum distance required to achieve diffusive mixing (i.e. x = 80 μm). Red dashed line represents the plateaued value ($\sim$ 60 $\mu m/t^{1/2}$).

distance leading to a steady increase of 0.3 per 20 μm distance increment for parameter A, as shown in Figure B.1, suggesting that the mixing conditions are identical at different locations in our observation area. The fitting constants 0.993, -1.05, and 0.43 were selected based on error minimization. The model used in detection PCR fits our systems where the concentration of the fluorescence varies over time. In a PCR reaction, the fluorescence intensity of the PCR solution is continuously measured over a period of time at a fixed spot. Initially, at early stages of PCR, the fluorescence intensity increases slowly until sufficient copies of the gene are made. With time, the intensity increases sharply until a plateau is reached when all the probes are consumed by the reaction. Therefore, the fluorescence intensity profile displays a logistic curve. Similarly, in our setup, as the diffusion of n-pentane takes place, the fluorescence intensity at a fixed location (80 μm) decreases according to a logistic function. At early times, the fluorescence intensity decays slowly as the concentration of n-pentane is low. With time, the intensity decreases sharply as the concentration of n-pentane increases until the intensity reaches a plateau when all the toluene has been replaced by n-pentane.

In Figure 3.3c, the front layer moving distance d normalized by the square root of time $t^{1/2}$ is plotted as a function of the distance d from the side channel. For a constant concentration source Fick's diffusion in 1-dimension scenario, the diffusion length d and time t follows:

$$\frac{d}{\sqrt{t}} \sim 2\sqrt{D} \tag{3.3}$$

D is diffusion coefficient, which is assumed to be constant in our system. The results of constant $\frac{d}{\sqrt{t}}$ suggest that mixing at a critical distance (i.e. 80 μm to the side channel) is well described by a diffusion process. At a distance from the side channel is less than 80 μm, the mixing is not well described by diffusion, which could be caused by the influence of the side channel. On the other hand, a longer distance means a longer diffusion time, which is undesirable as the maximal fluorescence intensity is reached in a shorter duration. Therefore, our observation area is kept at 80 μm to the side channel in the

following experiments. There is a critical value because of the momentum influence in the side channel, as we do not have a solid boundary such as a membrane to eliminate the influence of the side channel. Based on the observation, at distances longer than 80 μm, the convective effect of the flow is negligible and the transport of the dye is predominantly by diffusion in our system. It worth noting that 80 μm is not a universal value, and it may change if the experimental conditions change such as flow rate in the side channel or liquids in the microfluidic chamber.

The duration time for n-pentane replacing toluene is about 40 s over 491.5 μm distance. Since n-pentane diffusion rate follows Equation (3), $\frac{d}{\sqrt{t}}$ is constant, at around 60 $\mu m/s^{1/2}$, as shown in Figure 3.3c. At 40 s, the calculated travel distance for front layer is 379 μm, which is comparable with the actual moving distance, i.e. 491.5 μm. The difference between calculated and actual values may be from the non-diffusive behaviour below the critical distance of 80 μm.

Given that n-pentane diffusion from side channel into the main channel is a one-dimension diffusion in our system, the diffusion follows:

$$\frac{\partial c}{\partial t} = D\frac{\partial^2 c}{\partial x^2} \tag{3.4}$$

c is concentration of n-pentane, t is time, D is diffusivity of n-pentane in toluene and x is the distance to the side channel. Solving Equation (3.4), n-pentane concentration distribution along x-direction is:

$$c = c_B^{pen} erfc\left(\frac{x}{2\sqrt{Dt}}\right) \tag{3.5}$$

For a given time, n-pentane concentration distribution along x-direction follows error function. The error function distribution is proved in Figure B.2.

Assuming the ratio of the fluorescent dye Nile Red and toluene remains constant, from the intensity with time, we can obtain $r_{solvent/toluene}$ in the diffusive mixing process. As shown in Figure 3.4a and b, the intensity of fluorescence is quantified to obtain the change in the chemical composition in space and in time. Toluene concentration is estimated by $c \sim I$. Here

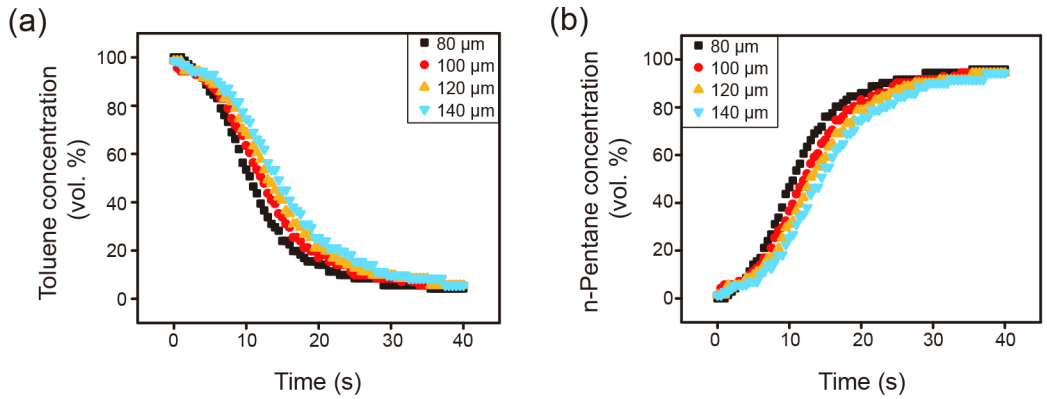

Figure 3.4: (a) Change in toluene concentration with time at 80 μm, 100 μm, 120 μm and 140 μm of distance (l) to the side channel. (b) Change in n-pentane concentration with time at 80 μm, 100 μm, 120 μm and 140 μm of distance to the side channel.

c is toluene concentration, and I is normalized fluorescence intensity. The diffusion of the probe in different solvents is assumed to be same, due to similar viscosity. Both n-pentane and toluene are good solvents of Nile red, our probe. At trace concentration (i.e. < 1 μM), the solubility of the dye in both solvents is likely to be negligible for the diffusivity. Toluene concentration decreases with diffusion time, while n-pentane concentration, reverse of the toluene concentration, increases with time.

3.3.2 Applications of the diffusive mixing device

The mixing device was used to observe precipitation of asphaltene from toluene by n-pentane. As shown in Figure. 3.5, the precipitation of asphaltene can be observed in situ. Images were taken from 80 μm which is the critical distance need to achieve diffusive mixing as also shown in Figure 3.3. Up to a distance of 80 μm, mixing may be influenced by the bulk flow of solution B. The high amount of precipitates observed at 80 μm is likely due to the convective mixing. However, at longer distances, the diffusive mixing is established and the amount of precipitates remain similar with distance. With the high resolution of TIRF – i.e. 200 nm – observation of individual asphaltene precipitates may also be possible.

The proposed device is not limited to the in situ asphaltene precipitation,

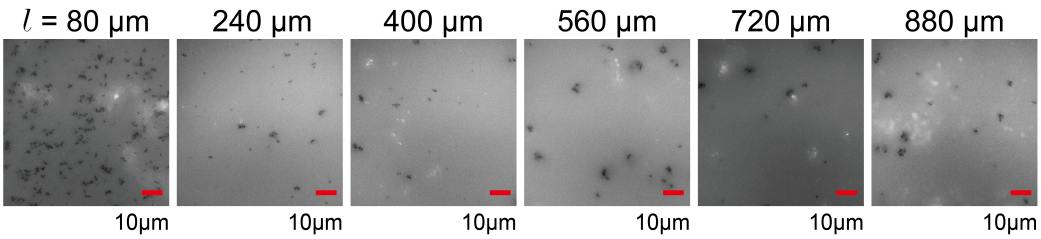

Figure 3.5: Total internal reflection (TIRF) microscopy images of asphaltene precipitation driven by diffusive mixing between an asphaltene solution in toluene as solution A and n-pentane as solution B. More precipitates observed at l of 80 μm is attributed to the difference in mixing condition near the side channel ($l < 80$ μm) and in the inner chamber ($l > 80$ μm).

but it can also be applied for studying dilution induced crystallization from a liquid mixture. The dilution induced crystallization occurs due to the reduced solubility of the solute in the liquid mixture by the addition of an antisolvent. Using the diffusive mixing device, we can visualize the crystallization process. As an example, we demonstrate in situ growth of β-alanine crystals by dilution of a ternary solution consisting of β-alanine, isopropyl alcohol, and water (solution A) by isopropyl alcohol (solution B). As solution B is diffused through the main channel, β-alanine becomes oversaturated and crystallizes on the surface of the channel as shown in Figure 3.6. Using the device shown here, it is possible to control the crystallization by tuning the mixing between antisolvent and the liquid mixture.

It worth noting that although surface properties, including hydrophobicity and roughness, do not affect the diffusion process in the main channel [120], the phase separation may be affected if the surface acts as nucleation sites. For instance, oil droplets from liquid-liquid phase separation may more readily occur on hydrophobic surfaces [259].

3.4 Conclusion

A method for in situ observation of precipitation and phase separation is shown here via a quasi-2D microfluidic device coupled with total internal reflection (TIRF) microscopy. The device enables controlled diffusive mixing between an

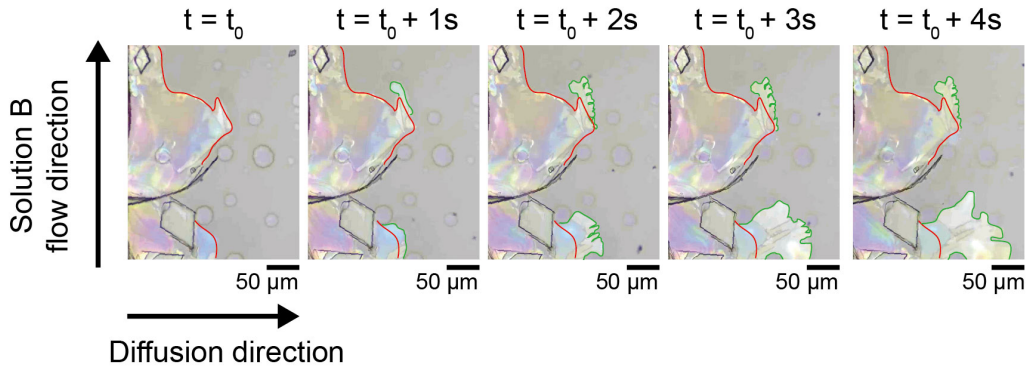

Figure 3.6: In situ crystallization of β-alanine using the diffusive mixing device. With time crystals –indicated in green line – grow in the direction of diffusive mixing. The red lines indicate the boundary of stationary crytals as reference.

asphaltene solution and a mixture of n-pentane and toluene. Using a fluorescent dye, the diffusive mixing front is determined, based on which a critical distance required to achieve fully diffusive mixing is obtained. Moreover, from the intensity profile of the fluorescent dye, the concentration profiles of n-pentane and toluene can be estimated. TIRF image shows the diffusive mixing is not influenced by asphaltene precipitation as well as the quantity of the precipitated particles. The set-up shown in this work is useful for high spatiotemporal study of precipitation dynamics for various applications including asphaltene precipitation, nanoparticle formation, crystal growth or protein precipitation.

Chapter 4

Primary Submicron Particles from Early Stage Asphaltene Precipitation Revealed In-situ by Total Internal Reflection Fluorescence Microscopy in a Model Oil System

Abstract

Paraffinic froth treatment (PFT) is an essential step in oil sands extraction. The ability to quantitatively understand and control asphaltene precipitation induced by solvent dilution is key to technology innovation in PFT process. In this work, we investigate the early stage of asphaltene precipitation in a model oil system in response to diffusive solvent addition in quasi-2D confinement. Using total internal reflection fluorescence microscope, we provide direct visualization of the size distribution and structural characteristics of asphaltene precipitates with a spatial resolution of 200 nm and temporal resolution of 250 ms. Our results show the correlation between the size and number of the asphaltene particles and the concentration of the paraffinic solvent in the diluent. Notably the aggregates were found to consist of primary submicron particles with a similar size from 200 nm to 400 nm in radius. These particles may be the primary elementary units that aggregate and form bigger particles via aggregation. The growth time of asphaltene particles decreases with increase n-pentane concentration in the observation area. The findings from this work provide new insight into the effects of solvent mixing on the size distribution and morphological characteristics of asphaltene precipitates that are important for association with water and solids and separation properties.

4.1 Introduction

Asphaltene is classified as the most complex and heaviest component in heavy oil, consisting of polynuclear aromatic species with different molecular weight, polarity, and heteroatom content. As a solubility class, asphaltene is insoluble in paraffinic solvents and soluble in aromatic solvents [205]. In the industrial process of oil sands extraction, bitumen with a considerable amount of fine solids and water is separated from oil sands ore by warm-water extraction to form bitumen froth. The froth typically consists of 60 $wt\%$ bitumen, 10 $wt\%$ mineral solids, and 30 $wt\%$ water [168]. In paraffinic froth treatment (PFT), solids and water are removed from the bitumen froth by adding paraffinic solvents at the solvent/bitumen ratio (S/B ratio) above a critical value, which triggers asphaltene precipitation and agglomeration with water drops and solids. Controlled asphaltene precipitation in PFT process is a key parameter to yield bitumen product in both high quality and high recovery [168, 232].

For several decades, extensive research has been conducted to understand molecular or colloidal structures, solubility and phase behavior of asphaltene in various media including solvents and bitumen. However, dilution-induced asphaltene precipitation in bitumen froth treatment is still one of the most important and challenging topics. In addition to complexity in chemical and physical properties of asphaltene and bitumen, asphaltene precipitation induced by solvent dilution involves dynamical processes over multiple length scales (from nanometer to millimeter) and varied time scale (from seconds to days). It is known that the onset and quantity of asphaltene precipitation are related to the solvent type, S/B ratio, temperature and pressure. For a given solvent, asphaltene precipitation occurs over a range of S/B ratios [205]. The size, density and structure of the asphaltene precipitates are important for the separation properties of their aggregates with water droplets and solids.

However, the morphology and structure of the precipitates are not well defined. The settling behavior suggests that asphaltene precipitates are porous and tenuous fractal structures with fluid trapped inside. A quicker settling

rate represents a larger fractal dimension and more compact particles [44]. The settling rate depends on the type of precipitant. For example, the rate of n-pentane precipitated asphaltene is two magnitudes higher than that of n-heptane precipitated asphaltene [44]. For a given type of precipitant, settling rate increases with the concentration of precipitant and then decreases at approximately 75 %. Based on the mean diameter of the precipitates, two classical models are applied to approximately describe the growth dynamics: diffusion-limited aggregation (DLA) and reaction-limited aggregation (RLA) [113, 242]. Transition from one model to the other was observed at different S/B ratios, although the mechanism for such transition is not fully understood [113, 185, 242].

In parallel, liquid-liquid microphase separation induced by dilution is ubiquitous in many other technological and industrial processes. A simple example is known as 'Ouzo' effect in a ternary mixture of oil, ethanol and water [258]: When water is added into a clear Greek alcoholic drink Ouzo, anise oils in the drink become oversaturated by dilution and spontaneously form nanodroplets in the cloudy mixture [213]. The same effect can also be seen when eucalyptus disinfectants and mosquito repellents in alcohol solutions are diluted with water [246]. In liquid-liquid microextraction, oil microdroplets from the spontaneous phase separation by dilution are the basic unit to concentrate and separate trace hydrophobic analytes from aqueous samples [170]. Gas molecules, small hydrophobic organics, lipids or polymers dissolved in a polar organic solvent all exhibit similar effects, forming bubbles, or nanoparticles upon dilution by a poor solvent. The process is also referred to as solvent exchange [255], nanoprecipitation [182], solvent displacement or solvent shifting [18, 108].

The key feature of the above spontaneous liquid-liquid phase separation is that the growth dynamics of individual domains is determined not only by concentration of the compositions (thermodynamic aspects), but also by the temporal and spatial characteristics of the mixing process of the solvents (dynamic aspects) [258]. How the solvent is added has a great impact on the size distribution, morphological characteristics, chemical and physical properties of

the formed new phase. The dilution-induced microphase formation is complex, influenced by several factors including solution composition [119] and mixing of the solvent and the solution [258]. Latest advance made in well-defined systems has provided a solid foundation to understanding another dilution-induced phase separation process in heavy oils: asphaltene precipitation. The experimental techniques and theoretical frameworks are transferable to the study of early stage dynamics of asphaltene precipitation induced by mixing with a paraffinic solvent.

There are knowledge gaps in early stage dynamics of asphaltene precipitation induced by paraffinic solvent addition. Direct visualization of the size distribution and structural characteristics of asphaltene precipitates from an early stage is challenging, largely due to the high optical density of the mixture mainly from asphaltene fractions. Measurements with improved spatial resolution were recently performed by using confocal laser-scanning microscopy in a transmission mode [185]. Size distribution of asphaltene aggregates in various solvents and precipitants were observed as a function of time when a very thin film of the mixture was confined between two plates [185]. The amount and the size distribution of asphaltene precipitates after phase separation were also studied by a confocal microscope and image processing technique [45, 91]. In the optical measurements above-mentioned, the concentration of asphaltene in the crude oil/solvent solution must remain very low ($< 0.2\ mg/ml$) to allow enough intensity of the light to pass through the samples. Therefore the measurements were either far below the concentration regimes in bitumen, or missed the entire early stage dynamics of the precipitation, due to the ratio of solvent already high above the critical ratio.

Total internal reflection fluorescence microscopic system (TIRF) is a technique that can largely overcome experimental difficulties from asphaltene while providing high temporal and spatial resolutions. In the configuration of TIRF, the light travels within a substrate (usually a thin glass slide) through total internal reflection and creates an evanescent field above the substrate [20]. The selective excitation and visualization of species in TIRF is confined in a narrow zone of the evanescent field generated from the total internal reflection. The

sampling zone in TIRF is approximately 150 nm adjacent to a substrate as well as what on the surface. The probe depth into the sampling zone depends on the refractive index of the media. The strong scattering background from the medium outside of the substrate can be largely neglected, which is the most desirable feature of TIRF configuration, compared to a transmission or reflection mode of an optical microscope. The difficulty from the high optical density will be largely overcome, due to the thin zone of the evanescent field. TIRF allows for following the microphase separation during solvent mixing.

The aim of this work is to in-situ study dynamics of asphaltene precipitation in response to different mixing processes of a model paraffinic solvent (i.e. n-pentane). Employing the experimental techniques of TIRF microscope for mixing in a quasi-2D chamber, our measurements will reveal the onset and temporal evolution of asphaltene precipitates during the dilution. The measurements will provide high temporal (~ 0.25 second) and spatial (~ 200 nm) resolutions at high asphaltene concentration. This work will reveal early stage asphaltene precipitation during diffusive mixing with a paraffinic solvent. Although convective mixing takes place in many solvent-induced precipitation processes including PFT, locally diffusive mixing may happen, particularly for a large volume and/or viscous liquids. Furthermore, diffusive mixing process allows us to understand the roles of solvent diffusion in the precipitation on a microscopic scale, laying the basis for a quantitative understanding of asphaltene precipitation under more complicated mixing conditions. Our results show that the sizes of asphaltene precipitates are associated with mixing conditions.

From TIRF images, we quantify the size distribution, particle quantity and surface coverage of asphaltene precipitates. Size of precipitate particles is an important parameter for asphaltene precipitation modeling [57, 58], associated with the degree of flocculation of the primary submicron particles. As the sedimentation of asphaltene precipitates is essential for sweeping down water and solids from bitumen in PFT [117, 118, 168], our work implies that mixing conditions may be an approach to form large aggregates of asphaltene with extended structures for efficiently cleaning up water and solids.

4.2 Experiment

4.2.1 Chemicals and sample preparation

Asphaltene used in this study was n-pentane precipitated asphaltene supplied by Quadrise Canada Corporation, and it was used as received. Toluene (ACS grade, Fisher Scientific, 99.9+%) was used as the solvent for asphaltene. The diluent was n-pentane (Fisher Scientific, 98%). Nile Red (Fisher Scientific) was used for microchamber characterization. CHNS/O Analyzer (Flash 2000, Thermo Scientific) was used to measure the organic element composition of asphaltene in the asphaltene sample, and the composition is 85.3 ± 0.9 $wt.\%$ of carbon, 8.2 ± 0.1 $wt\%$ hydrogen, 3.7 ± 0.1 $wt.\%$ of sulfur and 1.0 ± 0.0 $wt.\%$ of nitrogen.

The asphaltene in toluene solution was prepared as following: 20 g asphaltene was first dissolved in 200 mL toluene and then the mixture was shaken for 30 min and left still at room temperature for 1 day till asphaltene was fully dissolved. The mixture was filtered by using a PVFD filter paper with 0.22 μm pore size (Millipore) to remove any inorganic solids $>$ 0.22 μm in the asphaltene sample. After removal of toluene by rotatory evaporator, the obtained asphaltene is treated as both inorganic solids and solvent free asphaltene. It is worth noting that trace amount of inorganic solids with $<$ 0.22 μm size may still remain in the asphaltene after the filtration, but their impact on asphaltene precipitation was negligible in this study. 1.7 g of the treated asphaltene sample was redissolved in toluene with a total volume of 100 mL. The mixture was well shaken for 30 min and left for 1 day for asphaltene to be fully dissolved in toluene. The as-prepared asphaltene in toluene solution is named as 'solution A' with a concentration of 17 g/L.

The solvent (named 'solution B') used to precipitate asphaltene in all experiments was a mixture of n-pentane and toluene with the initial concentration of n-pentane in solution B (C_B^{pen}) from 70 % to 100 %, as shown in Table 4.1.

Table 4.1: Composition of solvents. For all cases, solution A is 17 g/L of asphaltene in toluene. C_B^{pen} is the initial concentration of n-pentane in solution B

C_B^{pen} (vol. %)	n-Pentane (vol. %)	Toluene (vol. %)
70	70	30
80	80	20
90	90	10
100	100	0

4.2.2 In-situ detection of asphaltene precipitates using quasi-2D microfluidic device and TIRF

A quasi-2D microfluidic device consisting of a shallow main channel (height = 20 μm) and a deep side channel (height = 260 μm) was used for the in-situ detection of asphaltene precipitation. Diffusive mixing between toluene and n-pentane was confirmed through fluorescence microscopy by doping toluene with Nile red. A minimum distance from the side channel to the main channel required to achieve fully diffusive mixing was obtained from the fluorescence characterization.

For the precipitation of asphaltene, the quasi-2D microfluidic device was pre-filled with a solution A. Solution B was introduced through the side channel at 5 mL/h continuously replacing solution A. The process proceeds till all solution A displaced from the chamber as sketched in Figure 4.1a. Once in the side channel, solution B diffused through the main channel to mix with solution A. No apparent convective flow was observed due to the shallow height of the main channel. Detailed characterization of diffusive mixing in the quasi-2D microfluidic device was described elsewhere [120, 131].

As solution B mixed with solution A, precipitation of asphaltene was observed using TIRF equipped with 60×/1.49 NA objective (DeltaVision OMX Super-resolution microscope, GE Healthcare UK limited, UK). The fluorophores in the asphaltene solution were excited with a green laser with wavelength λ = 488 nm and fluorescence emission was detected at 576 nm. The images were collected in a field of view of 82.5 μm × 82.5 μm distanced more than 80 μm from the side channel to eliminate the edge effect. The refractive indices

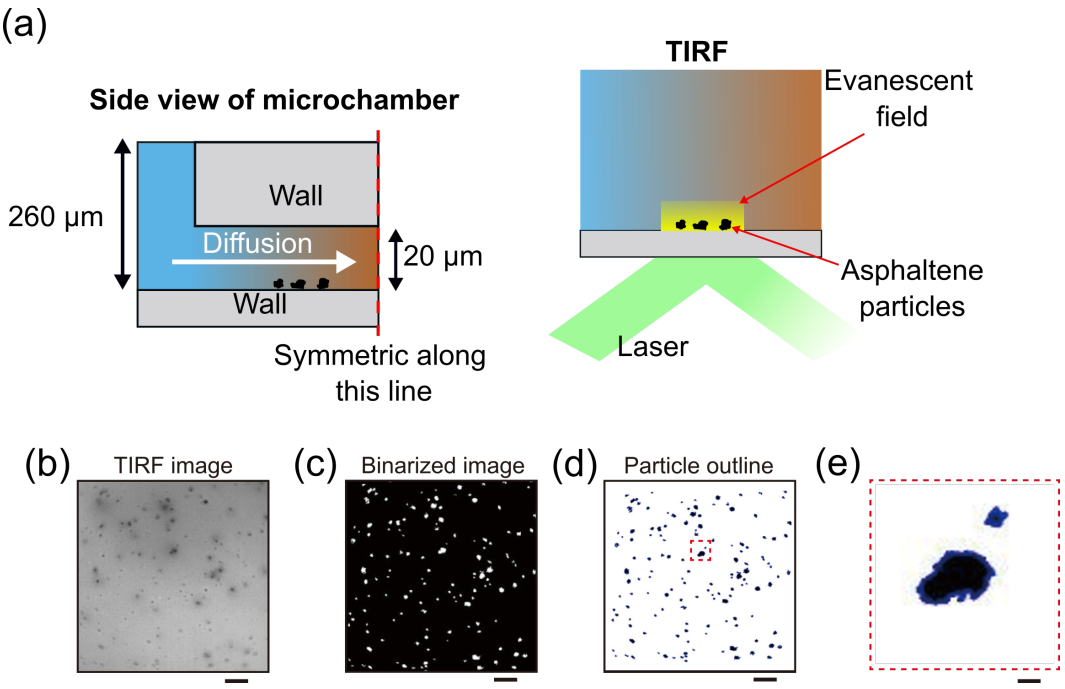

Figure 4.1: (a) Schematic representation of the microchamber and TIRF setup. (b) Representative TIRF image of asphaltene particles when asphaltene solution is displaced by solution B (n-pentane solution). The asphaltene particles appear as black dots. (c) Binary image processed by MATLAB code based on TIRF image with white dots representing asphaltene particles. (d) Outline asphaltene particles for further analysis. e) Zoomed-in image of an outlined particle to show the irregular structure of asphaltene particles. Scale bar is 10 μm.

of asphaltene (RI = 1.72), toluene (RI = 1.50), and n-pentane (RI = 1.36) needed for TIRF were taken from literature [39, 100, 225]. We note that the RI of 1.72 from the literature is not a universal value, possibly varying with the source of asphaltene. However, the contrast in TIRF imaging only requires the difference between asphaltene and the surrounding medium. As asphaltene precipitated out, fluorescence signal was quenched and the precipitates appeared dark. Although TIRF can detect objects on the solid surface as well as in the evanescent field, the precipitates in the images at our final stage are all on the surfaces, as our solution is already n-pentane without precipitates. Even if some objects are in the bulk, they may not be visible to our TIRF images if they move around. So even our images showing the dynamical process, the precipitates are mainly on the surface.

Confocal Laser Scanning Microscopy was performed on a Leica SP8 STED (Stimulated Emission Depletion) Falcon system (Leica microsystem, Germany) based on an inverted microscope (Leica DM8). The dried samples in ambient temperature were imaged with a $100\times/1.4$ NA immersion objective using 470 nm laser excitation in order to validate the image collected from TIRF and morphology of precipitated asphaltene processed from the image analysis. The same samples after TIRF experiment were used for the purpose. The solvent (i.e. n-pentane), which is already free of asphaltene after TIRF experiment, was removed by evaporation overnight, while asphaltene particles remain on the substrate. The fluorescence emission signal was collected between 478 nm to 670 nm range at a pixel size of 105 nm and using a dwelling time of 1.44 μs (400 Hz). Typically, 4 time line averaging was used to collect the images. The spatial resolution of confocal microscope is 120 nm. If the spacing between two neighboring domains is smaller than the spatial resolution, the separation between the domains cannot be resolved in the images. A more thorough description of the system could be found in the literature [147].

4.2.3 Image analysis of asphaltene precipitates

The series images extracted from the video frames were processed and analysed using a software programmed in MATLAB. Microscopic images often suffered

the problems, such as low contrast, noise and uneven background. Several image processing techniques were used to enhance the image, including stretching pixel intensity range, median filter, Gaussian noise filter and top-hat filtering. The enhanced image was then binarized with a selected threshold (T). If the intensity value of the pixel is smaller than T, it was converted to 0. The choice of T was arbitrary to a certain extent with a relationship with the maximum intensity in the whole image (I_{max}). The threshold was varied from 0.5 I_{max} to 0.8 I_{max} to capture as many particles as possible. The arbitrary of choosing threshold leads to 30 % uncertainty of the data.The objects smaller than 200 nm were removed using area opening and the objects along the image border were masked out because they are likely noise of the image as the size is already close to the spatial resolution of TIRF. The objects larger than 200 nm in radius (i.e. 400 nm in diameter) were reliable. For the 80 nm pixel size TIRF camera, objects larger than 200 nm radius contain more than 20 pixels.

The software measured the set of properties for each object in the binary image, including object centroid, area size, perimeter and radius of the precipitates. The centroid provided location information for further tracking the objects in the series images collected at different time. The white dots with irregular shape corresponded asphaltene particles, as shown in Figure 4.1b. The dots were then outlined by blue lines and the equivalent radius of particles was defined as the radius of the circle that has the same area as the irregular shape, as shown in Figure 4.1c and 4.1d. Particle quantity was obtained by counting the number of the white dots divided by the total observation area. Surface coverage was calculated by summing the areas occupied by particles divided by the total observation area.

4.3 Results

4.3.1 Morphology of early stage precipitates: primary submicron particle sizes

High spatial resolution images enabled by TIRF allow us to resolve the asphaltene aggregates formed by several particles. The asphaltene particles are

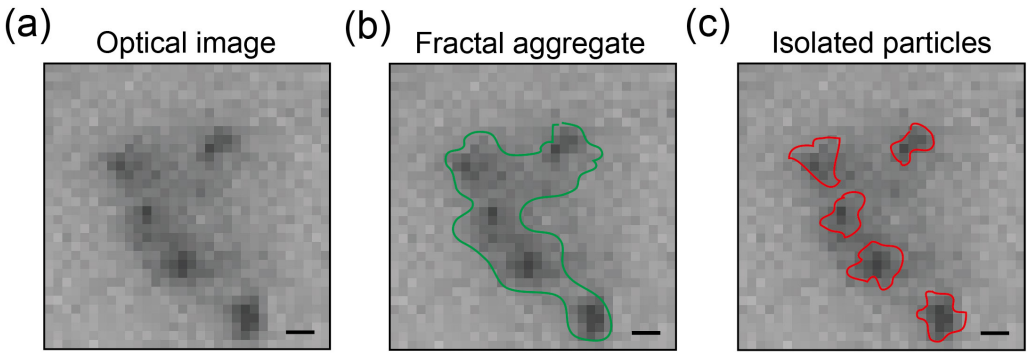

Figure 4.2: (a) Snapshot of an asphaltene aggregate at C_B^{pen} of 90 %. (b) Fractal structure of the asphaltene aggregate. (c) Isolate aggregate to primary submicron particles. Scale bar is 1 μm.

dispersed and there is little evidence of overlap when the images were taken. As shown in Figure 4.2, in the primary submicron particle study, aggregates are isolated into primary submicron particles. We define the primary submicron particles are the population with the most probable distribution. These primary submicron particles are larger than the spatial resolution limit (i.e. 200 nm), and therefore the images may reliably reveal their sizes. The aggregates are referred to as fractal aggregates in the confocal study.

The asphaltene particle parameters at final state were obtained by averaged value of three rounds of experiments after injecting solution B into the microfluidic device for sufficient time. Final state is defined as the state at which the asphaltene particle parameters (i.e. mean radius, particle quantity and surface coverage) are stable and the asphaltene in the mixture does not lead to further precipitation in measured time duration.

Figure 4.8a shows images of the final state of precipitated asphaltene particles over a large field of view for variety of particle sizes at different n-pentane concentration in solution B. The zoomed-in images correspond to the asphaltene particles in the corresponding color square in the large field of view. The detailed structure of asphaltene particles are revealed in the images. The asphaltene particles are either primary submicron particles or aggregates formed by several primary submicron particles.

To study the primary submicron particle size, the aggregates were isolated

into primary submicron particles. The primary submicron particle size was measured by counting pixels. Figure 4.8b shows the particle equivalent radius at C_B^{pen} of 70 % to 100 %. The data were collected based on a 82.5 μm × 82.5 μm area in each group of n-pentane concentration. Remarkably, the majority of primary submicron particle radii are distributed in a narrow range of 200 nm - 400 nm, independent of C_B^{pen}. The average radius is around 300 nm.

The primary submicron particle size of precipitated asphaltene was further confirmed by confocal microscope, as shown in Figure 4.3, where the confocal images were captured in air after precipitation with 100% n-pentane to avoid threshold influences on the detection in the solution. With neglecting the data of aggregates, the averaged equivalent particle radius measured from confocal images on the precipitates is around 250 nm, which is comparable to the value obtained from TIRF experiment in solutions. The average size of the primary submicron particle in the solvent is slightly larger than that in the dry state, consistent with swelling behavior of asphaltene in the solvent [192]. The results verified the presence of primary submicron particles, and the reliability of using TIRF to monitor the asphaltene precipitation solutions. Figure 4.3b has a peak from 0.2 μm to 0.4 μm in the relative frequency distribution based on quantity of asphaltene particles, representing primary submicron particles whose radius is from 0.2 μm to 0.4 μm. There are also some particles whose equivalent radius distribute from 0.4 μm to a few microns, representing aggregates with different sizes coexist with primary submicron particles. The absence of particles smaller than 0.2 micron is the result of the detection limit. Noise and small particles cannot be distinguished beyond the detection limit.

4.3.2 Influence of initial solvent concentration on asphaltene precipitates

Three characteristics of the asphaltene particles are studied in this section, including particle size distribution, particle quantity and surface coverage of asphaltene particles. Although asphaltene aggregates are formed by several primary submicron particles, aggregates were treated as single units rather than counting primary submicron particles in it when measuring particle size

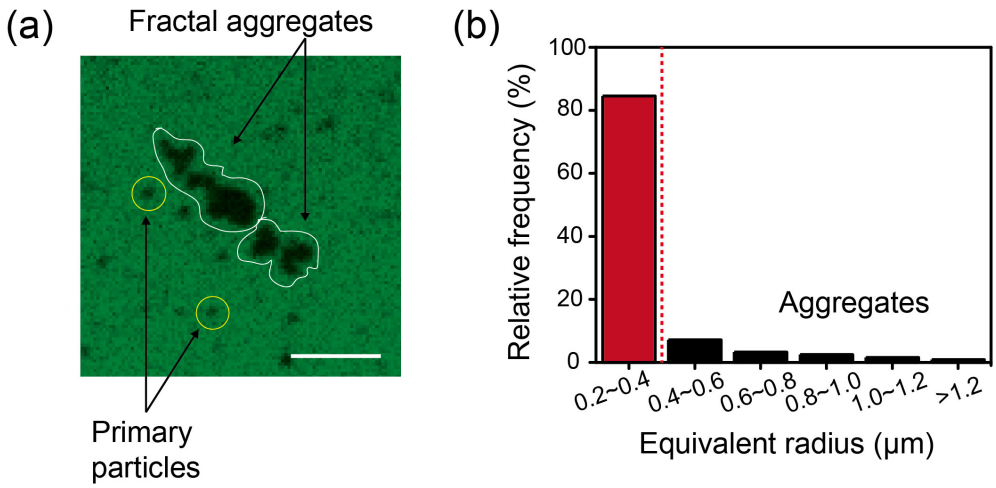

Figure 4.3: (a) Snapshots of confocal image of asphaltene particles at the concentration of n-pentane in solution B (C_B^{pen}) of 100 %. The image shows primary submicron particles co-exist with fractal aggregates. Scale bar is 4 μm. (b) Asphaltene particles equivalent radius relative frequency of confocal image of C_B^{pen} of 100 %. The column in red corresponds to the primary submicron particle in the image of (a).

and counting particle quantity. Particle quantity and surface coverage were normalized by the unit area in the field of view.

The morphology of asphaltene at final state is influenced by C_B^{pen}. Figure 4.4a shows particle quantity increases with n-pentane concentration in solution B. The asphaltene particle quantity at C_B^{pen} of 70 % is around 1 $\pm$ 1 per 1000 μm^2, and is around 12 $\pm$ 5 per 1000 μm^2 at C_B^{pen} of 100 %. Figure 4.4b shows asphaltene surface coverage increases with n-pentane concentration in solution B. The surface coverage at C_B^{pen} of 70 % is around 0.12 $\pm$ 0.10 %, while the surface coverage reaches around 1.76 $\pm$ 0.39 % at C_B^{pen} of 100 %. For precipitates that are too small to settle on the surface the precipitates can come close to the surface through Brownian motion, and stay there through non-specific interactions with the surface. Surface quantity and coverage are approximately proportional to the concentration of asphaltene precipitates in the bulk mixture. The concentration of precipitates in our experiments may not be constant with time. The surface coverage represents the concentration of precipitates in the entire process of solvent mixing.

Figure 4.5 shows influence of C_B^{pen} on asphaltene particle size distribution

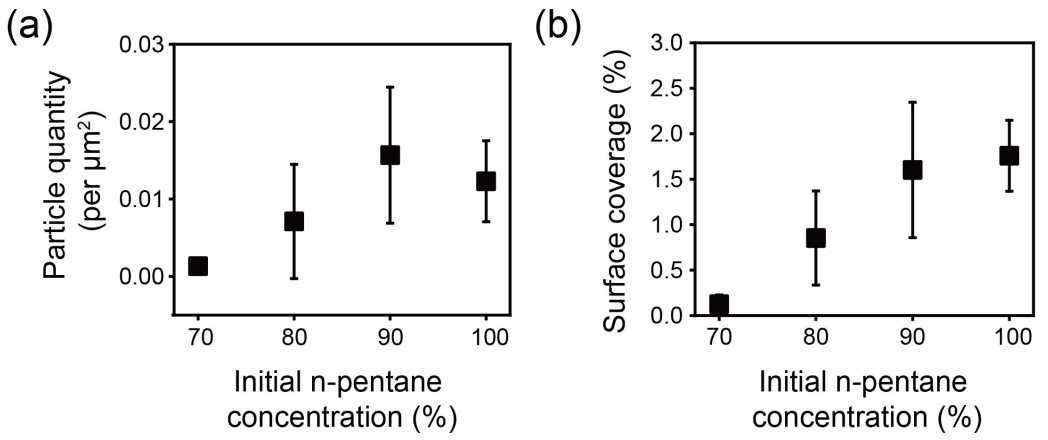

Figure 4.4: Final state asphaltene particle amount at the concentration of n-pentane in solution B (C_B^{pen}) of 70 % to 100 % : (a) particle quantity in the unit area, (b) surface coverage of asphaltene particles.

at final state. Experiments were repeated three times for each condition in order to reduce errors. There are always two types of particles, regardless of C_B^{pen}: primary submicron particles and aggregates. At the final state, the size distribution of the asphaltene has an obvious peak of primary submicron particles, as shown in Figure 4.5. The corresponding primary submicron particle size is consistent with the confocal result in Figure 4.3. The height of the peak appears to be lower than that in the confocal results. The difference may be mainly caused by the state of samples, where confocal microscope captures all the primary submicron particles in dried state while some of these particles in TIRF experiment are mobilized as a suspension in the solution medium. Asphaltene aggregates with different sizes are formed. TIRF results also show the existence of aggregates with different sizes from 0.4 μm to a few microns, which is consistent with the confocal result in Figure 4.3. The proportion of the primary submicron particles increases with decrease of C_B^{pen}, which means less aggregates are formed. In other word, the proportion of aggregates increases with increase of C_B^{pen}.

The final particles may represents the way how asphaltene precipitates evolve, triggered by mixing with n-pentane. Higher proportion of primary submicron particles at C_B^{pen}, as shown in Figure 4.5, is the consequence from an early stage of precipitation. More aggregates formed at higher C_B^{pen} is

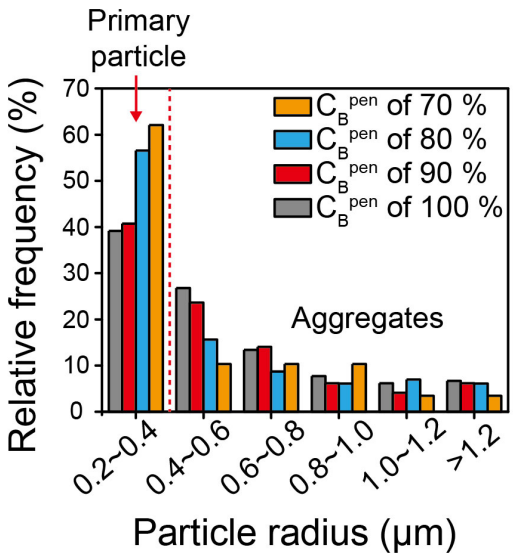

Figure 4.5: Relative frequency of asphaltene particle size distribution with C_B^{pen} of 70 % to 100 %.

equivalent to grown or aggregated precipitates. However, we do not know how the asphaltene aggregates from entities of even smaller sizes to primary submicron particles around 300 nm in radius, as the required spatial resolution is beyond the capacity of our technique.

4.3.3 Effects of n-pentane concentration on precipitation dynamics

We show the precipitates in-situ during diffusive mixing process with a spatial resolution around 200 nm in this section. The spatial resolution of the measurement is compromised due to continuous change in the medium properties.

Figure 4.6a and 4.6b show asphaltene precipitation precipitation process in-situ. Time 0 s is defined as the appearance time of the first particle (radius $>$ 200 nm) to be detected by TIRF. After a certain growth time, the surface coverage of the asphaltene particles in the observation area plateaus, as shown in Figure 4.7. The asphaltene particle growth time (i.e. duration from first asphaltene particle to the surface coverage reaches plateau) are different for different groups of n-pentane concentration in solution B. As shown in Figure 4.6c, the growth time at C_B^{pen} of 70 % and 80 % are both around 20 s, which

is higher than the growth time at C_B^{pen} of 90 % and 100 % around 5 s.

After reaching plateau, the asphaltene primary submicron particle size was analyzed by the same method described in the section 3.1. As shown in Figure 4.6c, the primary submicron particle size does not have detectable change after the growth time. Similar to the primary submicron particle radius at final state (i.e. after 5 min), the primary submicron particle radius is around 300 nm for the four groups. There is also no obvious dependence of asphaltene primary submicron particle size on n-pentane composition in solution B.

Finally we note that the chemical composition of mixture in the main channel can be estimated using the brightness of TIRF images. In the time course images from TIRF measurements, the brightness is determined by the emission light intensity of the fluorophores in the evanescent field (Figure C.1 in Supporting information). Two factors affect the emission light intensity: fluorophore concentration and penetration depth. Within the excitation wavelength range used in our experiment, only dissolved asphaltene have appropriate fluorophores for emission. Toluene and n-pentane have a weak emission (around 1000 a.u.), while precipitated asphaltene does not have obvious emission ($<$ 500 a.u.). In the solvent mixing process, dissolved asphaltene concentration decreases, due to dilution by n-pentane. Asphaltene precipitation also decreases the dissolved asphaltene concentration, when $r_{solvent/toluene}$ is higher than the onset ratio. The refractive index (RI) of n-pentane is 1.36, lower than that of toluene ($RI = 1.50$). The decrease of penetration depth (d_p) results in the decrease of excitation light intensity at a critical position during mixing. There is always a gradient from white to gray region from the mixing front. The signal from brightness can be obtained by gray scale value to estimate the solvent ratio. White region represents solution A, while gray region represents solution B (i.e. n-pentane and toluene mixture). We tracked the shift in the position along x-direction with the same brightness intensity (i.e. same concentration of dissolved asphaltene) with time. The data shown in Supporting Information indeed suggest that the mixing process is dominated by diffusion.

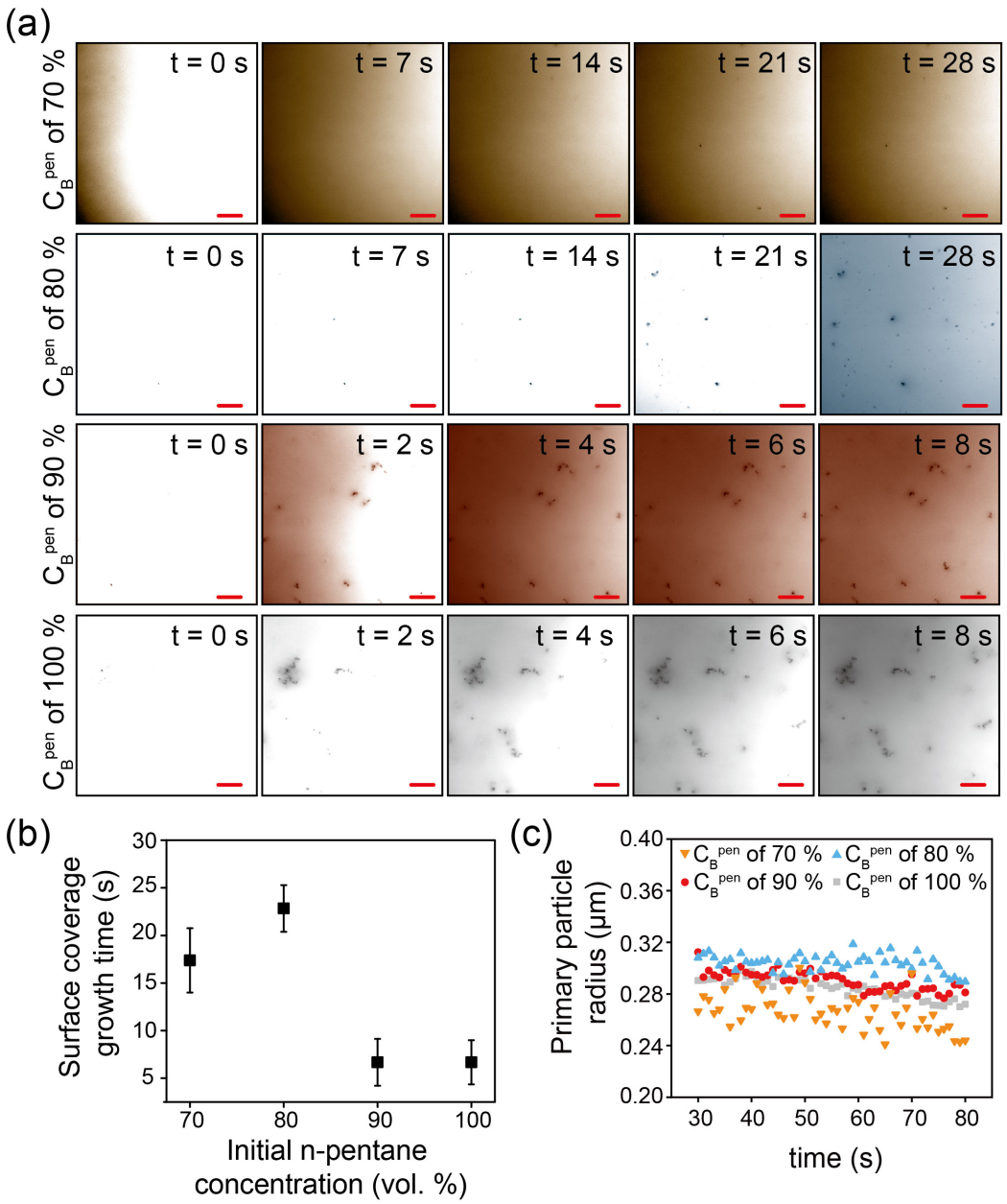

Figure 4.6: (a) Snapshots of asphaltene precipitation process at the concentration of n-pentane in solution B (C_B^{pen}) of 70 % to 100 %. Scale bar is 10 μm. (b) Asphaltene particle quantity growth time from the first particle appear till the surface coverage reaches plateau at C_B^{pen} of 70 % to 100 %. (c) Primary submicron particle size after 30 s.

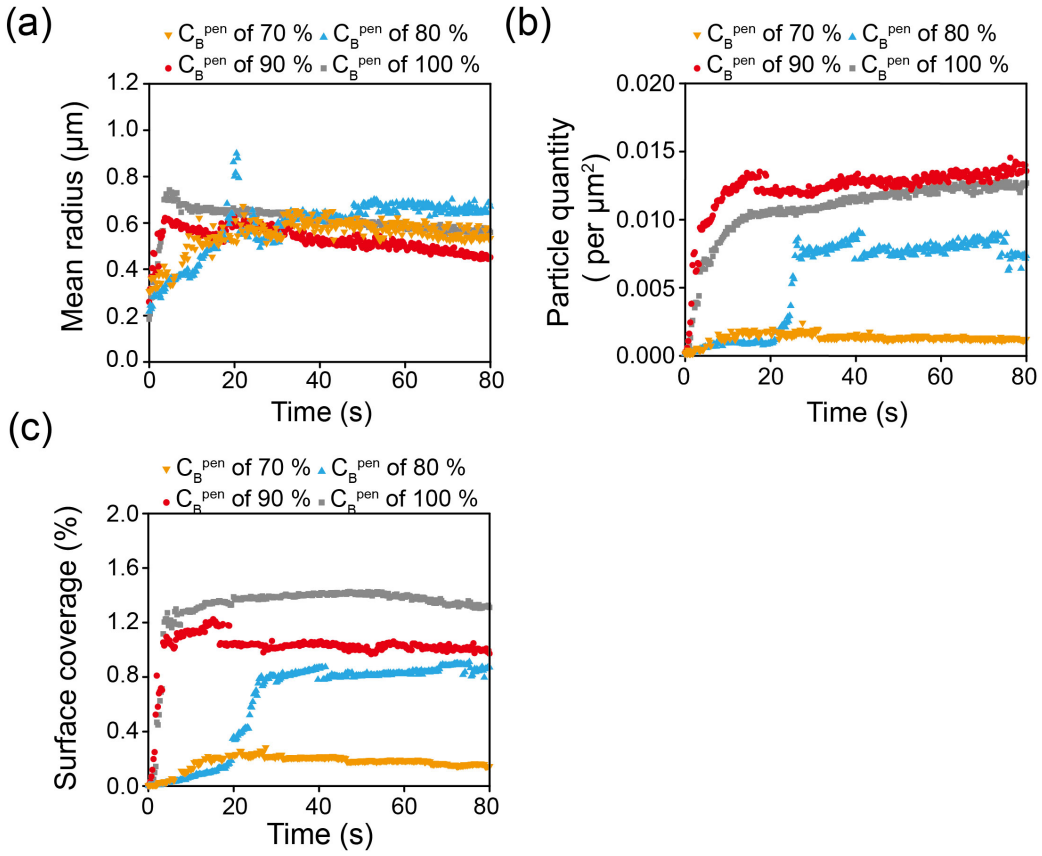

Figure 4.7: Asphaltene growth dynamics: (a) mean radius, (b) particle quantity (c) surface coverage. All of the three parameters increase at the first 30 s and reaches plateau afterwards for the concentration of n-pentane in solution B (C_B^{pen}) of 70 % and 80 %. The plateau is much earlier for C_B^{pen} of 90 % and 100 %.

4.4 Discussion

4.4.1 Possible mechanism for presence of primary submicron particles

The primary submicron particles observed by TIRF are not from settled precipitates under gravity as their sizes are too small to settle within the diffusion time of the solvent. Brownian motion of these particles is estimated as below [10]:

$$\overline{X}^2_{Brownian} = \frac{4RTK_m t}{3\pi^2 \mu N_a D} \tag{1}$$

$\overline{X}_{Brownian}$ is the moving distance of particles due to Brownian motion. R is gas constant. T is temperature, which is 294 K. K_m is correction for discontinuity of fluid, which is 1 for liquid. t is time of solvent diffuses across the observation field, which is 7.5 s as shown in Figure C.1a and C.1b. μ is the viscosity of the medium, which is assumed the same as the viscosity of n-pentane (i.e. 0.214 $mPa \cdot s$) because n-pentane concentration is high when asphaltene precipitation happens. N_a is Avogadro constant. D is the diameter of particles. Stokes settling motion of particles is estimated as below [10]:

$$\overline{X}_{settling} = \frac{(\rho_{asp} - \rho_{sol}) g D^2 t}{18\mu} \tag{2}$$

$\overline{X}_{settling}$ is moving distance of particles due to settling under gravity. g is gravity constant. ρ_{asp} is density of asphaltene, which is around 1176 kg/m^3 [25]. ρ_{sol} is the density of the solution, which is assumed the same as the density of n-pentane (i.e. 626 kg/m^3). Solving Equation 1 and 2, the calculation shows that asphaltene particles smaller than 0.7 μm in diameter do not settle due to Brownian motion. Primary submicron particles are much smaller than 0.7 μm, therefore not mainly from settling but possibly from proportional to the particle concentration.

There are theoretical models in literature to describe asphaltene precipitation based either on phase separation or on colloid interaction [3, 57, 76, 126, 163, 199, 209]. To rationalize our experimental results, here we focus

on the paradigm of the colloid theory for simplicity. The temporal evolution and the effects from asphaltene concentration observed in our results can be equivalently rationalized by a phase separation model.

According to the colloid theory of asphaltene precipitation [55, 77, 146, 262], asphaltene dispersed in a solvent exist in the form of colloids (namely asphaltene nano-aggregates [142]) with the size a few nanometers far below the spatial resolution of our measurements [235]. Mixing asphaltene in toluene with a paraffinic solvent reduces solvent strength in the liquid medium, which may shift the dominant colloidal interactions between asphaltene nano-aggregates from steric repulsion to van der Waals attraction according to classic DLVO theory [13, 76, 217, 218]. The concentration ratio of the paraffinic solvent to toluene ($r_{solvent/toluene}$) in the mixture has to be above a critical value (i.e. onset) [217] to initiate asphaltene precipitation [13, 146]. Those heavy aromatic species of asphaltene with the lowest solubility in the paraffinic solvent precipitate first from the mixture, some of which deposit on the surface and are captured as primary submicron particles in our experiments. Those primary submicron particles that still suspended in the mixture may grow by acting as preferential sites [76] for further aggregation and precipitation of lighter species of asphaltene.

Compared to the diffusion of the nano-aggregates, slow or fast precipitation of primary submicron particles would lead to different paths in increasing the sizes of the precipitates. In the case that precipitation kinetics is slower than the time for nano-aggregates to diffuse to the formed primary submicron particles, larger aggregates may form from growth by adding nano-aggregates, as well as from merging of more than one primary submicron particle. In the case that precipitation kinetics is faster than the diffusion of nano-aggregates to existing primary submicron particles, the precipitates may be mainly in the form of primary submicron particles. We believe that when the concentration of pentane is low (such as C_B^{pen} of 70 % or 80 %), our experiments more resemble the latter case that the precipitation of primary submicron particles is faster than the growth of primary submicron particles from nano-aggregates by diffusion. At a lower concentration of pentane in solution B, asphaltene is

more diluted before the threshold for precipitation is reached. With a small population of asphaltene in the mixture, the nano-aggregates take a longer time to diffuse into the formed primary submicron particles.

An interesting question is why primary submicron particles are observed in all C_B^{pen}. During diffusive mixing processes in our experiments, remaining soluble asphaltene in the mixture (C_{total}^{Asp}) decreases with time at the rate determined by diffusion process of solution B in the main channel. Hence how fast C_{total}^{Asp} decreases is independent of the initial concentration of n-pentane in solution B (C_B^{pen}). However, $r_{solvent/toluene}$ in the mixture is consistently lower for solution B with lower C_B^{pen}. What in common for all groups of solution B is the precipitation process of asphaltene at a high $r_{solvent/toluene}$, taking place as the asphaltene is nearly all depleted. Even for C_B^{pen} of 90% or 100%, asphaltene is gradually depleted by the precipitation of primary submicron particles with time, the nano-aggregates become less likely to diffuse to the existing primary submicron particles. During this final process of precipitation, primary submicron particles still form due to the low solvation strength in the mixture. However, as the mixture is already sufficiently diluted by n-pentane, the number density of the primary submicron particles is low so that the probability for primary submicron particle collision and aggregates is also low. Therefore, primary submicron particles could be observed for all conditions. As even more paraffinic solvent is added to the mixture, C_{total}^{Asp} eventually decreases to a certain limit and the precipitation terminates due to lack of sufficient asphaltene in the bulk solution. There are a low number of several large aggregates that may form from aggregates of discrete primary submicron particles, as shown in our images in Figure 4.8 and 4.3.

Asphaltene precipitation at high dilution is consistent with the size distribution observed in our experiments for solution B with low C_B^{pen}. The precipitates mostly consist of primary submicron particles with fewer large aggregates (shown in Figure 4.5) at C_B^{pen} of 80% and 70%. As comparison, the precipitated larger aggregates at C_B^{pen} of 100% and 90% observed in our TIRF images may consist of many primary submicron particles or aggregates from primary submicron particles with nano-aggregates.

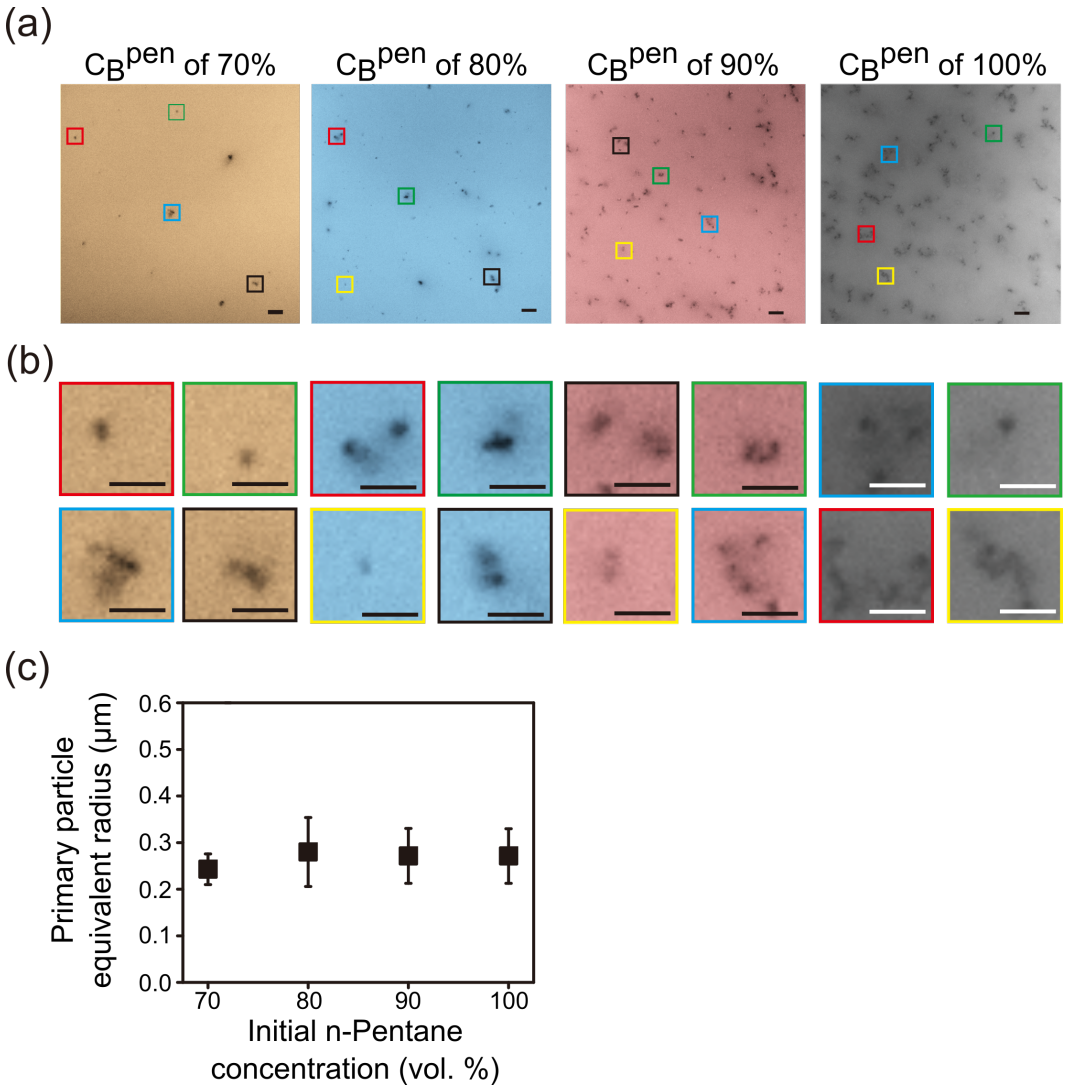

Figure 4.8: (a) TIRF images of asphaltene particles at the concentration of n-pentane in solution B (C_B^{pen}) of 70 % to 100 %. Scale bar is 5 μm. (b) Zoomed-in view of primary submicron particles shown in the TIRF images at locations with respective color box. Note: the images have been false-colored. Scale bar is 5 μm. (c) Primary submicron particle size at different n-pentane concentration in solution B. Error bar shows the standard deviation of the primary submicron particle radius based on three rounds of experiments.

4.4.2 Microscopic view of asphaltene precipitation dynamics

We observed in Figure 4.6 that the growth time at higher concentration of n-pentane is shorter than that at lower concentration. Below we will rationalize this interesting result. To simplify the analysis of the asphaltene growth process, we made the following assumptions: (1) the first asphaltene particle is detected at the time that $r_{solvent/toluene}$ reaches onset, which is 1.22 (i.e. n-pentane concentration is 55 $vol.\%$ in the mixture) according to the value in the literature [3, 95]. The exact number of onset is not a universal value. However, the following analysis holds for any number below 70 %. (2) The concentration ratio of asphaltene and toluene remains constant, determined by initial concentration of asphaltene in solution A.

Based on the assumption, there are two important moments for asphaltene precipitation during diffusive mixing processes in the experiments: The time when $r_{solvent/toluene}$ reaches onset and the time when C_{total}^{Asp} is too low and the precipitation terminates. As sketched in Figure 4.9, the two moments are labelled as t_1 and t_3 for C_B^{pen} of 100%, and t_2 and t_4 for C_B^{pen} of 70%. The growth time (Δt) is the time interval between these two moments, which is Δt_{100} and Δt_{70}, respectively. C_{total}^{Asp} in the mixture decreases from addition of solution B, but also from the mass loss after the onset due to asphaltene precipitation. The growth time of asphaltene precipitation is governed by the relative kinetics of precipitation versus diffusion.

The growth time Δt is estimated as below:

$$\Delta t \sim \frac{c_{onset}}{k_d \dot{\omega}_d + k_p \dot{\omega}_p} \tag{3}$$

Here c_{onset} is the asphaltene concentration in the mixture when n-pentane concentration reaches onset. $\dot{\omega}_d$ is the reduction rate in C_{total}^{Asp} in the mixture induced by dilution (black curve in the sketch), approximately the same for C_B^{pen} of 100% and 70% as both are controlled by the diffusion process. $\dot{\omega}_p$ is the reduction rate in C_{total}^{Asp} induced by precipitation (red curve in the sketch). k_d and k_p are coefficients of dilution and precipitation rate, respectively. k_d and k_p

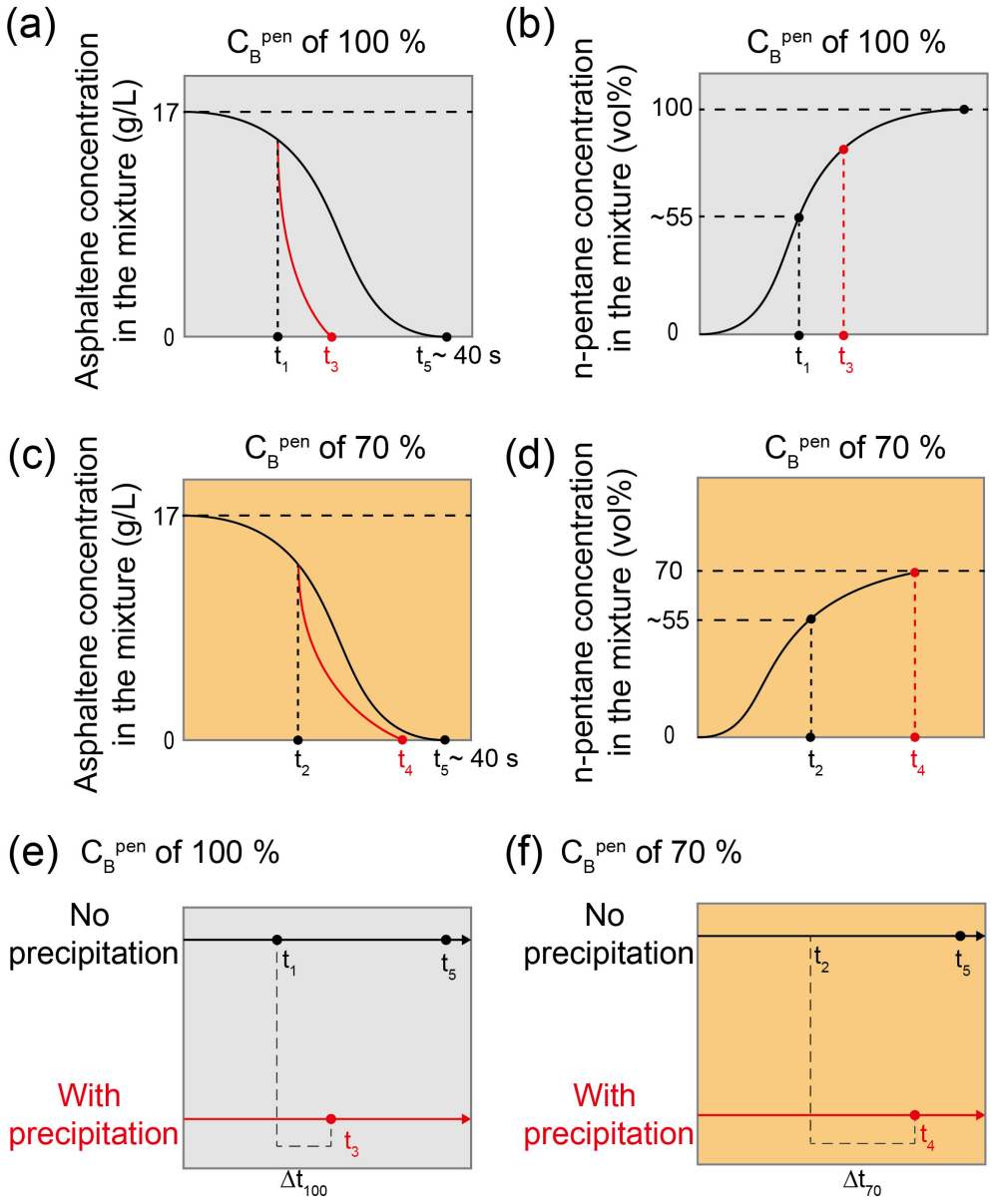

Figure 4.9: Sketch of asphaltene concentration as a function of time at C_B^{pen} of 70 % and 100 %. The black lines correspond to the no precipitation condition, while red lines correspond to the precipitation condition. t_1 and t_2 are the starting moments of asphaltene precipitation. t_3, t_4 and t_5 are stopping moments of asphaltene precipitation. The duration between the starting and stopping moments (Δt_{100} and Δt_{70} are the growth time of asphaltene particles.)

are different because dilution reduces all types of asphaltene but precipitation reduces the least soluble asphaltene. After the threshold concentration of n-pentane, the reduction of asphaltene concentration by precipitation can be much faster than by dilution at least for a short time window.

Based on colloidal theory, $\dot{\omega}_p$ can be estimated as below [57, 126, 207]:

$$\dot{\omega}_p = \alpha_{i,j}\beta_{i,j}c_i c_j \tag{4}$$

Here c_i and c_j represent concentration of asphaltene particle with size i and j. $\alpha_{i,j}$ and $\beta_{i,j}$ represent collision frequency and collision efficiency of asphaltene particle with size i and j, respectively. The collision efficiency $\beta_{i,j}$ increases exponentially with n-alkane concentration [126]. Especially when C_B^{pen} is higher than 80 $vol.\%$ because the dominated force changes from repulsion to attraction (i.e. the energy barrier is much lower) [217]. Therefore $\dot{\omega}_p$ is larger. Accordingly, the growth time Δt is shorter at larger C_B^{pen} based on Equation 3. In other words, with higher C_B^{pen}, the drop of C_{total}^{Asp} is sharper, due to faster precipitation. The asphaltene is depleted in a shorter period of time and the time window for precipitation is narrower. In contrast, with lower C_B^{pen}, the precipitation rate of asphaltene is slow, so asphaltene almost grows until the end of solvent displacement.

In our experiments, $r_{solvent/toluene}$ at any given time could be estimated from the composition measurements using fluorescence intensities from diffusive mixing between toluene doped with fluorescent dye and pure n-pentane. Assuming that fluorescent dye and toluene ratio remains constant, we can estimate compositions of toluene and n-pentane in the mixture in the main channel of the microchamber. Details of the mixing characterization are reported elsewhere.[131] Assuming that asphaltene precipitation after $r_{solvent/toluene}$ of 4 (i.e. n-pentane concentration is 80 $vol.\%$ in the mixture) does not contribute much to the aggregates observed at high C_B^{pen}, we estimated that it was approximately 5.5 s and 8.5 s at C_B^{pen} of 90 % and 100 %, respectively, to reach $r_{solvent/toluene}$ of 4 from the onset of 1.22. The duration is consistent with the growth time Δt of 90 % and 100 %. Our measurements were not sensitive

enough to distinguish if there is systematic difference between these two, but is enough to identify the difference between two high and two low groups of C_B^{pen}.

4.4.3 Implications to asphaltene colloid theory and paraffinic froth treatment

A question is why the primary submicron particles observed under various conditions are similar in size, all around 200-400 nm in radius. These particles were not observed in toluene solution at the same spatial resolution of our images. Clearly, the formation of primary submicron particles was induced by addition of n-pentane, after the solvation strength in the liquid medium was reduced. As solvation strength reduces by addition of n-pentane, asphaltene nano-aggregates may reorganize and form more compact and larger entities that become visible to our imaging technique, due to higher density relative to the surrounding liquid medium. The compact asphaltene entities stranded in the field of view were captured and monitored by our images. The reorganized and compact asphaltene entities formed at a low concentration of asphaltene at high dilution by n-pentane may be the primary submicron particles observed in our experiments. Similar sizes of primary submicron particles formed at low concentration of asphaltene (near the end of solvent diffusion even for C_B^{pen} of 100 %) could be due to that the formation process of the particles up to this size of 300 nm is fast, relative to dilution of asphaltene by diffusive mixing accompanied by the change in the solvation effect.

As mentioned in the introduction, paraffinic froth treatment (PFT) is an essential step in oil sands extraction to remove solids and water from bitumen froth through dilution by paraffinic solvents. Although PFT and many other solvent-induced phase separation processes are conducted through convective mixing, clearly local diffusive mixing is unavoidable, even for the case in a turbulence flow. In particular, for a large volume of liquid, viscous liquid or mixing confined in a small space, diffusive mixing may play a role as it is challenging to reach uniform mixing instantly. Before being uniformly mixed, the added solvent diffuses into bitumen. The early stage phase separation of

asphaltene influences the number density, size distribution and morphology of the precipitates, which may impact the subsequent agglomeration with fine solids and water droplets and their settlement in PFT process. Our results showed that when n-pentane concentration is high and asphaltene concentration is low, the precipitates are mainly in the form of primary submicron particles that may not contribute to the settling of water and solids directly, due to their small surface area, and slow settling rate under gravity. Moreover, it was also believed that water droplets in PFT are coated with asphaltene due to their surface activity [168]. The addition of a poor solvent may cause the formation of small asphaltene particles at droplet surface. The size of the asphaltene particles on water drops may play an important role in the settling process, because the interfacial properties of water drops may depend on the size of asphaltene particles. In analogy, the nanoparticle size and shape are essential to the stability of Pickering emulsions [31, 226]. As compared to larger particles, it is likely that small asphaltene particle may stabilize water droplets by reducing their coalescence, and hence hinder the separation process in PFT.

4.5 Conclusions

In this work, the asphaltene precipitation under diffusive mixing is tracked in-situ by TIRF microscope in a microfluidic chamber. Asphaltene precipitation occurs simultaneously during diffusion of n-pentane into the asphaltene solution. As n-pentane to toluene ratio exceeds onset with mixing, the interaction between asphaltene colloids changes from repulsive to attractive to form a new phase as precipitation. The asphaltene precipitation stops when the asphaltene concentration is not enough to provide source of asphaltene for precipitation. The diffusive mixing lasts for a few seconds and the asphaltene precipitation lasts for a similar time scale ($< 30\ s$). Two types of asphaltene particles (i.e. primary submicron particles and aggregates) are formed in the dilution induced precipitation. More aggregates are formed with higher initial n-pentane concentration, but the primary submicron particles with a similar size range from 200 nm to 400 nm in radius are observed independent of n-

pentane concentration. The findings from this project will provide new insight into the effects of solvent mixing on the onset, size distribution and morphological characteristics of asphaltene precipitates. This fundamental understanding may help design mixing conditions to achieve enhanced separation.

In addition to the parameters studied in this study, TIRF provides an opportunity for future work to investigate the effects of many other interesting parameters that are important to asphaltene precipitation. Some examples are type and initial concentration of asphaltene, temperature, precipitant type, solid contents and others.

Chapter 5

Size Distribution of Primary Submicron Particles and Larger Aggregates in Solvent-Induced Asphaltene Precipitation in a Model Oil System

Abstract

Asphaltene precipitation is a crucial phase separation phenomenon in the oil industry, especially in paraffinic froth treatment to extract bitumen from oil sands ores. This work reveals the ubiquitous presence of particles at 0.2 to 0.4 μm in radius, defined as primary sub-micron particles (PSMPs) at early stage asphaltene precipitation from diffusive mixing with solvents. We observed PSMPs in a quasi-2D chamber where asphaltene solution (the model oil) is displaced by 3 paraffinic solvents, the blends of solvents, and solvents containing inhibitor at low concentrations. The yield and size distribution of asphaltene particles are affected not only by the Hildebrand solubility parameter of the precipitants but also by the diffusion coefficients of the asphaltene solution and the precipitant. Even though n-pentane is a stronger solvent than n-heptane, the yield of asphaltene in the diffusive mixing chamber is close because of the difference in the diffusion coefficient between n-pentane and n-heptane in asphaltene solution. The results of n-heptane and n-decane blends reveal that the increase of the ratio of PSMPs compared with pure n-heptane or n-decane. The inhibitors significantly decrease the aggregation rate of PSMPs, displayed as a higher ratio of PSMPs compared to a non-inhibitor group. The Population Balance Model (PBM) with the Hildebrand solubility parameter has been used to model particle size distribution. Good agreement has been achieved between numerical predictions and the experimental data. It indicates that the colloid theory can describe the size distribution of PSMPs and larger aggregates in early stage of asphaltene precipitation. This study

illustrates the importance of mixing dynamics on the size distribution in asphaltene precipitation. The findings can be useful for accurate modelling of the hydrocarbon separation or asphaltene precipitation.

5.1 Introduction

Induced precipitation is a common process for the extraction and separation of certain compositions from a mixed source. Asphaltene precipitation is utilized in paraffinic froth treatment (PFT) units to remove water and solids impurities in the crude oils [75]. Asphaltene is enriched on polyaromatic cores [47] and defined as the components of crude oil that are insoluble in n-alkane solvents (i.e., n-pentane or n-heptane) and soluble in aromatic solvents (i.e., benzene or toluene) [232]. On the other hand, asphaltene precipitation during the transportation of crude oil may cause severe problems such as blockage of pipelines [96, 113]. Temperature [14], pressure [86], gas injection [244, 245], asphaltene concentration [84], solvent (precipitant) type [4, 66, 212], and solvent to crude oil ratio [4, 58, 88, 126, 167, 175, 212] have been shown to play significant roles to control the kinetic of asphaltene precipitation.

In general, the yield of asphaltene increases with the solvency effect of precipitant, which can be achieved by increasing the concentration of n-alkanes and changing to shorter chain-length n-alkanes [175]. From a solution viewpoint, the increase of the solid-liquid equilibrium ratio from solvency effect results in asphaltene changes from a liquid phase to a solid phase [171]. From a colloidal viewpoint, asphaltene colloids aggregates disperse in crude oils and are stabilized by the steric repulsion of the extended structure [78, 217, 218]. Changing surrounding conditions, such as medium composition [125], induces the collapse of the extended structure. The steric repulsion between asphaltene colloids reverses to van der Waals attraction [217, 218], under which asphaltene colloids aggregate to grow larger. Based on the Yen-Mullins model, asphaltene molecules form nano-aggregates, and nano-aggregates form clusters. The aggregation of cluster leads to the further growth of asphaltene [139, 142], and manifest as phase separation. The collision efficiency between asphaltene particles increases with the solvency effect [217]. Small asphaltene particles grow large and appear as a new phase. Either viewpoint indicates high solvency effect is conducive to the destabilization and aggregation of asphaltene. Besides, asphaltene precipitates are porous and tenuous fractal structures. Settling be-

havior suggests that the morphology of asphaltene precipitate is also affected by the precipitant composition. The settling rate of asphaltene particles in n-pentane is two magnitudes higher than in n-heptane [44], indicating a higher fractal dimension and larger aggregates.

Adding inhibitors have complicated effects on asphaltene precipitation. Usually the inhibitor can slow down the aggregation rate [22]. However, for some specific cases, adding inhibitors may have the opposite effect and accelerate aggregation [90]. The importance of inhibitors on destabilization and aggregation of asphaltene particles needs to be further investigated. In addition to precipitant composition (thermodynamic aspect), recent works show the growth dynamics of an individual domain during dilution-induced phase separation is also determined by the temporal and spatial characteristics of the mixing (i.e., hydrodynamics aspect) [131, 258]. Mixing dynamics determines the local and temporal concentration of the precipitant, which can significantly affect the early stage of phase separation [131, 258].

Despite the importance of the precipitant on asphaltene precipitation, most studies have used a batch system to mix bitumen or other model oils with a precipitant from which an aliquot is picked for observation [113, 125, 232]. Although these setups can provide information on the morphology of the precipitated asphaltene, it is difficult to decouple the effects from solubility parameters and diffusion from external mixing.

Recently, micro platform device has been leveraged to study asphaltene precipitation [138, 148, 190, 191]. We developed a quasi-2D microfluidic chamber to study asphaltene precipitation in-situ [129, 131]. Unlike using a mixer to control mixing dynamics in a bulk system, the mixing in the microchamber was controlled by diffusion in the confined space inside the quasi-2D channel [120]. The precipitated asphaltene can be in-situ visualized by a total internal reflection fluorescence microscope (TIRF) with a high spatial resolution ($\sim 200\ nm$) through an opaque medium containing asphaltene [60, 62, 63]. We found the presence of primary sub-micron particles (PSMPs) with an equivalent radius of 0.2 to 0.4 μm from asphaltene precipitation in n-pentane[129]. However, the ubiquitous formation and distribution of PSMPs are still unknown in other

types of precipitants and a real bitumen system.

The aim of this work is to understand size distribution of primary submicron particles and their aggregates in asphaltene precipitation induced by diffusive mixing with different precipitants. In total, 23 types of precipitants were examined, including three types of solvents pentol (n-pentane-toluene mixture), heptol (n-heptane-toluene mixture), and dectol (n-decane-toluene mixture), the mixture of n-heptane and n-decane, and the solutions containing an inhibitor. Although n-decane is not a predominant solvent in the PFT facility, including n-decane in our study helps us understand a general principle for more types of solvents. Concentrations of the inhibitors ranging from 10 to 10,000 *ppm* are studied. The maximal concentration 10,000 *ppm* in our experiments may be too high for actual applications, but allows for fundamental understanding of asphaltene behavior at extreme conditions. The population balance model (PBM) was established to relate the particle size distribution to the properties of the precipitant. The good agreement between the prediction from the PBM model and the experimental results suggests that the colloid theory may describe the precipitation from PSMPs to larger aggregates. It is worth noting that a real bitumen system was also investigated to compare the results from the model asphaltene in toluene solution. The findings of this work provide a further understanding of the solvent composition influence on asphaltene precipitation. The novelty of this work is development and validation of the PBM model referring to particles size distribution for aggregates in solvent-induced asphaltene precipitation.

5.2 Experimental methods

5.2.1 Chemical and sample preparation

Asphaltene was prepared from Murphy Oil (USA) n-pentane asphaltene (i.e., C5-asphaltene). Bitumen sample was an Athabasca bitumen supplied by Sycrude, Canada, Ltd. The elementary composition of the asphaltene sample can be found in our previous research [129]. Toluene (Fisher Scientific, ACS grade, 99.9%+) was used as the solvent of asphaltene. n-Pentane (Fisher

Scientific, 98%), n-heptane (Fisher Chemical, 99%), and n-decane (Fisher Scientific, 99.3%+) were used as solvents. Nonylphenol (Aldrich, technical grade) was used as an inhibitor.

Asphaltene was treated following the same method reported in the previous study [129] to remove any inorganic solids. In brief, the raw asphaltene was dissolved in toluene and used 0.22 μm polyvinylidene difluoride (PVDF) filter paper to remove any inorganic solids. A rotary evaporator was then used to remove any toluene to obtain the 'inorganic solid-free' asphaltene. 17 g of inorganic solid-free asphaltene was dissolved in toluene to 1 L to prepare the asphaltene in toluene solution at the concentration of 17 g/L, labeled as solution A1. The bitumen sample was diluted by toluene to 100 g/L and filtrated by the same method as asphaltene sample to remove any inorganic solids. The treated bitumen solution was used as solution A2. With $\sim$ 17 $wt.\%$ C5-asphaltene in Athabasca bitumen [168], the asphaltene concentration in 100 g/L bitumen solution was same as that in the toluene solution.

5.2.2 Compositions and diffusion coefficients of solution B of n-pentane, n-heptane, and n-decane

In total, 23 types of precipitants were used to investigate the solvency effect on asphaltene precipitation. 3 pure solvents were n-pentane, n-heptane, and n-decane. The paraffinic solvent was blended with toluene to prepare 9 types of solutions of B_{PT}, B_{HT}, and B_{DT} at the initial concentration (ϕ_0) listed in Table 5.1. The mixing duration of the asphaltene solution and the precipitant in our quasi-2D mixing chamber was only tens seconds, as confirmed in the earlier work [131]. The concentration of the paraffinic solvent in the initial solutions of B_{PT}, B_{HT}, and B_{DT} had to be high enough (i.e., minimum is 70%) for the formation of detectable asphaltene particles. Mixtures of n-heptane and n-decane at three concentrations were studied, as shown in Table 5.2. Solutions B_{PT} and B_{HT} were chosen to study asphaltene precipitation in a real bitumen system. The inhibitor nonylphenol at 4 concentrations of 10 to 10000 ppm was added to solutions of A1, B_{PT}, and B_{HT}. The experiments followed the same procedure as above without nonylphenol in solutions A1 or B_{PT} and B_{HT}.

Hildebrand solubility parameter (δ) was used to quantify the solvency effect. For example, the larger of δ difference between asphaltene and solvent, the more asphaltene or the earlier of onset of asphaltene precipitates. Asphaltene was considered as an entire group and the Hildebrand solubility parameter was 24.2 $MPa^{1/2}$ [83]. Although asphaltene consisted of different fractions, our fluorescence spectrum could not identify the difference of the precipitates (Figure D.3). δ for the pure n-alkanes were adopted from the literature [26]. δ for the mixtures were calculated based on the volume fraction of the components (ϕ_i) and Hildebrand solubility parameter of each components (δ_i), $\delta_{mixture} = \Sigma\delta_i\phi_i$ [12, 216]. The relationship between δ and the composition of the precipitants was shown in Figures 5.1(a)(b).

Table 5.1: Composition of the mixtures of n-alkanes and toluene.

n-Pentane		n-Heptane		n-Decane	
ϕ_0^{pen}	δ $(MPa^{1/2})$	ϕ_0^{hep}	δ $(MPa^{1/2})$	ϕ_0^{dec}	δ $(MPa^{1/2})$
70%	15.5	70%	16.1	70%	16.5
80%	15.0	80%	15.8	80%	16.3
90%	14.7	90%	15.5	90%	16.0
100%	14.3	100%	15.2	100%	15.8

Table 5.2: Composition of the mixtures of n-heptane and n-decane.

	Composition		δ $(MPa^{1/2})$
	n-Heptane (vol.%)	n-Decane (vol.%)	
n-Heptane	100	0	15.2
Mixture 1	80	20	15.3
Mixture 2	50	50	15.5
Mixture 3	20	80	15.7
n-Decane	0	100	15.8

We compared the diffusion coefficients of n-alkanes in toluene as shown in Figure 5.1(c). The diffusion coefficients of n-pentane, n-heptane, and n-decane were simulated by UNIFAC (see details in Supporting information). Diffusion coefficient of n-pentane in toluene (D_{pt}) was higher than n-heptane (D_{ht}) or n-decane (D_{dt}) (i.e., D_{pt} ¿ D_{ht} ¿ D_{dt}). Mixing of n-alkane and toluene was a mutual diffusion process, affected by the concentration of toluene. Diffusion

coefficient of the paraffinic solvent decreased during the mixing process. However, D_{pt} ¿ D_{ht} ¿ D_{dt} held for all of toluene concentration, in the particular at higher concentration of toluene.

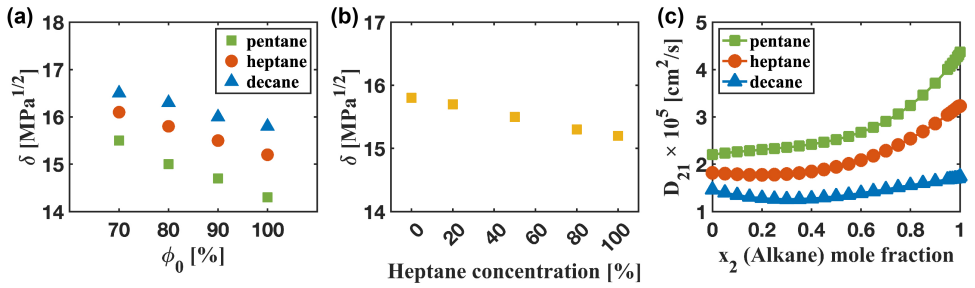

Figure 5.1: Hildebrand solubility parameter and diffusion coefficient versus composition of the precipitant: (a) mixture of n-alkanes and toluene, (b) mixture of n-heptane, and n-decane. (c) Diffusion coefficient of n-pentane, n-heptane, and n-decane in mixtures with toluene.

5.2.3 Detection and analysis of asphaltene precipitates

A quasi-2D microfluidic chamber was used to induce asphaltene precipitation by diffusive mixing with solutions of B_{PT}, B_{HT}, and B_{DT}, as shown in Figures 5.2(a)(b). More details of the quasi-2D microfluidic were described in our previous works [129, 131]. In brief, under ambient temperature (i.e., 19 - 21$°C$) and pressure (i.e., 1 atm), solution A1 pre-filled the microfluidic chamber. Paraffinic solvent (i.e., one of solutions B_{PT}, B_{HT}, and B_{DT}) was then injected through the deep side channels. The paraffinic solvent transversely diffused into the main quasi-2D channel. Asphaltene precipitation began when the precipitant concentration reached the onset and finished when the concentration of asphaltene in the mixture was too low for precipitation, as sketched in Figure 5.2(c). The diffusion length was defined as 82.5 μm in the direction of the concentration gradient (x-direction in Figure 5.2(a)).

We noted that the density difference between solution A1 and precipitants did not influence the mixing dynamics in our confined quasi-2D channel, in contrast to a mixing process in a large bulk system. The buoyancy and gravity effects in our chamber could be estimated by a dimensionless number, Rayleigh number (Ra): $Ra = \frac{\Delta\rho g(h/2)^3}{\mu D_{21}}$ [258]. $\Delta\rho$ was the density difference between n-

alkanes and toluene, g was the gravity acceleration constant, h was the height of the chamber, μ was the dynamic viscosity of toluene, and D_{21} was the diffusion coefficient of n-alkanes and toluene. The contribution of asphaltene on density and viscosity was negligible due to the small amount. $Ra \approx 2$ for n-pentane and toluene (a combination with the largest density difference), which was three magnitudes smaller than the critical Ra (i.e., $Ra = 1708$) [258]. Therefore, the mixing dynamics in all of our experiments were not affected by gravity.

Total internal reflection fluorescence microscope (DeltaVision OMX Super-resolution microscope, GE Healthcare UK Limited, UK) was used to detect the asphaltene particles. The images of asphaltene particles were captured after injecting paraffinic solvent for five minutes. MATLAB (The MathWorks, Inc., US) was used for image analysis to get the particle size, surface coverage, and particle quantity. The details of the process for image analysis could be found in our previous work [129, 131]. Briefly, surface coverage was normalized by the unit area in the field of view. Fractal aggregates were treated as single units rather than counting primary sub-micron particles when particle quantity was counted.

5.3 Population balance model

Conventional aggregation of particles was a multi-step process, including micro-floc growth stage and large floc growth stage [36]. Primary particles (basic units) formed micro-flocs (intermedium basic units) with a coagulant at the micro-floc growth stage. At the large floc growth stage, micro-flocs formed large flocs by binding points of micro-flocs [222]. The same mechanism might describe asphaltene precipitation (Figure 5.3). Nano-aggregates (basic units) formed primary submicron particles (PSMPs) (intermedium basic units) in the precipitation stage. The PSMPs formed fractal flocs via further aggregation at the aggregation stage. Fractal aggregates were formed by aggregation of PSMPs rather than directly incorporating asphaltene nano-aggregates. The size distribution discussed in this study was the particles larger than 0.2 μm

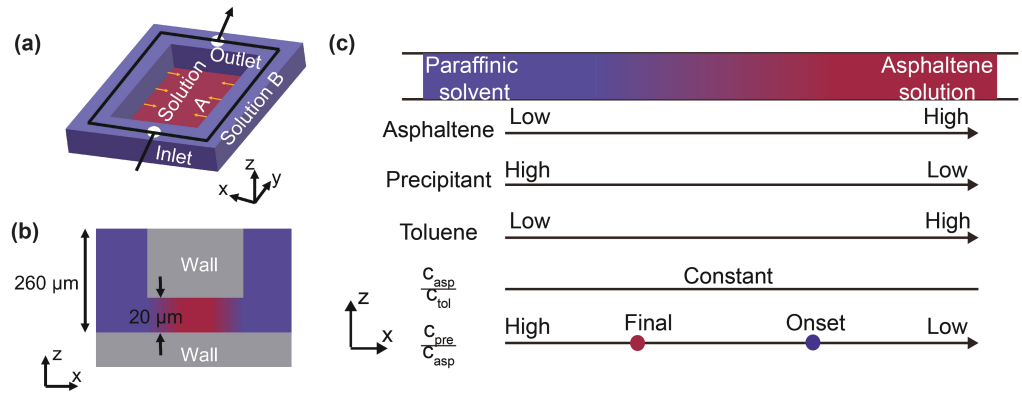

Figure 5.2: (a) Sketch of the quasi-2D microchamber used in this study. The black arrow indicates the flow direction of the precipitant. Yellow arrows indicate the diffusion direction of the precipitant. (b) Side view of the cross-section of the microchamber. (c) Schematic of the concentration of chemical composition in the diffusive mixing zone in the quasi-2D channel. Purple and red dots indicate the chemical composition of onset and stop point for asphaltene precipitation, respectively. ($\frac{c_{asp}}{c_{tol}}$) is the ratio between asphaltene to toluene. ($\frac{c_{pre}}{c_{asp}}$) is the ratio between precipitant to asphaltene.

in radius that were detectable in our TIRF images.

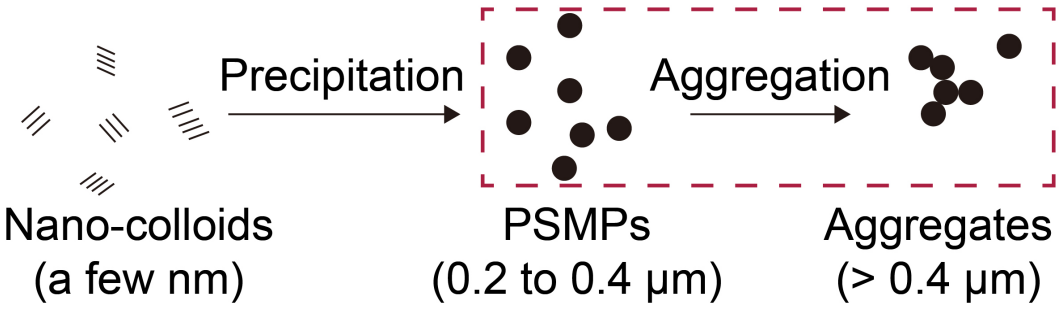

Figure 5.3: Sketch of the formation of PSMPs by asphaltene precipitation and the aggregation of PSMPs to form aggregates. Sizes in the brackets are the area equivalent radius. The size distribution obtained from our measurements reflects the step in the red box.

Population balance model (PBM) was used to describe the particle aggregation and to relate the size distribution of asphaltene aggregates with the properties of the precipitant. Smoluchowski equation for aggregation of primary units was [64]:

$$\frac{dn_k}{dt} = \frac{1}{2}\sum_{i+j=k} K_{i,j} n_i n_j - n_k \sum_{i\geq 1} K_{i,k} n_i \tag{5.1}$$

where n_i, n_j, and n_k were the number concentration of particles with sizes i, j, and k, respectively. t was time. $K_{i,j}$ was the collision kernel of aggregation, which could be estimated by Equation (5.2): [126]

$$K_{i,j} = \frac{2RT}{3\mu}\frac{(d_i + d_j)^2}{d_i d_j}\beta \tag{5.2}$$

where R was the ideal gas constant, T was temperature, μ was viscosity, d_i and d_j were the diameters of particles with size i and j, respectively, and β was collision efficiency, which could be estimated by Equation (5.3) [126]:

$$\beta \propto exp[-\frac{\psi_e}{k_B T(\delta_{asp} - \delta_{sol})^2}] \tag{5.3}$$

where ψ_e was the maximum energy barrier constant, k_B was Boltzmann constant, δ_{asp} and δ_{sol} were Hildebrand solubility parameters of asphaltene and the paraffinic solvent, respectively. In the diffusive mixing process, δ_{sol} varied with time due to the change in the concentration of the paraffinic solvent, depending on the concentration of the paraffinic solvent and the diffusion coefficient [12, 216]:

$$\delta_{sol} = \delta_{alk}\phi_{alk} + \delta_{tol}\phi_{tol} = \delta_{alk} \times \phi(t,l) + \delta_{tol} \times (1 - \phi(t,l)) \tag{5.4}$$

where δ_{alk} and δ_{tol} represented Hildebrand solubility parameters of the paraffinic solvent and toluene, respectively, ϕ_{alk} and ϕ_{tol} were volume fractions of the paraffinic solvent and toluene, respectively, and $\phi(t,l)$ was the volume fraction of the paraffinic solvent at a given time and position: $\phi(t,l) = \phi_0 erfc(\frac{l}{2\sqrt{D_{21}t}})$ [131]. l was the distance to the side channel, ϕ_0 was the initial volume fraction of the paraffinic solvent, and t was time. $erfc$ was a complementary error function, which could be expressed as: $erfc(x) = 1 - erf(x)$, $erf(x) = \frac{2}{\sqrt{\pi}}\int_0^x e^{-t^2}dt$.

In this study, the mean size (r_{psmp}) of the primary sub-micron particles (PSMPs) (i.e., basic units) was 0.3 μm in radius [129]. Asphaltene was destabilized and forms PSMPs. It was assumed that all of the asphaltene PSMPs were formed at the moment that the paraffinic solvent concentration was higher

than the onset (i.e., the threshold of solvent concentration to promote the asphaltene precipitation as PSMPs) upon destabilization kinetics was relatively quick compared with further aggregation of PSMPs. The surface coverage of asphaltene particles (SC) observed in TIRF images was not affected by the aggregation of PSMPs. Therefore, the initial quantity (Q_p) for the PBM was calculated based on SC divided by the area of PSMPs at the final state: $Q_p = SC/\pi r_{psmp}^2$. Q_p was the initial quantity of the PSMPs.

Based on these assumptions and relations, the initial Smoluchowski equation could be rewritten as below:

$$\frac{dn_k}{dt} = \frac{8RT}{3\mu} exp[-\frac{\psi_e}{k_B T(\delta_{asp} - (\delta_{alk} \times \phi(t,l) + \delta_{tol} \times (1 - \phi(t,l)))^2}] \sum_{i+j=k} n_i n_j - n_k \sum_{i \geq 1} n_i \tag{5.5}$$

The size distribution of the asphaltene particles at different times could be calculated by solving Equation (5.5). The asphaltene aggregates in the experimental results were classified into three size bins. The number of equations to be solved could be narrowed down to three ordinary differential equations (ODEs), representing three bins for the particles sizes. The first bin represented PSMPs ($\sim$ 0.3 μm), the second bin was for the particles with a size of 0.4 μm to 0.6 μm, and the last one was for the particles with a size of 0.6 μm to 0.8 μm. The particles larger than 0.8 μm were not considered in PBM due to the quantity of them being less than 20% of the total quantity in the experimental data. It is worth mentioning that our results show the size distribution when the precipitant already displaced the asphaltene solution in the quasi-2D chamber. The mixing duration started from the moment that the concentration of paraffinic solvent was higher than the onset and finished at the moment that asphaltene solution was sufficiently diluted by the solvent. This duration for asphaltene precipitation depended on the concentration and diffusion coefficient of the paraffinic solvent [131]. The parameters depended on the paraffinic solvent were specified for each condition, and the equations were solved separately. The first part of Equation (5.5) on the right side of the equation was a function of time and did not depend on the number density of

particles, and thus, a parameter B(t) was introduced as:

$$B(t) = \frac{8RT}{3\mu} exp[-\frac{\psi_e}{k_B T(\delta_{asp} - (\delta_{alk} \times \phi(t,l) + \delta_{tol} \times (1 - \phi(t,l)))^2}] \quad (5.6)$$

Viscosity of the mixtures were calculated based on Grunberg-Nissan law: $log(\mu) = N_1 log(\mu_1) + N_2 log(\mu_2)$ [80]. N_1 and μ_1 were the molar fraction and viscosity of component 1, respectively [208], N_2 and μ_2 were the molar fraction and viscosity of component 2, respectively.

Considering the birth and death of particles in each bin with aggregation of smaller particles and collisions with other particles to form larger particles, the three mentioned equations could be written as followed:

$$\frac{dn_1}{dt} = -B(t)n_1(n_1 + n_2 + n_3) \quad (5.7a)$$

$$\frac{dn_2}{dt} = B(t)(n_1 n_1 - n_2(n_1 + n_2 + n_3)) \quad (5.7b)$$

$$\frac{dn_3}{dt} = B(t)(n_1 n_2 - n_3(n_1 + n_2 + n_3)) \quad (5.7c)$$

n_1, n_2, and n_3 referred to the concentration of the three bin sizes. The systems of ODEs were solved numerically using MATLAB (2021a) for each condition, and the results were compared with the experimental measurements. The solution strategy in MATLAB was to use the standard solver ode45, which used a six-stage, fifth order, Runge-Kutta method to solve the equations. The time step was 0.001 s, and for the initial condition, it was assumed that all of the particles were in the first bin (primary particles) at $t = 0$. The equations were coded as a function in MATLAB, and ode45 was used to calculate the final size distribution. In Equations (5.6)(5.7), the only unknown parameter was ψ_e. We estimated ψ_e based on the size distribution of the group of ϕ_0^{pen} of 100 % and applied the estimated value of ψ_e to other solvent conditions. The effects from the solvents on collision efficiency were already included in the Hildebrand solubility terms. ψ_e in our model should cover other effects, such as polarization or variety in the sub-fraction of asphaltene. ψ_e was approximated to be a constant because our asphaltene sample was from the same batch. The

size distribution of asphaltene aggregates was modelled based on solving the PBM, collision kernels, and initial conditions.

5.4 Results

5.4.1 Morphology of asphaltene particles precipitated induced by n-alkane and toluene mixture

Figures 5.4(a)-(c) are the images of asphaltene particles precipitated in 12 types of precipitants, including pentol (n-pentane-toluene mixture), heptol (n-heptane-toluene mixture), and dectol (n-decane-toluene mixture). In the TIRF images, captured at the end of mixing [129], the black dots represent the precipitated asphaltene particles as portrayed in Figures 5.4(a)-(c).

The TIRF images of the precipitates show both individual particles (defined as PSMPs) and fractal aggregates. The dark speckles in the fractal aggregates have a similar size to the individual particles. Individual particles and fractal aggregates are observed in pure n-heptane and n-decane, as shown in Figures 5.4(d)(e) and Figure D.2. The formation of PSMPs is in good agreement with the previous study of n-pentane [129]. Furthermore, PSMPs and fractal aggregates also form by mixing with a diluted n-alkane of ϕ_0 with the concentration from 70% to 90%. The results show that the formation of the PSMPs is ubiquitous in asphaltene precipitation induced by mixing with a paraffinic solvent, regardless of the type and concentration of the solvent.

The surface coverage (SC) of asphaltene precipitates reflects the yield of the asphaltene during precipitation. The yield of asphaltene is the lowest in n-decane for the pure solvents, and the difference between n-pentane and n-heptane is not notable. For each type of solvent, the SC of asphaltene particles increases with the initial n-alkane concentration (ϕ_0). It means the yield of the asphaltene increases with ϕ_0. For the same type of solvent, δ decreases with the increase of ϕ_0, leading to increased SC and the quantity (Q) of asphaltene particles in the final state. Figures 5.5(a)(b) show the quantitative analysis of SC and Q based on the TIRF optical images. Interestingly, to reach the same SC or Q, the requirement of δ follows the trend of $\delta_{pen} < \delta_{hep} < \delta_{dec}$. In other

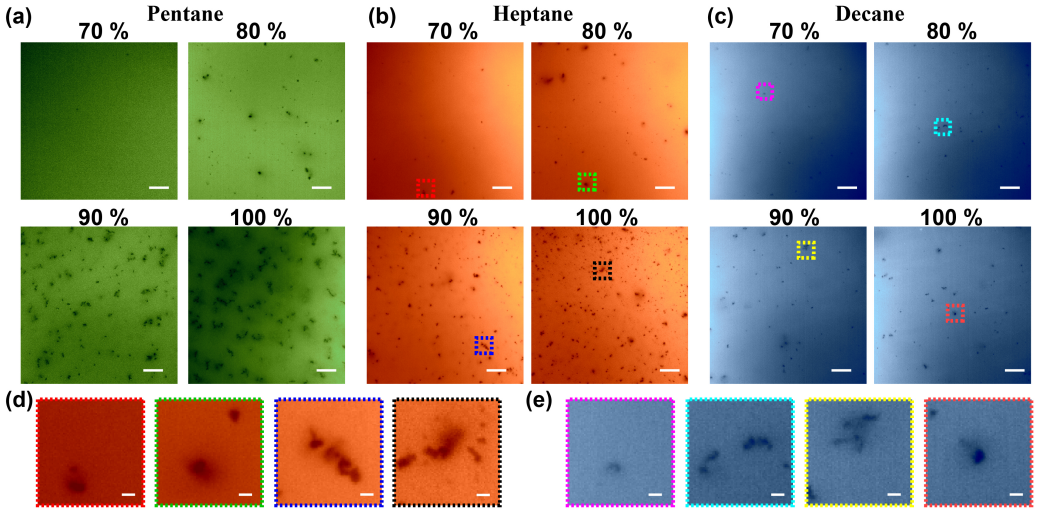

Figure 5.4: TIRF images of asphaltene particles at the final state. Precipitation is induced by (a) pentol, (b) heptol, and (c) dectol, and the corresponding zoomed-in images of (d) heptol and (e) dectol at locations with respective color boxes. The length of the scale bar is 10 μm in (a-c), and is 1 μm in (d-e). The images are false-colored.

words, δ of the precipitant is not the only dominated factor that determines SC and Q of asphaltene precipitates.

The same SC of two groups does not necessarily correspond to similar Q. For example, SC of 100% of ϕ_0^{pen} is close to 100% of ϕ_0^{hep}. However, Q of 100% of ϕ_0^{pen} is about half of Q from 100% of ϕ_0^{hep}. The reason is that aggregates are treated as one unit in Q analysis. The SC of one aggregate is higher than that of one PSMP.

Analysis of the size distribution of asphaltene particles shows that the number of PSMPs is always the highest, followed by the aggregates with the size of 0.4 to 0.6 μm. The same trend was observed, regardless of the type of solvent and solvent concentration in the mixture. The R_p is defined as the ratio between the number of the individually dispersed PSMPs to Q. Notably, at ϕ_0 of 100% and 90%, the R_p of n-pentane is lower than n-heptane and n-decane, as shown in Figures 5.6(a)(b). But in n-pentane, more very large aggregates are formed in the range larger than 0.8 μm. At low ϕ_0, R_p of n-pentane, n-heptane, and n-decane are similar, as shown in Figures 5.6(c)(d). Nevertheless, large aggregates (> 0.8 μm) form in n-pentane is more significant

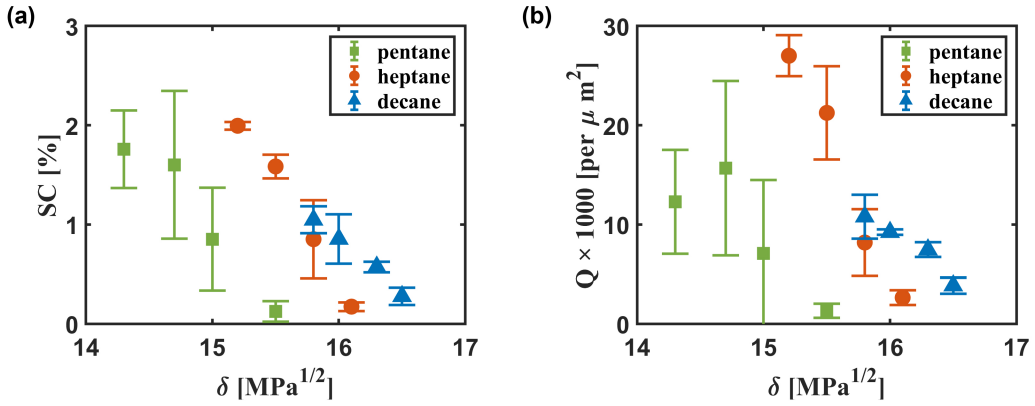

Figure 5.5: (a) Surface coverage (SC) and (b) particle quantity (Q) in the unit area of the final state of asphaltene particles. Precipitation is induced by pentol, heptol, and dectol. For pentol, heptol, and dectol, Hildebrand solubility parameter (δ) from high to low corresponds to ϕ_0 ranging from 70% to 100%.

than in n-heptane and n-decane.

The size distribution of asphaltene particles estimated by PBM is shown in Figures 5.6(a)-(d). The simulated data agree well with the experimental data except for ϕ_0 of 70%. It is worth noting that our PBM can not simulate particles larger than 0.8 μm, but experimental data include particles larger than 0.8 μm. However, the influence is negligible as the fraction of particle larger than 0.8 μm is always less than 20%. The reason for this error is that there are too few statistics (less than 20 particles) because the concentration of the paraffinic solvent is close to the onset, leading to the difference between the experimental and fitting results. Good agreement between the experimental data and prediction of PBM in particle size distribution suggests that the aggregation of nano-colloids may well explain the asphaltene growth kinetics from PSMPs to larger aggregates. The effects of different types of precipitants on the kinetics of asphaltene precipitation are described by varying the collision kernel and number density of asphaltene particles.

At a high solvent concentration of paraffinic solvent, PSMPs yield is high, which gives rise to lower R_p (Figures 5.6(e)(f)). The minimum of R_p appears at n-pentane of ϕ_0^{pen} of 100 %, which has the largest SC (i.e., the largest quantity of PSMPs). The influence of the initial condition of Q_p on R_p is significant at

a small quantity of PSMPs range (i.e., $Q_p < 300$), but it is not obvious at a large quantity of PSMPs range (i.e., $Q_p > 600$). The collision frequency (i.e., the probability of particle collisions) dominates at a small particle quantity, while for a large particle quantity, the collision efficiency (i.e., the success rate of aggregation dominates R_p. The collision efficiency depends on the type of solvent, because of the difference of Hildebrand solubility parameter (δ). Figures 5.6(e)(f) also indicates that R_p of n-heptane is higher than n-pentane and n-decane, although our experimental data are not as distinct as the prediction from the model.

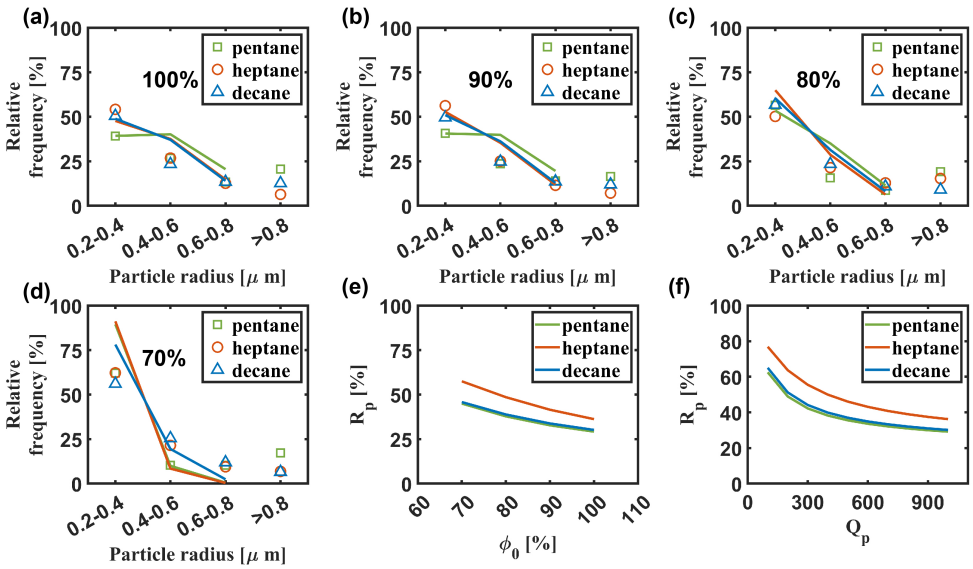

Figure 5.6: Relative frequency of asphaltene particle size distribution with ϕ_0 of (a) 100%, (b) 90%, (c) 80%, (d) 70%. The solid lines show the results predicted from PBM. (e) Effect of n-alkane on R_p. The initial condition of the quantity of PSMPs is 1000. (f) Effect of the initial quantity of PSMPs on R_p. The initial condition of ϕ_0 of the solvents is 100%. At a low quantity of PSMPs region (i.e., $Q_p < 300$), the influence of the initial condition on R_p is very significant. Nevertheless, this dependence is not apparent at the high quantity of PSMPs region (i.e., $Q_p > 600$).

5.4.2 Morphology of asphaltene particles precipitated induced by the mixture of n-heptane and n-decane

Figure 5.7(a) shows the TIRF image of asphaltene particles precipitated in the mixture of n-heptane and n-decane with 0% to 100% n-heptane. It is

found that, with the increase of n-heptane concentration, more asphaltene particles are formed. Figure 5.7(b) shows that the formation of both PSMPs and aggregates, further illustrating the ubiquitous presence of the PSMPs in the mixture of paraffinic solvents.

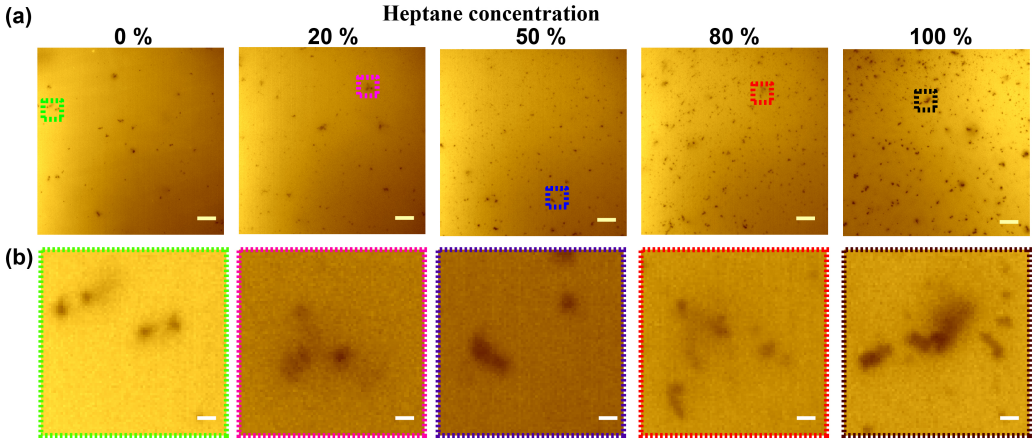

Figure 5.7: (a) TIRF images of asphaltene particles at the final state. The mixture of n-heptane and n-decane induces precipitation, and (b) the corresponding zoomed-in TIRF images at locations with respective color boxes. The length of the scale bar is 10 μm in (a), and is 1 μm in (b). The images are false-colored.

Consistent with the results of asphaltene precipitation induced by pentol, heptol, and dectol, both SC and Q decrease with the increase in δ of the mixture of n-heptane and n-decane as shown in Figures 5.8(a)(b). Also, PSMPs are the most, followed by aggregates in the next size bin from 0.4 to 0.6 μm, which is the same as pentol, heptol, and dectol. It is important to note that the R_p of the three mixture groups is higher than the pure n-heptane and n-decane. However, Figure 5.8(c) revealed that the ratio of aggregates ranging from 0.4 to 0.6 μm of the mixtures has the consistently opposite relationship with the PSMPs.

Interestingly, Figure 5.8(c) shows that asphaltene particles precipitated in the mixtures of n-heptane and n-decane have higher R_p compared with pure n-heptane or n-decane. This attributes to the different diffusion coefficients of n-heptane and n-decane to toluene. n-Heptane diffuses and induces the initial formation of PSMPs faster. n-Decane follows up and dominates the

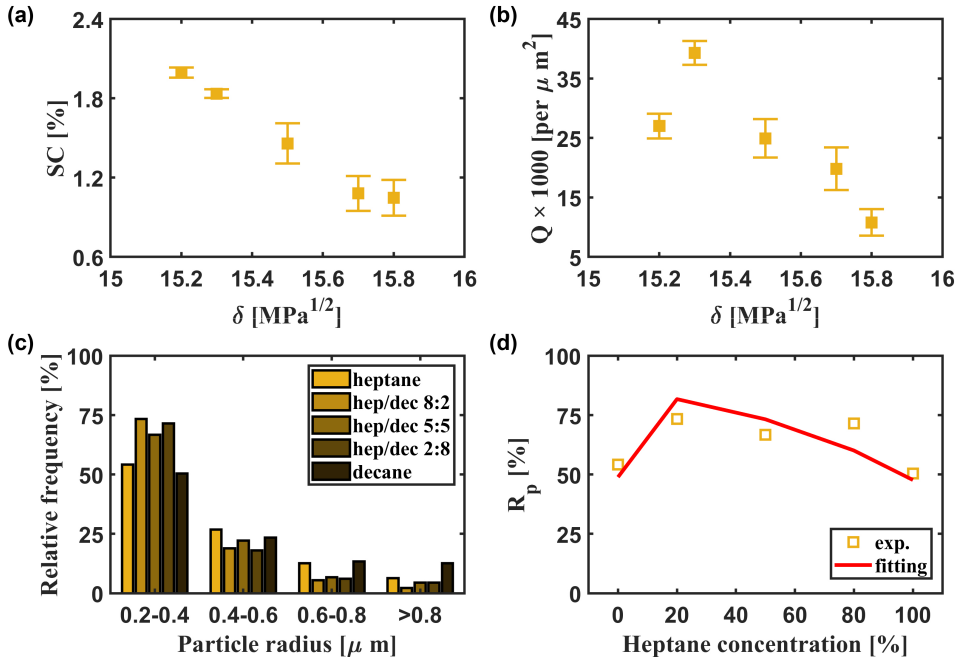

Figure 5.8: (a) Surface coverage (SC) and (b) particle quantity (Q) in the unit area of asphaltene particles at the final state. Precipitation is induced by the mixture of n-heptane and n-decane. Hildebrand solubility parameter (δ) from high to low corresponds to n-heptane concentration from 0% to 100%. (c) Relative frequency of asphaltene particle size distribution for different n-heptane and n-decane mixtures. (d) Comparison of R_p of the experimental and prediction results from PBM.

subsequent aggregation of the PSMPs. As shown in Equation (5.3), collision efficiency in n-decane is lower than n-heptane, so that the probability of the aggregates is lower than pure n-heptane. The PBM results are consistent, and show induces larger R_p (Figure 5.8(d)).

5.4.3 Morphology of asphaltene particles precipitated in bitumen

Compared with our model oil of 17 g/L asphaltene in toluene in the present work, the chemical composition of the natural bitumen is more complicated. More than asphaltene, bitumen contains saturates, aromatic, and resins (SAR) [75]. In this investigation, bitumen was also studied to examine the influence of SAR.

The TIRF optical images are shown in Figure D.1. PSMPs also exist

in the precipitate form of asphaltene particles from bitumen. As shown in Figures 5.9(a)(b), SC and Q of asphaltene particles from bitumen solution and model oil system are similar. The minimal difference may be caused by the uncertainty of asphaltene concentration in bitumen. The R_p of bitumen and asphaltene solution are also close. SAR does have significant impact on the asphaltene precipitation, but it just did not observed by our technique. One contribution for SAR is the solvency effect that they have a similar effect as good solvents (e.g. AR) and poor solvent (e.g. S). Also the toluene in solution A1 is significant which may have an even better solvency effect than AR fractions. Our technique does not have the sensitivity to distinguish the difference when the particles have grown to sub-microns.

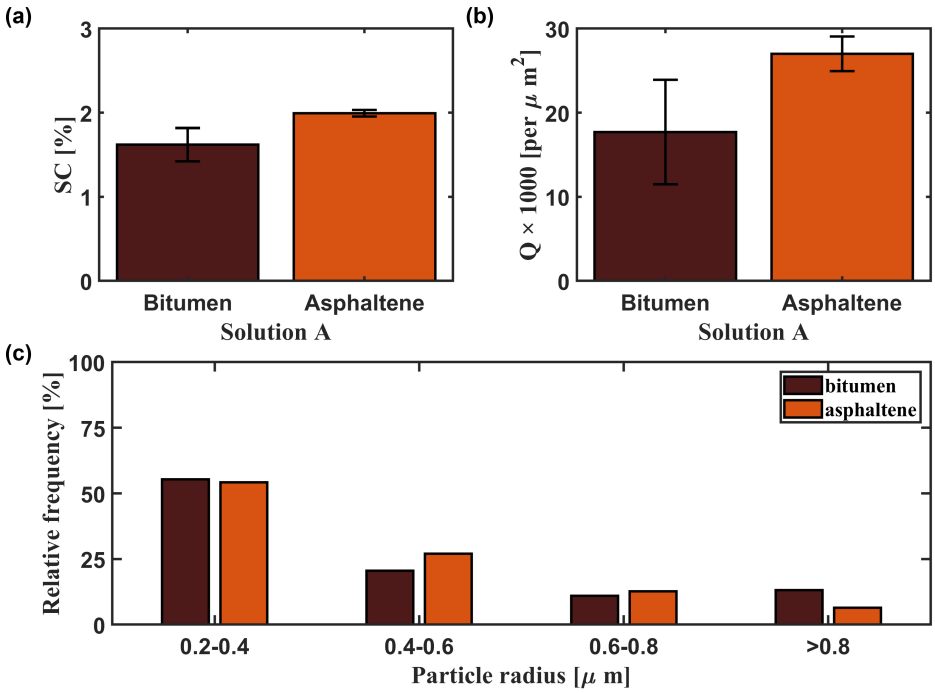

Figure 5.9: (a) Surface coverage (SC) and (b) particle quantity (Q) in the unit area of the final state of asphaltene particles precipitate from bitumen and asphaltene solution. Precipitation is induced by n-heptane. (c) Comparison of the relative frequency of asphaltene particle size distribution for asphaltene and bitumen solution.

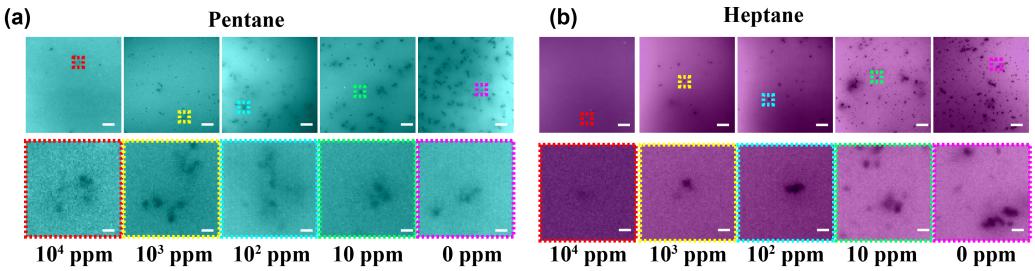

Figure 5.10: TIRF images of asphaltene particles at the final state with the addition of inhibitor from 0 to 10000 ppm. Precipitation is induced by (a) n-pentane and (b) n-heptane. The bottom rows are zoomed-in images of PSMPs at locations with respective color boxes. Note: The images have been false-colored. The length of the scale bar is 10 μm, and is 1 μm in the zoomed-in images. The images are false-colored.

5.4.4 Morphology of asphaltene particles precipitated in the solution with inhibitor

Chemicals that can prohibit the precipitation of asphaltene are called inhibitors [22, 159]. In this study, we keep the concentration of the inhibitor of nonylphenol in the asphaltene solution and precipitant the same. Figures 5.10(a)(b) are the TIRF optical images of asphaltene particles precipitate with the addition of the inhibitor in n-pentane and n-heptane at the concentration of the inhibitor from 0, 10, 100, 1000, to 10000 *ppm*. It is worth noting that some of the asphaltene particles appear as white particles in the TIRF optical images, indicating higher fluorescence intensity from the particles than from the surrounding medium. This may be due to the quenching effect of asphaltene particles being reduced by the inhibitor. The zoomed-in images show the formation of PSMPs. As inhibitor concentration increases, fewer asphaltene particles are observed from TIRF images (Figure 5.10).

In literature, 10000 *ppm* nonylphenol can reduce asphaltene precipitation [22]. We found that the inhibiting effect depends on the types of paraffinic solvent. As shown in Figure 5.11(a), the SC of asphaltene particles decreases with the addition of nonylphenol. As the concentration of nonylphenol increases, the lower surface is covered by asphaltene particles for both n-pentane and n-heptane. However, for n-heptane, both formations of PSMPs and fractal aggregates are inhibited, which is reflected in the corresponding reduction of SC

and Q, as shown in Figures 5.11(a)(b). In the case of n-pentane, the effect of nonylphenol on inhibition is mainly to the aggregation of PSMPs. Therefore, while decreasing SC, Q is increasing.

Figures 5.11(d)(e) show the two highest peaks are of PSMPs and aggregates from 0.4 to 0.6 μm with the addition of the inhibitor in n-pentane and n-heptane. In case of n-pentane, as nonylphenol concentration increases, the inhibition effect of aggregation of PSMPs becomes stronger, resulting in R_p increases and less fractal aggregates forming. For n-heptane, adding nonylphenol from 0 to 100 ppm leads to a similar decrease in the formation of PSMPs and aggregation. The size distribution does not change significantly. The addition of nonylphenol from 100 to 10000 ppm inhibits relatively more aggregation of PSMPs than the formation of PSMPs. For the change from 100 to 10000 ppm, n-heptane shows similar results to n-pentane.

Asphaltene molecules have been shown to form nano-aggregates in toluene at low concentrations ($\sim$ 0.1 g/L) [27, 136]. The concentration of asphaltene 17 g/L is used in this study where the majority motif of asphaltene is nano-aggregates. In colloidal theory, the extended structure of the asphaltene colloids collapses in precipitant, so van der Waals attraction leads to the aggregation of asphaltene nano-aggregates and appears as a new phase formation when the asphaltene aggregates grow large enough [78, 217].

The inhibitor molecules may adsorb on the polyaromatic rings of asphaltene molecules and becomes part of the extended structure around polyaromatic cores [174]. The adsorbed inhibitor molecules enhance the steric repulsion between asphaltene nano-aggregates [174], leading to lower attraction between asphaltene. Thus, adding the inhibitor, whose δ is 19.3 $MPa^{1/2}$ [26], decreases the solubility parameter of asphaltene (δ_{asp}). With decreasing δ_{asp}, PBM model can fit the R_p at different inhibitor concentrations, as shown in Figures 5.11(f)(g). The exact values of δ_{asp} for the PBM fitting are shown in Figure 5.11(c).

The molar mass of asphaltene nano-aggregates is approximately 1,000 to 30,000 g/mol [2, 25, 236]. Therefore, nano-aggregate concentration in our system is 5.7 $\times$ 10^{-4} mol/L to 1.7 $\times$ 10^{-2} mol/L based on 17 g/L asphal-

tene in toluene. For 10,000 *ppm* inhibitor, the concentration is 4.3×10^{-2} mol/L, which is higher than the concentration of asphaltene nano-aggregates. On average, each nano-aggregate at least adsorbs one nonylphenol molecule, resulting in the decrease of δ_{asp} for all asphaltene. The estimated value of δ_{asp} is lower than 24 $MPa^{1/2}$, which is smaller than the pure asphaltene (i.e., 24.2 $MPa^{1/2}$.) Thus, nano-aggregates are less likely to grow large enough to PSMPs as a new phase and PSMPs are less likely to grow larger via further aggregation, resulting in SC becomes to a third and R_p doubles in both n-pentane and n-heptane cases.

In the case of 10 to 1,000 *ppm* of inhibitor on average, some PSMPs may have none or a minimal number of inhibitor molecules. δ_{asp} of the inhibitor-free asphaltene is not changed, and they can aggregate to form fractal aggregates as normal. The quantity of the inhibitor-free asphaltene particles increases with the decrease of the inhibitor concentration. Therefore, the SC decreases, and R_p increases accordingly with the increase of inhibitor concentration.

However, for inhibitor concentration from 0 to 1000 *ppm*, SC decreases slightly from 1.7% to 1.4%, but R_p increases from 40% to 80% in n-pentane. This indicates that the inhibition in n-pentane is mainly on the aggregation of PSMPs because the δ_{pen} (i.e., 14.3 $MPa^{1/2}$) is lower than δ_{hep} (i.e., 15.2 $MPa^{1/2}$). Although δ_{asp} decreases from 24.2 $MPa^{1/2}$ to $\sim$ 23.5 $MPa^{1/2}$ (Figure 5.11(c)), n-pentane is still strong enough to provide sufficient collision frequency for nano-aggregate to grow to PSMPs after adding inhibitor. However, as the particle grows, the number of inhibitor molecules in one asphaltene particles increases, resulting in the further decrease of δ_{asp}. The corresponding increase of steric repulsion results in PSMPs not being aggregated. Then, n-pentane is not adequately strong for further aggregation. Therefore, most of the particles exist as PSMPs, displayed as R_p is approximately doubled with the addition of inhibitors.

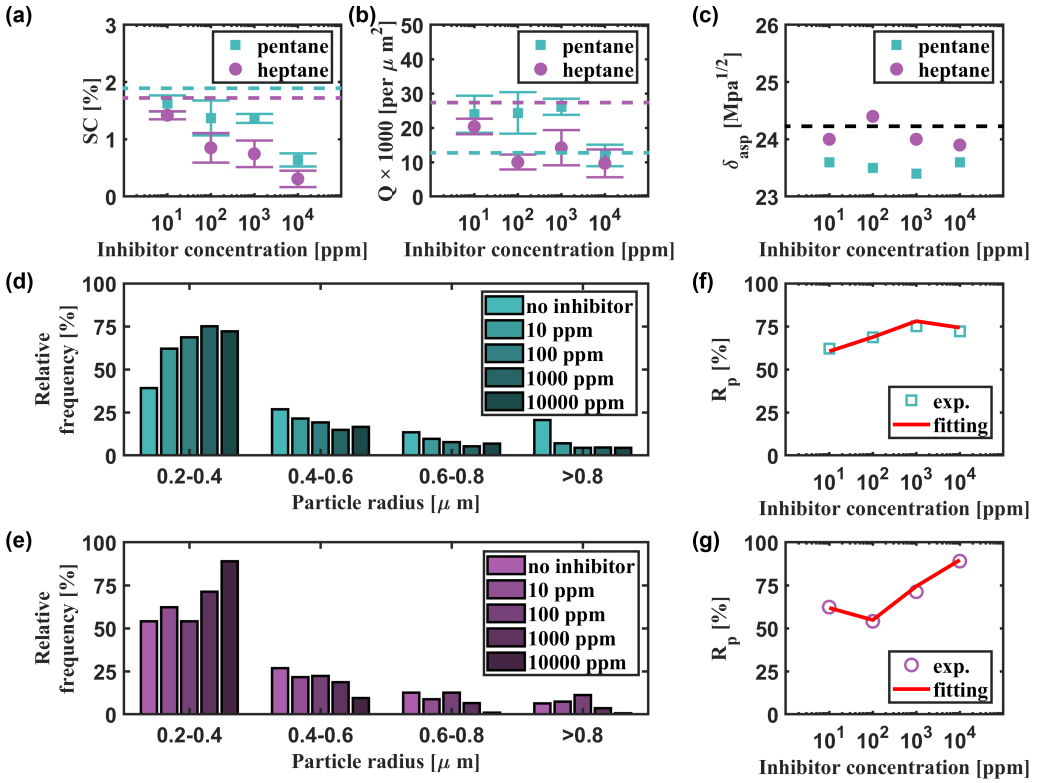

Figure 5.11: (a) Surface coverage (SC) and (b) particle quantity (Q) as a function of the concentration of inhibitor. Cyan and purple dotted lines SC and Q of asphaltene particles precipitated in n-pentane and n-heptane without inhibitor, respectively. (c) δ_{asp} is varied in the PBM model to fit the experimental data. The black dotted line represents δ_{asp} of inhibitor-free asphaltene. Influence of inhibitor on the particle size distribution of asphaltene particles precipitated in (d) n-pentane and (e) n-heptane. Comparison of R_p of the experimental and prediction results from PBM in (f) n-pentane and (g) n-heptane.

5.5 Further discussion: solvency influence on the yield of asphaltene particles

This research agrees with the results obtained in the previous study that stronger solvent (i.e., lower δ) enhances asphaltene precipitation in terms of yield and size at thermodynamic aspect [113, 125, 133]. In addition, mixing dynamics, which are not well controlled and investigated in the conventional study, significantly affect asphaltene precipitation. Diffusion coefficient (D_{21}), collision frequency ($\alpha_{i,j}$), and efficiency ($\beta_{i,j}$) determine both yield and the particle size distribution (in PBM model). In addition, diffusion coefficients

influence the yield via the mixing time.

Even though it is still controversial whether the asphaltene precipitation is a phase change process or a colloidal growth process, most works [66, 78, 217, 242] agree that larger absolute value of the difference of δ between asphaltene and precipitant enhances asphaltene precipitation. Hildebrand solubility parameter difference between asphaltene and n-pentane is larger than n-heptane and n-decane ($\delta_{asp} - \delta_{pen}$ ¿ $\delta_{asp} - \delta_{hep}$ ¿ $\delta_{asp} - \delta_{dec}$) [83]. Larger difference of δ increases the collision efficiency of asphaltene nano-aggregates due to the decreasing of steric repulsion. Therefore, the rate of asphaltene precipitation in terms of SC in n-pentane is higher than n-heptane and n-decane.

However, we found that precipitants with the same δ do not necessarily lead to the same levels of SC and Q. Specifically, δ for precipitants of ϕ_0^{pen} of 70 % is the same as that of ϕ_0^{hep} of 90 %. But both SC and Q of ϕ_0^{hep} of the latter are 15 times higher than those of the former. Our results suggest that apart from δ (thermodynamic aspect), the mixing process (hydrodynamic aspect) of asphaltene solution and the precipitant may play a role in asphaltene precipitation.

The diffusive mixing process in our quasi-2D micro channel allows for quantitative analysis of the effects from diffusion coefficients. Our previous work [129, 131] showed that in the chamber with the same dimensions it took about tens seconds for the chemical composition to transit from the asphaltene solution to pure the paraffinic solvent supplied from the side chamber. At a given time in the mixing process, the ratio between precipitant to asphaltene (R) increases (Figure 5.2(c)) along the concentration gradient from the asphaltene solution towards the paraffinic solvent. Asphaltene precipitation takes place at the location where the ratio R is above the onset. For a given location, the ratio R gradually increases with time and reaches the onset, from which moment the asphaltene precipitation begins. Eventually, the mixture containing asphaltene in the location is nearly replaced by the precipitant, and the precipitation finishes due to the lack of the source of asphaltene. Mixing retention time (t_R) is defined as the time duration between the start of asphaltene precipitation and the end. For a higher diffusion coefficient(i.e., n-pentane),

the retention time (t_R) of mixing is shorter. Therefore, mixing retention time of n-pentane (t_{Rpen}) is shorter than n-heptane (t_{Rhep}), and t_{Rhep} is shorter than n-decane (t_{Rdec}).

The final yield of asphaltene is the result of the coupled effects from the precipitation rate of asphaltene and the mixing retention time. Although δ follows $\delta_{asp} - \delta_{pen}$ ¿ $\delta_{asp} - \delta_{hep}$, the mixing retention time follows t_{Rpen} ¡ t_{Rhep} due to D_{pt} ¿ D_{ht}. Consequently, the SC of n-pentane and n-heptane are similar. On the other hand, the precipitation rate of asphaltene is low in n-decane, although the mixing retention time is longer than t_{Rpen} and t_{Rhep}, SC from n-decane is still lower than from n-pentane and n-heptane.

For pentol, heptol, and dectol, the diffusion coefficients of n-alkanes with respect to initial ϕ_0 vary in a small range (Figure 5.1(c)). Therefore, the effect from the difference of diffusion coefficient is negligible, compared to that from the variance of δ at different ϕ_0. Both SC and Q increase with the decrease of δ, as observed in our results.

5.6 Conclusions

This work compares 23 types of precipitants to induce asphaltene precipitation under diffusive mixing in a quasi-2D microfluidic chamber. TIRF captures the precipitated asphaltene particles to exhibit a high spatial resolution. The formation of PSMPs (i.e., size range from 0.2 to 0.4 μm in radius) is ubiquitous in the diffusive mixing quasi-2D microfluidic chamber. The formation of PSMPs is independent of the type and concentration of solvents, the presence of inhibitors, and the asphaltene solution is model oil or bitumen. However, for the size distribution, the mixture of n-heptane and n-decane produces the highest R_p in the diffusive mixing process. The yield of asphaltene increases with the decrease of the Hildebrand solubility parameter, also influenced by the diffusion coefficient. Both the yield of the precipitated asphaltene and the PSMPs ratio can be tuned by changing the type and composition of the precipitant. Population balance model (PBM) is developed and validated by the in-house experimental data in terms of the size distribution of the asphaltene

particles. The results of R_p from the PBM are in good agreement with the experimental results at different solvent conditions. In addition to the solvents, the inhibitor can prohibit both the formation and aggregation of PSMPs in the diffusive mixing system. The experimental data of adding inhibitors can be fitted by adjusting δ_{asp} in PBM, which is a determining factor of the energy barrier between asphaltene particles, suggests that the prohibition effect of inhibitors may be caused by increasing the energy barrier between asphaltene particles. Excellent agreement of fitting shows that the parameters in PBM are likely to be reasonable. PBM provides the foundation for modelling real processes.

The findings from this work imply that it may be worthwhile for industry to pursue the best match mixing solvents so that large asphaltene precipitates may form in a reasonable short mixing time. The best match mixing solvents may flocculate more solids and water droplets without excessive loss of hydrocarbon. In future, it will be necessary to perform similar quantitative study on asphaltene precipitation as the solvent is mixed at controlled flow rate. Such study may confirm the significance of fast mixing dynamics on dilution-induced asphaltene precipitation.

Chapter 6

Viscosity-Mediated Growth and Coalescence of Surface Nanodroplets

Abstract

Solvent exchange is a simple method to produce surface nanodroplets on a substrate for a wide range of applications by displacing a solution of good solvent, poor solvent, and oil (solution A) by a poor solvent (solution B). In this work, we show that the growth and coalescence of nanodroplets on a homogeneous surface is mediated by the viscosity of the solvent. We show that at high flow rates of viscous solution B, the final droplet volume deviates from the scaling law that correlates the final droplet volume to the flow rate of nonviscous solution B, reported in previous work. We attribute this deviation to a two-regime growth in viscous solution B, where transition from an initial, fast regime to a final slow regime is influenced by the flow rate. Moreover, viscous solution B hinders the coalescence of growing droplets, leading to a distinct bimodal distribution of droplet size with stable nanodroplets in contrast to a continuous size distribution of droplets in nonviscous case. We demonstrate that the group of small droplets produced in a high-viscosity environment may be applied for enhanced fluorescence detection with higher sensitivity and shorter response time. The finding of this work can potentially be applied for mediating the size distribution of surface nanodroplets on a homogeneous surface without templates.

6.1 Introduction

Surface nanodroplets have attracted significant research interest, due to various applications for micropatterning, [253] optical lenses,[162, 231] chemical and biological analysis,[71, 248] and crystallization [197]. Tuning the size distribution of droplets is important for droplet-based sensing,[223] biochemical assays,[82] miniaturized substrates for cell culture[210], fabrication of nanostructures from ionic liquids, [241] and many others. Currently methods such as inkjet-based droplet printing,[51, 201] and droplet deposition on pre-patterned substrate[154, 251] are widely used to for producing droplet with a defined size. However, complicated procedures, dedicated equipment, or long process time are often required for the formation of large quantity of nanodroplets. Some of the methods are not applicable for producing surface droplets immersed in a liquid medium.

Recently, solvent exchange process has been developed as a bottom-up approach to reliable formation of surface nanodroplets, providing control over final droplet volume, composition as well as number density.[116, 162, 258] These droplets are usually up to a few hundred nanometers in the maximal apex and several to tens microns in lateral diameter. The solvent exchange process is versatile, thus enabling novel applications of surface nanodroplets including liquid-liquid extraction [110, 115] and *in-situ* determination of partition coefficient [111]. In a typical solvent exchange process, surface nanodroplets are formed by exposing the substrate surface to a good solvent (Solution A) which is subsequently displaced by a poor solvent (Solution B). At the mixing front of Solution A and B, droplets nucleate and grow due to local oversaturation of droplet liquid in the mixture. At the end of the process, the final droplet volume can be controlled by tuning several parameters such as flow rate, compositions of Solution A and B as well as the channel dimensions.[249] Changing flow rate of Solution B can vary droplet sizes without changing the solution composition for solvent exchange. Droplet size control by the flow rate can be advantageous when solubility phase diagram of the ternary mixture in Solution A is not available. For a given channel dimension

and oil concentration, the droplet volume scales with the flow rate following the scaling law $Vol_f \sim Pe^{\frac{3}{4}}$. Here, Vol_f is the final droplet volume per unit area and Pe is the Péclet number defined as $Pe = Q/(wD)$ where Q is the flow rate of Solution B, w is the channel width and D is the diffusivity of oil.[258]

The base size, spacing and position of the droplets by solvent exchange can be tuned precisely on a surface with chemical micropatterns [23]. However, on a homogeneous smooth surface the size distribution of droplets is uncontrolled, due to stochastic nature of nucleation, growth and coalescence from oversaturation in the surrounding [29, 152, 230, 252]. In a similar process of droplet formation from condensation [28, 249, 260], the viscosity of the solution cast on the surface has been shown to an important parameter to eliminate the undesirable coalescence of droplets. When two droplets are surrounded by a highly viscous fluid, their coalescence is delayed due to slower displacement of liquid between them [49, 121].

In this work, we study the effect of solution viscosity on the droplet formation by solvent exchange. In particular, we demonstrate that when viscosity of Solution B is higher than that of Solution A, the final droplet size becomes independent of flow rate at sufficiently high flow rates. Importantly, the high viscosity of solutions surrounding the droplets hinders their coalescence, resulting in a bimodal size distribution. We will demonstrate that the small droplets produced via hindering coalescence enhance the fluorescence intensity in detection with higher sensitivity and shorter time. The findings of this work may provide a method for producing surface nanodroplets as templates for materials fabrication with hierarchical structures, such as polymer films with bimodal pore sizes [97, 237, 249] or microlens with largely different focusing length.

6.2 Experimental

6.2.1 Substrate and solutions

A Si substrate was rendered hydrophobic by coating a monolayer of octadecyltrichlorosilane (OTS) (95%, Alfa Aesar) following the protocol reported else-

where.[258] The substrate of OTS coated Si was sonicated in ethanol (90%, Fisher Scientific) and dried by air before use.

The solvent exchange process to generate surface nanodroplets was performed in a custom-built fluid chamber with an inlet and an outlet (Fig. S1a). The chamber was 5.8 cm long, 1.3 cm wide and 0.97 mm high. Glass was used as the top cover, allowing for observation of the droplets using an upright optical microscope. Solution A consisting of ethanol, water and 1,6-hexanediol diacrylate (HDODA) (99%, Alfa Aesar) was injected into the chamber using a syringe pump (NE-1000, Pumpsystems Inc.). Subsequently, a solution of glycerol (99.5%, Fisher BioReagents) in HDODA-saturated water (Solution B) was injected into the chamber to displace the Solution A and form surface nanodroplets. The viscosity of Solution B is adjusted by the concentration of glycerol,[48, 80, 214] and the values were calculated using Grunberg-Nissan equation.[80]. The variation in surface tension during solvent exchange is negligible because even for pure glycerol the surface tension is only slightly lower than pure water (∼64 mN/m vs 72 mN/m). Composition of Solution A and B were varied to test the effect on the droplet formation including groups 1, 2 and 3 with different viscosity of Solution B and groups 4, 5 and 6 with different oil concentrations. Viscosity of Solution A and Solution B are shown in Table 1.

6.2.2 Characterization of the droplets

Optical microscope (Nikon ECLIPSE Ni) equipped with a camera (Nikon DS-Fi3) was used to obtain images of the droplets. The droplet volume per unit surface area (V/A) and size distribution were obtained by analyzing more than 1 mm^2 from each image using ImageJ. From each image, the occupied surface area (S) of each droplet was obtained to calculate its corresponding equivalent lateral radius (R) with R=$\sqrt{\frac{S}{\pi}}$ and further the volume of droplet (V_{drop}) could be estimated using the contact angle (θ).

For the measurement of contact angle of the nanodroplets, surface profile of polymerized HDODA droplets were obtained via atomic force microscope (AFM) by tapping mode. A representative AFM image of droplet is attached

in shown in Fig. 1b. The polymerized nanodroplets were obtained by following the method reported in our previous work.[258] Contact angle was then calculated by fitting a circle equation to the obtained profile. The contact angle of the droplets on OTS-Si were measured to be $\sim 9^\circ$ with 7.4 cP solution B and $\sim 8^\circ$ with 12.8 cP and 18.0 cP solution B. The contact angle was assumed to be constant for different droplet sizes, as the variation of contact angle is very small with the droplet size.[258]

6.2.3 Extraction of Nile Red from water using nanodroplets

Extraction and detection of Nile Red (Sigma Aldrich, $\lambda_{ex} \sim 554$ nm, $\lambda_{em} \sim 638$ nm) from water was performed using the droplets produced from the solvent exchange process with high viscosity Solution B. Here, we used HDODA as the oil component, making Solution A at ethanol : water : HDODA = 48.1 : 48.1 : 3.8 (in wt%). We used glycerol to increase the viscosity of Solution B to $\mu_B \sim$ 7.4 cP. Droplets were formed on OTS-Si via standard solvent exchange with Solution A and B at flow rate of 96 mL/h. Subsequently, a sample solution containing trace of Nile Red in water was injected at the same flow rate. As the sample solution was introduced into the chamber, Nile Red was extracted to the HDODA droplets, and fluorescence signal was detected in the droplets under green laser. The fluorescence signal intensity of the Nile Red in droplets was measured using self-written MATLAB codes.

6.3 Results and discussion

6.3.1 Effect of viscosity on droplet growth dynamics

The solvent exchange process relies on the phase separation caused by the oversaturation of oil as the mixture of oil/good solvent/poor solvent (Solution A) is replaced by the oil-saturated poor solvent (Solution B). As shown in the ethanol/water/HDODA ternary phase diagram (Fig.6.1c), Solution A is a homogeneous solution with the compositions above the binodal line. As Solution B is introduced into the chamber to gradually displace Solution A, diffusive

mixing between the two solutions takes place and the composition of the mixture cross the Ouzo region surrounded by spinodal and binodal lines.[213, 246] The change in composition triggers liquid-liquid phase separation due to local oversaturation in the mixing zone and finally leads to the formation of droplets on the substrate. After solvent exchange, the droplets are stable in Solution B and reach the final state where no change in droplet sizes with time is observed. Surface nanodroplets are also produced even if the viscosity of Solution B is adjusted using glycerol. The phase diagram obtained with glycerol solution remains similar to that of water, especially near Ouzo region (Fig. 6.1d). This similarity suggests that liquid-liquid phase separation and droplet formation would also occur using viscous Solution B in solvent exchange.

However, when the viscosity of Solution B is increased by addition of glycerol, droplet growth dynamics is clearly different from the non-viscous case. To compare the growth dynamics between non-viscous ($\mu_B \sim 1$ cP) and viscous cases ($\mu_B \sim 7.4$ cP), we track the lateral radius (R) of droplets for a period of more than 15 s (Fig. 6.2). As shown in Fig. 6.2, at a given time, droplets grow faster in the case of using water as Solution B compared to the case of using glycerol solution. Although droplets grow at a similar rate initially for the first 3 s, the droplet size reaches a plateau to a value between $15 \sim 20$ μm after $\sim$3 s in the case of glycerol solution. On the other hand, the droplet size for water case lies between $20 \sim 30$ μm and still continues to grow with time, with growth dynamics following $R(t) \sim C_0 erf(t/\tau)^{\frac{1}{2}}$ where C_0 is a prefactor, and τ is growth time, as reported in our recent work. [62] The values used for fitting were $C_0 = 30$ and $\tau \sim 5.66$ for non-viscous case of water and $C_0 = 19$ and $\tau \sim 0.29$ for the viscous case of glycerol solution. The fact that both of these values are different for non-viscous and viscous cases indicates substantial difference in their growth dynamics.

It is worth mentioning that in this set of our experiments, a horizontal setup had to be employed to track the change in droplet size with time during the solvent exchange. In such configuration, gravity may influence the growth of the droplets.[239]. To determine the influence of gravity, Archimedes number comparing the gravitational force to viscous force was calculated for both cases.

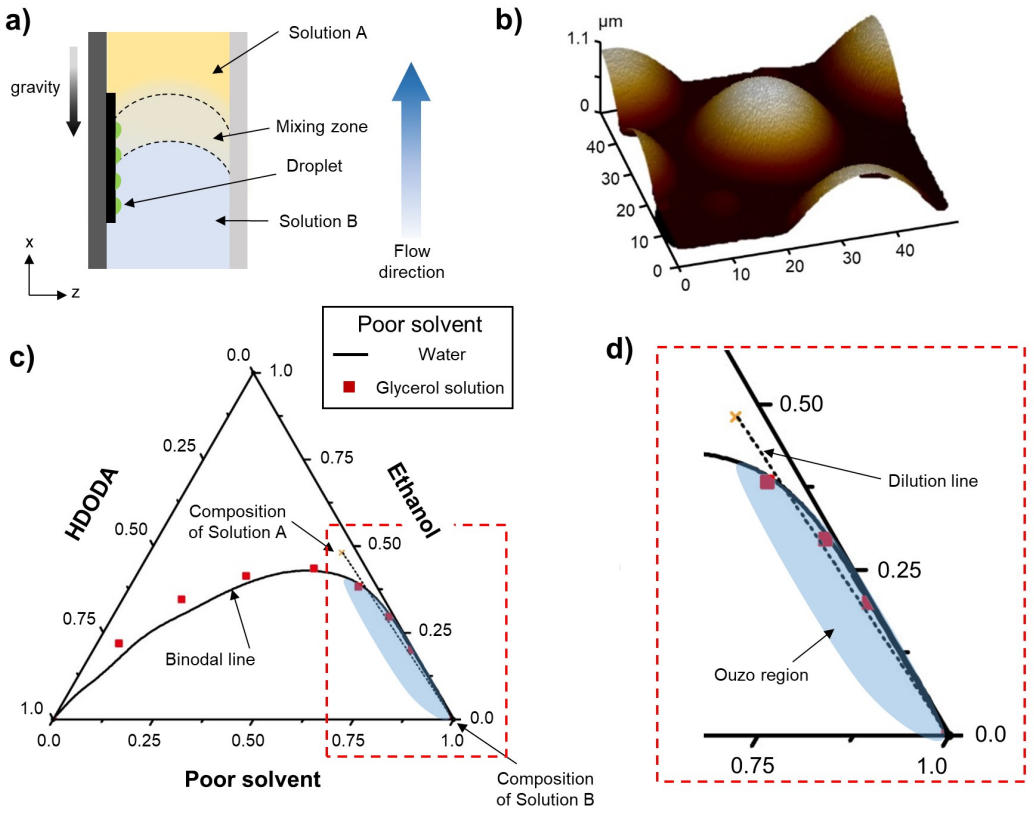

Figure 6.1: (a) Schematic of solvent exchange process. Since the flow direction is from bottom to top, in positive x direction, any influence of gravity on the flow profile can be prevented. (b) Atomic force microscope (AFM) image of a polymerized droplet. (c) Ternary phase diagram of HDODA, ethanol and water plotted along with that of glycerol solution. Addition of glycerol does not change the phase diagram much, especially near Ouzo region shown in color blue. During solvent exchange, Solution B (either water or glycerol solution) gradually displaces Solution A following the dilution path (dashed line). As the composition crosses the binodal line, phase separation occurs forming droplets. (d) The zoom-in view of the phase diagram near Ouzo region.

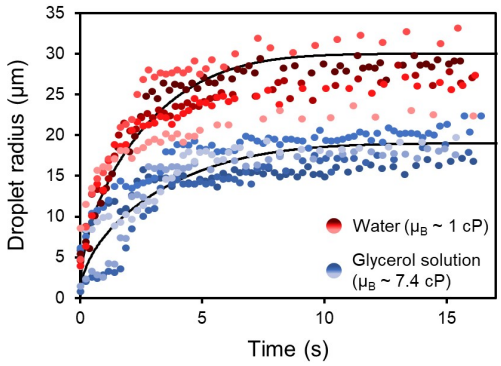

Figure 6.2: Droplet growth dynamics for the cases with water (red) and glycerol solution (blue) as Solution B. For the case of glycerol solution, the droplet radius plateaus after ∼3 s. In contrast, droplet continues to grow for the case of water.

$$Ar = \frac{gh^3\Delta\rho}{\nu^2\rho_B} \tag{1}$$

where g = 9.81 m/s^2 is the gravitational acceleration, h is the channel height (250 μm), $\Delta\rho$ is the density difference between Solution A (ρ_A) and Solution B (ρ_B), and ν is the kinematic viscosity of Solution B at composition of glycerol:water = 51:49. In the non-viscous case, Ar $\sim$ 16 whereas in the viscous case Ar $\sim$ 0.7 indicating that gravity would influence the growth in the non-viscous case, leading to smaller droplet volume as reported in literature.[239] Even though Ar $>$ 1 in the non-viscous case, the droplet growth is still much faster compared to the viscous case clearly demonstrating the influence of viscosity on the dynamics of droplet growth.

6.3.2 Effect of viscosity on final droplet size

Fig. 6.3 shows the optical images of the final state of the surface nanodroplets formed by Solution B with viscosity of 7.4 cP to 18.0 cP at flow rate from 4 mL/h to 96 mL/h. For all values of viscosity, the size of droplets was observed to increase with increase in the flow rate. However, above a certain flow rate, no significant change in size was observed. Instead smaller droplets were formed in between the already-growing large droplets. The trend was more pronounced at higher viscosity (i.e. 18.0 cP). Notably, for 18.0 cP, small

droplets were observed starting at 4 mL/h with no drastic increase in size of already formed droplets at higher flow rates. However, for the case with viscosity $\sim$ 7.4 cP, small droplets were formed at a higher flow rate and the size of primary droplets were observed to increase with flow rate until it plateaued at Q = 24 mL/h.

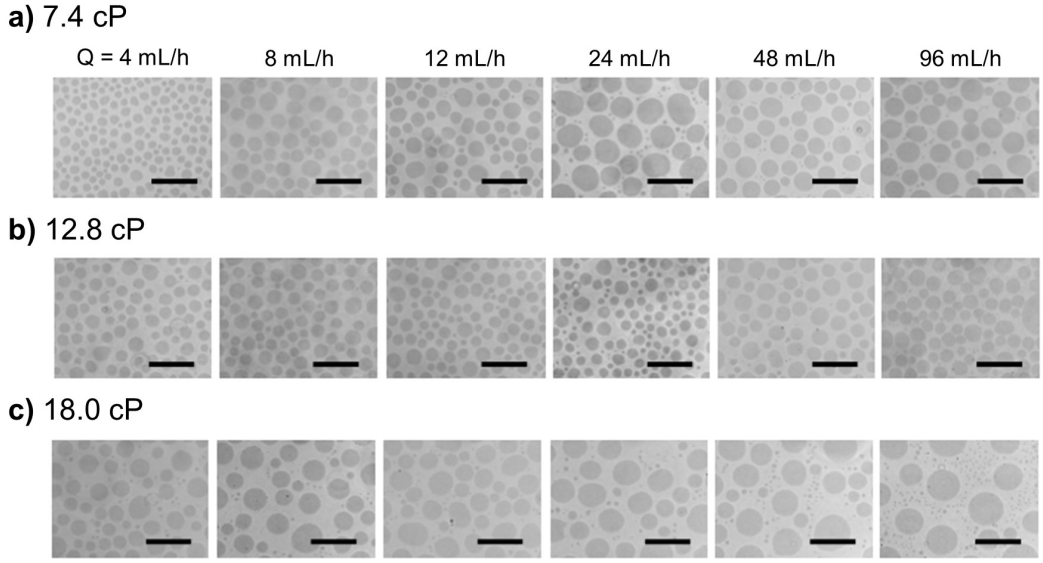

Figure 6.3: Optical images of droplets formed at flow rates from 4 to 96 mL/h with different viscosity of Solution B. (a) $\mu_B \sim$ 7.4 cP, (b) $\mu_B \sim$ 12.8 cP, (c) $\mu_B \sim$ 18.0 cP. Scale bar: 50 μm.

Fig. 6.4a and b show the probability distribution function (PDF) of volume of individual droplets (V_{drop}) at the final state formed by Solution B with viscosity $\sim$ 18.0 cP for different flow rates as well as for non-viscous cases obtained at 6 mL/h and 48 mL/h reported in our previous work [258]. Here, the viscosity of Solution A was kept at $\sim$ 1 cP. For all cases, a bimodal distribution is observed with a peak located at lg(V_{drop}) $\sim$ -1 to 0.2 corresponding to the small droplets and another peak near lg(V_{drop}) $\sim$ 2.2 to 2.7 corresponding to large droplets. This is clearly different from the case when both solutions are non-viscous ($\mu \sim$ 1.0 cP), where size distribution was continuous with one broad peak indicating a continuous size distribution [258].

The bimodal distribution of droplet size is also evident for other viscosity values. Fig. 4c shows the PDF of droplet sizes produced at 96 mL/h for

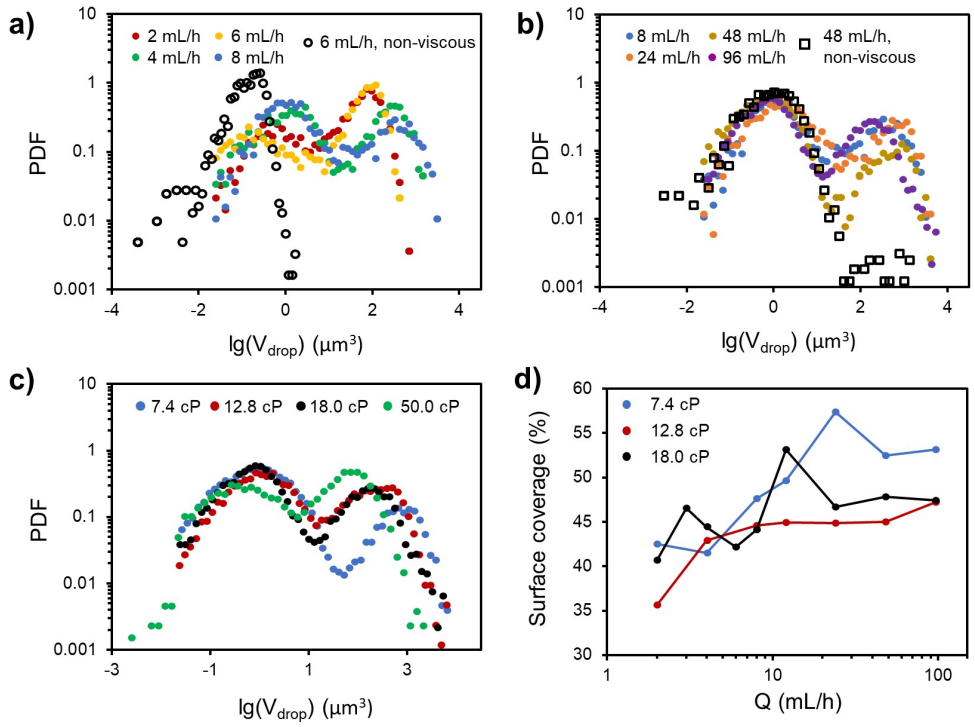

Figure 6.4: Probability distribution function (PDF) of droplet volume (V_{drop}) at the final state produced (in μm^3) with Solution B viscosity of 18.0 cP at (a) 2 to 8 mL/h and (b) 8 to 96 mL/h. As comparison, both plots also show the PDF of non-viscous case for a) 6 mL/h and b) 48 mL/h obtained from analysis the images published in Ref.15 (c) PDF of droplet volume (V_{drop}) at the final state produced (in μm^3) produced at 96 mL/h for Solution B viscosity from 7.4 to 50 cP. (d) Surface coverage versus flow rate with different solution B viscosity. The surface first increases with flow rate, while plateau after the flow rate reaching 12 mL/h.

Solution B with viscosity from 7.4 to 50 cP. All the distributions have two distinct peaks, reflecting the presence of two groups of droplets with vastly different sizes. Notably, while the sizes of large droplets are noticeably different for different viscosity values, small droplets are similar in size regardless of viscosity. Fig. 6.4d shows the surface coverage measured at different flow rates for the Solution B viscosity of 7.4, 12.8 and 18.0 cP. When the flow rates are low, surface coverage increases with flow rate. However, after a certain point (i.e. 12 mL/h), the surface coverage fluctuates between 45 and 55%, consistent with the distribution of droplet sizes shown in Fig. 6.4a,b.

The other notable difference between viscous and nonviscous cases is the

influence of flow rate on the droplet size. High viscosity of Solution B leads to the independence of droplet size on flow rate, reflected as deviation from the scaling law of $Pe^{3/4}$, previously confirmed for the non-viscous solution B [258]. Fig. 5a shows the dependency of total droplet volume per observation area (shown as lg(V/A)) on flow rate (shown as lg(Q)) with dotted lines representing best fit lines with 3/4 slope according to the scaling law. In all cases, the data deviates from the power of 3/4 after certain lg(Q) value but remains at a plateau. As the oil concentration is varied, the plateau of the droplet size is still observed, that is, the total droplet volume per observation area (V/A) becomes independent of the flow rate when the flow rate is higher than a critical value (Fig. 6.5).

6.3.3 Flow rate-independence and two-regime growth of droplets at high viscosity

The universality of the scaling law correlating the droplet volume per unit surface area to the Pe with the power of 3/4 has been verified through several studies using different variables such as chamber height, solvent exchange direction, oil with different viscosity, and initial solution composition[162]. It is surprising that the higher viscosity of Solution B compared to that of Solution A leads to flow-rate independence, especially in the high flow rate regime. We propose the following two-regime growth model to rationalize the effect of viscosity on the dynamics of droplet growth during the solvent exchange.

When using viscous Solution B, the entire process of the droplet growth may be divided into a fast-growth regime (regime 1) and a slow-growth regime (regime 2) as sketched in Fig. 6.6. In the fast-growth regime, the viscosity in the mixing zone is still low due to the higher amount of non-viscous Solution A compared to Solution B, and droplet growth follows the process same as the non-viscous Solution B, as reported before [258]. Briefly, $\dot{m} = 4\pi\rho_{oil}R^2\dot{R} = 4\pi DR^2\partial_r c|_R$, where m is droplet mass, ρ_{oil} is density of oil, R is lateral droplet radius, D is diffusivity and c is concentration of oil. Here, the concentration gradient at the interface ($\partial_r c|_R$) is the gradient between the oil concentration in the bulk flow (c_∞) and at the interface of droplets ($c_{s,poor}$) divided by the

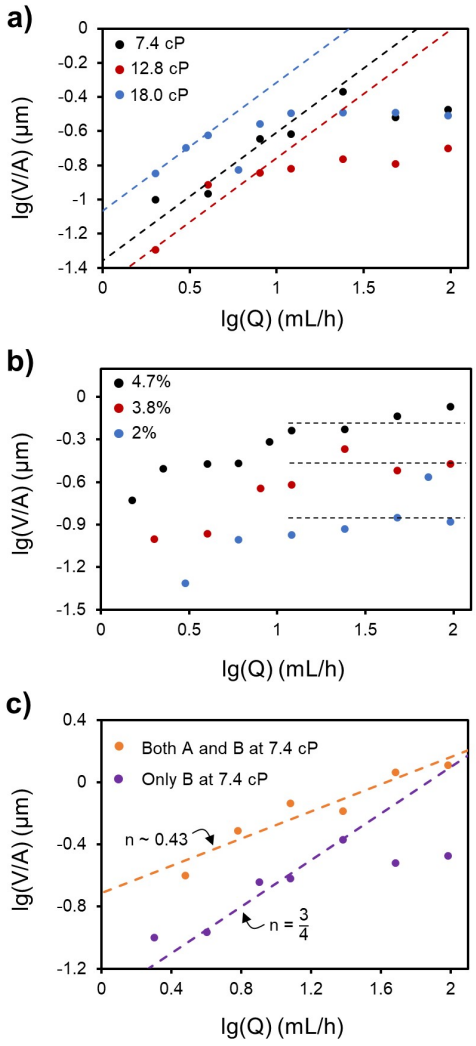

Figure 6.5: (a) Droplet volume per unit area (V/A) produced using different flow rates (Q) at Solution B viscosity of 7.4, 12.8 and 18.0 cP. The dashed lines show the slope of 3/4 according to the scaling law $Vol_f \sim Pe^{\frac{3}{4}}$. For all viscosity values, the trend deviates at high flow rates. (b) V/A produced using different Q at Solution B viscosity of 7.4 cP with different oil concentrations in Solution A. As shown by the dashed lines, V/A plateaus at high Q for all oil concentrations. (c) V/A produced using different flow rates at viscosity of 7.4 cP for both Solution A and B (orange) or for Solution B only (purple). Orange dashed line shows that while V/A scales with Q, the slope is lower than 3/4 (n $\sim$ 0.43). Purple dashed line with slope 3/4 shows the deviation of data at high Q.

thickness of the concentration boundary layer (λ_1).[258] In the mixing zone, the diffusion of oil into the droplets is influenced by Taylor dispersion,[16, 79, 204] so $\lambda_1 \sim R/\sqrt{Pe}$. Therefore, the concentration gradient becomes:

$$\partial_r c|_R \sim \frac{c_\infty(t) - c_{s,poor}}{\lambda_1} \sim c_{s,poor}\frac{\zeta(t)}{\lambda_1} \sim c_{s,poor}\sqrt{Pe(t)}R^{-1}\zeta(t) \tag{2}$$

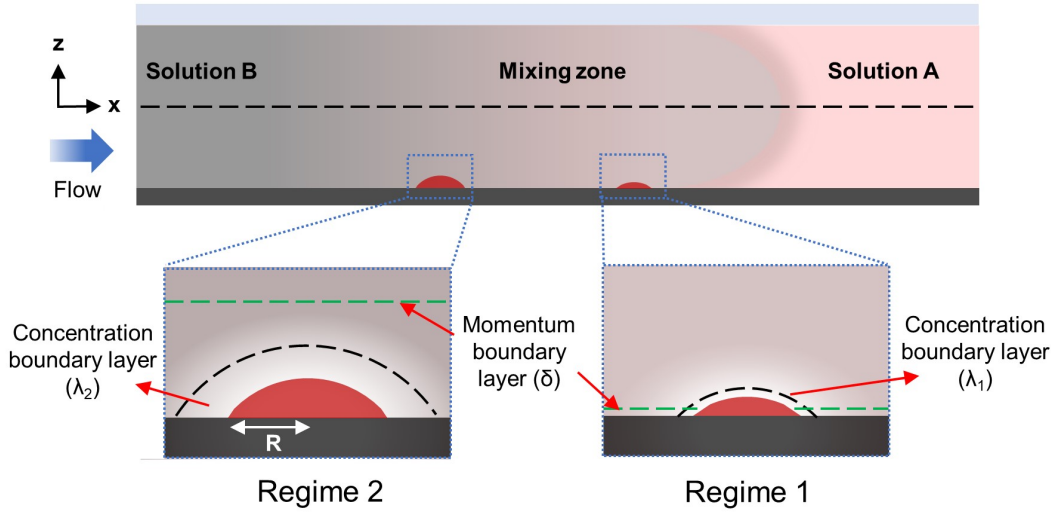

Figure 6.6: Sketch showing two-regime growth model in a viscous solution. In regime 1, the concentration boundary layer is much thinner than the droplet and growth follows the scaling law. In regime 2, as viscosity increases, the concentration boundary layer becomes nested in the momentum boundary layer. At the same time, the concentration boundary layer becomes comparable to the size of droplet, minimizing the influence of Taylor dispersion and slowing down the growth.

where $\zeta(t)$ denotes the oversaturation profile of oil. Then, using the concentration gradient and mass balance around the droplet, we obtain:

$$R\dot{R} \sim \frac{D(t)c_{s,poor}}{\rho_{oil}}\sqrt{Pe(t)}\zeta(t) \tag{3}$$

Here, both D and Pe change with time during the droplet formation as the viscosity of the medium in the mixing zone increases. In regime 1, because the ratio of Solution B compared to Solution A is still low, the change of D and Pe with time is not significant, therefore the droplet growth is enhanced by increase in Pe of Solution B. In non-viscous case, both D and Pe are almost constant during the solvent exchange, the above theoretical analysis explains

the scaling law of final droplet size with $Pe^{3/4}$ as reported in the previous work. [258]

The high viscosity of Solution B eventually starts to influence the mass transport for droplet growth. The momentum boundary layer (δ) above the solid surface increases with time by following the Blasius solution ($\delta \sim 1/\sqrt{Re}$). Here the local diffusivity D and Reynolds number ($Re = \frac{\rho U d}{\mu}$ with ρ density of fluid, U local velocity, and d characteristic length) at a fixed point on the surface decreases with time as the ratio of Solution B in the mixing zone increases. As δ becomes large enough, the concentration boundary layer is nested in the momentum boundary layer with a small gradient from the wall but a large thickness. The influence from the maximum velocity of the external flow on droplet growth becomes negligible at $\lambda_1 \sim R/\sqrt{Pe} \sim R$ (i.e the concentration boundary layer thickness is comparable to the droplet size). The growth of droplets now transitions into the second regime (regime 2) with negligible effect from advection where the concentration gradient around the growing droplet is:

$$\partial_r c|_R \sim c_{s,poor} \frac{\zeta(t)}{\lambda_2} \sim c_{s,poor} R^{-1} \zeta(t) \tag{4}$$

$$R\dot{R} \sim \frac{D(t) c_{s,poor}}{\rho_{oil}} \zeta(t) \tag{5}$$

Different from eq. 3, Pe is not included in eq. 5. The final droplet volume R_f is the combination of both regimes:

$$\int_0^{R_f} R dr \sim \frac{c_{s,poor}}{\rho_{oil}} [\int_0^{\tau_1} D(t) \sqrt{Pe(t)} \zeta(t) dt + \int_{\tau_1}^{\tau_2} D(t) \zeta(t) dt] \tag{6}$$

Here τ_1 is time duration of regime 1, and τ_2 - τ_1 is time duration of regime 2. The total growth time τ_2, influenced by the channel height, diffusivity and Taylor-Aris dispersion. [62] For two extreme cases, the droplet growth either follows Pe scaling law $Vol_f \sim Pe^{3/4} \sim Q^{3/4}$, same as the case of non-viscous Solution B[258], or is independent of the flow rate or thus Pe. We are not able to provide a solution for eq. 6, due to complicated inter-correlation of various parameters. In particular, the droplets start to form stochastic ally all the time

from different over saturation, leading to heterogeneous size distribution and different concentration boundary layer thickenss. However, the above analysis shows that as a result of more viscous Solution B than Solution A, the final droplet size is influenced by flow rate Q (or Pe), growth time in each regime (τ_1 and τ_2-τ_1), diffusivity and their dependence with time.

At low flow rates, the droplet growth in regime 1 is dominant while at fast flow rates, the growth in regime 2 prevails. The critical flow rate where the transition from regime 1 to 2 occurs is influenced by the viscosity of Solution B. At a higher viscosity of Solution B, the transition from regime 1 to 2 takes place at a slower flow rate. Our analysis is consistent with the trend shown in Fig. 6.5.

Flow rate-independence is not observed when both viscosity of Solution A and B are increased to $\sim$ 7.4 cP (Fig. 6.5c). Droplet size increases with the flow rate of Solution B, but with a lower slope compared to the non-viscous case. The final volume of droplets still scale with Pe but with less dependence. The less dependence is from smaller droplets formed at higher flow rates, which may be attributed to reduced diffusivity of oil in a viscous medium. Less oil is transported from the mixing front to the growing droplets on the surface due to high viscosity in the time window before all the mixture is advected by the bulk flow.

6.3.4 Influence of two-regime growth on droplet size distribution

The two-regime growth mode may also explain the bimodal distribution of the final droplet size. As Solution B is introduced and oversaturation occurs, the first generation of droplets in response to the oversaturation nucleate and grow till the surface coverage is close to a maximum of $\sim$ 50 %.[230] This plateau is determined by the contact angle of the droplets on the surface [230]. Then the second generation of the droplets start to form on the bare substrate freed from the coalescence of the larger droplets. However, in contrast to the non-viscous case, the second generation of droplets do not coalesce due to the high viscosity of the surrounding environment as sketched in Fig. 6.7. These

small droplets do not grow much as the growth enters the slow regime 2. As a result, although a second generation of droplets form on the void spaces, coalescence between these droplets as well as with the first generation droplets is hindered because displacing the liquid between the droplets is now more difficult. Therefore, by the end of solvent exchange, the droplets from second generation constitute the group of the small droplets resulting in a bimodal distribution of sizes. The bimodal size distribution remain stable over time after the solvent exchange.

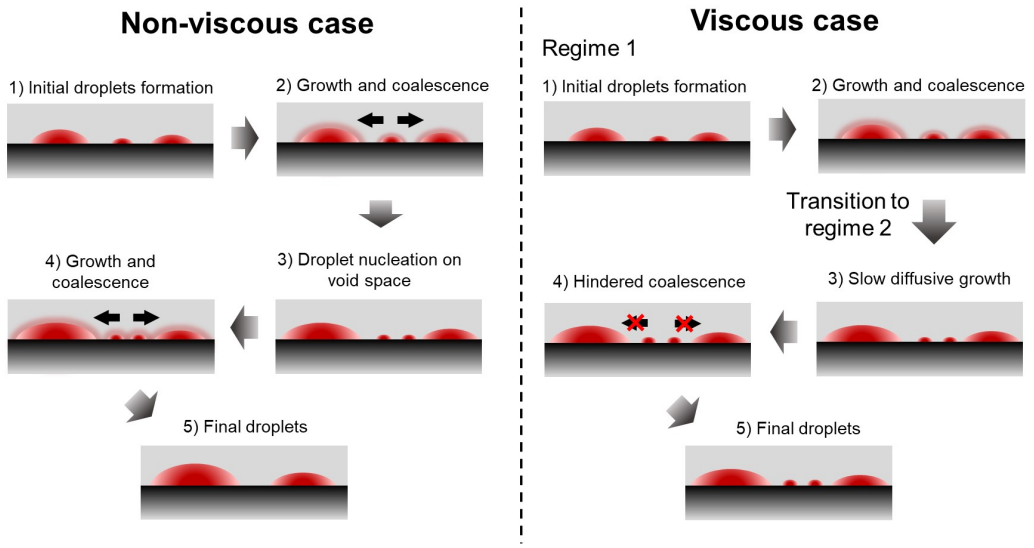

Figure 6.7: Sketch showing the droplet growth modes in non-viscous case (left) and viscous case (right). The non-viscous case is always in regime 1 where the droplets form, grow and coalesce throughout the entire solvent exchange process. In contrast, when viscosity of Solution B is high, droplet only grows in regime 1 after which growth becomes slow and coalescence is inhibited due to high viscosity.

6.3.5 Enhanced detection of fluorescence by small droplets

In last section, we will demonstrate that the small droplets formed from viscous Solution B may be used for enhanced fluorescence detection. In our experiments water doped with a fluorescence dye (Nile Red) was injected into the chamber after the droplet formation in viscous Solution B. Once in contact with the solution, all droplets extract the dye from the solution. Our measure-

ments show that the fluorescence intensity inside the droplets was significantly higher than the background as shown in Fig. 6.8. Interestingly, the intensity increases faster inside small droplets compared to large droplets (Fig. 6.8c). As the normalized concentration of the dye in the solution is around 80% of the maximal concentration in the bulk flow, the intensity in the small droplets is about $0.7 \sim 0.75$, but only $0.45 \sim 0.55$ in the large droplets.

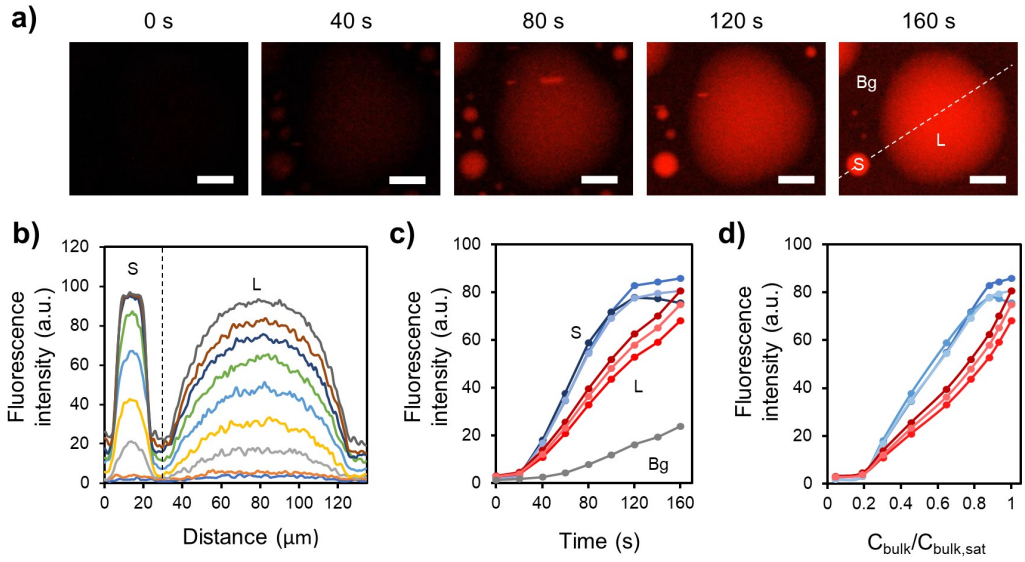

Figure 6.8: Enhancement of fluorescence intensity in small droplets (a) Fluorescence images of two droplets at different times upon exposure to fluorescence dye solution. Scale bar = 25 μm (b) Intensity profile through a straight line across the center of the two droplets as shown the last image of a) at different times. (c) Intensity of three small droplets (blue), three large droplets (red), and the background (grey) at different times. (d) Intensity of small and large droplets for different concentrations of dye in the bulk relative to the saturation concentration in the bulk.

The enhanced fluorescence intensity from small droplets may be due to the difference in the concentration of the dye in the droplets at given extraction time. As the solution of the dye is in contact with droplets, the dye molecules are extracted from water. At given time, the concentration of the extracted dye in the droplets is determined by the partition coefficient, which is the ratio between the concentration of dye in oil to the concentration of dye in water at equilibrium, the surface-to-volume ratio of the droplets, mass transfer co-

efficients and extraction efficiency. [93]. For larger surface-to-volume ratio, the concentration of dye in the droplets is expected to be higher from faster extraction by smaller droplets. Part of the enhancement in the fluorescence intensity may be also attributed to lens effect of droplets. In previous reports, it has been shown that droplets can focus light to enhance the fluorescence intensity and enable more sensitive detection.[97, 248] The smaller droplets in our experiments have higher curvature so they can have stronger focusing effect for the emitted light from the fluorescence molecules. Such enhanced sensitivity from small droplets may find applications in chemical analysis, as fluorescence signal is widely used in sensing and biomedical analysis, for example the product from polymerase chain reaction in identification of nucleic acid sequence.

6.4 Conclusion

We study the effect of the viscosity of surrounding fluid on the droplet formation by solvent exchange. Different from the non-viscous case, the growth of droplets is independent of the flow rate when the viscous solution is fast. We propose a two-regime growth model of droplets to explain the viscosity effect. In the first regime, droplet growth is still influenced by the external flow rate, while in the second regime the droplet growth relies on the diffusion of oil due to high viscosity. The effect from the solution viscosity can be used to mediate final droplet sizes and to obtain distinct bi-model distribution of the droplet size on a homogeneous surface, which may be applied in tuning the size distribution of droplets for various applications. As demonstrated in this work, strong intensity from fluorescence molecules is obtained from stable small droplets due to focusing effect.

Chapter 7

Size Distribution of Asphaltene Precipitates Induced by Displacing a Model Oil with a Paraffinic Solvent

Abstract

Solvent exchange is a controlled method to study the dilution-induced phase separation process by displacing a mixture of good solvent, poor solvent, and solute with a poor solvent. Solute gradually becomes oversaturated during the process and nucleates to a new phase. This work utilizes the solvent exchange method to reveal the effect of the mixing dynamics on the asphaltene precipitation process under 20 different conditions using the same chemical. The external mixing between the asphaltene solution and paraffinic solvent is highly controlled. We used an optical microscope and total internal reflection fluorescence microscope to detect asphaltene particles, and the resolution reached $\sim 200\ nm$. A finite element method with a coupled multi-physics approach is used to simulate the evolution of oversaturation pulse in the solvent exchange process. Based on the simulation results, we predicted the effect of the flow rate, dimension and orientation of the microfluidic chamber and temperature on the surface coverage and size distribution of asphaltene particles. The experimental results of all factors agree with the predictions obtained based on the simulation. Local concentration and shear forces are the two main reasons for the change of asphaltene precipitation caused by mixing dynamics. However, the influence of thermodynamics is more critical than the mixing dynamics with temperature changes. Through a combination of experiment and simulation, this work illuminates the significance of the transportation process for the final morphology of asphaltene particles. This study provides new insight into the mechanism of mixing dynamics on asphaltene precipita-

tion. A smart mixing may be applied to paraffinic froth treatment (PFT) to boost new phase formation without excessive solvent consumption.

7.1 Introduction

Asphaltene is a complex mixture containing polycyclic aromatic hydrocarbons [183] and is defined by solubility class that is soluble in aromatic solvents such as benzene and toluene and insoluble in n-alkanes solvents such as n-pentane and n-heptane [75]. The largest component of crude oil is asphaltene, which has an exceptionally high molecular weight. It is well known that oil-water separation in the oil industry plays important challenges. The presence of asphaltene hinders the coalescence of oil-water emulsions [122, 124], causing operational cost and production challenges by forming flocculation and deposits in the reservoirs and transportation pipes. Undesirable asphaltene precipitation in the transportation pipes can cause severe problems such as clogging and blocking [102, 265]. On the other hand, dilution-induced asphaltene precipitation has been utilized in paraffinic froth treatment (PFT) units to remove impurities in bitumen such as water and solids by adding paraffinic solvent into bitumen [168]. The precipitated asphaltene can be used as raw materials to make value-added products, such as absorbent [9, 160, 206]. Therefore, it is of importance to understand and control asphaltene precipitation.

Asphaltene is considered to form nanoscale-sized nano-aggregates and clusters and stabilized in crude oil or aromatic solvents [65, 139, 142, 235]. Asphaltene dispersed in toluene is more stable due to the interaction balance of van der Waals attraction, and steric repulsion originated from side alkane chains. Adding n-alkanes such as paraffinic solvents leads to the collapse of the side alkane chain layer and a decrease in steric repulsion. Consequently, asphaltene nano-aggregates grow to a larger size and manifest as a new phase [217, 218]. The effective parameters that may affect asphaltene precipitation include temperature [159], pressure [4], addition of inhibitors [6], solvent to bitumen (S/B) ratio [88, 175], and type of the solvent [5].

Recently, the effect of the hydrodynamic aspect on asphaltene precipitation has attracted the attention of researchers to understand aggregate formation. In a conventional bulk system, crude oil and paraffinic solvents are added into a container and mixed by a mixer. As a result, the shear force caused

by the agitation enhances the growth rate of asphaltene particles, but the size of asphaltene particles plateaued at a smaller size [166]. Nevertheless, the mixture of crude oil and different combinations of paraffinic solvents in a microcapillary is injected into a microcapillary together. The increase of the flow rate helps to reduce asphaltene deposition on the surface to minimize the possibility of blocking problems [34]. Still, the deposition rate of asphaltene is enhanced [8, 33]. Therefore, the increased flow rate may also lead to the formation of larger particles [114].

The influence of hydrodynamics on asphaltene precipitation is mainly from two aspects. Firstly, due to the effect of shear force on asphaltene aggregation and fragmentation [65, 144, 165, 169]. Secondly, due to the heterogeneity of local concentration at the initial stage (early stage) of asphaltene precipitation [37, 59, 135, 187]. Indeed, extensive studies have been carried out to predict the deposition. However, there are knowledge gaps in the dynamics of dilution-induced asphaltene precipitation at the early stage. Importantly, the effects of local concentration and convection on asphaltene precipitation are challenging due to the poor mixing control. Another side, the sampling procedures make it impossible to control convection. The results obtained from the direct visualization of asphaltene particles at a submicron scale may not be sufficient to investigate early-stage asphaltene precipitation due to the limited resolution of conventional optical microscopes. Recently, microfluidic devices have been applied in the study of asphaltene precipitation due to less demand for solvent and high reproducibility of results [138, 148]. In a quasi-2D microfluidic chamber, the mixing is mainly dominated by diffusion. The characteristics of the precipitates reveal the local concentration influence at the early stage of asphaltene precipitation [129, 131, 132].

Solvent exchange, also called solvent shifting or solvent displacement has shown promise in a quantitative understanding of solvent-induced phase separation. Our earlier works on dynamics of phase separation under controlled mixing, including nanobubble and nanodroplet formation [130, 158], oiling out crystallization [50, 256], and polymer nanoprecipitation [250] revealed fundamental insights using solvent exchange process. The approach of solvent ex-

change is displacing a suitable solvent with a poor solvent. Consequently, the new phase nucleates and grows at the mixing front of good and poor solvent due to an oversaturation pulse [62]. The solvent exchange process is a well-controlled mixing system, which can be described by the advective diffusion equation [258]. Overall, the diffusive and convective mixing in the system is controllable by varying the dimension of the microfluidic chamber and the injection rate of the solvents. To our knowledge, such fundamental studies on asphaltene precipitation are not yet reported in the open literature. Strictly speaking, the orientation and channel height of the chamber, the flow rate of the mixing, and the operating temperature can change the final morphology of asphaltene precipitates in terms of SC and size distribution at submicron and micron scales.

This research aims to understand the solvent-induced asphaltene precipitation under controlled convective mixing. The microchannel flow rate, dimension and orientation enable the control of local solvent concentration and local shear force in the experiments. Systematic numerical investigations based on the finite element method (FEM) using COMSOL Multiphysics for different geometric and flow conditions are performed to visualize the oversaturation pulse in the solvent exchange process. Through numerical results, we identified the generation of convective rolls when the channel height is more significant than a specific value under gravity and buoyancy force. Furthermore, the total internal reflection fluorescence microscope (TIRF) and optical microscope are used to resolve the asphaltene particles at submicron and micron scales. In this work, the surface coverage (SC) is characterized to represent the asphaltene yield approximately. The size distribution at submicron and micron scales is specified to investigate the aggregation of asphaltene particles. The findings of this work provides new insights into the influence of mixing condition on asphaltene precipitation. The implication is that the optimized flow condition may mediate the asphaltene precipitation without leveraging solvents. This work is not only applicable to asphaltene precipitation but also has implications for other dilution-induced phase separation processes.

7.2 Experimental

7.2.1 Chemical and substrate preparation

Murphy Oil (USA) provided the C5-asphaltene (i.e., n-pentane precipitated asphaltene) used in this project. The analysis of elementary analysis and the pre-treated method of the asphaltene sample can be found in our previous research [129]. In brief, raw asphaltene sample was dissolved in toluene (Fisher Scientific, ACS grade, 99.9 %+) to remove any inorganic solvents by 0.22 μm polyvinylidene difluoride (PVDF) filter paper. A rotary evaporator was then used to remove toluene from the 'inorganic solid free' asphaltene. 17 g of inorganic solid-free asphaltene sample was then dissolved in toluene to 1 L to obtain the asphaltene in toluene solution (i.e., solution A). n-Heptane (Fisher Chemical, 99%) was used as the solvent (i.e., solution B) for asphaltene precipitation.

A high-precision cover glass (Azer Scientific) was used as the substrate. Before the experiment, the cover glass was sonicated in toluene for 5 minutes and dried by air to remove any contaminates.

7.2.2 Solvent exchange process

The solvent exchange process was performed in a custom-built microchamber. The apparatus is shown in Figure 7.1(a). The micro-channel was 3.5 cm long and 5 mm wide. Glass was used as top and a rubber ring in between the glass and substrate was used to seal the system. The channel height was adjusted by using rubber rings with different thicknesses.

The model oil was first injected into the microchamber using a syringe pump (NE-1,000, Pumpsystems Inc.). Afterwards, n-heptane was injected into the device to displace solution A, creating a mixing front between solution A and solution B as shown in Figure 7.1(b). The asphaltene precipitation began at the moment that the concentration of n-heptane is higher than the onset point in the mixing front. At the moment that solution A had been displaced by solution B, asphaltene precipitation stopped due to lack of dissolved asphaltene. After injecting 2.5 mL solution B (i.e., at least ten times the total

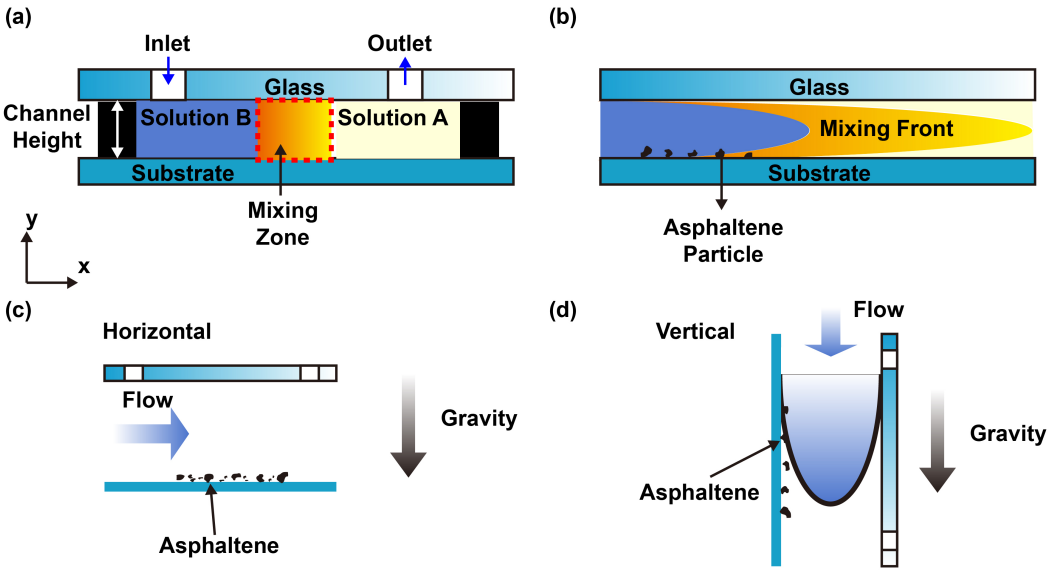

Figure 7.1: (a) Sketch of the microchamber used in this study. (b) Zoomed-in image of the mixing front in a). The x direction is the direction of the flow. The microchamber is placed (c) horizontally, (d) vertically to examine the effect of orientation.

volume of solution A), the asphaltene precipitation was considered finishing and defined as the final state. Air was injected into the chamber to drive away from the remaining liquid. The mean flow velocity of air for liquid removal was kept at a constant value, 5 mm/s, in all of the experimental conditions. After this point, the substrate was ready to be examined by microscopes. The device was placed horizontally (Figure 7.1(c)) and vertically (Figure 7.1(d)) to examine gravitational effect.

7.2.3 Flow rate, channel height, orientation, and temperature

This work investigated the influence of four aspects on asphaltene precipitation, including injection rate of solution B, channel height, orientation of the microfluidic chamber, and temperature. A horizontally placed 1,000 μm device was used to study the influence of flow rate under ambient condition (i.e., 19 - 21°C, 1 atm). The injection rate of solution B varied from 15 mL/h to 150 mL/h. The Reynolds number (Re) and Péclet number (Pe) were calculated from $Re = \frac{Q}{wv}$ and $Pe = \frac{Q}{wD}$, respectively [258]. Table 7.1 listed the channel

height and the corresponding Re and Pe.

Table 7.1: Flow rate and the corresponding Reynolds number and Péclet number

Flow Rate (mL/h)	Reynolds Number	Péclet Number
15	1.37	458
30	2.73	916
60	5.47	1,832
90	8.20	2,747
120	10.94	3,663
150	13.67	4,579

Seven rubber rings of thicknesses from 90 μm to 1,000 μm were used as spacers to investigate the effects of channel height. The microfluidic chamber was placed horizontally at ambient conditions. The buoyancy and gravity effects of different channel heights can be estimated by a dimensionless number, Rayleigh number (Ra), as shown in Equation (2.23) [258]. Table 7.2 showed the corresponding Rayleigh number of each channel height. The injection rate of solution B was kept at 30 mL/h.

$$Ra = \frac{\Delta\rho g(h/2)^3}{\mu D} \tag{7.1}$$

where $\Delta\rho$ is the density difference between solution A and solution B. g is the gravitational constant. h is the channel height, μ is the viscosity of solution B, and D is the diffusion coefficient.

Table 7.2: Channel height and the corresponding Rayleigh number in the experiments

Channel Height (μm)	Rayleigh Number
90	219
180	1,753
260	5,283
340	11,814
430	23,899
510	39,873

To study the influence of chamber orientation, the device filled with so-

lution A was placed horizontal and vertically (Figure 7.1(c)-(e)). Solution B was then injected at 30 mL/h.

Four elevated temperature at 35 °C, 50 °C, 58 °C, and 65 °C were compared with the results of the ambient temperature. All the solutions were immersed in the water bath for 30 min before the experiments to reach thermal equilibrium. The entire solvent exchange system, including the horizontally placed microchamber and pipes, were immersed into the water bath to keep the temperature constant during the experiments. The channel height was kept 1,000 μm and the injection rate of solution B was 90 mL/h at the elevated temperatures.

7.2.4 Observation and characterization of the asphaltene sample

Total internal reflection fluorescence (TIRF) mode of a confocal microscope (Leica TCS SP8) was used to capture high-resolution images. A 488-nm laser was used to excite the fluorophores of asphaltene. The spatial resolution was $\sim$ 200 nm to show the details of asphaltene particles at the submicron scale. An optical microscope (Nikon ECLIPSE Ni) equipped with Nikon DS-FI3 camera was used to detect asphaltene particles at the micron scale. MATLAB (The MathWorks, Inc., US) and ImageJ (open source software) were used to analyze the images. The details of the process for image analysis can be found in our previous work [129, 131]. In brief, the main steps were to transform the microscopy images into binary images and then obtain the information of particles such as perimeter and area. The particle size distribution smaller than one micron was obtained from the TIRF images, while the surface coverage and particle size distribution larger than one micron were obtained from the optical microscope images.

7.2.5 COMSOL model description

Transport of diluted species

The transport of diluted species models solved the chemical species transport through diffusion and convection. This method solved the mass conservation

equation for oversaturation pulse. The following governing equations were solved based on the finite element method. Mass balance equation is:

$$\frac{\partial C_i}{\partial t} + \nabla . J_i + \vec{U} . \nabla C_i = 0 \tag{7.2}$$

where, C_i, D_i, $\vec{U}$, J_i are the concentration of species, diffusion coefficient, mass average velocity vector, and mass diffusive flux vector. The mass flux J_i defined as $J_i = -D_i \nabla Ci$.

Level-set model

A conservative Level-Set method [202] was coupled with the transport of diluted species model to visualize the influence from gravity. In addition to the transport of diluted species model governing equations, the numerical solver solved the following governing equation for the phases. The governing equations consisted of continuity, incompressible Navier-Stokes equation, and coupled with the Level-Set equation. Equation of continuity is:

$$\nabla . \vec{U} = 0 \tag{7.3}$$

Equation of motion is:

$$\rho \frac{\partial (\vec{U})}{\partial t} + \rho \nabla . (\vec{U}\vec{U}) = -\nabla P + \nabla . \mu (\nabla \vec{U} + \nabla \vec{U}^T) + \rho g + \vec{F}_{SF} \tag{7.4}$$

where $\vec{U}$, ρ, μ, P, and $\vec{F}_{SF}$ are velocity, density, dynamic viscosity of fluid, pressure, and interfacial tension force, respectively.

Equation of Level-Set (LS) Function is:

$$\frac{\partial \phi}{\partial t} + \vec{U} . \nabla \phi = 0 \tag{7.5}$$

where $\vec{U}$ and ϕ are the velocity and LS function, respectively. The Level-Set function acted as signed distance from the curvature between positive and negative magnitudes of d. Where $d = d(\vec{r})$ is the shortest distance of a point $\vec{r}$ from interface at time t and zero value is assigned at the interface [203]. In the LS method, fluid 1 domain represented the interface where $\phi < 0.5$, and fluid 2 corresponded to the region where $\phi > 0.5$. The Level-Set function was used

to smooth the fluid properties across the interface and physical properties of fluids were calculated based on the volume average as a function of Level-Set variable.

Computational parameters and implementation

Systematic numerical investigations were performed to understand the mixing condition during solvent exchange process inside the microchannel. Two-dimensional transient numerical simulations were performed using the finite element method based solver COMSOL Multiphysics V. 6.0. (COMSOL AB, Stockholm, Sweden). Different microchannel geometries (i.e., height, see Table 7.2) and at various flow rates [52] were studied. Unsteady state diffusion equation coupled with the velocity field were solved to obtain the evolution of the mixing front with space and time [240]. The velocity inlet boundary condition was applied to the inlet, and the pressure outlet boundary condition was used at the microchannel outlet as shown in Figure 7.2(a). The no-slip boundary condition was imposed for the top and bottom wall and inflow with zero concentration at the inlet and outflow. Initially, at time t=0, the oversaturation pulse in a narrow region (i.e., 100 μm thick) was initialized vertically along the inlet with a uniform concentration of solution B. The oversaturation pulse was convected and diffused simultaneously inside the microchannel when the flow started from the channel. The computational domain meshed with quadrilateral mesh elements, and the grid independence study was initially performed using different mesh element sizes ranging from 0.10 to 0.0125 mm as shown in Figure 7.2(b). The velocity profiles were compared for different mesh as shown in Figure F.4, and optimum mesh element size was considered for the numerical investigations. Mesh quality and number of elements details were reported in Table F.1. Different set of simulations were performed for the same flow conditions (Pe, Ra, Re, h, and Q) as used for the experimental section. All the simulations were performed in high performance computing (HPC) facility. For each simulation 48 CPUS used to run the 30 s flow time.

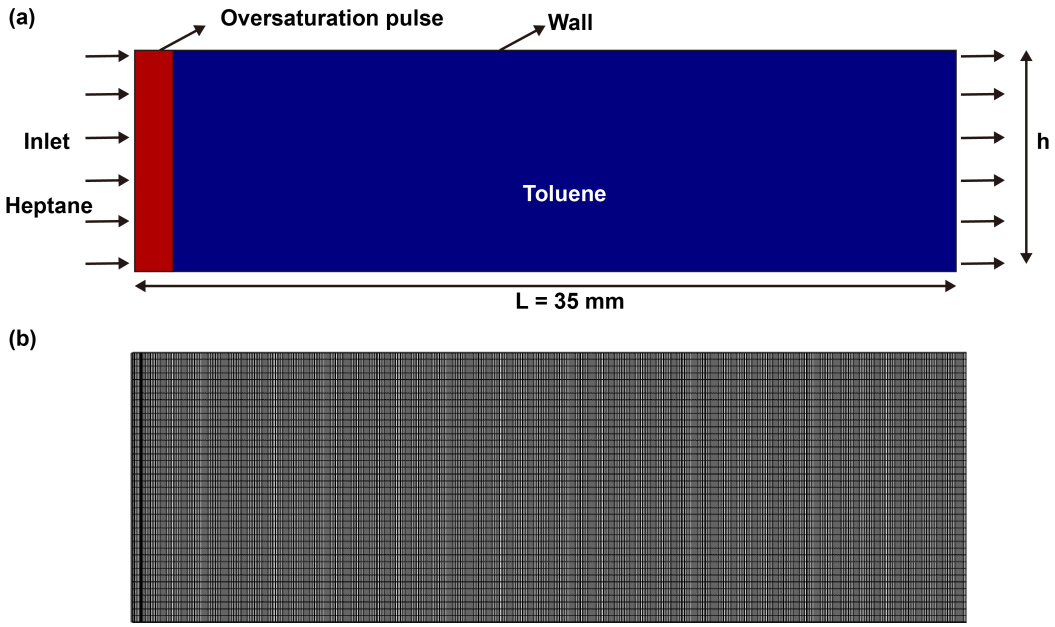

Figure 7.2: (a) 2D schematic representation computational domain with dimension and imposed boundary condition and (b) computational gird.

7.3 Results and discussion

In the solvent exchange process, solution B gradually displaces solution A. Simultaneously, asphaltene diffuses from solution A towards solution B, and n-heptane diffuses from solution B towards solution A. The S/B ratio of the mixture is gradually higher than the onset, at which point the asphaltene is 'oversaturated'. For a specific position on the substrate, the asphaltene is not oversaturated initially in toluene. Then, the oversaturation pulse arrives and triggers asphaltene precipitation. Asphaltene solution is entirely displaced by n-heptane, and asphaltene is not oversaturated, leading to precipitation stops due to lack of dissolved asphaltene. The duration of the oversaturation pulse is independent of the flow velocity due to the no-slip boundary and depends on the diffusion of chemicals from the mixing front to the substrate [258]. Therefore, the new phase formation on the substrate is determined by the profile of the mixing front.

We first describe the mixing dynamics based on the COMSOL simulation in the following sections. All of the results were in line with our experimental data.

7.3.1 Effect of the flow rate

COMSOL simulation results show the profile of the oversaturation pulse (Figure 7.3) at different flow rates in the same chamber. The non-blue area is the mixing front, and the color scale bar indicates the corresponding chemical composition of the system. At Pe of 458, the oversaturation pulse passes through the entire chamber in 16 s. At the highest Pe of 4,578, the duration of the pulse is approximately 2.7 s. Although the time for the precipitation is considerably shorter at larger Pe, the oversaturation levels near the bottom wall are similar through the entire process at all Pe, as exhibited by the consisting blue zone on the bottom in all snapshots. Therefore, diffusion of asphaltene and n-heptane towards the substrate at different Pe should be comparable because the concentration gradient is identical, resulting in a similar SC of asphaltene on the bottom wall. At any given moment, the level of the oversaturation on the top plate is substantially higher at lower Pe, which may lead to more precipitates on the top surface.

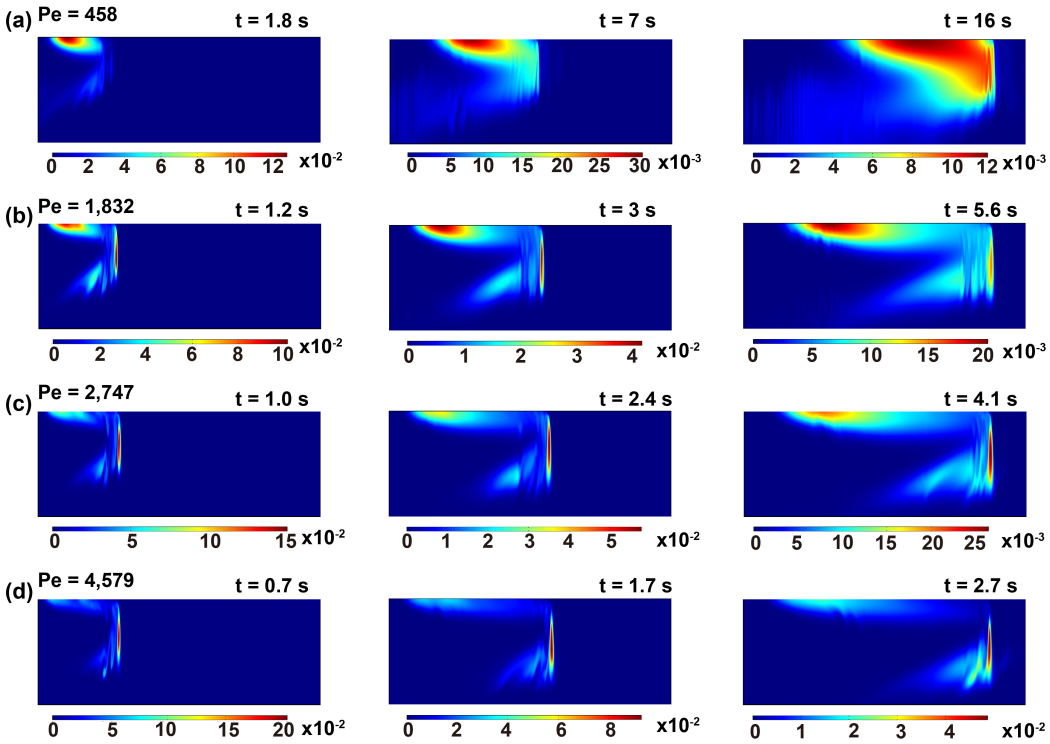

Figure 7.3: COMSOL simulation for the profile of the oversaturation pulse at (a) Pe = 458, (b) Pe = 1,832, (c) Pe = 2,747, and (d) Pe = 4,579.

Figure 7.4(a) shows the optical images of asphaltene precipitation in the solvent exchange with injection rate of solution B from 15 mL/h to 150 mL/h (i.e., Pe from 458 to 4,579). The black dots are asphaltene particles on the substrate placed on the bottom wall. It is worth mentioning that only the area with particles is considered. The areas of asphaltene layers, as shown in Figure F.1(b), are omitted when analyzing surface coverage (SC) and the size distribution of asphaltene particles because these large deposits may be settlements from the bulk. Figure 7.4(b) shows SC of the asphaltene particles divided by the total area, which is approximately independent of Pe and is always $\sim$ 14%, which is in line with what we would expect from the COMSOL simulation in Figure 7.3 because of the similar asphaltene mass transfer processes.

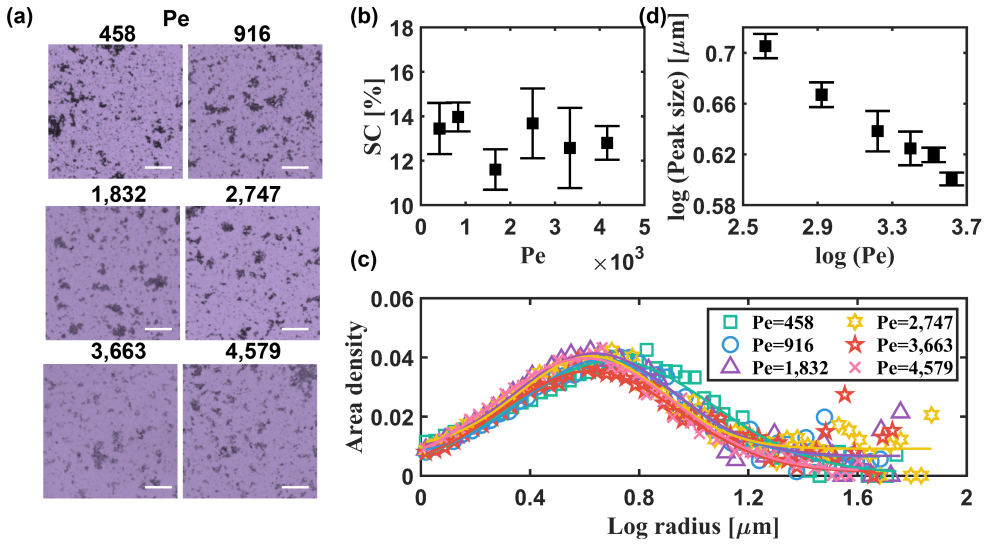

Figure 7.4: (a) Optical images of asphaltene at the final state of different Péclet numbers. The length of the scale bar is 20 μm. The images are false-colored. (b) SC of asphaltene at the final state as a function of Péclet number. (c) Size distribution of asphaltene particles for different flow rates. The solid lines are the Gaussian fitting for the results. (d) The peak size of (c) vs. Péclet number.

Figure 7.4(c) shows the size distribution of asphaltene particles. The distribution is plotted based on area density instead of the number density [127] to compare with the conventional study in a bulk system. Interestingly, the Gaussian distribution can fit the area density-based size distribution for each

Pe. This Gaussian distribution is consistent with the presented results in a conventional mixing system [127]. The peaks of the size distribution in Figure 7.4(c) shift to the left with the increase of Pe, indicating the size of asphaltene particles decreases with the increase of Pe (Figure 7.4(d)).

Figure 7.5(a) is the TIRF images of asphaltene particles at different Pe. The white speckles are the asphaltene particles due to the natural fluorescence property of asphaltene under 488 nm laser excitation in air. Number density-based relative frequency is introduced to analyze the size distribution quantitatively. The relative frequency of each size bin is calculated by the number of particles of the corresponding size divided by the total number of particles. For primary submicron particles (PSMPs), which are defined as the radius from 200 to 400 nm [129], the relative frequency denotes the aggregation degree of the early stage. A high relative frequency of PSMPs (R_p) represents the low possibility of PSMPs aggregating into larger particles after the precipitation. From the quantitative examination, as shown in Figure 7.5(b), R_p decreases with the increase of Pe.

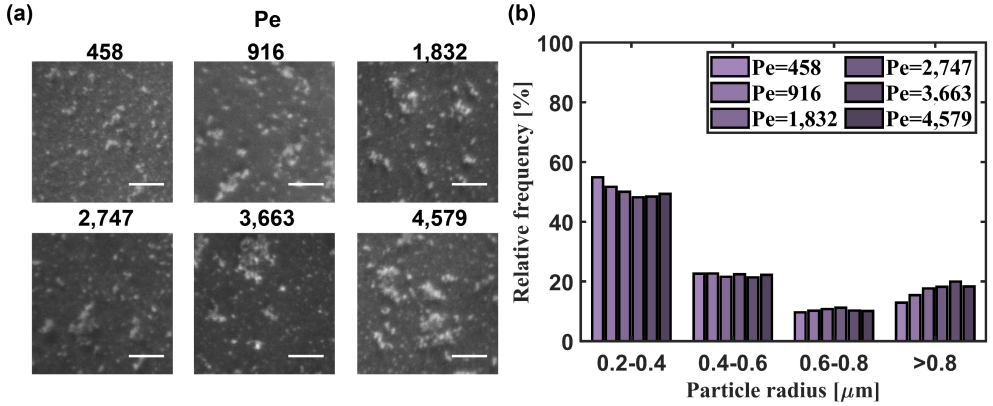

Figure 7.5: (a) TIRF images of asphaltene at the final state of different Péclet numbers. The length of the scale bar is 5 μm. (b) Relative frequency of size distribution of asphaltene particles at different flow rates.

Interestingly, the size of asphaltene particles correlates with the flow rate because of the mass transfer process of asphaltene from the oversaturation pulse to the substrate. The size decreases with Pe at micron-scale (Figure 7.4(c)) but increases at submicron scale (Figure 7.5(b)). The particle aggre-

gation and fragmentation process are discussed to examine the reasons for the opposite trend of size distribution at submicron and micron scales. Based on the Smoluchowshi aggregation model, the aggregation is:

$$\frac{dn_k}{dt} = \frac{1}{2}\sum_{i+j=k} K_{i,j} n_i n_j - n_k \sum_{i\geq 1} K_{i,k} n_i \tag{7.6}$$

where n_i, n_j, and n_k is the quantity change of particle of size i, j, and k, respectively. t is time, and $K_{i,j}$ is aggregation kernel, which is calculated by $K_{i,j} = \alpha_{i,j}\beta_{i,j}$, where $\alpha_{i,j}$ is the collision frequency and $\beta_{i,j}$ is the collision efficiency of particles. $\beta_{i,j}$ is:

$$\beta_{i,j} \propto exp[-\frac{1}{k_B T(\delta_{asp} - \delta_{sol})^2}] \tag{7.7}$$

where k_B is Boltzmann constant, δ_{asp} and δ_{sol} are Hildebrand solubility parameters of asphaltene and the paraffinic solvent, respectively. $\alpha_{i,j}$ is driven by two factors in our system, including Brownian motion and shear force [143, 166, 195, 207]:

$$\alpha_{i,j} = \frac{2}{3}\frac{RT}{\mu}\frac{(d_i + d_j)^2}{d_i.d_j} + \frac{G}{6}(d_i + d_j)^3 \tag{7.8}$$

where R is the ideal gas constant. T is temperature. μ is viscosity. d_i, and d_j are the diameters of particles with sizes i and j, respectively, G is the shear rate, defined as the velocity gradient.

The oversaturation level near the bottom wall is similar at all Pe (Figure 7.3). Regardless, the velocity gradient between the maximum point of the flow and the minimum point adjacent to the substrate increases with Pe. The increased shear force leads to the increase of aggregation of PSMPs at an early stage (Equation (7.8)), ultimately resulting in a lowering in R_p (Figure 7.5(b)).

However, shear force brings an increase in the aggregation and the fragmentation of aggregates. The mechanism of fragmentation induced by shear rate is the different pressures on the opposite sides of the aggregates [153]. The fragmentation rate (B_i) increases with the particle volume (V_i) and the shear rate ($B_i = kG^y V_i^{1/3}$), where k is a proportional fitting constant, y is a constant inversely proportional to the interaction strength between particles

[32, 98, 149, 166]. Therefore, when the asphaltene particles are large enough (i.e., at the micron scale), the fragmentation yielded by shear force is more important than the aggregation, resulting in the decrease of particle size with the increase of shear rate (Figure 7.4(d)).

7.3.2 Effect of the channel height

A dimensionless number (Rayleigh number, Ra) is used to quantitatively analyze the impact of channel height on SC (Table 7.2). The oversaturation levels near the bottom wall are always high, as exhibited by the red color in Figure 7.6. At Ra of 219, the oversaturation pulse passes through the chamber in 2.1 s. At the highest Ra of 39,873, the duration of the pulse is approximately 9.3 s. The increased duration of the oversaturation pulse provides a longer time for asphaltene precipitation and aggregation. Therefore, mass transfer of asphaltene from the oversaturation pulse to the substrate should increase with the increase of the Ra, resulting in a higher SC and larger size of asphaltene particles.

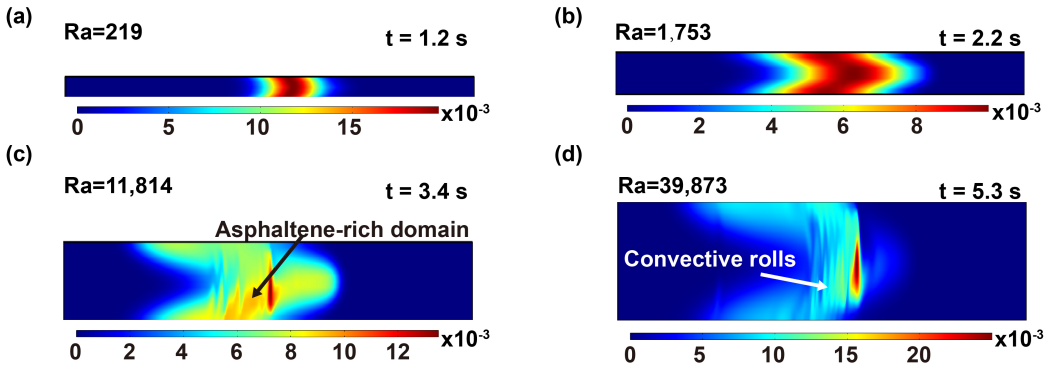

Figure 7.6: COMSOL simulation for the profile of the oversaturation pulse at (a) Ra = 219, (b) Ra = 1,753, (c) Ra = 11,814, and (d) Ra = 39,873.

Figure 7.7(a) shows the optical microscope images of asphaltene precipitates in channel heights from 90 μm to 510 μm under the same Pe. It is found that more asphaltene particles are formed with the increase of the channel height. Meanwhile, the size of asphaltene particles increases with the increase of the channel height. SC increases with Ra (Figure 7.7(b)). The relationship is almost linear. However, the linear relationship is not held when the

channel height is 1,000 μm as shown in Figure F.1(a). At 1000 μm, many asphaltene deposits do not exist as particles but form a layer of sediments, as shown in Figure F.1(b). The formation of a larger SC and a layer of sediments of asphaltene are compatible with the expectation based on COMSOL simulations.

Figure 7.7(c) shows the size distribution of asphaltene particles as a function of Ra. The size distribution for each Ra can be fitted by Gaussian distribution. The Gaussian curve peaks increased from ~ 0.2 to ~ 0.9 with Ra from 219 to 39,873. It indicates that the majority particle radius increases from 1.6 μm to 7.9 μm (Figure 7.7(d)). Particle size increases with Ra because better solution mixing leads to an increase in particle collision efficiency β in Equation (7.7), resulting in particles growing larger. Therefore, the observations are consistent with our predictions based on COMSOL simulations.

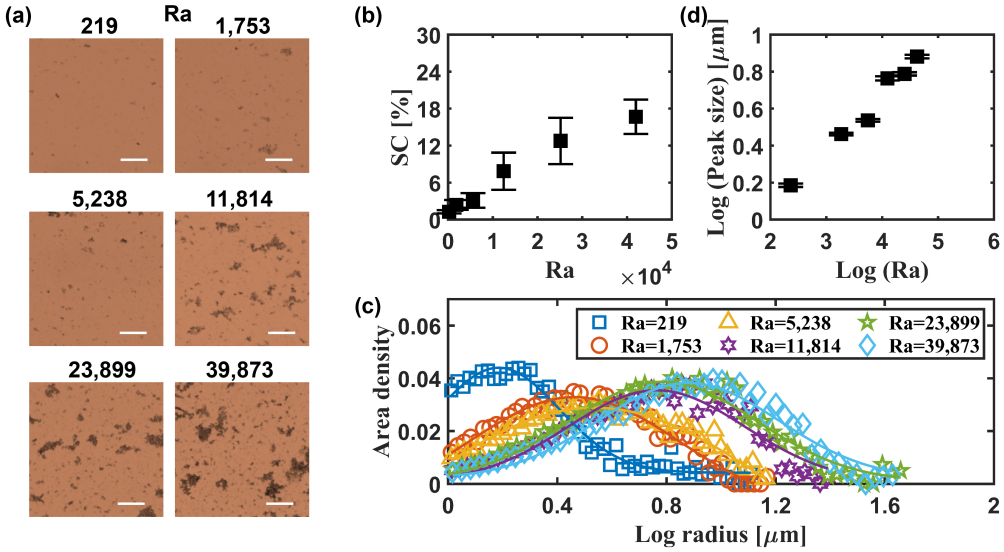

Figure 7.7: (a) Optical images of asphaltene at the final state of different channel heights. The length of the scale bar is 20 μm. The images are false-colored. (b) SC of asphaltene at the final state as a function of Rayleigh number. (c) Size distribution of asphaltene particles for different channel heights. The scatters are the experimental data and the solid lines are the Gaussian fitting for the results. (d) The corresponding peak size of Gaussian fitting of (c) vs. channel height.

COMSOL simulations for the vertically placed devices also show that the duration of the oversaturation pulse increases with the increase of the channel

height, as shown in Figure 7.8(d), which is consistent with the horizontally placed devices. Therefore, the SC increases with the channel height and the size distribution shifts to the right with the increase of channel height (Figure 7.8(a)(b)(c)).

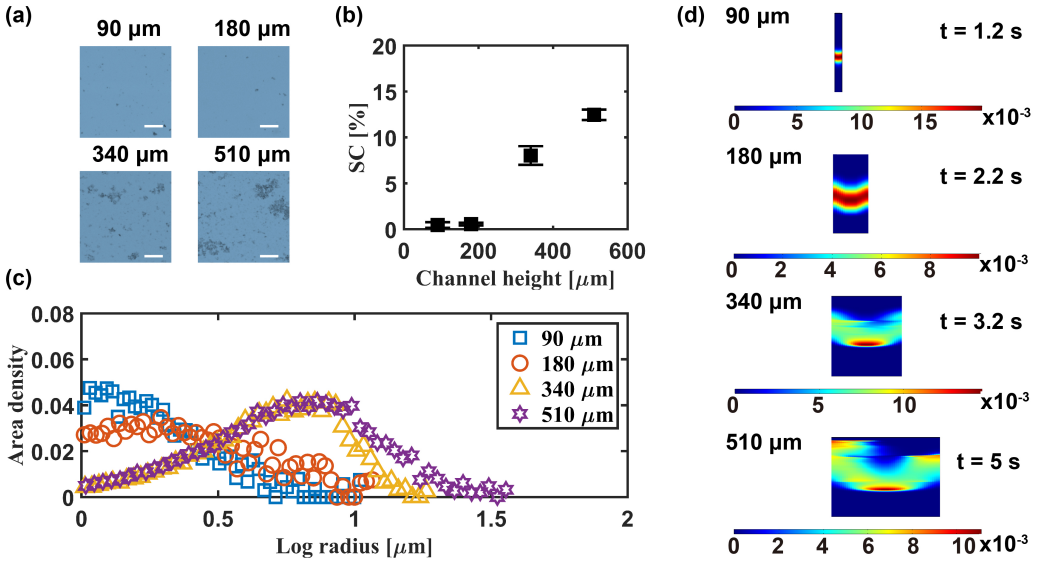

Figure 7.8: (a) Optical images of asphaltene at the final state of different channel heights. The length of the scale bar is 20 μm. The images are false-colored. (b) Surface coverage of asphaltene at the final state as a function of channel heights. (c) Size distribution of asphaltene particles for different temperatures. The solid lines are the Gaussian fitting for the results. (d) COMSOL simulation for the profile of the oversaturation pulse at different channel heights.

TIRF images of the final state are captured to show the details of asphaltene particles at the submicron scale, as shown in Figure 7.9(a). As shown in Figure 7.9(b), R_p decreases from $\sim 65\%$ to $\sim 52\%$ with the increase of Ra from 219 to 39,873, reflecting the aggregation of particles is more intensified in the channel with a more significant height. Correspondingly, the proportion of large particles, especially those larger than 0.8 μm, increases with the increase of the channel height. The observation at the submicron scale is consistent with that of the micron scale.

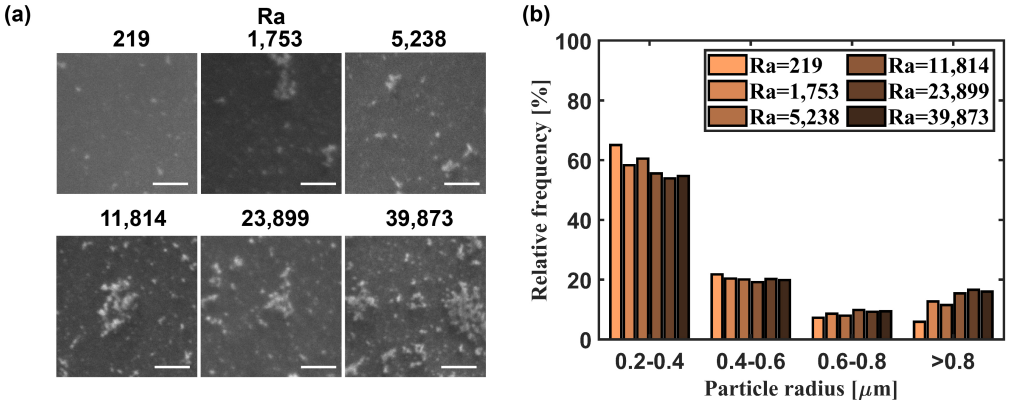

Figure 7.9: (a) TIRF images of asphaltene at the final state of different channel heights. The length of the scale bar is 5 μm. (b) Relative frequency of the size distribution of asphaltene particles of different channel height.

7.3.3 Effect of the chamber orientation

In the device with the same channel height, the oversaturation pulse takes the same time to pass through the channel in both horizontal and vertical devices. However, the details are different. When the channel height is 510 μm (Ra is 39,873 for the horizontally placed device), COMSOL simulation shows that the formation of convective rolls (Figure 7.6(d)) in the horizontally placed device, leading to better mixing between solutions A and B. The final maximum oversaturation level for the horizontally placed device is approximately 0.02, while the one for the vertically placed device is approximately 0.01. In addition, the oversaturation area is not in the middle but shifts downwards and thus closer to the bottom wall because the asphaltene is heavier compared with n-heptane and toluene, an asphaltene-rich domain forms at the tail of the profile of the oversaturation pulse (Figure 7.6(c)). However, the asphaltene-rich domain does not appear in the vertically placed cases. The loss of convective rolls and asphaltene-rich domain in the vertically placed devices results in reduced mass transfer compared to horizontally placed devices. Therefore, diffusion of asphaltene and n-heptane towards the substrate of the vertically placed device should be smaller than the horizontally placed device, resulting in the decrease of SC and left-shift of the particle size distribution.

Figure F.3(a) shows the comparison of optical images of asphaltene pre-

cipitates between horizontally and vertically placed devices. The horizontally placed device has a higher SC of asphaltene particles than the vertically placed device, especially for 510 μm (Figure F.3(b)). SC increases from $\sim$ 12% to $\sim$ 18%, revealing more asphaltene deposits on the substrate, consistent with our expectation from the COMSOL simulation.

The simulation of 1,000 μm group displays stack-like extreme convective rolls and very large asphaltene-rich region (Figure F.2). Therefore, the SC may increase sharply when the channel height is 1,000. The formation of the layer of sediments in the 1,000 channel height group proves our prediction F.1(b).

Orientation direction can also affect the size distribution of the asphaltene particles deposited on the substrate. Figure F.3(d)-(f) reveals the rightwards shift of particle size in the horizontally placed device, meaning the asphaltene particles are relatively large in horizontally placed devices compared with the vertically placed ones. However, the shift of size distribution is not observed in the 90 μm microchamber (Figure F.3(c)). This is due to Ra is smaller than the critical value when the channel height is 90 μm. The convective rolls and asphaltene-rich domain are not observed in the horizontally placed device.

In the solvent exchange process, particles may form on the substrate and in the bulk of the liquid simultaneously. The particles formed in bulk may settle down onto the substrate under gravity in the horizontally placed device. This is mainly due to the competition between gravity and Brownian motion. Brownian motion of the particles ($\overline{X}_{Brownian}$) is [10]:

$$\overline{X}^2_{Brownian} = \frac{4RTK_m t}{3\pi^2 \mu N D} \tag{7.9}$$

where R is the ideal gas constant, T is temperature, K_m is the correction for discontinuity of fluid, which is 1 for liquid. t is time, which is calculated by dividing the volume of the microchamber by the flow rate, μ is the viscosity of the solvent, N is Avogadro constant, D is the diameter of particles. The Stokes settling motion of a particle is [10]:

$$\overline{X}_{Settling} = \frac{(\rho_{asp} - \rho_{sol})gD^2t}{18\mu} \tag{7.10}$$

where ρ_{asp} is the density of asphaltene and ρ_{sol} is the density of the solvent. For each channel height, only the particles with a diameter larger than 8 μm (logarithm radius is 0.6) can settle under gravity. However, the rightwards shift is observed of particles smaller than 8 μm in Figure F.3(d). In addition, particles larger than 8 μm in Figure F.3(c) of 90 μm device do not show a rightwards shift. Therefore, gravity-induced settlement is not the reason for the rightwards shift in horizontally placed devices. The increase of particle size is also due to the enhancement of solution mixing in the horizontally placed device.

7.3.4 Effect of temperature on asphaltene precipitation

The density difference between solutions A and B changes minor with the change in temperature (Table F.2). The duration for the oversaturation pulse to pass the entire channel is approximately 4 s at all of the examined temperatures. Figure 7.10 shows the profile of the oversaturation pulse near the bottom wall does not change much with the increase in temperature, as indicated by the consistent blue zone. In addition, the experiment is processed in the 1,000 μm chamber, there should be sufficient mixing in all of the temperatures due to the convective rolls shown in Figure F.2. Therefore, mixing at all the temperatures we studied should be adequate.

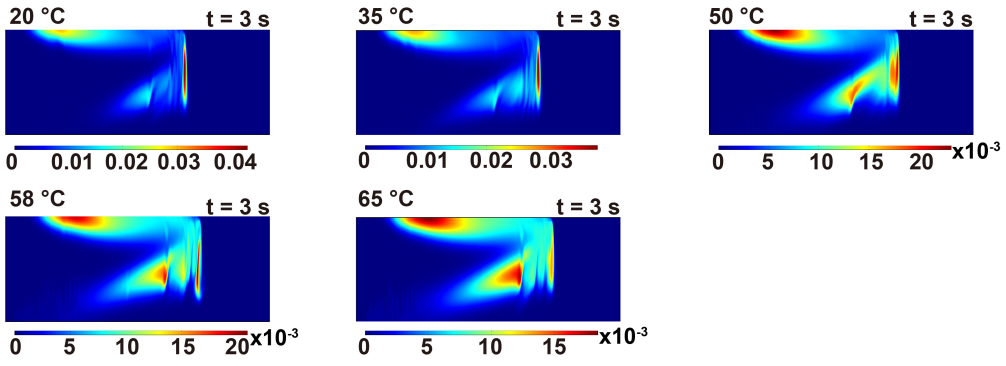

Figure 7.10: COMSOL simulation results of the oversaturation profile at 20 $°C$, 35 $°C$, 50 $°C$, 58 $°C$, and 65 $°C$.

Figure 7.11(a) shows the optical image of asphaltene particles at different temperatures. In general, SC exhibits a decreasing trend, and the size shows a rightwards shift trend with the increase of temperature (Figure 7.11(b)-(d)). The experiment results are mainly due to the thermodynamics influence. Asphaltene is a mixture of different fractions, and the increase in temperature resulted in some asphaltene fractions becoming soluble in asphaltene. These asphaltene fractions do not precipitate, resulting in a decrease of SC. This observation is consistent with the previous study in a conventional bulk system [232].

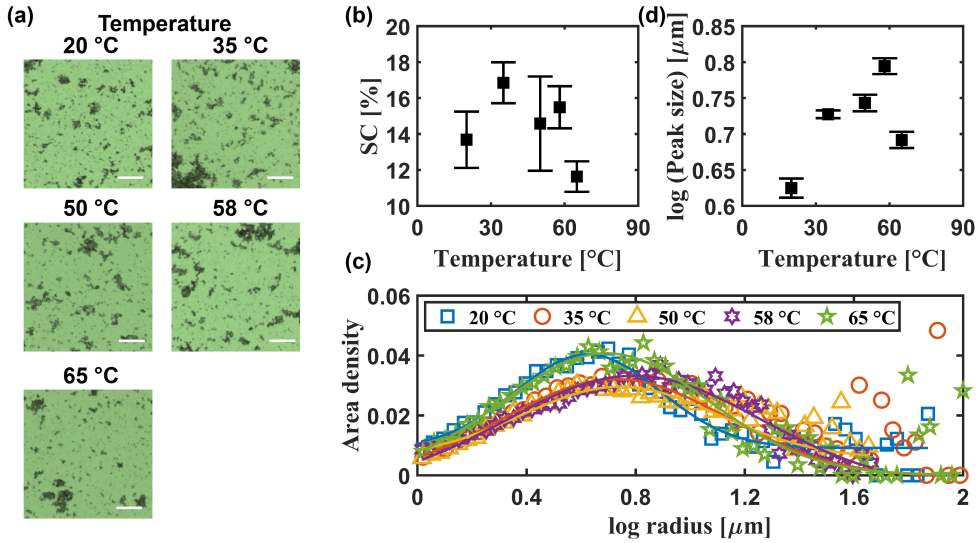

Figure 7.11: (a) Optical images of asphaltene at the final state of different temperatures. The length of the scale bar is 20 μm. The images are false-colored. (b) Surface coverage of asphaltene at the final state as a function of temperature. (c) Size distribution of asphaltene particles for different temperatures. The solid lines are the Gaussian fitting for the results. (d) The peak size of (c) vs. temperature.

Figure 7.12(a) shows the TIRF images of asphaltene particles. The quantitative size distribution at the submicron scale is shown in Figure 7.12(b). In summary, PSMPs are less likely to aggregate into fractal particles with increasing temperature.

Equation (7.7)(7.8) show both the collision frequency and efficiency increase with temperature. Therefore, the overall right-shift trend in micron scale is expected in Figure 7.11(c)(d). However, it is surprising that R_p in-

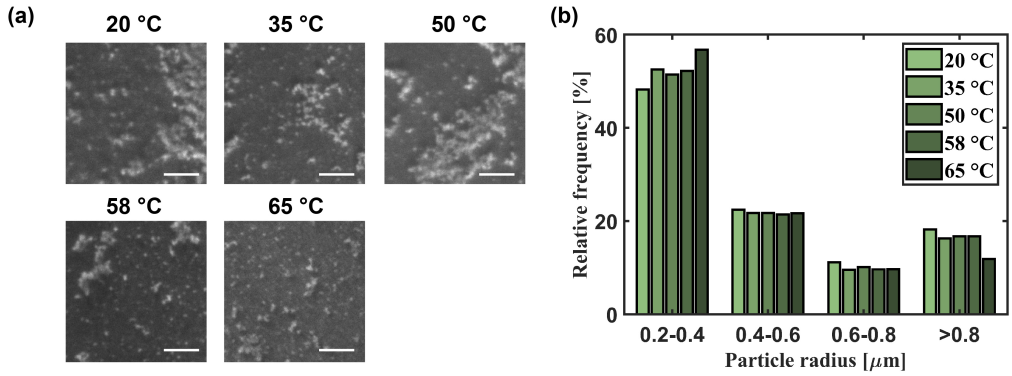

Figure 7.12: (a) TIRF images of asphaltene at the final state of different temperatures. The length of the scale bar is 5 μm. (b) Relative frequency of size distribution of asphaltene particles at different temperatures.

creases apparently from $\sim$ 48% to $\sim$ 58% with the increase of temperature at the submicron scale (Figure 7.12(b)).

Asphaltene is a mixture of several fractions [1]. The response of different fractions to temperature is different [234]. The increase in temperature causes some fractions of asphaltene become more soluble in n-heptane. The Hildebrand solubility parameter difference in Equation (7.7) is lower. The repulsive interaction between this 'soluble-like' fraction of asphaltene particles is high when they form PSMPs, causing a decrease in collision efficiency for further aggregation. In addition, a decrease in SC also leads to less possibility of PSMPs aggregation [132]. As a result, the PSMPs formed by these 'soluble-like' asphaltene do not aggregates but exist as PSMPs on the substrate to cause a higher R_p.

7.4 Conclusions

The solvent exchange method investigated the dilution-induced asphaltene precipitation under controlled external mixing. The profile of the oversaturation pulse of the 20 different mixing conditions in the solvent exchange process was simulated by a finite element method coupled with a multi-physics approach using COMSOL. The asphaltene precipitates were detected by an optical microscope and a total internal reflection fluorescence microscope in

the experiment. Based on COMSOL simulations, we predict the asphaltene precipitation under the condition of changing the flow rate, channel height, orientation, and temperature. The experimental observation results agree well with our expectations. The agreement between experimental surface coverage and the oversaturation level visualized in COMSOL has an important implication: Mixing conditions determine the local oversaturation level that correlates well with the surface coverage of asphaltene.

A combination of the experimental and simulation results demonstrated the significance of mixing dynamics on the morphology of the asphaltene precipitates. We also found that shear force and local concentration are the two main factors leading to the effect of mixing dynamics on the surface coverage and size distribution of asphaltene particles of asphaltene precipitation. This work provides new insights into the significance of mixing dynamics on asphaltene precipitation. It may be worthwhile for the industry to pursue the optimal flow rate, temperature, orientation, and dimension of units to achieve the best mixing without excessive usage of solvents. In future, it will be essential to expand the asphaltene system to more dilution-induced phase separation systems to confirm further the hydrodynamic influence on the nucleation and formation of new phases.

Chapter 8

Conclusions and Future Work

8.1 Conclusions

In summary, the contribution of this work was a deeper understanding of asphaltene precipitation under controlled mixing conditions. In addition to thermodynamics, our study demonstrated the significance of the hydrodynamics in asphaltene precipitation. Under the same precipitant concentration, the surface coverage and size distribution of asphaltene precipitates could be changed by changing the mixing conditions. Our findings may lead to the development of smart mixing in PFT process to induce asphaltene precipitation with reduced paraffinic solvents without additional energy input or major changes to current equipment and facilities.

A method was proposed for in-situ observation of asphaltene precipitation and phase separation by a quasi-2D microfluidic device coupled with total internal reflection fluorescence (TIRF) microscope. The device enabled controlled diffusive mixing between an asphaltene solution and a mixture of n-pentane and toluene. The diffusive mixing front was characterized by fluorescent dye. Based on the results of fluorescence, the critical distance to achieve fully diffusive mixing was determined and the concentration of pentane and toluene could be estimated. TIRF imaging showed the diffusive mixing was not influenced by the asphaltene precipitation in terms of yield and size of asphaltene particles. The device could be used for a high spatiotemporal resolution study of precipitation potentially, including asphaltene precipitation and oiling-out crystallization.

Second, asphaltene precipitation under diffusive mixing was tracked by TIRF. The asphaltene precipitation appeared simultaneously when n-pentane mixed with the asphaltene solution. The precipitation happened at the moment that n-pentane concentration was higher than a critical value and stopped when the concentration of the dissolved asphaltene was not enough. The precipitation lasted from a few seconds to tens of seconds, depending on the concentration of n-pentane. Primary submicron particles (PSMPs) and fractal aggregates were formed in the precipitation. PSMPs were spherical particles with a radius of 200 to 400 nm, independent of solvent concentration. Fractal aggregates were relatively large particles formed by PSMPs. The ratio of the PSMPs in asphaltene particles decreased with the increase in solvent concentration.

Third, Asphaltene precipitation was compared in 23 types of solvents under a diffusive-dominated mixing process. The formation of PSMPs (particle size ranging from 0.2 to 0.4 μm) was prevalent in diffusion-mixed quasi-2D microfluidic chambers, independent of concentration and type of the solvents. The type and concentration of the solvents affected the size distribution of asphaltene particles. The mixture of n-heptane and n-decane produced the highest ratio of PSMPs in asphaltene particles. The diffusion coefficient was found to be a significant factor except for the Hildebrand Solubility parameter on the yield of asphaltene. Both the yield and size distribution could be tuned by changing the type and concentration of the solvents. In addition, the population balance model (PBM) fitted well with the experiment, laying the foundation for PBM to simulate the real industrial process.

Fourth, the growth and coalescence of surface nanodroplets in a viscosity-mediated surrounding were investigated to show the dilution-induced phase separation in the high viscous medium. The total volume of the surface nanodroplets was scaled with $Pe^{3/4}$ in a certain Pe range. Different from the low-viscous case, the growth of nanodroplets was independent of Pe after a critical value. We proposed a two-regime growth model to explain the effect of viscosity. In the first regime, Pe affected the growth of nanodroplets. In the second regime, the concentration boundary layer became nested in the mo-

mentum boundary layer due to the high viscosity, where nanodroplet growth depended on oil diffusion. The effect of solution viscosity could be used to adjust the final droplet size and obtain different bimodal distributions of nanodroplet size on a uniform surface, which could be used to adjust the droplet size distribution for different applications.

Fifth, the asphaltene precipitation induced by the solvent exchange was studied under the controlled external mixing. COMSOL simulation was used to simulate the mixing dynamics during the solvent exchange process. Simulation-based prediction results could be well in line with experimental observations with the change of flow rate, channel height, and orientation. Shear force and local concentration were two important reasons for the effect of mixing dynamics on asphaltene precipitation. In the case of sufficient mixing, an increase in temperature led to a decrease in the amount of asphaltene precipitation because some fractions of asphaltene became soluble in n-heptane with an increase in temperature.

8.2 Future work

Although great effort has been done to study the asphaltene precipitation under controlled flow conditions, the unavoidable limits of time and techniques prevent investigation on some topics. Here are some directions worth continuing to explore.

First, the microfluidic chambers we used to control the mixing have no or very little convection. For some passive mixing microfluidic chambers, the mixing can be super fast. The mixing is induced by the intrinsic structure of the device. Asphaltene precipitation process can be investigated in these microfluidic chambers.

Second, we observe the existence of asphaltene particles at the submicron scale. However, the path from nanoaggregates to PSMPs is not clear. Utilizing some higher resolution optical microscopes may be able to solve this problem such as structured illumination microscopy (SIM), stimulated emission depletion (STED), and near-field optical random mapping (NORM) microscopy. It

is worth noting that these microscopes often require a very strong excitation laser, which can lead to the fusion of the asphaltene particles.

Third, the concentration of asphaltene in our solution is relatively high compared with the conventional study but is still low compared with real bitumen.

Fourth, the current model oil does not contain water and mineral solids. It remains unanswered whether the water or mineral solids has impact on the morphology and yield of asphaltene precipitation. Adding water and mineral solids can bring the system closer to a real PFT unit. The effect of asphaltene precipitation on the stability of water-in-oil emulsions can also be studied under controlled flow conditions.

References

1. Acevedo, S., Castro, A., V'asquez, E., Marcano, F. & Ranaudo, M. A. Investigation of physical chemistry properties of asphaltenes using solubility parameters of asphaltenes and their fractions A1 and A2. *Energy & Fuels* **24,** 5921–5933 (2010).
2. Acevedo, S. *et al.* Molecular Weight of Petroleum Asphaltenes: A Comparison between Mass Spectrometry and Vapor Pressure Osmometry. *Energy & Fuels* **19,** 1548–1560 (2005).
3. Agrawal, P., Schoeggl, F., Satyro, M., Taylor, S. & Yarranton, H. Measurement and modeling of the phase behavior of solvent diluted bitumens. *Fluid Phase Equilibria* **334,** 51–64 (2012).
4. Akbarzadeh, K., Alboudwarej, H., Svrcek, W. Y. & Yarranton, H. W. A generalized regular solution model for asphaltene precipitation from n-alkane diluted heavy oils and bitumens. *Fluid Phase Equilibria* **232,** 159–170 (2005).
5. Alboudwarej, H., Akbarzadeh, K., Beck, J., Svrcek, W. Y. & Yarranton, H. W. Regular solution model for asphaltene precipitation from bitumens and solvents. *AIChE journal* **49,** 2948–2956 (2003).
6. Alemi, F. M. *et al.* Experimental and DFT studies on the effect of carbon nanoparticles on asphaltene precipitation and aggregation phenomena. *Chemical Engineering Journal* **422,** 130030 (2021).
7. Alhreez, M. & Wen, D. Molecular structure characterization of asphaltene in the presence of inhibitors with nanoemulsions. *RSC advances* **9,** 19560–19570 (2019).
8. Ali, M. & Islam, M. The effect of asphaltene precipitation on carbonate-rock permeability: an experimental and numerical approach. *SPE Production & Facilities* **13,** 178–183 (1998).
9. Alivand, M. S. *et al.* Tuning the surface chemistry and porosity of waste-derived nanoporous materials toward exceptional performance in antibiotic adsorption: Experimental and DFT studies. *Chemical Engineering Journal* **374,** 274–291 (2019).
10. Allen, T. *Particle size measurement* (Springer, 1990).

11. Almasi, M. Molecular interactions and structural studies of toluene and (C5 - C10) 1-alkanol; mutual diffusion and virial coefficients. *Journal of Molecular Structure* **1230,** 129624 (2021).

12. Angle, C. W., Long, Y., Hamza, H. & Lue, L. Precipitation of asphaltenes from solvent-diluted heavy oil and thermodynamic properties of solvent-diluted heavy oil solutions. *Fuel* **85,** 492–506 (2006).

13. Anisimov, M. *et al.* Effects of resins on aggregation and stability of asphaltenes. *Energy & Fuels* **28,** 6200–6209 (2014).

14. Arciniegas, L. M. & Babadagli, T. Asphaltene precipitation, flocculation and deposition during solvent injection at elevated temperatures for heavy oil recovery. *Fuel* **124,** 202–211 (2014).

15. Arends, G. F., You, J. B., Shaw, J. M. & Zhang, X. Enhanced displacement of phase separating liquid mixtures in 2D confined spaces. *Energy & Fuels* **35,** 5194–5205 (2021).

16. Aris, R. On the dispersion of a solute in a fluid flowing through a tube. *Proceedings of the Royal Society of London. Series A. Mathematical and Physical Sciences* **235,** 67–77 (1956).

17. Atta, A. M., Elsockary, M. A., Kandil, O. F. & Mohamed, Z. M. Using of modified plastic waste based on poly (ethylene-co-acrylic acid) grafts to solve transportation problem of petroleum crude oil. *Journal of dispersion science and technology* **29,** 7–19 (2008).

18. Aubry, J., Ganachaud, F., Cohen Addad, J.-P. & Cabane, B. Nanoprecipitation of polymethylmethacrylate by solvent shifting:1. boundaries. *Langmuir* **25,** 1970–1979 (2009).

19. Awan, M. A. & Dymond, J. Transport properties of nonelectrolyte liquid mixtures. XI. Mutual diffusion coefficients for toluene+ n-hexane and toluene+ acetonitrile at temperatures from 273 to 348 K and at pressures up to 25 MPa. *International Journal of Thermophysics* **22,** 679–700 (2001).

20. Axelrod, D. in *Fluorescence Microscopy of Living Cells in Culture Part B. Quantitative Fluorescence Microscopy—Imaging and Spectroscopy* (eds Taylor, D. L. & Wang, Y.-L.) 245–270 (Academic Press, 1989).

21. Axelrod, D. Total internal reflection fluorescence microscopy. *Methods in cell biology* **89,** 169–221 (2008).

22. Balestrin, L. B. d. S., Francisco, R. D., Bertran, C. A., Cardoso, M. B. & Loh, W. Direct Assessment of Inhibitor and Solvent Effects on the Deposition Mechanism of Asphaltenes in a Brazilian Crude Oil. *Energy & Fuels* **33,** 4748–4757 (2019).

23. Bao, L., Rezk, A. R., Yeo, L. Y. & Zhang, X. Highly ordered arrays of femtoliter surface droplets. *Small* **11,** 4850–4855 (2015).

24. Bao, L., Werbiuk, Z., Lohse, D. & Zhang, X. Controlling the growth modes of femtoliter sessile droplets nucleating on chemically patterned surfaces. *Journal of Physical Chemistry Letters* **7,** 1055–1059 (2016).

25. Barrera, D., Ortiz, D. & Yarranton, H. Molecular weight and density distributions of asphaltenes from crude oils. *Energy & Fuels* **27,** 2474–2487 (2013).

26. Barton, A. F. *CRC handbook of solubility parameters and other cohesion parameters* (Routledge, 2017).

27. Betancourt, S. S. *et al.* Nanoaggregates of Asphaltenes in a Reservoir Crude Oil and Reservoir Connectivity. *Energy & Fuels* **23,** 1178–1188 (2009).

28. Beysens, D. & Knobler, C. Growth of breath figures. *Physical Review Letters* **57,** 1433 (1986).

29. Beysens, D. Dew nucleation and growth. *Comptes Rendus Physique* **7,** 1082–1100 (2006).

30. Bhagat, A. A. S., Peterson, E. T. & Papautsky, I. A passive planar micromixer with obstructions for mixing at low Reynolds numbers. *Journal of micromechanics and microengineering* **17,** 1017 (2007).

31. Bizmark, N. & Ioannidis, M. A. Nanoparticle-stabilised emulsions: Droplet armouring vs. droplet bridging. *Soft Matter* **14,** 6404–6408 (2018).

32. Boadway, J. D. Dynamics of growth and breakage of alum floc in presence of fluid shear. *Journal of the Environmental Engineering Division* **104,** 901–915 (1978).

33. Boek, E. S., Ladva, H. K., Crawshaw, J. P. & Padding, J. T. Deposition of colloidal asphaltene in capillary flow: experiments and mesoscopic simulation. *Energy & Fuels* **22,** 805–813 (2008).

34. Boek, E. S., Wilson, A. D., Padding, J. T., Headen, T. F. & Crawshaw, J. P. Multi-scale simulation and experimental studies of asphaltene aggregation and deposition in capillary flow. *Energy & Fuels* **24,** 2361–2368 (2010).

35. Bokobza, L., Bruneel, J.-L. & Couzi, M. Raman spectroscopy as a tool for the analysis of carbon-based materials (highly oriented pyrolitic graphite, multilayer graphene and multiwall carbon nanotubes) and of some of their elastomeric composites. *Vibrational Spectroscopy* **74,** 57–63 (2014).

36. Bubakova, P., Pivokonsky, M. & Filip, P. Effect of shear rate on aggregate size and structure in the process of aggregation and at steady state. *Powder Technology* **235,** 540–549 (2013).

37. Buckley, J. S., Fan, T., Tong, Z. & Morrow, N. R. *Mixing small amounts of crude oil with large amounts of asphaltene precipitant* in *Proceedings of the International Society of Core Analysts Symposium* (2006), 1–12.

38. Buckley, J. S. & Wang, J. Crude oil and asphaltene characterization for prediction of wetting alteration. *Journal of Petroleum Science and Engineering* **33,** 195–202 (2002).

39. Buckley, J. *et al.* Asphaltene precipitation and solvent properties of crude oils. *Petroleum Science and Technology* **16,** 251–285 (1998).

40. Buenrostro-Gonzalez, E., Lira-Galeana, C., Gil-Villegas, A. & Wu, J. Asphaltene precipitation in crude oils: Theory and experiments. *AIChE Journal* **50,** 2552–2570 (2004).

41. Burke, N. E., Hobbs, R. E. & Kashou, S. F. Measurement and Modeling of Asphaltene Precipitation (includes associated paper 23831). *Journal of Petroleum Technology* **42,** 1440–1446 (1990).

42. Campa, V. M. *et al.* Endocytosis as a biological response in receptor pharmacology: Evaluation by fluorescence microscopy. *PloS One* **10,** e0122604 (2015).

43. Carteau, D., Pianet, I., Brunerie, P., Guillemat, B. & Bassani, D. M. Probing the initial events in the spontaneous emulsification of trans-anethole using dynamic NMR spectroscopy. *Langmuir* **23,** 3561–3565 (2007).

44. Casas, Y. A., Duran, J. A., Schoeggl, F. F. & Yarranton, H. W. Settling of asphaltene aggregates in n-alkane diluted bitumen. *Energy & Fuels* **33,** 10687–10703 (2019).

45. Castillo, J., Hung, J., Goncalves, S. & Reyes, A. Study of asphaltenes aggregation process in crude oils using confocal microscopy. *Energy & Fuels* **18,** 698–703 (2004).

46. Chacón-Patiño, M. L., Rowland, S. M. & Rodgers, R. P. Advances in asphaltene petroleomics. part 1: asphaltenes are composed of abundant island and archipelago structural motifs. *Energy & Fuels* **31,** 13509–13518 (2017).

47. Chen, P. *et al.* Ex Situ and In Situ Thermal Transformations of M-50 Pitch Revealed by Non-contact Atomic Force Microscopy. *Energy & Fuels* (2021).

48. Cheng, N.-S. Formula for the viscosity of a glycerol- water mixture. *Industrial & Engineering Chemistry Research* **47,** 3285–3288 (2008).

49. Chiesa, M. *et al.* Investigation of the role of viscosity on electrocoalescence of water droplets in oil. *Separation and Purification Technology* **50,** 267–277 (2006).

50. Choi, H., Wei, Z., You, J. B., Yang, H. & Zhang, X. Effects of Chemical and Geometric Microstructures on the Crystallization of Surface Droplets during Solvent Exchange. *Langmuir* **37,** 5290–5298 (2021).

51. Cole, R. H. *et al.* Printed droplet microfluidics for on demand dispensing of picoliter droplets and cells. *Proceedings of the National Academy of Sciences* **114,** 8728–8733 (2017).

52. *COMSOL Multiphysics*® v. 6.0. (2021). `www.comsol.com`.

53. Da Costa, L. M. *et al.* Density functional theory investigation of the contributions of π-π stacking and hydrogen-bonding interactions to the aggregation of model asphaltene compounds. *Energy & Fuels* **26,** 2727–2735 (2012).

54. Dandekar, A. Y., Andersen, S. I. & Stenby, E. H. Measurement of viscosity of hydrocarbon liquids using a microviscometer. *Journal of Chemical & Engineering Data* **43,** 551–554 (1998).

55. Derakhshesh, M., Gray, M. R. & Dechaine, G. P. Dispersion of asphaltene nanoaggregates and the role of Rayleigh scattering in the absorption of visible electromagnetic radiation by these nanoaggregates. *Energy & Fuels* **27,** 680–693 (2013).

56. Desportes, S. *et al.* Fluorescence lifetime imaging microscopy for in situ observation of the nanocrystallization of rubrene in a microfluidic setup. *Chemical Physics Letters* **446,** 212–216 (2007).

57. Duran, J., Schoeggl, F. & Yarranton, H. Kinetics of asphaltene precipitation/aggregation from diluted crude oil. *Fuel* **255,** 115859 (2019).

58. Duran, J. *et al.* Nature of asphaltene aggregates. *Energy & Fuels* **33,** 3694–3710 (2018).

59. Durand, E. *et al.* Effect of chemical composition on asphaltenes aggregation. *Energy & Fuels* **24,** 1051–1062 (2010).

60. Dyett, B., Hao, H., Lohse, D. & Zhang, X. Coalescence driven self-organization of growing nanodroplets around a microcap. *Soft Matter* **14,** 2628–2637 (2018).

61. Dyett, B., Yu, H. & Zhang, X. Formation of surface nanodroplets of viscous liquids by solvent exchange. *Eur. Phys. J. E: Soft Matter Biol. Phys.* **40,** 26 (2017).

62. Dyett, B. *et al.* Growth dynamics of surface nanodroplets during solvent exchange at varying flow rates. *Soft Matter* **14,** 5197–5204 (2018).

63. Dyett, B. P. & Zhang, X. Accelerated formation of H2 Nanobubbles from a surface nanodroplet reaction. *ACS Nano* **14,** 10944–10953 (2020).

64. Elimelech, M., Gregory, J. & Jia, X. *Particle deposition and aggregation: measurement, modelling and simulation* (Butterworth-Heinemann, 2013).

65. Elkhatib, O., Chaisoontornyotin, W., Gesho, M. & Goual, L. Nanoscale investigation of asphaltene deposition under capillary flow conditions. *Energy & Fuels* **34,** 5148–5158 (2019).

66. Enayat, S. *et al.* On the development of experimental methods to determine the rates of asphaltene precipitation, aggregation, and deposition. *Fuel* **260,** 116250 (2020).

67. *Engineering ToolBox* Online (2001). `https://www.engineeringtoolbox.com`.

68. Eyssautier, J. *et al.* Mesoscale organization in a physically separated vacuum residue: Comparison to asphaltenes in a simple solvent. *Energy & Fuels* **26,** 2680–2687 (2012).

69. Fish, K. N. Total internal reflection fluorescence (TIRF) microscopy. *Current Protocols in Cytometry* **50,** 12–18 (2009).

70. Ganachaud, F. & Katz, J. L. Nanoparticles and nanocapsules created using the Ouzo effect: spontaneous emulsification as an alternative to ultrasonic and high-shear devices. *ChemPhysChem* **6,** 209–216 (2005).

71. Garcia-Cordero, J. L. & Fan, Z. H. Sessile droplets for chemical and biological assays. *Lab on a Chip* **17,** 2150–2166 (2017).

72. Gonçalves, F., Hamano, K., Sengers, J. & Kestin, J. Viscosity of liquid toluene in the temperature range 25–75° C. *International Journal of Thermophysics* **8,** 641–647 (1987).

73. Gong, X. *et al.* The crystal hotel: A microfluidic approach to biomimetic crystallization. *Advanced Materials* **27,** 7395–7400 (2015).

74. Goual, L., Sedghi, M., Wang, X. & Zhu, Z. Asphaltene aggregation and impact of alkylphenols. *Langmuir* **30,** 5394–5403 (2014).

75. Gray, M. R. *Upgrading oilsands bitumen and heavy oil* (University of Alberta, 2015).

76. Gray, M. R., Tykwinski, R. R., Stryker, J. M. & Tan, X. Supramolecular assembly model for aggregation of petroleum asphaltenes. *Energy & Fuels* **25,** 3125–3134 (2011).

77. Gray, M. R. & Yarranton, H. W. Quantitative modeling of formation of asphaltene nanoaggregates. *Energy & Fuels* **33,** 8566–8575 (2019).

78. Gray, M. R., Tykwinski, R. R., Stryker, J. M. & Tan, X. Supramolecular Assembly Model for Aggregation of Petroleum Asphaltenes. *Energy & Fuels* **25,** 3125–3134 (2011).

79. Grossmann, S. & Lohse, D. Fluctuations in turbulent Rayleigh–Bénard convection: The role of plumes. *Physics of Fluids* **16,** 4462–4472 (2004).

80. Grunberg, L. & Nissan, A. H. Mixture law for viscosity. *Nature* **164,** 799–800 (1949).

81. Grushka, E. & Kikta, E. J. Extension of the chromatographic broadening method of measuring diffusion coefficients to liquid systems. I. Diffusion coefficients of some alkylbenzenes in chloroform. *The Journal of Physical Chemistry* **78,** 2297–2301 (1974).

82. Haidas, D. *et al.* Microfluidic platform for multimodal analysis of enzyme secretion in nanoliter droplet arrays. *Analytical Chemistry* **91,** 2066–2073 (2018).

83. Haji-Akbari, N., Masirisuk, P., Hoepfner, M. P. & Fogler, H. S. A unified model for aggregation of asphaltenes. *Energy & Fuels* **27,** 2497–2505 (2013).

84. Haji-Akbari, N., Teeraphapkul, P. & Fogler, H. S. Effect of asphaltene concentration on the aggregation and precipitation tendency of asphaltenes. *Energy & Fuels* **28,** 909–919 (2014).

85. Harada, M. & Kamigaito, Y. Nucleation and aggregative growth process of platinum nanoparticles studied by in situ quick XAFS spectroscopy. *Langmuir* **28,** 2415–2428 (2012).

86. Hirschberg, A., deJong, L., Schipper, B. & Meijer, J. Influence of Temperature and Pressure on Asphaltene Flocculation. *Society of Petroleum Engineers Journal* **24,** 283–293 (June 1984).

87. Hirschberg, A. Role of asphaltenes in compositional grading of a reservoir's fluid column. *Journal of Petroleum Technology* **40,** 89–94 (1988).

88. Hristova, E., Tchoukov, P., Stoyanov, S. R. & McFarlane, R. Asphaltene Precipitation Onsets in Relation to the Critical Dilution of Athabasca Bitumen in Paraffinic Solvents. *Energy & Fuels* (2022).

89. Hu, Y.-F. & Guo, T.-M. Effect of temperature and molecular weight of n-alkane precipitants on asphaltene precipitation. *Fluid Phase Equilibria* **192,** 13–25 (2001).

90. Huffman, M. & Fogler, H. S. Asphaltene destabilization in the presence of dodecylbenzene sulfonic acid and dodecylphenol. *Fuel* **304,** 121320 (2021).

91. Hung, J., Castillo, J. & Reyes, A. Kinetics of asphaltene aggregation in toluene- heptane mixtures studied by confocal microscopy. *Energy & Fuels* **19,** 898–904 (2005).

92. Iwahashi, M., Yamaguchi, Y., Ogura, Y. & Suzuki, M. Dynamical structures of normal alkanes, alcohols, and fatty acids in the liquid state as determined by viscosity, self-diffusion coefficient, infrared spectra, and 13CNMR spin-lattice relaxation time measurements. *Bulletin of the Chemical Society of Japan* **63,** 2154–2158 (1990).

93. Jeannot, M. A. & Cantwell, F. F. Solvent microextraction into a single drop. *Analytical Chemistry* **68,** 2236–2240 (1996).

94. Jha, B., Cueto-Felgueroso, L. & Juanes, R. Fluid mixing from viscous fingering. *Physical review letters* **106,** 194502 (2011).

95. Johnston, K., Schoeggl, F., Satyro, M., Taylor, S. & Yarranton, H. Phase behavior of bitumen and n-pentane. *Fluid Phase Equilibria* **442,** 1–19 (2017).

96. Joshi, N. B., Mullins, O. C., Jamaluddin, A., Creek, J. & McFadden, J. Asphaltene Precipitation from Live Crude Oil. *Energy & Fuels* **15,** 979–986 (2001).

97. Kaneko, T., Sun, Y., Nakajima, H., Uchiyama, K. & Zeng, H. Droplet sensitized fluorescence detection for enzyme-linked immune sorbent assays on microwell plate. *Analytical Chemistry* **91,** 5685–5689 (2019).

98. Kapur, P. Self-preserving size spectra of comminuted particles. *Chemical Engineering Science* **27,** 425–431 (1972).

99. Karnik, R. *et al.* Microfluidic platform for controlled synthesis of polymeric nanoparticles. *Nano Letters* **8,** 2906–2912 (2008).

100. Kedenburg, S., Vieweg, M., Gissibl, T. & Giessen, H. Linear refractive index and absorption measurements of nonlinear optical liquids in the visible and near-infrared spectral region. *Optical Materials Express* **2,** 1588–1611 (2012).

101. Kerl, K. & Varchmin, H. Refractive index dispersion (RID) of some liquids in the UV/VIS between 20° C and 60° C. *Journal of Molecular Structure* **349,** 257–260 (1995).

102. Keshmiri, K., Huang, H. & Nazemifard, N. Microfluidic platform to evaluate asphaltene deposition during solvent-based extraction of bitumen. *Fuel* **239,** 841–851 (2019).

103. Kharrat, A. M., Zacharia, J., Cherian, V. J. & Anyatonwu, A. Issues with comparing SARA methodologies. *Energy & Fuels* **21,** 3618–3621 (2007).

104. Kim, Y.-Y. *et al.* The effect of additives on the early stages of growth of calcite single crystals. *Angewandte Chemie* **129,** 12047–12052 (2017).

105. Kueh, B. *et al.* Asphaltene-derived activated carbon and carbon nanotube membranes for CO2 separation. *Energy & Fuels* **32,** 11718–11730 (2018).

106. Kumar, A., Chowdhury, S. & Shaw, J. M. Shared Depletion and Restabilization Colloidal Interactions in Phase Diagrams for Silica Nanoparticle and Asphaltene+ Polystyrene+ Solvent Mixtures. *Energy & Fuels* **34,** 15234–15245 (2020).

107. Lemmon, E. W., McLinden, M. O. & Friend, D. G. *Thermophysical properties of fluid systems, NIST chemistry webbook* (National Institute of Standards and Technology, Gaithersburg MD, 20899, 2008).

108. Lepeltier, E., Bourgaux, C. & Couvreur, P. Nanoprecipitation and the "ouzo effect": Application to drug delivery devices. *Advanced Drug Delivery Reviews* **71,** 86–97 (2014).

109. Li, M., Bao, L., Yu, H. & Zhang, X. Formation of multicomponent surface nanodroplets by solvent exchange. *The Journal of Physical Chemistry C* **122,** 8647–8654 (2018).

110. Li, M., Dyett, B., Bansal, V. & Zhang, X. Functional femtoliter droplets for ultrafast nanoextraction and supersensitive online microanalysis. *Small* **15,** 1804683 (1 2019).

111. Li, M., Dyett, B. & Zhang, X. Automated femtoliter droplet-based determination of oil–water partition coefficient. *Analytical Chemistry* **91,** 10371–10375 (2019).

112. Li, M., Yu, H., Bao, L., Dyett, B. & Zhang, X. Controlled addition of new liquid component into surface droplet arrays by solvent exchange. *Journal of colloid and interface science* **543,** 164–173 (2019).

113. Li, X., Guo, Y., Boek, E. S. & Guo, X. Experimental study on kinetics of asphaltene aggregation in a microcapillary. *Energy & Fuels* **31,** 9006–9015 (2017).

114. Li, X. *et al.* Experimental study for the impacts of flow rate and concentration of asphaltene precipitant on dynamic asphaltene deposition in microcapillary medium. *Journal of Petroleum Science and Engineering* **162,** 333–340 (2018).

115. Lohse, D. Towards controlled liquid–liquid microextraction. *Journal of Fluid Mechanics* **804,** 1–4 (2016).

116. Lohse, D., Zhang, X., *et al.* Surface nanobubbles and nanodroplets. *Reviews of modern physics* **87,** 981 (2015).

117. Long, Y., Dabros, T. & Hamza, H. Stability and settling characteristics of solvent-diluted bitumen emulsions. *Fuel* **81,** 1945–1952 (2002).

118. Long, Y., Dabros, T. & Hamza, H. Structure of water/solids/asphaltenes aggregates and effect of mixing temperature on settling rate in solvent-diluted bitumen. *Fuel* **83,** 823–832 (2004).

119. Lu, Z., Xu, H., Zeng, H. & Zhang, X. Solvent effects on the formation of surface nanodroplets by solvent exchange. *Langmuir* **31,** 12120–12125 (2015).

120. Lu, Z. *et al.* Universal nanodroplet branches from confining the Ouzo effect. *Proceedings of the National Academy of Sciences* **114,** 10332–10337 (2017).

121. Luo, X. *et al.* Electrocoalescence criterion of conducting droplets suspended in a viscous fluid. *The Journal of Physical Chemistry C* **123,** 19588–19595 (2019).

122. Ma, J. *et al.* A novel oxygen-containing demulsifier for efficient breaking of water-in-oil emulsions. *Chemical Engineering Journal* **385,** 123826 (2020).

123. Mansur, C. R., de Melo, A. R. & Lucas, E. F. Determination of asphaltene particle size: influence of flocculant, additive, and temperature. *Energy & Fuels* **26,** 4988–4994 (2012).

124. Mao, X. *et al.* Novel Fe3O4 based superhydrophilic core-shell microspheres for breaking asphaltenes-stabilized water-in-oil emulsion. *Chemical Engineering Journal* **358,** 869–877 (2019).

125. Maqbool, T., Balgoa, A. T. & Fogler, H. S. Revisiting asphaltene precipitation from crude oils: A case of neglected kinetic effects. *Energy & Fuels* **23,** 3681–3686 (2009).

126. Maqbool, T., Raha, S., Hoepfner, M. P. & Fogler, H. S. Modeling the aggregation of asphaltene nanoaggregates in crude oil- precipitant systems. *Energy & Fuels* **25,** 1585–1596 (2011).

127. Maqbool, T., Raha, S., Hoepfner, M. P. & Fogler, H. S. Modeling the aggregation of asphaltene nanoaggregates in crude oil- precipitant systems. *Energy & Fuels* **25,** 1585–1596 (2011).

128. Masliyah, J., Zhou, Z. J., Xu, Z., Czarnecki, J. & Hamza, H. Understanding water-based bitumen extraction from Athabasca oil sands. *The Canadian Journal of Chemical Engineering* **82,** 628–654 (2004).

129. Meng, J., You, J. B., Hao, H., Tan, X. & Zhang, X. Primary submicron particles from early stage asphaltene precipitation revealed in situ by total internal reflection fluorescence microscopy in a model oil system. *Fuel* **296,** 120584 (2021).

130. Meng, J., You, J. B. & Zhang, X. Viscosity-mediated growth and coalescence of surface nanodroplets. *The Journal of Physical Chemistry C* (2020).

131. Meng, J. *et al.* Microfluidic device coupled with total internal reflection microscopy for in situ observation of precipitation. *The European Physical Journal E* **44,** 1–8 (2021).

132. Meng, J. *et al.* Size distribution of primary submicron particles and larger aggregates in solvent-induced asphaltene precipitation in a model oil system. *Fuel* **322,** 124057 (2022).

133. Mitchell, D. L. & Speight, J. G. *Solubility of (athabasca bitumen) asphaltenes in (44) hydrocarbon solvents* 1973.

134. Mohammadi, M. *et al.* Inhibition of asphaltene precipitation by TiO2, SiO2, and ZrO2 nanofluids. *Energy & Fuels* **25,** 3150–3156 (2011).

135. Morozov, E. V. & Martyanov, O. N. Reversibility of asphaltene aggregation as revealed by Magnetic Resonance Imaging in situ. *Energy & Fuels* **31,** 10639–10647 (2017).

136. Mostowfi, F., Indo, K., Mullins, O. C. & McFarlane, R. Asphaltene Nanoaggregates Studied by Centrifugation. *Energy & Fuels* **23,** 1194–1200 (2009).

137. Mouza, A., Patsa, C.-M. & Schönfeld, F. Mixing performance of a chaotic micro-mixer. *Chemical Engineering Research and Design* **86,** 1128–1134 (2008).

138. Mozaffari, S., Ghasemi, H., Tchoukov, P., Czarnecki, J. & Nazemifard, N. Lab-on-a-chip systems in asphaltene characterization: a review of recent advances. *Energy & Fuels* **35,** 9080–9101 (2021).

139. Mullins, O. C. The modified Yen model. *Energy & Fuels* **24,** 2179–2207 (2010).

140. Mullins, O. C. The asphaltenes. *Annual review of analytical chemistry* **4,** 393–418 (2011).

141. Mullins, O. C., Sheu, E. Y., Hammami, A. & Marshall, A. G. *Asphaltenes, heavy oils, and petroleomics* (Springer Science & Business Media, 2007).

142. Mullins, O. C. *et al.* Advances in asphaltene science and the Yen–Mullins model. *Energy & Fuels* **26,** 3986–4003 (2012).

143. Nassar, N. N., Betancur, S., Acevedo, S., Franco, C. A. & Cortés, F. B. Development of a population balance model to describe the influence of shear and nanoparticles on the aggregation and fragmentation of asphaltene aggregates. *Industrial & Engineering Chemistry Research* **54,** 8201–8211 (2015).

144. Nguyen, D. D., Daneshfar, R., Dehaghani, A. H. S. & Su, C.-H. The effect of shear rate on aggregation and breakage of asphaltenes flocs: experimental study and model-based analysis. *Journal of Molecular Liquids* **325,** 114861 (2021).

145. Nikooyeh, K. & Shaw, J. M. On the applicability of the regular solution theory to asphaltene+ diluent mixtures. *Energy & Fuels* **26,** 576–585 (2012).

146. Ollinger, J. *et al.* Gold core nanoparticle mimics for asphaltene behaviors in solution and at interfaces. *Energy & Fuels* **30,** 10148–10160 (2016).

147. Paddock, S. W. Confocal laser scanning microscopy. *Biotechniques* **27,** 992–1004 (1999).

148. Pagán Pagán, N. M., Zhang, Z., Nguyen, T. V., Marciel, A. B. & Biswal, S. L. Physicochemical Characterization of Asphaltenes Using Microfluidic Analysis. *Chemical Reviews* (2022).

149. Pandya, J. & Spielman, L. Floc breakage in agitated suspensions: theory and data processing strategy. *Journal of Colloid and Interface Science* **90,** 517–531 (1982).

150. Pandya, J. & Spielman, L. Floc breakage in agitated suspensions: effect of agitation rate. *Chemical Engineering Science* **38** (1983).

151. Park, J. H., Hussam, A., Couasnon, P., Fritz, D. & Carr, P. W. Experimental reexamination of selected partition coefficients from Rohrschneider's data set. *Analytical Chemistry* **59,** 1970–1976 (1987).

152. Park, K.-C. *et al.* Condensation on slippery asymmetric bumps. *Nature* **531,** 78–82 (2016).

153. Parker, D. S., Kaufman, W. J. & Jenkins, D. Floc breakup in turbulent flocculation processes. *Journal of the Sanitary Engineering Division* **98,** 79–99 (1972).

154. Paulssen, D., Feng, W., Pini, I. & Levkin, P. A. Formation of liquid–liquid micropatterns through guided liquid displacement on liquid-infused surfaces. *Advanced Materials Interfaces* **5,** 1800852 (2018).

155. Peña, M. D. & Tardajos, G. Isothermal compressibilities of n-alkanes and benzene. *The Journal of Chemical Thermodynamics* **10,** 19–24 (1978).

156. Peng, S., Lohse, D. & Zhang, X. Microwetting of supported graphene on hydrophobic surfaces revealed by polymerized interfacial femtodroplets. *Langmuir* **30,** 10043–10049 (2014).

157. Peng, S., Lohse, D. & Zhang, X. Spontaneous pattern formation of surface nanodroplets from competitive growth. *ACS Nano* **9,** 11916–11923 (2015).

158. Peng, S., Spandan, V., Verzicco, R., Lohse, D. & Zhang, X. Growth dynamics of microbubbles on microcavity arrays by solvent exchange: Experiments and numerical simulations. *Journal of Colloid and Interface Science* **532,** 103–111 (2018).

159. Peramanu, S., Clarke, P. F. & Pruden, B. B. Flow loop apparatus to study the effect of solvent, temperature and additives on asphaltene precipitation. *Journal of Petroleum Science and Engineering* **23,** 133–143 (1999).

160. Plata-Gryl, M., Momotko, M., Makowiec, S. & Boczkaj, G. Characterization of diatomaceous earth coated with nitrated asphaltenes as superior adsorbent for removal of VOCs from gas phase in fixed bed column. *Chemical Engineering Journal* **427,** 130653 (2022).

161. Qi, Z. *et al.* Asphaltene deposition during bitumen extraction with natural gas condensate and naphtha. *Energy & Fuels* **32,** 1433–1439 (2018).

162. Qian, J., Arends, G. F. & Zhang, X. Surface nanodroplets: formation, dissolution, and applications. *Langmuir* **35,** 12583–12596 (2019).

163. Rahimi, H. & Solaimany Nazar, A. R. Asphaltene aggregates fractal restructuring model, a population balance approach. *Energy & Fuels* **24,** 1088–1093 (2010).

164. Rahmani, N. H., Dabros, T. & Masliyah, J. H. Evolution of asphaltene floc size distribution in organic solvents under shear. *Chemical Engineering Science* **59,** 685–697 (2004).

165. Rahmani, N. H., Dabros, T. & Masliyah, J. H. Online optical monitoring of asphaltene aggregation. *Industrial & Engineering Chemistry Research* **44,** 75–84 (2005).

166. Rahmani, N. H., Masliyah, J. H. & Dabros, T. Characterization of asphaltenes aggregation and fragmentation in a shear field. *AIChE journal* **49,** 1645–1655 (2003).

167. Ramos-Pallares, F., Santos, D. & Yarranton, H. W. Application of the Modified Regular Solution Model to Crude Oils Characterized from a Distillation Assay. *Energy & Fuels* **34,** 15270–15284 (2020).

168. Rao, F. & Liu, Q. Froth treatment in Athabasca oil sands bitumen Recovery Process: A Review. *Energy & Fuels* **27,** 7199–7207 (2013).

169. Rastegari, K., Svrcek, W. Y. & Yarranton, H. W. Kinetics of asphaltene flocculation. *Industrial & Engineering Chemistry Research* **43,** 6861–6870 (2004).

170. Rezaee, M. *et al.* Determination of organic compounds in water using dispersive liquid–liquid microextraction. *Journal of Chromatography A* **1116,** 1–9 (2006).

171. Rodriguez, S. *et al.* Regular solution based approach to modeling asphaltene precipitation from native and reacted oils: Part 3, visbroken oils. *Fuel* **257,** 116079 (2019).

172. Rogel, E., Leon, O., Espidel, Y. & Gonzalez, Y. Asphaltene stability in crude oils. *SPE Production & Facilities* **16,** 84–88 (2001).

173. Rogel, E. Simulation of interactions in asphaltene aggregates. *Energy & Fuels* **14,** 566–574 (2000).

174. Rogel, E. Effect of inhibitors on asphaltene aggregation: A theoretical framework. *Energy & Fuels* **25,** 472–481 (2011).

175. Rogel, E. & Moir, M. Effect of precipitation time and solvent power on asphaltene characteristics. *Fuel* **208,** 271–280 (2017).

176. Rutledge, R. Sigmoidal curve-fitting redefines quantitative real-time PCR with the prospective of developing automated high-throughput applications. *Nucleic Acids Research* **32,** e178–e178 (2004).

177. Saad, S. *et al.* Transformation of petroleum asphaltenes to carbon fibers. *Carbon* (2022).

178. Sagdeev, D., Fomina, M., Mukhamedzyanov, G. K. & Abdulagatov, I. Experimental Study of the Density and Viscosity of n-Heptane at Temperatures from 298 K to 470 K and Pressure upto 245 MPa. *International Journal of Thermophysics* **34,** 1–33 (2013).

179. Santos, F. J. *et al.* Standard reference data for the viscosity of toluene. *Journal of Physical and Chemical Reference Data* **35,** 1–8 (2006).

180. Schlumberger. *VMG Symmetry* v2021.2 (2021). `https://www.software.slb.com/products/symmetry`.

181. Scholten, E., van der Linden, E. & This, H. The life of an anise-flavored alcoholic beverage: Does its stability cloud or confirm theory? *Langmuir* **24,** 1701–1706 (2008).

182. Schubert, S., Delaney Jr, J. T. & Schubert, U. S. Nanoprecipitation and nanoformulation of polymers: from history to powerful possibilities beyond poly(lactic acid). *Soft Matter* **7,** 1581–1588 (5 2011).

183. Schuler, B., Meyer, G., Peña, D., Mullins, O. C. & Gross, L. Unraveling the molecular structures of asphaltenes by atomic force microscopy. *Journal of the American Chemical Society* **137,** 9870–9876 (2015).

184. Schulze, M., Lechner, M. P., Stryker, J. M. & Tykwinski, R. R. Aggregation of asphaltene model compounds using a porphyrin tethered to a carboxylic acid. *Organic & Biomolecular Chemistry* **13,** 6984–6991 (2015).

185. Seifried, C. M., Crawshaw, J. & Boek, E. S. Kinetics of asphaltene aggregation in crude oil studied by confocal laser-scanning microscopy. *Energy & Fuels* **27,** 1865–1872 (2013).

186. Sekine, K., Okamoto, A. & Hayashi, K. In situ observation of the crystallization pressure induced by halite crystal growth in a microfluidic channel. *American Mineralogist* **96,** 1012–1019 (2011).

187. Shalygin, A. S., Kozhevnikov, I. V., Kazarian, S. G. & Martyanov, O. N. Spectroscopic imaging of deposition of asphaltenes from crude oil under flow. *Journal of Petroleum Science and Engineering* **181,** 106205 (2019).

188. Shelfantook, W. E. A perspective on the selection of froth treatment processes. *The Canadian Journal of Chemical Engineering* **82,** 704–709 (2004).

189. Shin, H. & Polikar, M. *Optimizing the SAGD process in three major Canadian oil-sands areas* in *SPE Annual Technical Conference and Exhibition* (2005).

190. Sieben, V. J., Tharanivasan, A. K., Andersen, S. I. & Mostowfi, F. Microfluidic approach for evaluating the solubility of crude oil asphaltenes. *Energy & Fuels* **30,** 1933–1946 (2016).

191. Sieben, V. J., Tharanivasan, A. K., Ratulowski, J. & Mostowfi, F. Asphaltenes yield curve measurements on a microfluidic platform. *Lab on a Chip* **15,** 4062–4074 (2015).

192. Sirota, E. Swelling of asphaltenes. *Petroleum Science and Technology* **16,** 415–431 (1998).

193. Sitnikova, N. L., Sprik, R., Wegdam, G. & Eiser, E. Spontaneously formed trans-anethol/water/alcohol emulsions: mechanism of formation and stability. *Langmuir* **21,** 7083–7089 (2005).

194. Smoluchowski, M. v. Versuch einer mathematischen Theorie der Koagulationskinetik kolloider Lösungen. *Zeitschrift für physikalische Chemie* **92,** 129–168 (1918).

195. Solaimany-Nazar, A. R. & Rahimi, H. Dynamic determination of asphaltene aggregate size distribution in shear induced organic solvents. *Energy & Fuels* **22,** 3435–3442 (2008).

196. Soleymanzadeh, A., Yousefi, M., Kord, S. & Mohammadzadeh, O. A review on methods of determining onset of asphaltene precipitation. *Journal of Petroleum Exploration and Production Technology* **9,** 1375–1396 (2019).

197. Stephens, C. J., Kim, Y.-Y., Evans, S. D., Meldrum, F. C. & Christenson, H. K. Early stages of crystallization of calcium carbonate revealed in picoliter droplets. *Journal of the American Chemical Society* **133,** 5210–5213 (2011).

198. Subramanian, D. & Firoozabadi, A. *Effect of surfactants and water on inhibition of asphaltene precipitation and deposition* in *Abu Dhabi International Petroleum Exhibition and Conference* (2015).

199. Subramanian, S., Simon, S. & Sjöblom, J. Asphaltene precipitation models: a review. *Journal of Dispersion Science and Technology* **37,** 1027–1049 (2016).

200. Sudarsan, A. P. & Ugaz, V. M. Fluid mixing in planar spiral microchannels. *Lab on a Chip* **6,** 74–82 (2006).

201. Sun, Y., Chen, X., Zhou, X., Zhu, J. & Yu, Y. Droplet-in-oil array for picoliter-scale analysis based on sequential inkjet printing. *Lab on a Chip* **15,** 2429–2436 (2015).

202. Sussman, M., Smereka, P. & Osher, S. A level set approach for computing solutions to incompressible two-phase flow. *Journal of Computational physics* **114,** 146–159 (1994).

203. Sussman, M. *et al.* An adaptive level set approach for incompressible two-phase flows. *Journal of Computational Physics* **148,** 81–124 (1999).

204. Taylor, G. I. Dispersion of soluble matter in solvent flowing slowly through a tube. *Proceedings of the Royal Society of London. Series A. Mathematical and Physical Sciences* **219,** 186–203 (1953).

205. Taylor, S. D., Czarnecki, J. & Masliyah, J. Refractive index measurements of diluted bitumen solutions. *Fuel* **80,** 2013–2018 (2001).

206. Tehrani, N. H. M. H. *et al.* Novel asphaltene-derived nanoporous carbon with NS-rich micro-mesoporous structure for superior gas adsorption: Experimental and DFT study. *Chemical Engineering Journal* **358,** 1126–1138 (2019).

207. Thomas, D., Judd, S. & Fawcett, N. Flocculation modelling: a review. *Water Research* **33,** 1579–1592 (1999).

208. ToolBox, E. *Dynamic Viscosity Liquids* Online. 2008. https://www.engineeringtoolbox.com/absolute-viscosity-liquids-d_1259.html.

209. Torkaman, M., Bahrami, M. & Dehghani, M. Influence of temperature on aggregation and stability of asphaltenes. I. Perikinetic aggregation. *Energy & Fuels* **31,** 11169–11180 (2017).

210. Tronser, T., Demir, K., Reischl, M., Bastmeyer, M. & Levkin, P. A. Droplet microarray: Miniaturized platform for rapid formation and high-throughput screening of embryoid bodies. *Lab on a Chip* **18,** 2257–2269 (2018).

211. Van Driessche, A. E., García-Ruiz, J. M., Delgado-López, J. M. & Sazaki, G. In situ observation of step dynamics on gypsum crystals. *Crystal Growth & Design* **10,** 3909–3916 (2010).

212. Vilas Bôas Fávero, C., Maqbool, T., Hoepfner, M., Haji-Akbari, N. & Fogler, H. S. Revisiting the flocculation kinetics of destabilized asphaltenes. *Advances in Colloid and Interface Science* **244.** Special Issue in Honor of the 90th Birthday of Prof. Eli Ruckenstein, 267–280 (2017).

213. Vitale, S. A. & Katz, J. L. Liquid droplet dispersions formed by homogeneous liquid- liquid nucleation:"The Ouzo effect". *Langmuir* **19,** 4105–4110 (2003).

214. Volk, A. & Kähler, C. J. Density model for aqueous glycerol solutions. *Experiments in Fluids* **59,** 1–4 (2018).

215. Wang, H. *et al.* Ultrasensitive Picomolar Detection of Aqueous Acids in Microscale Fluorescent Droplets. *ACS sensors* (2021).

216. Wang, J. & Buckley, J. S. Asphaltene Stability in Crude Oil and Aromatic SolventsThe Influence of Oil Composition. *Energy & Fuels* **17,** 1445–1451 (2003).

217. Wang, S., Liu, J., Zhang, L., Masliyah, J. & Xu, Z. Interaction forces between asphaltene surfaces in organic solvents. *Langmuir* **26,** 183–190 (2010).

218. Wang, S., Liu, J., Zhang, L., Xu, Z. & Masliyah, J. Colloidal interactions between asphaltene surfaces in toluene. *Energy & Fuels* **23,** 862–869 (2009).

219. Wang, T. *et al.* In situ observation of nucleation and crystallization of a single nanoparticle in transparent media. *The Journal of Physical Chemistry C* **124,** 15533–15540 (2020).

220. Wang, Y.-W., Kim, Y.-Y., Stephens, C., Meldrum, F. & Christenson, H. In situ study of the precipitation and crystallization of amorphous calcium carbonate (ACC). *Crystal Growth & Design* **12,** 1212–1217 (2012).

221. Wang, Y., Zeng, B., Zhao, Y., Li, S. & Zhang, X. Formation of polystyrene microlenses via transient droplets from the ouzo effect for enhanced optical imaging. *The Journal of Physical Chemistry C* **123,** 14327–14337 (2019).

222. Wang, Z., Nan, J., Ji, X. & Yang, Y. Effect of the micro-flocculation stage on the flocculation/sedimentation process: The role of shear rate. *Science of The Total Environment* **633,** 1183–1191 (2018).

223. Wang, Z., Zhang, L., Liu, J., Jiang, H. & Li, C. Flexible hemispheric microarrays of highly pressure-sensitive sensors based on breath figure method. *Nanoscale* **10,** 10691–10698 (2018).

224. Wattana, P., Fogler, H. S., Yen, A., Carmen García, M. D. & Carbognani, L. Characterization of polarity-based asphaltene subfractions. *Energy & Fuels* **19,** 101–110 (2005).

225. Wattana, P., Wojciechowski, D. J., Bolaños, G. & Fogler, H. Study of asphaltene precipitation using refractive index measurement. *Petroleum Science and Technology* **21,** 591–613 (2003).

226. Weijgertze, H. M., Kegel, W. K. & Zanini, M. Patchy rough colloids as Pickering stabilizers. *Soft Matter* **16,** 8002–8012 (2020).

227. Wiehe, I. A., Yarranton, H. W., Akbarzadeh, K., Rahimi, P. M. & Teclemariam, A. The paradox of asphaltene precipitation with normal paraffins. *Energy & Fuels* **19,** 1261–1267 (2005).

228. Xia, H., Wan, S., Shu, C. & Chew, Y. Chaotic micromixers using two-layer crossing channels to exhibit fast mixing at low Reynolds numbers. *Lab on a Chip* **5,** 748–755 (2005).

229. Xu, C. *et al.* Synthesis of graphene from asphaltene molecules adsorbed on vermiculite layers. *Carbon* **62,** 213–221 (2013).

230. Xu, C. *et al.* Collective interactions in the nucleation and growth of surface droplets. *Soft Matter* **13,** 937–944 (2017).

231. Xu, M., Zhou, Z., Wang, Z. & Lu, H. Self-assembled microlens array with controllable focal length formed on a selective wetting surface. *ACS Applied Materials & Interfaces* **12,** 7826–7832 (2020).

232. Xu, Y. Asphaltene Precipitation in Paraffinic Froth Treatment: Effects of Solvent and Temperature. *Energy & Fuels* **32,** 2801–2810 (2018).

233. Xuan, W., Wang, H. & Xia, D. In-situ observation of crystallization inside coal slags and influence of crystals on flow behavior. *Fuel* **251,** 242–248 (2019).

234. Yang, Z. *et al.* Effect of precipitating environment on asphaltene precipitation: precipitant, concentration, and temperature. *Colloids and Surfaces A: Physicochemical and Engineering Aspects* **497,** 327–335 (2016).

235. Yarranton, H. W. *et al.* On the size distribution of self-associated asphaltenes. *Energy & Fuels* **27,** 5083–5106 (2013).

236. Yarranton, H. W., Alboudwarej, H. & Jakher, R. Investigation of Asphaltene Association with Vapor Pressure Osmometry and Interfacial Tension Measurements. *Industrial & Engineering Chemistry Research* **39,** 2916–2924 (2000).

237. Yasuga, H., Kamiya, K., Takeuchi, S. & Miki, N. Self-generation of two-dimensional droplet array using oil–water immiscibility and replacement. *Lab on a Chip* **18,** 1130–1137 (2018).

238. You, J. B., Lohse, D. & Zhang, X. Tuning Composition of Multicomponent Surface Nanodroplets in a Continuous Flow-In System. *Advanced Materials Interfaces* **8,** 2101126 (2021).

239. Yu, H., Lu, Z., Lohse, D. & Zhang, X. Gravitational effect on the formation of surface nanodroplets. *Langmuir* **31,** 12628–12634 (2015).

240. Yu, H., Maheshwari, S., Zhu, J., Lohse, D. & Zhang, X. Formation of surface nanodroplets facing a structured microchannel wall. *Lab on a Chip* **17,** 1496–1504 (2017).

241. Yu, H. *et al.* Formation of surface protic ionic liquid nanodroplets for nanofabrication. *Advanced Materials Interfaces* **7,** 1901647 (2020).

242. Yudin, I. *et al.* Mechanisms of asphaltene aggregation in toluene–heptane mixtures. *Journal of Petroleum Science and Engineering* **20,** 297–301 (1998).

243. Zahabi, A., Gray, M. R., Czarnecki, J. & Dabros, T. Flocculation of silica particles from a model oil solution: effect of adsorbed asphaltenes. *Energy & Fuels* **24,** 3616–3623 (2010).

244. Zanganeh, P., Dashti, H. & Ayatollahi, S. Visual investigation and modeling of asphaltene precipitation and deposition during CO2 miscible injection into oil reservoirs. *Fuel* **160,** 132–139 (2015).

245. Zanganeh, P., Dashti, H. & Ayatollahi, S. Comparing the effects of CH4, CO2, and N2 injection on asphaltene precipitation and deposition at reservoir condition: A visual and modeling study. *Fuel* **217,** 633–641 (2018).

246. Zemb, T. N. *et al.* How to explain microemulsions formed by solvent mixtures without conventional surfactants. *Proceedings of the National Academy of Sciences* **113,** 4260–4265 (2016).

247. Zeng, B., Wang, Y., Zhang, X. & Lohse, D. Solvent exchange in a hele–shaw cell: Universality of surface nanodroplet nucleation. *The Journal of Physical Chemistry C* **123,** 5571–5577 (2019).

248. Zeng, H. *et al.* Droplet enhanced fluorescence for ultrasensitive detection using inkjet. *Analytical Chemistry* **88,** 6135–6139 (2016).

249. Zhang, A., Bai, H. & Li, L. Breath figure: A nature-inspired preparation method for ordered porous films. *Chemical Reviews* **115,** 9801–9868 (2015).

250. Zhang, C., Pansare, V. J., Prud'Homme, R. K. & Priestley, R. D. Flash nanoprecipitation of polystyrene nanoparticles. *Soft Matter* **8,** 86–93 (2012).

251. Zhang, H.-L., Bucknall, D. G. & Dupuis, A. Uniform nanoscopic polystyrene patterns produced from a microscopic mold. *Nano Letters* **4,** 1513–1519 (2004).

252. Zhang, R., Liao, W., Sun, Y., Heng, J. Y. & Yang, Z. Investigating the role of glass and quartz substrates on the formation of interfacial droplets. *The Journal of Physical Chemistry C* **123,** 1151–1159 (2018).

253. Zhang, R., Wang, Y. & Yang, Z. Spatially arranging interfacial droplets at the oil–solid interface. *Soft Matter* **16,** 107–113 (2020).

254. Zhang, X. H. & Ducker, W. Formation of interfacial nanodroplets through changes in solvent quality. *Langmuir* **23,** 12478–12480 (2007).

255. Zhang, X. H., Quinn, A. & Ducker, W. A. Nanobubbles at the interface between water and a hydrophobic solid. *Langmuir* **24,** 4756–4764 (2008).

256. Zhang, X., Wei, Z., Choi, H., Hao, H. & Yang, H. Oiling-Out Crystallization of Beta-Alanine on Solid Surfaces Controlled by Solvent Exchange. *Advanced Materials Interfaces* **8,** 2001200 (2021).

257. Zhang, X. *et al.* From transient nanodroplets to permanent nanolenses. *Soft Matter* **8,** 4314–4317 (16 2012).

258. Zhang, X. *et al.* Formation of surface nanodroplets under controlled flow conditions. *Proceedings of the National Academy of Sciences* **112,** 9253–9257 (2015).

259. Zhang, X. *et al.* Propelling microdroplets generated and sustained by liquid–liquid phase separation in confined spaces. *Soft Matter* (2021).

260. Zhang, Y. & Wang, C. Micropatterning of proteins on 3D porous polymer film fabricated by using the breath-figure method. *Advanced Materials* **19,** 913–916 (2007).

261. Zhang, Y. *et al.* Understanding the effects of sample preparation on the chemical structures of petroleum imaged with noncontact atomic force microscopy. *Industrial & Engineering Chemistry Research* **57,** 15935–15941 (2018).

262. Zhao, B. & Shaw, J. M. Composition and size distribution of coherent nanostructures in Athabasca bitumen and Maya crude oil. *Energy & Fuels* **21,** 2795–2804 (2007).

263. Zhigaltsev, I. V. *et al.* Bottom-up design and synthesis of limit size lipid nanoparticle systems with aqueous and triglyceride cores using millisecond microfluidic mixing. *Langmuir* **28,** 3633–3640 (2012).

264. Zhu, Q. *et al.* Prediction of mutual diffusion coefficients in binary liquid systems with one self-associating component from viscosity data and intra-diffusion coefficients at infinite dilution. *Chemical Engineering Science* **147,** 118–127 (2016).

265. Zi, M., Wu, G., Wang, J. & Chen, D. Investigation of gas hydrate formation and inhibition in oil-water system containing model asphaltene. *Chemical Engineering Journal* **412,** 128452 (2021).

Appendix A

List of Terms

Nano-aggregates: Aggregates formed by $\sim$ 6 asphaltene molecules, which have a single disordered stack in the interior with peripheral alkane.

Clusters: Clusters formed by $\sim$ 8 nano-aggregates.

Nanocolloids: a collective term for nano-aggregates and clusters.

Primary submicron particles (PSMPs): Asphaltene particles with an equivalent radius of 0.2 to 0.4 microns.

Fractal aggregates: Asphaltene particles with an equivalent radius larger than 0.4 microns.

Appendix B

Supporting Information for Chapter 3

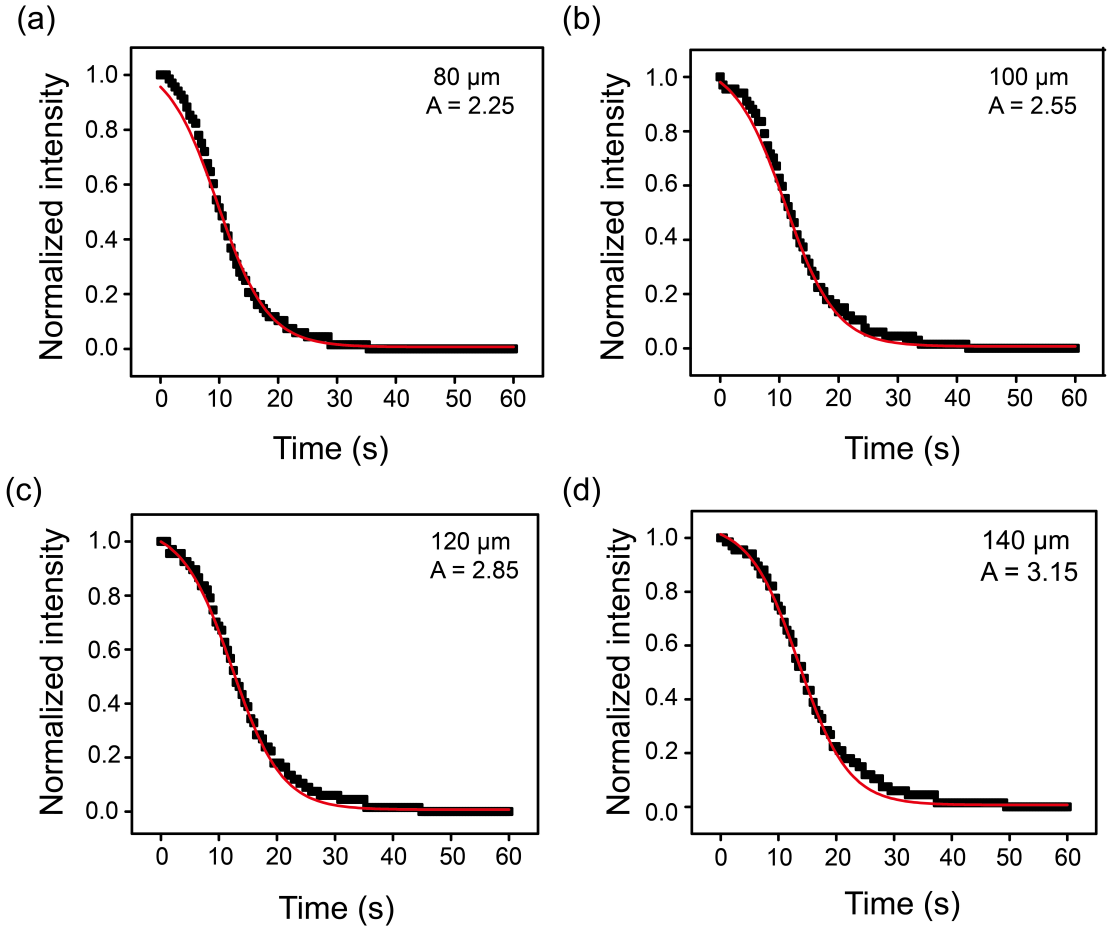

Figure B.1: Fitting of n-pentane normalized intensity relationship with time at different distance to the side channel: c) 80 μm, d) 100 μm, e) 120 μm, f) 140 μm.

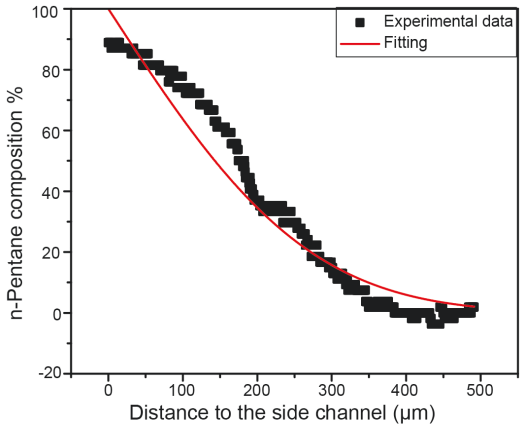

Figure B.2: Normalized intensity distribution along x-direction at 20 s and fitting by error function.

Appendix C

Supporting Information for Chapter 4

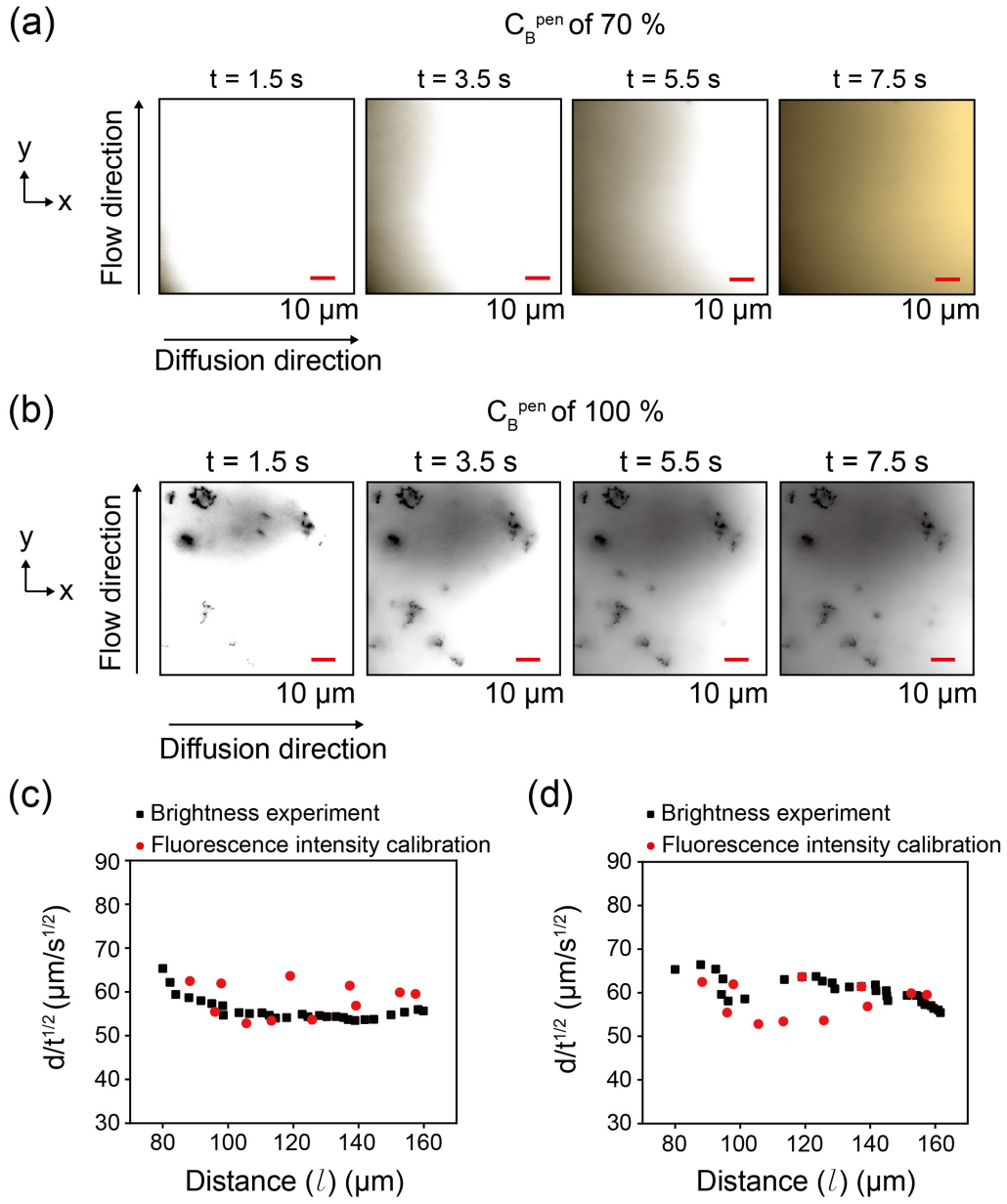

Figure C.1: a) Snapshots of background brightness change during solvent mixing process observed by TIRF microscope. Note: the images have been false-colored. b) Snapshots of asphaltene gradually precipitation with n-pentane diffusion. Asphaltene starts to precipitate in this process and form black dots in the images. c) Comparison between the gray front movement $d/\sqrt{t}$ at the concentration of n-pentane in solution B (C_B^{pen}) of 70 % with the characterization experiment with fluorescence calibration. d) Comparison between the gray front movement $d/\sqrt{t}$ at the concentration of n-pentane in solution B (C_B^{pen}) of 100 % with the characterization experiment with fluorescence calibration.

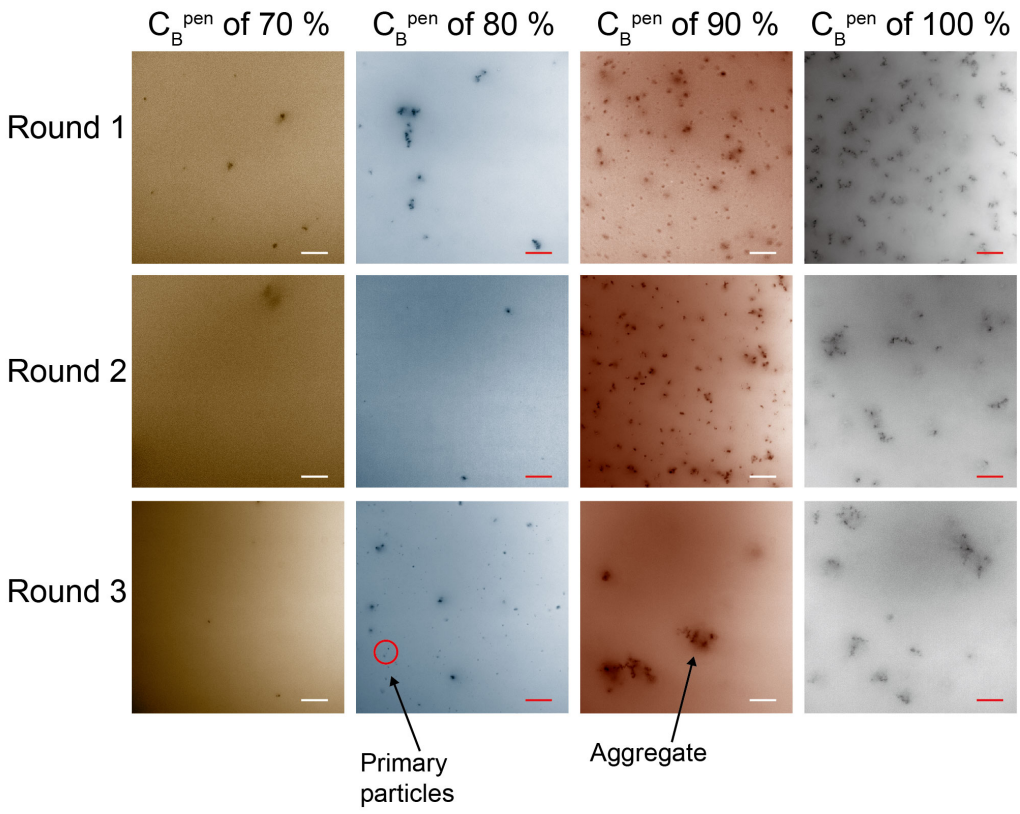

Figure C.2: Three rounds of experiments to show the primary particles co-exist with aggregates. Scale bar is 10 μm

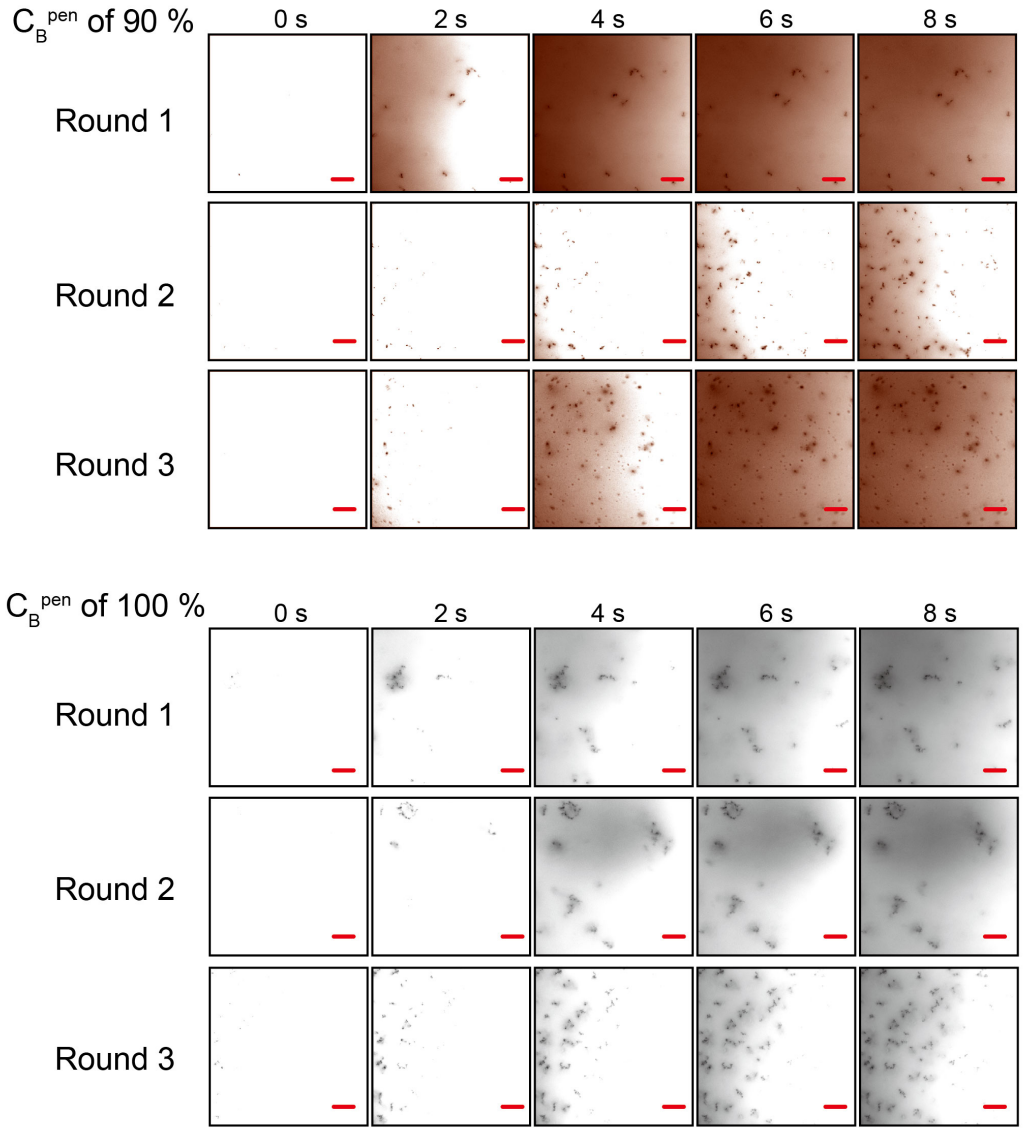

Figure C.3: Three rounds of experiments to show the growth dynamics of asphaltene particles at the concentration of n-pentane in solution B (C_B^{pen}) of 90 % and 100 %. Scale bar is 10 μm.

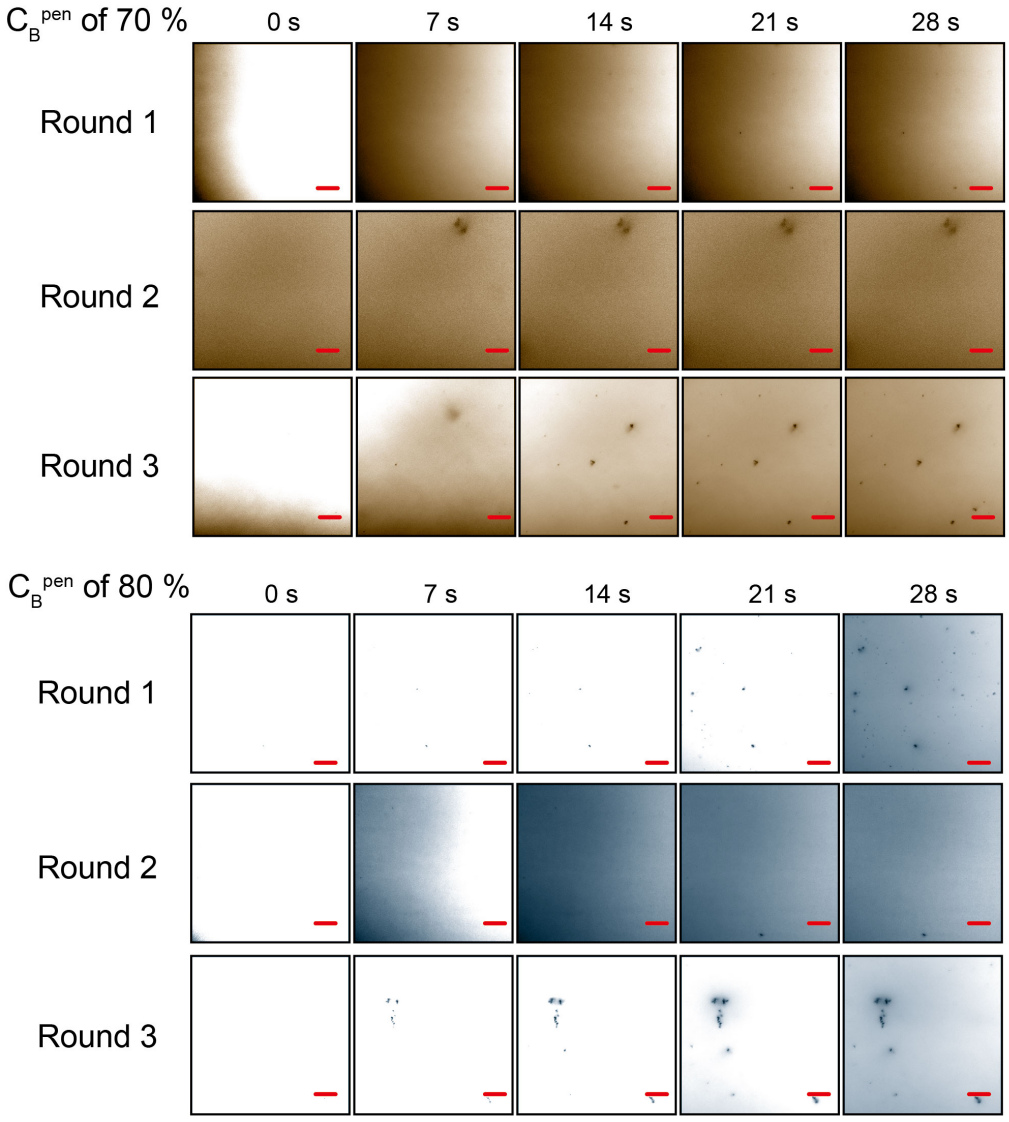

Figure C.4: Three rounds of experiments to show the growth dynamics of asphaltene particles at the concentration of n-pentane in solution B (C_B^{pen}) of 70 % and 80 %. Scale bar is 10 μm.

Appendix D

Supporting Information for Chapter 5

D.1 Optical images of asphaltene particles precipitate from bitumen

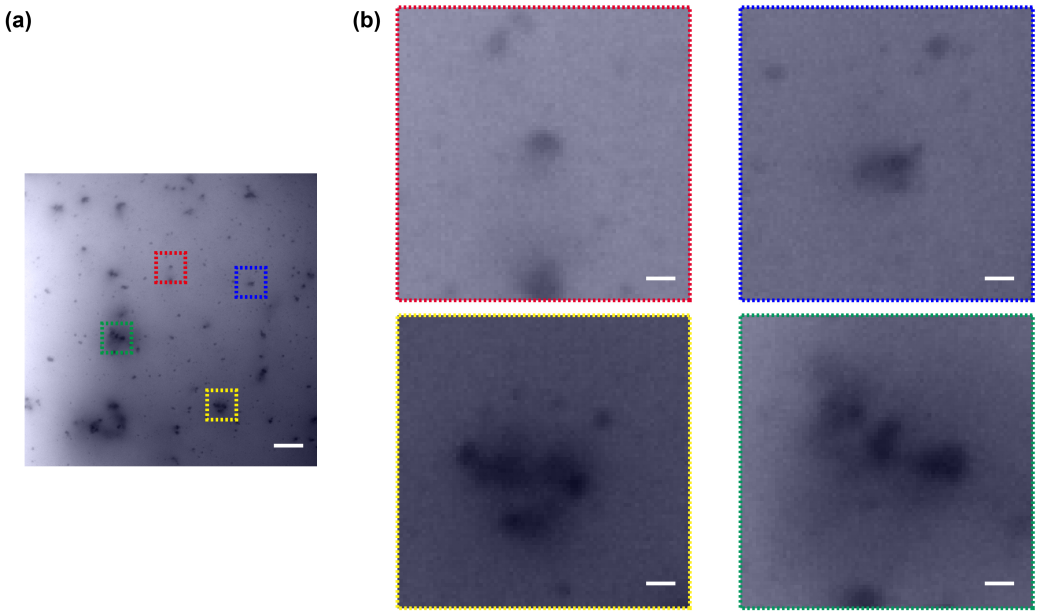

Figure D.1: a) TIRF images of asphaltene particles at 5 *min* from bitumen. Precipitation is induced by heptane. The length of the scale bar is 10 μm. b) Zoomed-in images of primary sub-micron particles in a) at locations with respective color boxes. The length of the scale bar is 1 μm. The images are false-colored.

D.2 AFM images of asphaltene particle precipitated by mixing heptane with asphaltene solution

One of our sample (asphaltene precipitation induced by n-heptane) was examined by an atomic force microscopy (AFM) (Bruker diInnova) tapping mode. AFM images were obtained with a cantilever and the 3D image was obtained by image analysis of NanoScope Analysis 1.5 (Brucker, Corp., US). However, AFM cannot track the asphaltene precipitation in-situ. The AFM pictures were captured under dry state.

As shown in Figure D.2, no particles smaller than PSMP are observed. The size of PSMPs was around 100 to 200 nm in radius, which was slightly smaller than the observation by TIRF of asphaltene particles in solvent. This size shrinkage was caused by the swelling of asphaltene in solvents [192].

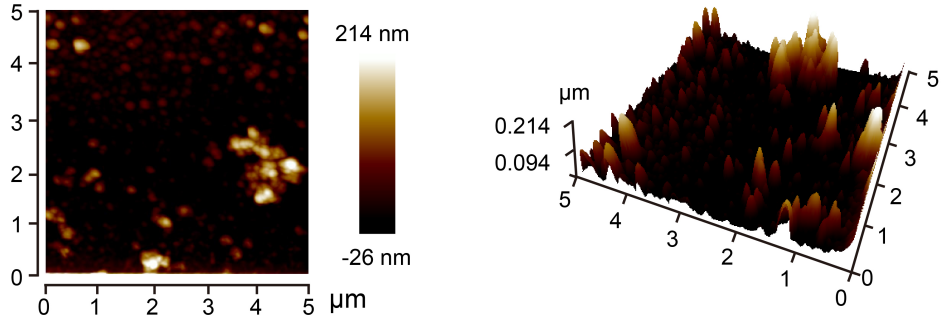

Figure D.2: 2D and 3D AFM images to show the asphaltene particles at the final state.

D.3 Chemical structure of the asphaltene particles precipitated in different types of solvents

Confocal laser scanning microscope (Leica TCS SP5, Mannheim, Germany) was used to measure the emission spectrum of asphaltene particles. An Argon laser was used to excite the samples. The intensity of the fluorescence emission was measured at a 5 nm interval from 500 nm to 700 nm and the fluorescence

spectrum was plotted within the range of wavelength.

Figure D.3 shows the fluorescence spectra for asphaltene particles precipitated in different types of alkanes and their mixture with toluene, as well as the mixture of heptane and decane. The spectra are normalized with three particles of each condition. Under 488 nm excitation, all spectra show a wide band from 500 nm to 700 nm. The wideband attributes to the chemical structure complexity of asphaltene molecules.

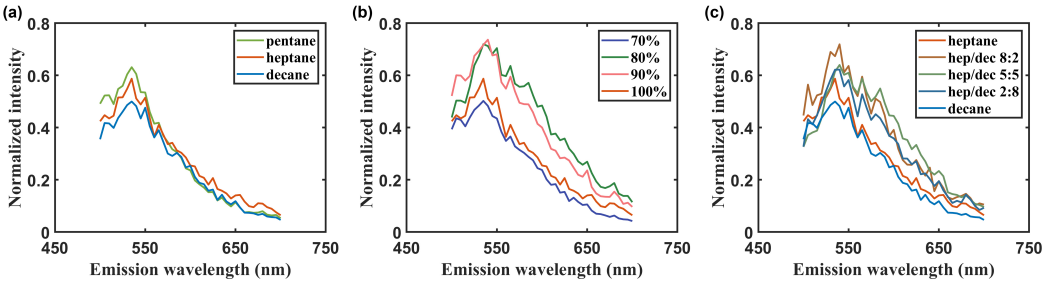

Figure D.3: Fluorescence spectrum of asphaltene particles precipitated under a) different types of solvents, b)heptol with different heptane concentrations, and c) heptane-decane mixtures with different heptane concentrations.

The highest peak always appears at around 540 nm. Primary sub-micron particles and large aggregates have similar spectra, indicating the chemical structure of these two types of particles do not have different chemical structures.

D.4 Estimation of mutual diffusion coefficients

Mutual diffusivities of toluene-alkane binary mixtures were approximated using a modified Darken model [11, 264].

$$D_{ij} = \left(x_j D_i^* + x_i D_j^*\right) \Gamma \tag{D.1}$$

The Darken model includes a thermodynamic correction factor (Γ) which considers the change in activity coefficient (γ_i) of the solute within a chemical potential gradient. The activity coefficient values were obtained at $T = 298.15K$ using the UNIFAC thermodynamic model within the software package Symmetry (Figure D.4a) [180]. The simulation results, including activity

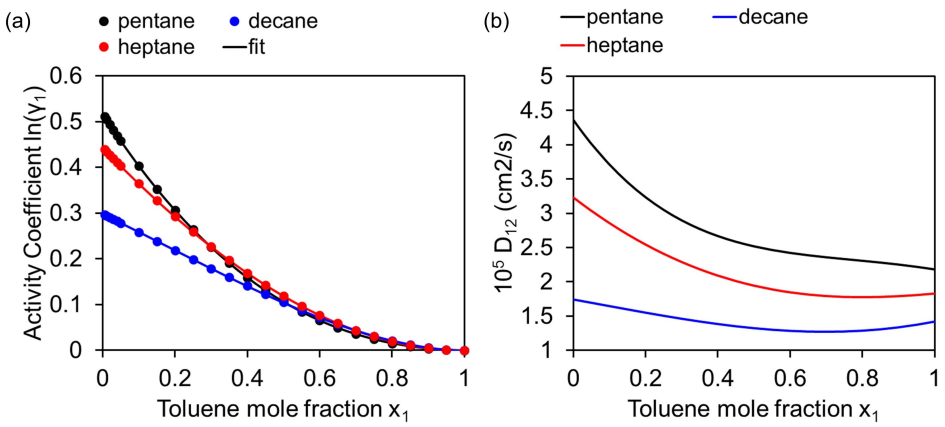

Figure D.4: a) Calculated activity coefficients in binary toluene-alkane mixtures at 298.15 K with UNIFAC. b) Diffusion coefficients of toluene in different alkanes and mixture compositions.

and diffusion coefficients are validated by comparing with the experimental value reported in the previous literature [19, 81, 151]. Values were fit to polynomial equations to obtain their derivative for Γ calculations as a function of mixture composition.

$$\Gamma = 1 + x_i \left(\frac{\partial \ln \gamma_i}{\partial x_i} \right) \tag{D.2}$$

The self-diffusion coefficients (D_1^* and D_2^*) in the Darken model (Equation D.1) were approximated using the Wilke-Chang equation for binary liquids (Equation D.3). M_j, T, μ_j and $V_{i,BP}$ represent the molecular weight of the solvent, temperature, solvent viscosity, and molar volume of solute at normal boiling point conditions, respectively. The pure compound properties summarized in Table D.1 were obtained from the NIST database. The association factor $\psi_j = 1.0$ for unassociated solvents.

$$D_i^* = \frac{7.4 \times 10^{-8} \left(\psi_j M_j\right)^{0.5} T}{\mu_j \times V_{i,BP}^{0.6}} \tag{D.3}$$

The simulation values were validated with experimental data reported in the literature, as shown in Table. D.2. The simulation values were very close to the reported experimental values. Therefore, our UNIFAC simulation was reliable and the diffusion coefficients were verified.

Table D.1: Pure compound properties obtained from NIST for each species [72, 107].

Compound	Formula	M (g/mol)	T_{BP} (K)	V_{BP} (cm^3/mol)	μ (cp)
Toluene	C_7H_8	92.14	383.8	118.26	0.558
Pentane	C_5H_{12}	72.15	309.2	118.33	0.245
Heptane	C_7H_{16}	100.20	371.5	163.14	0.390
Decane	$C_{10}H_{22}$	142.28	447.3	235.60	0.848

Table D.2: Comparison between reported experimental and UNIFAC simulation values of activity and diffusion coefficient

Activity			Diffusion coefficient (m^2/s)		
	Experimental value in literature [151]	Simulation value		Experimental value in literature [19, 81]	Simulation value
Toluene in n-pentane	1.944	1.67	n-decane in toluene	1.85×10^{-9}	1.46×10^{-9}
Toluene in n-heptane	1.511	1.55	Toluene in n-heptane	3.24×10^{-9}	3.23×10^{-9}
Toluene in n-decane	1.262	1.35			

Appendix E

Supporting Information for Chapter 6

Below we show the scheme for solvent exchange process using custom-built chamber. The fluid chamber is sealed by four clamps. Solution A and B are injected continuously into the fluid chamber to form nanodroplets on the substrate. The solvent exchange is processed vertically to avoid gravity effect. The inlet is connected a syringe filled with Solution B. A syringe pump is used to control the injection rate. The outlet is connected to a residue flask.

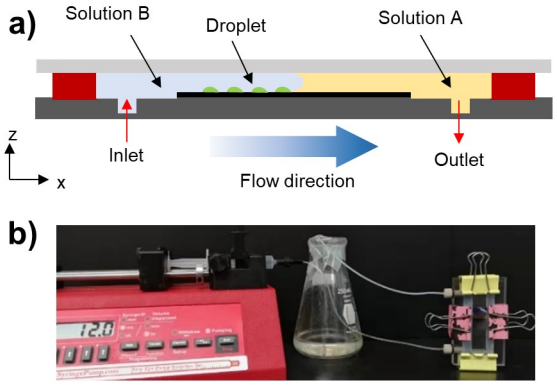

Figure E.1: a) Schematic showing the solvent exchange process using custom-built chamber. Solution A and B are injected continuously into the chamber to form surface nanodroplets. b) Image showing the vertical setup for removing the influence of gravity during solvent exchange.

Appendix F

Supporting Information for Chapter 7

F.1 Large asphaltene layer

When the channel height of the microfluidic chamber is 1000 μm, we noted the formation of large asphaltene layer, as shown in Figure F.1(b). The corresponding COMSOL simulation is shown in Figure F.2.

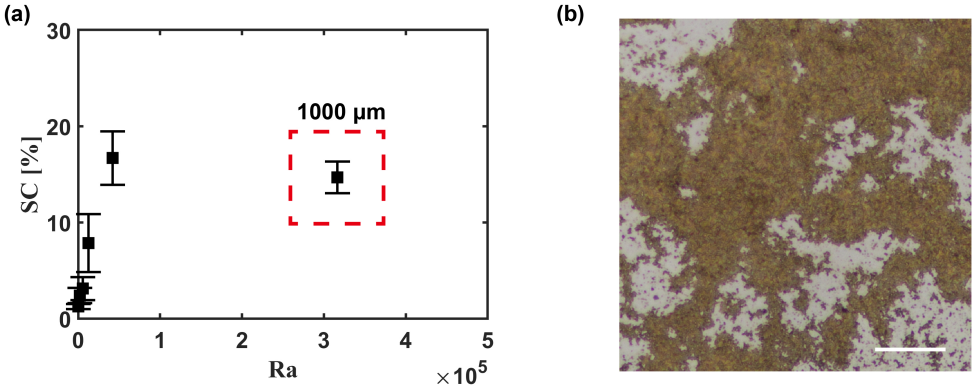

Figure F.1: (a) SC of asphaltene at the final state as a function of Rayleigh number. The red-colored point is 1000 μm channel height. (b) Optical image of layer of sediments in the 1000 μm channel height. The length of the scale bar is 50 μm.

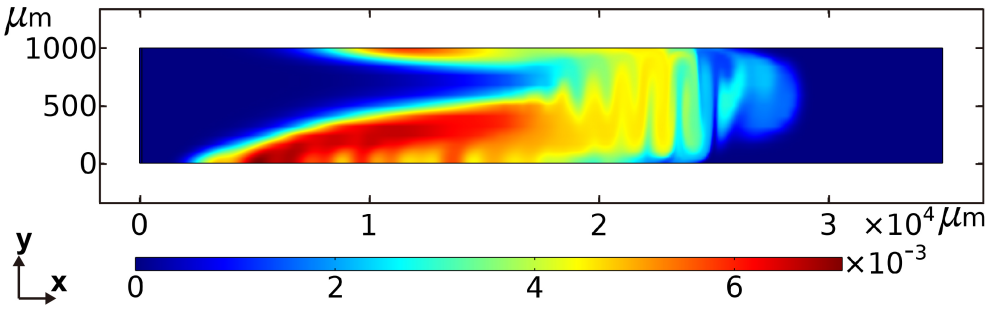

Figure F.2: COMSOL simulations for the profile of the pulse of oversaturation in horizontally placed 1000 μm microchannel.The black arrow shows the stack-like convective rolls

Table F.1: Mesh details for the grid independence study

Grid	Total number of elements	Number of boundary elements	Maximum element size (mm)	Average mesh quality (skewness)	Difference (%) w.r.t. G7
G1	3,500	730	0.1000	1.0	4.06
G2	6,552	978	0.0750	1.0	2.81
G3	14,000	1,460	0.0500	1.0	1.76
G4	25,218	1,949	0.0375	1.0	1.34
G5	35,008	2,248	0.0320	1.0	0.95
G6	56,000	2,920	0.0250	1.0	0.51
G7	224,000	5,840	0.0125	1.0	-

F.2 COMSOL simulation parameters at different temperatures

Density and viscosity of n-heptane and toluene at different temperatures were obtained from the literature, as summaried in Table F.2.

Mutual diffusion coefficients of toluene and n-heptane binary mixture at different temperatures were calculated as the same method as we used in the previous study [132]. The estimated diffusion coefficients at different temperatures are summarized in Figure F.5.

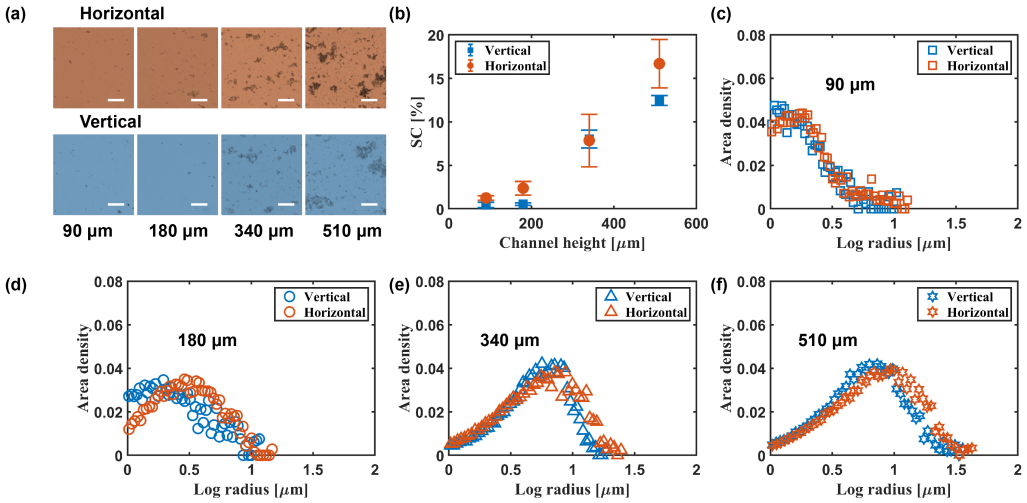

Figure F.3: (a) Optical images of asphaltene at the final state in vertical and horizontally placed devices. The channel heights are 90 μm, 180 μm, 340 μm, and 510 μm from left to right. The length of the scale bar is 20 μm. The images are false-colored. (b) Comparison of SC of vertically and horizontally place devices. Size distribution of asphaltene particles in vertically and horizontally placed devices with channel heights of (c) 90 μm, (d) 180 μm, (e) 340 μm, and (f) 510 μm.

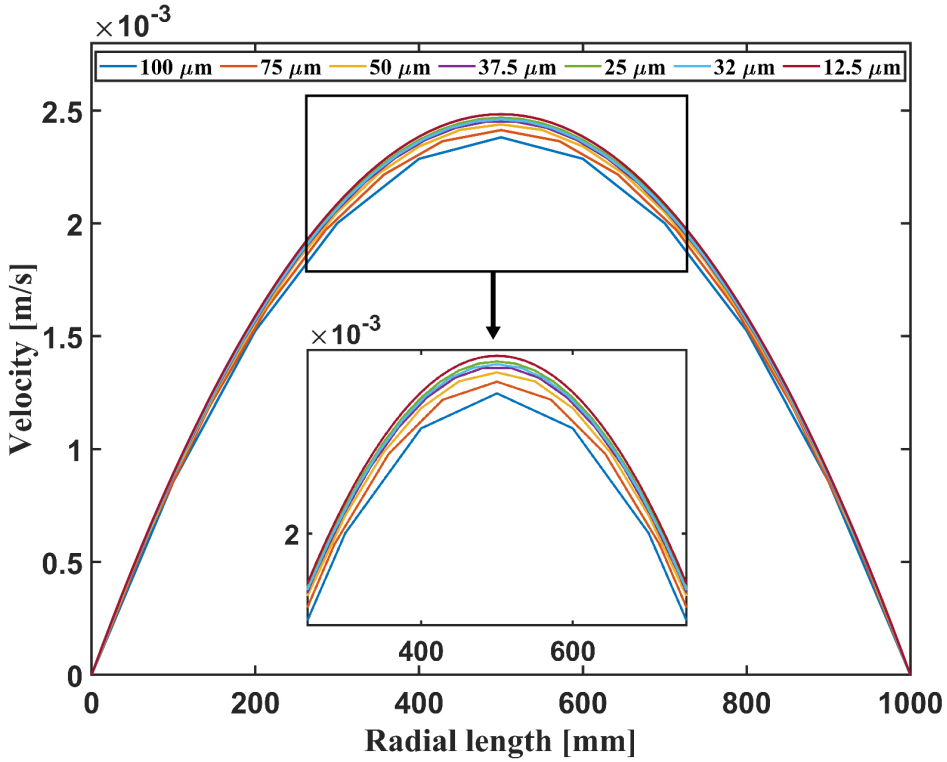

Figure F.4: Influence of grid numbers on the inlet velocity profiles along the radial direction.

Table F.2: Density and viscosity of n-heptane and toluene at different temperatures

	Density (g/cm^3)		Viscosity $(mPa \cdot s)$	
	n-Heptane	Toluene	n-Heptane	Toluene
20 °C	0.684 [54]	0.867 [67]	0.417 [54]	0.590 [179]
35 °C	0.671 [155]	0.853 [67]	0.348 [178]	0.494 [179]
50 °C	0.658 [92]	0.839 [67]	0.315 [92]	0.422 [179]
58 °C	0.649 [178]	0.832 [67]	0.275 [178]	0.390 [179]
65 °C	0.645 [178]	0.825 [67]	0.264 [178]	0.365 [179]

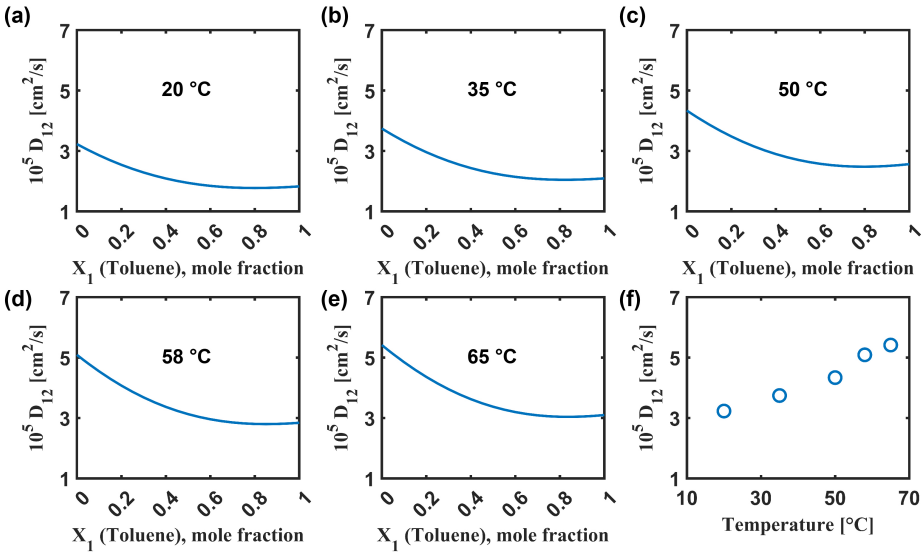

Figure F.5: Diffusion coefficients of toluene in n-heptane at (a) 20 $°C$, (b) 35 $°C$, (c) 50 $°C$, (d) 58 $°C$, (e) 65 $°C$. Diffusion coefficient of toluene in n-heptane vs. temperature.